Fundamental investigation of the rearrangement and detachment of particle structures on/from stretchable filter fibers

Zur Erlangung des akademischen Grades eines

Doktors der Ingenieurwissenschaften (Dr.-Ing.)

von der KIT-Fakultät für
Chemieingenieurwesen und Verfahrenstechnik
des Karlsruher Instituts für Technologie (KIT)
genehmigte

Dissertation

von
M. Sc. Lukas Matthias Poggemann
aus Witten

Tag der mündlichen Prüfung: 23.09.2024

Erstgutachter: Prof. Dr.-Ing. habil. Achim Dittler
Zweitgutachter: Prof. Dr.-Ing. Sergiy Antonyuk

Abstract

Depth filters are used in air conditioning, clean rooms, and process technology to remove particles from gas flow. Particle separation occurs inside the filter, first on the individual fibers and then in the porous structure of the fiber matrix. As the operating time increases, particle material accumulates in the filter, leading to an increase in pressure drop and subsequently, increased energy consumption. Finally, the filter is replaced to minimize the increased pressure drop and make room for new particle material to be separated. The development of pressure drop is an indicator of the energy consumption during the filtration process. The development of the pressure drop and the critical pressure drop determine the service life of a fibrous filter. In fibrous filters particle separation occurs in the upper third of the filter, starting from the upstream side. Regeneration of fibrous filters is not common. The particle material within the filter is inhomogeneously distributed, which affects separation efficiency and increase of pressure drop during the filtration process. However, to address this issue, a possible solution is to transfer particulate material from the upstream area, first third of the filter, to the empty space downstream of the filter before the critical pressure drop is reached.

The desired method to enable this transfer is to stretch the collector and introduce shear and tensile stress into the separated particle structure while applying a low velocity airflow. Stretching the collector as an external excitation is intended to lower the threshold for detachment of particle structures by the air flow. A detailed understanding of the rearrangement and detachment of particle material induced by stretching is necessary for a successful implementation of this method in an entire future filter system. To gain a comprehensive understanding of the micromechanical processes, experiments are conducted on simplified collector models of a depth filter, such as a stretchable single fiber and a stretchable fiber array. The detachment of separated particle structures from a filtration collector contradicts the actual concept of a filter, nevertheless previous studies have already investigated and obtained the detachment of particles from a non-stretchable (stiff) single fibers induced by air flow above the normal level of filtration. In this study the non-stretchable (stiff) fiber did

not initiate any rearrangement or detachment of particle structures. For investigation with a stretchable single fiber or fiber array, there are currently no studies available on the rearrangement and detachment of particle structures. The main objective of this work (dissertation) is to evaluate the influence of process parameter such as flow velocity, stretching velocity, and particle structure morphology on the rearrangement and detachment of particle structures from a stretchable filter fiber and from a stretchable fiber array.

The investigation in this work are performed in five consecutive steps which evaluate the rearrangement and detachment of particle structures on a single fiber (micro level) and on a more complex fiber array (meso level). The different steps are based on five different experimental studies.

The evaluation of process parameters, such as flow velocity and stretching velocity, during a single stretching cycle with a single stretchable fiber (micro level) and a compact particle structure is the focus of the first step. To stretch the fiber, a special fiber clamping device was developed. The experiments showed that particle structures are rearranged and detached at flow velocities of less than $1\,m\,s^{-1}$ and simultaneous stretching at different stretching velocities. During the experiments, it was observed that the particle structure on the fiber is rearranged radial and rotates with the fiber regardless of the stretching velocity and flow velocity. Additionally, the experiments obtained that the V-cracks develop always from the top of the particle structure on the fiber during stretching. Only minimal detachment of particle structures was observed without a simultaneous air flow and fiber stretching only. In the experiments was obtained that a residual structure remains on the fiber after detachment of large particle structures from the fibers during one stretching cycle.

In the second step, AFM measurements are conducted to measure the adhesion force between particles of spheriglass and polystyrene and the fiber in various stretching states. This is done to estimate the ratio of adhesion force between the fiber and the particle and the contact of particle-particle. A reduction in the adhesive force between the particle and fiber was observed in the adhesive force measurements with the AFM, which could be attributed to an increase in fiber elongation. In order to identify the underlying cause of this phenomenon, the surface roughness of the polyurethane filter fiber was characterized in different stretching states using an AFM and white light interferometry. These experiments revealed a significant increase in surface roughness when the fiber was stretched. The adhesion force measurement results indicate that the reduction in adhesion force between a single particle and the fiber is a function of the increase in surface roughness. As with these experiments in this work, models can be used to quantify this phenomenon. Nevertheless, the ratio of adhesive force is more favorable for the bond between particle and fiber in every stretching state than between particle and particle.

In the third step, the size and moment of detachment of the detached particle structures is determined during five consecutive stretching cycle of a single fiber (micro level). Additionally, the cumulative fraction of the detached particulate structure is determined after each stretching cycle. Before the start of fiber stretching (5 stretching cycle), a compact particle structures of different size is separated on the fiber. To detect detached particle structures directly below the fiber and observe the cracking of the particle structure on the fiber during stretching, a laser light sheet measurement technique based on the detection principle of scattered light including a camera technique was established. The stretching experiments obtained that the detachment of particle structures is strongly influenced by the air flow velocity. An increase in the air flow velocity from $0.05\,m\,s^{-1}$ to $0.8\,m\,s^{-1}$ resulted in a shift for the moment of the detachment from 20 to 38.7 % to 0 to 15 % fiber stretching. Furthermore, it was found that even with a low fiber flow velocity of $0.05\,m\,s^{-1}$, the particle structure could be completely detached by repeated stretching with stretching velocities between 0.6 to $12\,mm\,s^{-1}$. Further, the experiments revealed that the detached particle structures of the first stretching cycle are larger than those of the following four stretching cycles. Additionally, the experiments revealed a correlation between the local V-shaped cracking of the particle structure, the observed residual structures on the fiber, and the failure of cohesion and adhesion within the particle structure on the fiber. These observations provide indirect evidence of the effect of the measured adhesive forces between particles, particles, and particle-fiber in the context of the stretching experiment.

In the fourth step the focus is on the separation of a particle structure on a fiber array (meso level). The separation process of dendritic and compact particle structures (St=0.52 - 10.05) on the fiber array and in the fiber interspaces is evaluated using in situ image analysis in the direction of flow. The evaluation is performed until a TIF (time integrated flow) of $2.8 \cdot 10^8\,\#\,mm^{-2}$ is reached where some particle structures on the fiber array are clogged. The combination of observing the growth of the particle structure during separation on the fiber array and weighing the particle mass on the fiber array results in a growth kinetics for a particle structure of different morphology on an array. Differences can be observed between compact particle structure with large mass and dendritic particle structure with large and wide form (in direction of flow) but with less mass due to high porosity. Automated MATLAB© image analysis is used to determine the size and number of particle bridges between neighboring fibers as well as the growth of pores in the interspaces of the inner fibers of the array. The image analysis identifies characteristic features, such as the widely branched dendritic particle structure on the array with a rapid growth of small pores. The size of pores ranged from 3 to $78\,\mu m$. In contrast, the growth of the compact structures resulted in large bridges of up to $270\,\mu m$ along the fiber axis.

The fifth step focuses on rearranging and detaching particle structures from a fiber array (meso level) during five consecutive stretching cycles. The moment of detachment and size of the detached structures are determined using a laser light sheet measurement technique, as in the experiments with a single fiber and five consecutive stretching cycles. An image analysis was used to determine the relative free projection area in the fiber interspaces, providing information on the free flowable area between the fibers of the fiber array. Furthermore, a qualitative analysis of the crack patterns and particle structure rearrangement was conducted based on their morphology (compact or dendritic) and growth state (non-clogged or clogged). The flow velocity and stretching velocity chosen for the stretching test with a fiber are based on the results obtained from experiments with single fibers and ranged between $0.05\,m\,s^{-1}$ and $0.8\,m\,s^{-1}$. The stretching velocity varied between $0.6\,mm\,s^{-1}$ and $1.2\,mm\,s^{-1}$. As in the experiments with a single fiber, rearrangement and subsequent detachment of the particle structure from the fiber array were observed. In some cases, radial rearrangement and rotation of the particle structures were also detected. A modification was made to the fiber clamping device to adjust the distance between fibers in the array during stretching, allowing a transition from uniaxial to biaxial stretching with the fiber clamping device. This modification enables the generation of a stress with shear and tensile forces in the clogged particle structure on the fiber array. This results in noticeable crack patterns and detachment of particle structures, that could not be observed before with a clogged structure with simple uniaxial stretching

The presented five steps provide experimental results that help to quantify the influencing factors on the rearrangement and detachment of particle structures during the stretching procedure of a single fiber (micro level) and a filter array (meso level). Based on this, the present work contributes significantly to the future of fundamental investigations on a complete stretchable filter (macro level) and lead the way to an optimization of the filtration process for fibrous filters.

Zusammenfassung

Tiefenfilter werden beispielsweise in Klima-, Reinraum- und Prozesstechnik zur Entfernung von Partikeln aus feststoffbeladenen Gasströmen verwendet. Die Partikelabscheidung findet dabei im Inneren des Filters zunächst an den einzelnen Faser und dann in der porösen Struktur der Fasermatrix statt. Mit zunehmender Betriebszeit akkumuliert sich Partikelmaterial im Filter, was eine Erhöhung des Druckverlusts und folgend einen erhöhten Energieverbrauch verursacht. Schlussendlich wird der Filter ausgetauscht, um dem erhöhten Druckverlust zu minimieren und Platz für neues Partikelmaterial zur Abscheidung zu schaffen. Der Druckverlust ist ein Indikator für den Energieverbrauch während des Filtrationsprozesses. Der Verlauf des Druckverlusts und der kritische Druckverlust bestimmen die Lebens- und Nutzungdauer eines Filtermediums.
Bei Tiefenfiltern erfolgt die Ablagerung in der Regel im oberen Drittel des Filters, ausgehend von der Anströmseite. Folglich entsteht eine ungleichmäßige Verteilung des Partikelmaterials. Eine Regeneration des Filters wird im Rahmen der Tiefenfiltration in der Regel nicht durchgeführt. Um dennoch einen neuen Ansatz zu wählen und die Abscheideleistung aufrechtzuerhalten, sowie den Druckverlust zu verringern, bevor der kritischer Druckverlust erreicht wird, soll eine neue mögliche Lösung darin bestehen, partikelförmiges Material kontrolliert aus den stromaufwärts gelegenen ersten Drittel des Filterbereichs in den Leerraum stromabwärts des Filters zu transferieren.

Die dazu angestrebte Methode liegt in der Dehnung des Kollektors und dem Einbringen von Scher- und Zugspannungen in die Partikelstruktur bei gleichzeitiger Anströmung im filtrationsrelevanten Bereich. Die externe Anregung des Kollektors durch Dehnung soll dabei die Schwelle für die Ablösung durch die Anströmung absenken werden. Für die erfolgreiche Implementierung dieser Methode in einem gesamten Filtersystem ist das detaillierte Grundverständnis der durch Dehnung induzierten Umlagerung und Ablösung von Partikelmaterial notwendig. Um eine detailliertes Verständnis der mikromechanischen Vorgänge zu erhalten werden somit zunächst die Experimente auf vereinfachten Modellen eines Tiefenfilters wie einer dehnbaren Einzelfaser und einem dehnbaren Faserarray durchgeführt. Grundsätz-

lich widerspricht die Idee der Ablösung von abgeschiedenen Partikelstrukturen der eigentlichen Idee eines Filters. Dennoch wurden auch schon in vorangegenangen Untersuchungen zur strömungsinduzierten Ablösung von Partikeln von einer nicht dehnbaren (starren) Einzelfaser durchgeführt. Die nicht dehnbare Faser diente dabei aber nicht als Initiator für eine Umlagerung oder Ablösung. Im Fall der dehnbaren Einzelfaser sind noch keinen Untersuchungen zur Umlagerung und Ablösung von Partikelstrukturen vorhanden. Das Hauptziel ist somit die Evaluation von Einflussfaktoren wie Anströmgeschwindigkeit, Dehngeschwindigkeit und Morpholgie der Partikelstruktur auf die Umlagerung und Ablösung von Partikelstrukturen auf und von einer dehnbaren Filterfaser und nachfolgend dann von einem dehnbaren Faserarray.

Die experimentellen Untersuchungen der Einflussfaktoren auf das Umlagerung- und Ablöseverhalten der Partikelstrukturen von der Einzelfaser (Mikro Level) und dem Faserarray (Meso Level) in dieser Arbeit erfolgt in fünf Schritten, die auf fünf verschiedenen Studien basieren.

In einem ersten Schritt wird der Einfluss der Prozessparameter der Anströmgeschwindigkeit und der Dehngeschwindigkeit einer mit einer kompakten Partikelstruktur beladenen Einzelfaser (Mikro Level) während eines einzigen Dehnzyklus evaluiert. Um die Dehnung der Faser durchzuführen wurde ein spezieller Faserhalter zur Dehnung der Faser entwickelt. In den ersten Tests konnte gezeigt werden, dass bei Anströmgeschwindigkeiten der Faser von kleiner $1\,m\,s^{-1}$ und gleichzeitiger Dehnung unterschiedlicher Geschwindigkeit Umlagerung und Ablösung von Partikelstrukturen detektiert werden. Es konnte während der Versuche beobachtet werden, dass die Partikelstruktur auf der Faser unabhängig von der Dehngeschwindigkeit und der Anströmgeschwindigkeit radial mit der Faserrotation luv und lee rotiert. Es wurde darüber hinaus gezeigt, dass Aufbruch der Partikelstruktur immer von der Oberseite der Struktur auf der Faser ausgeht. Ohne eine gleichzeitige Anströmung mit alleiniger Dehnung war nur sehr geringfügige Ablösung von Partikelstrukturen möglich. Es war auch festzustellen, dass nach der Ablösung von Partikelstrukturen immer eine Residualstruktur auf der Faser zurückbleibt.
Im zweiten Schritt wird für eine Abschätzung des Haftkraftverhältnisse zwischen der Faser und den Spheriglasspartikeln eine Studie zur Haftkraftmessung zwischen Partikeln der Materialien Spheriglass und Polystyrene und der Faser in verschiedenen Dehnungszuständen vorgenommen. Darüber hinaus wird die Oberfläche der Polyurethanfaser in verschiedenen Dehnzuständen, welche äquivalent zum Experiment sind, charakterisiert und die Oberflächenrauigkeit bestimmt. Die Untersuchungen wurde dabei mit dem Rasterkraftmikroskop und dem Weißlichtinterferometrie durchgeführt. Durch die Dehnung der Faser wird mittels Messtechnik eine deutliche Erhöhung der Rauigkeit festgestellt. Mittels Haftkraftmessungen zwischen Partikeln und der Faser in unterschiedlichen Dehnzuständen konnte nachfolgend nachgewiesen

werden, dass die Erhöhung der Oberflächenrauigkeit einen reduzierenden Einfluss auf die Haftkraft zwischen Partikel und Faser hat. Unabhängig davon konnte in den Haftkraftmessungen festgestellt werden, dass die Haftkraft zwischen Partikel und Faser über der zweier Partikeln liegt.

Im dritten Schritt wird die Größe und der Moment der Ablösung der abgelösten Partikelstrukturen in einer 5-fachen Dehnung der mit einer kompakten Partikelstruktur beladenen Einzelfaser (Mikro Level) bestimmt. Zusätzlich erfolgt die Bestimmung des relativen abgelösten Anteils der Partikelstruktur. Zu Beginn der fünf Dehnzyklen ist jeweils eine von zwei unterschiedlich großen Partikelstrukturen auf der Faser abgeschiedenen. Für die Detektion der abgelösten Partikelstrukturen direkt unterhalb der Faser, sowie die Beobachtung des Strukturaufbruchs wurde eine selbst konstruierte Laser-Licht Messtechnik auf dem Prinzip der Streulichtmesstechnik, sowie die Beobachtung mittels Kameratechnik genutzt. Insgesamt ergab sich eine stark durch die Anströmgeschwidigkeit dominierte Ablösung von Partikelstrukturen, worin eine Verschiebung des schwerpunktmäßigen Moments der Ablösung im Dehnbereich der Faser von 20 - 38.7 % zu 0 - 15 % durch eine Steigerung der Anströmung von $0.05\,m\,s^{-1}$ auf $0.8\,m\,s^{-1}$ detektiert werden konnte. Darüber hinaus konnte festgestellt werden, dass trotz geringer Anströmgeschwindigkeiten der Faser von $0.05\,m\,s^{-1}$ dank mehrmaliger Dehnung bei einer Dehngeschwindigkeit zwischen 0.6 bis $12\,mm\,s^{-1}$ eine vollständige Ablösung der Partikelstruktur realisiert werden konnte. Es konnte zudem festgestellt werden, dass die abgelösten Partikelstrukturen des ersten Dehnzylkus größer sind, als die der nachfolgenden vier Dehnzyklen. Zudem wurde herausgearbeitet wie die der lokale V-förmige Rissbildung der Partikelstruktur, das Versagen von Kohäsion und Adhäsion in Rahmen der Partikelstruktur auf der Faser mit dem Ablösen der Struktur von der Faser zusammenhängen.

Im nächste und vierte Schritt liegt der Fokus auf der Betrachtung der Abscheidung einer Partikelstruktur auf dem Faserarray (Meso Level). Dabei wird der Abscheideprozess der dendritischen und kompakten Partikelstrukturen (St=0.52 - 10.05) auf den Fasern und in den Faserzwischenräumen kontinuierlich mittels in situ Bildanalyse in Anströmrichtung ausgewertet und bis zum clogging point und einer TIF von $2.8 \cdot 10^8\,\#\,mm^{-2}$ bei einzelnen Partikelstrukturen auf dem Array begleitet. In Kombination mit der Bilanzierung der abgeschiedenen Masse auf dem Array ergibt sich eine Wachstumskinetik der Partikelstrukturen, die Unterschiede hinsichtlich der kompakten Abscheidung mit viel Masse und der großflächigen Abscheidung der dendritischen Strukturen mit weniger Masse (in Beobachtungsrichtung) zeigt. Ebenso erfolgt mit einer automatisierten MATLAB©Bildauswertung eine Detektion von Brückenbildung und Porenwachstum zwischen den inneren Fasern des Arrays. Dabei konnte die charakteristischen Merkmale wie die weitverzweigten dendritischen Randstrukturen der Partikelstrukturen auch im Porenwachstum erfasst werden, da sich dabei viele kleine Poren mit wenigen Mikrometer (3 - $78\,\mu m$) ergaben. Im Gegensatz dazu ergab sich

beim Brückenwachstum der kompaktenstrukturen große Brücken von bis zu 270 μm entlang der Faserachse.

Das Ziel des fünften Schritt ist es, erste Informationen über die Umlagerung und Ablösung von Partikelstrukturen auf/von einem Faserarray (Mesoebene) während fünf aufeinanderfolgender Dehnzyklen zu erhalten und dabei die Unterschiede und zusätzlichen . Es wird dabei wie schon in den fünf aufeinanderfolgenden Versuchen mit der partikelbeladenen Einzelfaser mit der Laser-Licht Messtechnik quantitativ der Moment der Ablösung der Partikelstrukturen während der Dehnung und auch die Größe der abgelösten Agglomerate erfasst. Des weiteren erfolgt eine Analyse der relativen Belegung der Faserzwischenräume, welche für eine Beurteilung einer potentiellen Durchströmung relevant ist. Darüber hinaus wurde eine qualitative Analyse der Rissmuster und der Umlagerung der Partikelstrukturen auf der Grundlage ihrer Morphologie (dendritisch oder kompakt) und ihres Wachstumszustands (non-clogged, clogged durchgeführt. Die Wahl der Anströmgeschwindigkeit und Dehngeschwindigkeit während der Dehnversuche Faserarray erfolgte aus den Erfahrungen der Ergebnisse mit den Einzelfasern und lag zwischen 0.05 $m\,s^{-1}$ und 0.8 $m\,s^{-1}$. Die Dehngeschwindigkeit wurde zwischen 0.6 $mm\,s^{-1}$ und 1.2 $mm\,s^{-1}$ variiert. So konnten, wie schon in den Experimenten an der Einzelfaser, Umlagerungsereignisse und nachfolgende Ablösung der Partikelstruktur vom Faserarray detektiert werden. Auch eine radiale Umlagerung und Rotation der Partikelstrukturen war teilweise zu beobachten. Mit einer Modikation des Faserhalters wurde eine Möglichkeit geschaffen den Abstand der Faser im Array während der Dehnung zu verkleinern und zu vergrößern und so statt einer uniaxialen Dehnung eine biaxialen Dehnung zu etablieren. Es konnte so ein mehrdimensionaler Spannungzustand mit Scher- und Zugkräfte in der gecloggten Partikelstruktur auf dem Faserarray erzeugt werden, der sich deutlich in ausgeprägteren Rissmustern und Ablösung von Partikelstrukturen zeigte.

Die Arbeit leistet eine wichtige Beitrag auf mikroskopischer und mesoskopischer Ebene für die kommenden Untersuchungen an einem zukünftigen dehnbaren Filter (Makro Level) und dem dafür notwendigen Verständnis der bei der Dehnung ablaufenden Umlagerungs- und Ablöseprozessen der Partikelstrukturen, sowie dem Einfluss der verschiedenen Prozessgrößen.

Erklärung

Erklärung

==========

Ich versichere hiermit wahrheitsgemäß, die Arbeit selbstständig verfasst und keine anderen als die angegebenen Quellen und Hilfsmittel benutzt, die wörtlich oder inhaltlich übernommenen Stellen als solche kenntlich gemacht und die Satzung des Karlsruher Instituts für Technologie (KIT) zur Sicherung guter wissenschaftlicher Praxis in der jeweils gültigen Fassung beachtet zu haben.

Berlin, 25. Oktober 2024 _____

Lukas Poggemann

Contents

Abstract iii

Zusammenfassung vii

Erklärung xi

1 Introduction 1

1.1 Fundamentals on the separation of a particulate structure on a stretchable single fiber or fiber array . . . 4

1.1.1 Separation mechanism and resulting structure morphology . . . 4

1.1.2 Setup and methods for the separation of a particle structure on the stretchable fiber and fiber array . . . 7

1.2 Fundamentals on the detachment of particle structures from a single fiber or a fiber array . . . 11

1.2.1 Detachment of particles from single filter fibers due to air flow . 11

1.2.2 Detachment of particles from single filter fibers due to external excitation and air flow . . . 12

1.2.3 Tensile stress within particle structures . . . 13

1.2.4 Adhesion force between particle-particle and particle-fiber . . . 14

1.2.5 Stretching of a polymeric single fiber or a fiber array . . . 16

1.2.6 Setup and methods for measurement of adhesion force between a single particle and a fiber . . . 18

1.2.7 Setup and methods for measurement of size and moment of detachment of detached particle structures during fiber stretching 19

2 Thesis outline 21

2.1 Research Gap and Idea . . . 21

2.2 Research Aim of this Work . . . 22

2.3 Manuscript Overview . . . 23

3 Detachment of particulate structures from an elastic single fiber 29
3.1 Introduction: . . . 30
3.2 Materials and Methods: . . . 35
3.2.1 Fiber and Aerosol: . . . 35
3.3 Experimental Set-up and Procedure: . . . 35
3.3.1 Set-up for fiber loading process with particulate material . . . 35
3.3.2 Fiber mounting device . . . 38
3.3.3 Stretching set-up and Stretching procedure . . . 38
3.3.4 Evaluation of experimental results and method of frame fitting . 40
3.4 Results and discussion . . . 42
3.4.1 Details on qualitative and quantitative data/combination with supplementary data . . . 42
3.4.2 Stretching without airflow . . . 43
3.4.3 Stretching with airflow . . . 46
3.4.4 Impact of different airflow velocities on the detachment behavior of particle structures on the fiber . . . 50
3.4.5 Hypothesis concerning behavior of particle structures on elastic single fiber during stretching based on the observation/crack formation in matrix on elastic substrate . . . 55
3.5 Conclusion and Outlook . . . 57

4 Investigation on the change of pull-off force between particulate material and an elastic fiber 61
4.1 Introduction . . . 62
4.2 Material and Methods . . . 67
4.2.1 Materials and sample preparation . . . 67
4.2.2 Experimental Setup and Measurement Procedure of Adhesion Force . . . 68
4.2.3 Evaluation of the measurement in direct contact to the polymeric fiber in the stretching device . . . 69
4.2.4 Experimental Setup for Surface Characterization . . . 70
4.3 Theory . . . 71
4.4 Results and Discussion . . . 73
4.4.1 Measurement of surface roughness and Peak-to-Peak distance . 73
4.4.2 Measurement of pull-off-force . . . 77
4.4.3 Discussion of the findings concerning the interaction of surface properties and adhesion force . . . 82
4.5 Conclusion . . . 85

5 Detachment of particulate structures during multiple stretching cycle of the single filter fiber 89
5.1 Introduction . . . 90

5.2 Materials and Methods . . . 93
5.2.1 Fibre and Particulate Material . . . 93
5.2.2 Aerosol Generation and Loading Procedure . . . 93
5.2.3 Multiple Stretching Cycle . . . 95
5.2.4 Large Structure Detection System . . . 97
5.2.5 Determination of Cumulative Fraction of Detached Particle Structure from Total Structure and Residual Structure on Fiber . 99
5.3 Results and Discussion . . . 100
5.3.1 Variation of Particle Loading Time . . . 100
5.3.2 Influence of Elongation Velocity . . . 104
5.3.3 Development of Structure Size . . . 107
5.4 Conclusions and Outlook . . . 109

6 Morphology of particulate structures on a fiber array before and at clogging point in gas-particle-filtration process 113
6.1 Introduction . . . 114
6.2 Experimental Methods . . . 117
6.2.1 Fiber Array and Particulate Material . . . 117
6.2.2 Particulate Loading and Gravimetric Measurements of Particle Structure on the Fiber Array . . . 118
6.2.3 In Situ Observation of Particulate Structure Development . . . 120
6.3 Results and Discussion . . . 124
6.3.1 Gravimetric Measurements of the Particulate Material . . . 124
6.3.2 Accumulation of Particulate Material before Clogging . . . 126
6.3.3 Development of Structures before and in the Clogging Phase . . 129
6.3.4 Size of Pores and Bridges . . . 133
6.4 Conclusions and Outlook . . . 138

7 Rearrangement and detachment of particle structure from a fiber array 141
7.1 Introduction . . . 142
7.2 Material and Methods . . . 146
7.2.1 Fibers and particulate material . . . 146
7.2.2 Stretching device . . . 146
7.2.3 Aerosol Generation and Loading Procedure . . . 148
7.2.4 Stretching Procedure . . . 150
7.2.5 Experimental Setup for Size Characterization . . . 150
7.2.6 Determination of relative projection area of free space in the fiber interspaces . . . 152
7.3 Results and Discussion . . . 154
7.3.1 Morphology of particulate structure on the fiber array before clogging . . . 154
7.3.2 Detachment of particle structures from a fiber array before clogging . . . 155

7.3.3 Development of relative free projection area . . . 159
7.3.4 Morphology and behavior of detachment of particulate structure on the fiber array after clogging . . . 162
7.3.5 Detachment of particle structures from a fiber array after clogging 163
7.3.6 Size of detached particle structures during stretching cycle . . . 167
7.3.7 Initiated multiaxial stress into particulate structure . . . 168
7.4 Conclusion . . . 171
7.5 Outlook . . . 172

8 Summarizing Conclusions 175
8.1 Single stretching of a stretchable single fiber (micro level) with a compact particle structure . . . 176
8.2 Measurement of adhesion force between a single particle and polyurethane fiber . . . 177
8.3 Multiple stretching of a single fiber (micro level) with a compact particle structure of different height . . . 179
8.4 Development of a compact or dendritic particle structure on a fiber array (meso level) . . . 181
8.5 Rearrangement and detachment of a particle structure on/from a stretchable fiber array . . . 183
8.5.1 Stretching experiments with a non-clogged particle structure on the fiber array . . . 183
8.5.2 Stretching experiments with a clogged particle structure on the fiber array . . . 184
8.5.3 Multiaxial stretching of a fiber array with a clogged and compact particle structure . . . 185

9 Outlook 187
9.1 Evaluation of characteristics of a stretchable filter . . . 188
9.2 Operational strategy for a stretchable filter . . . 189

Abbreviations 191

Symbols 193

Acknowledgment 197

Declaration of Generative AI and AI-assisted technologies in the writing process 199

List of Publications 201
Peer-Reviewed Journal Papers . . . 201
Conference Talks . . . 202
Conference Posters . . . 202

Bibliography **203**

Appendix **219**
A List of Figures 219
B List of Tables 227

1
Introduction

Depth filters are widely used and established in processes for separating a continuous phase (gas) from a dispersed phase (particles) within the fiber matrix. Their applications range from air conditioning and air purification to the treatment of industrial process gases [43, 128, 171]. When evaluating a filtration process, it is important to consider three main parameters: separation efficiency, pressure drop and the total loading capacity [144, 11]. Pressure drop is an indicator of the energy consumption during the filtration process. The pressure drop curve and the final pressure drop determine the service life of a filter [162].

Figure 1.1 shows a qualitative progression of pressure drop during depth filtration

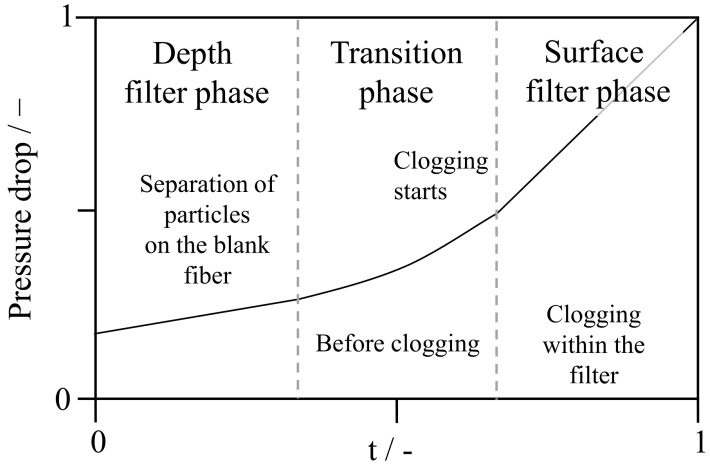


Figure 1.1: *Qualitative progress of pressure drop over filtration time. Modified from Penicot et al. [103] and Thomas et al. [152].*

process including the three characteristic phases of pressure drop. The separation

process begins with the accumulation of particles on each blank fiber during the depth filter phase of pressure drop. This is followed by the formation of larger particle structures and secondary separation on pre-existing structures. The primary cause for of increased pressure drop during the transition phase is the accumulation of particulate material within the fiber matrix. As the upstream filter layer and the interspaces between the fibers become clogged with a particle structure, more particulate material is separated on the surface of the filter. In the surface phase of pressure drop, the pressure drop increases linearly with the collected mass in the filter [13, 54].
For depth filters, separation usually occurs within the top third or half of the filter, starting from the face side [136, 47]. This leads to a less uniform distribution of the particulate material. As a result, there is an increase in pressure drop. When reaching a critical pressure drop in the transition or in the surface filter phase (see Figure 1.1), the filter is replaced and the filter medium should be disposed of as described in DIN 779 [28]. Regeneration is not typically done in the context of depth filtration [18, 56, 27]. To maintain separation efficiency and potentially reduce pressure drop before reaching a critical pressure drop, one potential solution is to remove particulate material from upstream filter fibers in a controlled manner and transfer to void space downstream the filter.

The target method for removing or detaching particulate material and unclogging the upstream layers is to **stretch the collector (filter)**. By stretching the collector, shear and tensile stress are applied to the separated particulate structure. The particulate material shall be transported further downstream the fiber matrix to clear up void space at the upstream part of the filter. In investigations by Ziskind et al. [177] and Tippayawong and Preechawuttipong [156], an external excitation such as vibration in addition to the applied airflow, act as a trigger for detachment of particle. The external excitation influences the threshold for removal between surface adhesion and the aerodynamic lift or drag from the flow. This should enable particle resuspension from surfaces as described by Ziskind et al. [177] and Ziskind [176].
To successfully implement this approach for weakening particle structure by stretching, a detailed understanding of the rearrangement and detachment behavior of particle structures on/from the stretchable collector is necessary. Micromechanical interactions of the particles with the collector and within the particle structure are crucial in its rearrangement and detachment behavior. To gain a detailed understanding and observe the rearrangement and detachment of particle structures on a filter fiber, simplified model like a single fiber or a fiber array are used. Overall the approach to particle structure detachment from a stretchable collector differs from the original idea of the filtration collector, which is to collect particles. In addition, **previous studies** conducting experiments with **a stiff and non-stretchable** single **fiber**.

Löffler [81] demonstrated the first investigation on the conditions for particle structure detachment from a non-stretchable "stiff" single fiber during regular filtra-

tion operations and for optimizing air flow conditions. In the experiments detachment of particle structures was solely caused by increased velocity of applied air flow as flow forces increased. The non-stretchable single fiber did not act as an initiator for a rearrangement and detachment process of particle structures. In the case of a stretchable single filter fiber, the rearrangement and detachment of particle structures has not been studied yet.

The primary aim of this work (dissertation) is to investigate the **rearrangement and detachment of particle structures** on a simplified **stretchable** collector as the **single fiber (micro level)** or the **fiber array (meso level)**. The **initiator** for rearrangement and detachment of particle structures should be the **stretching of the collector** and a simultaneous air flow.

An experiment, regardless of whether its with a single fiber or a fiber array, always **consists** of the **separation of a particle structure** on the collector and a **subsequent stretching of the fiber(s)** mostly with simultaneous particle-free air flow. The following sections present the **fundamentals and methods** separately, divided into the topics **separation** (section 1.1) and **detachment** (section 1.2) of the particle structure.

1.1 Fundamentals on the separation of a particulate structure on a stretchable single fiber or fiber array

1.1.1 Separation mechanism and resulting structure morphology

To perform investigations on the rearrangement and detachment behavior of a particle structure during collector stretching, first step is to **separate a particle structure on the fiber or fiber array** with **compact or dendritic morphology**. The shape and form of the separated particle structure on a single fiber or fiber array, known as the morphology of the structure, significantly will influence the rearrangement and detachment behavior of the particle structure when the collector (single fiber or fiber array) is stretched. In detail, the morphology of a structure will influence its mechanical stability, resulting flow forces, and porosity [81]. Therefore, it is crucial to consider morphology of the particle structure when analyzing the rearrangement and detachment behavior during the stretching experiments. The following explanations

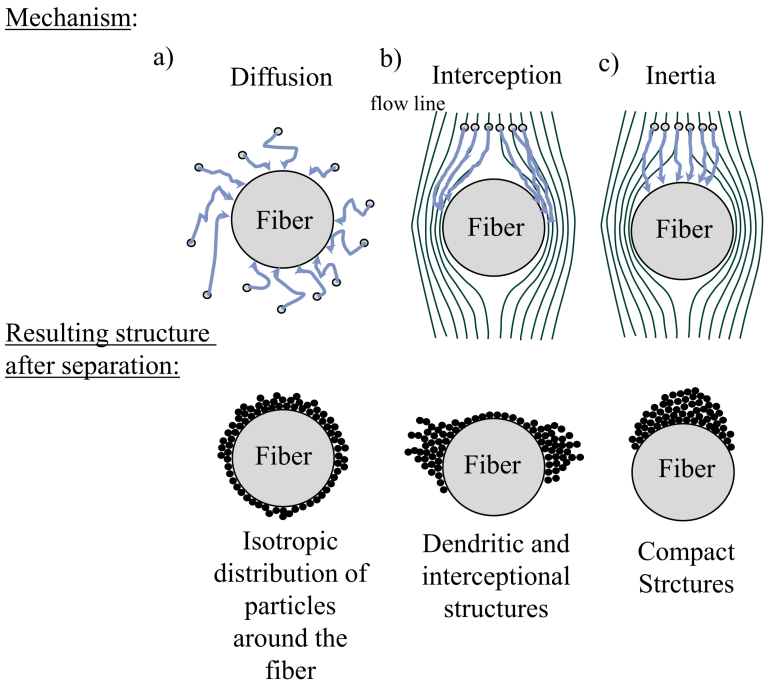


Figure 1.2: *Schematic of separation of particles at a single fiber with different separation mechanism a) diffusion, b) interception, c) inertia adapted from Löffler [81], Kanaoka et al. [65], and Zoller [178]. Below the resulting particle structure on the fiber with the assumed form/morphology as Kanaoka et al. [65] showed in his studies. It is assumed that fiber and particles are electrically neutral and that the air flow is constant and perpendicular.*

demonstrate the formation of a particle structure on a single fiber, which can be basically transferred to the fiber array as shown by Müller et al. [92]. The formation and the final morphology of the particle structure on the single fiber in this present work

are mainly influenced by separation mechanisms such as **diffusion**, **interception** and **inertia** (see Figure 1.2). The resulting structures are based on the work and prediction of Kanaoka et al. [65] and Kasper et al. [70].

Additionally, there are mechanisms that only occur on previously separated structures, such as rebound, rearrangement and erosion. The individual separation mechanisms are clearly characterized using monodisperse material. Figure 1.2 shows the most important three separation mechanisms for this work and a schematic of the resulting structures on a single fiber with a monodispers material.
The significance of different separation mechanisms during the formation of particle structure is based on the flow conditions like the flow velocity u, particle properties as the particle diameter d_p and the material density $\rho_{particle}$, and fiber properties like fiber diameter d_F. Dimensionless numbers can be used to predict the significance of each specific mechanism.

Monodisperse particle material is commonly used in literature to study individual separation mechanisms due to simplified physical dependencies [65, 70]. However, in this work, polydisperse particle material (Spheriglass 5000) was used, resulting in parallel occurrence of different mechanisms with varying significance due to differences in particle diameter. However, one mechanism dominates, resulting in the characteristic morphology of the structure. In this work, the dimensionless numbers were calculated using $d_{50,3}$. There are a few studies that have already addressed the separation of polydisperse material on a single fiber or a fiber array. Investigations on the mechanism of inertia and interception were performed by Zoller [178], Szabadi et al. [148] and Zhu et al. [174] and on the mechanism by diffusion by Szabadi et al. [149],Wongsri et al. [165] and Jung et al. [62]. In the following the key mechanisms for separation on a stretchable fiber and a stretchable fiber array are described.

Diffusion
At low flow velocities, particles are separated on the entire surface around the fiber through the diffusion impact mechanism (see Figure 1.2 a)) [65]. The particles collide with the fiber due to random collisions with gas molecules and other particles. They randomly move through space (Brownian motion). Experiments have demonstrated this mechanism on a chain of spheres and on a single metal fiber with a particle fraction of carbon black [22, 148]. Kanaoka-like structures have been observed in numerical calculations of particle separation [35, 20]. The dimensionless number to characterize this impact mechanism by diffusion is the Péclet number Pe (see equation 1.1).

$$Pe = \frac{d_F\, u}{D_{Diffusion}} \tag{1.1}$$

Herein the particle diffusion constant $D_{Diffusion}$ is a decisive parameter in addition to the flow velocity u and fiber diameter d_F [82]. This work relates to experiments with

a single fiber where the Péclet number was $3.2 \cdot 10^7$ and the experiments with a fiber array, where the Péclet number was between $2.72 \cdot 10^6$ to $4.90 \cdot 10^7$.

Interception
If particle diameter becomes larger or the air flow velocity increases, the particle finish to move by Brownian motion instead they follow the streamline around the fiber and come into contact due to geometric expansion of the fiber or already separated particles, an impact on the blocking effect occurs (see Figure 1.2 b)). This mechanism is named interception. The impact point of the particles due to inception is more at the edge of the fiber, where they can form dendritic structures [31]. structures with branches closed to stagnation point can be formed [120, 70, 174]. The dimensionless number for this mechanism is the interception parameter R (see equation 1.2).

$$R = \frac{d_p}{d_F} \tag{1.2}$$

Herein the influencing parameter are the particle diameter d_p and the fiber diameter d_F. The experiments in this work with the single fiber and the array obtained the interception numbers of 0.09. In the experiments with a fiber array the formation of dendritic structures has been more stressed as the structure grow into the interspaces between fibers and block free space. In a filter, this can have a significant impact on the increase in pressure drop, as described by Hosseini and Tafreshi [48].

Inertia
As the flow velocity is increased, the particles leave the path of the streamlines around the fiber due to their inertia and collide near the stagnation point of the fiber. The particles move in a straight line towards the fiber and forming a compact particle structure as shown in the studies by Rembor [118], Schollmeier [131], and Zoller [178]. As shown in Figure 1.2 c), this structure is formed at the zenith of the fiber/stagnation point. Neglecting particle bouncing causes the impact point to shift from the fiber's sides towards its stagnation point at an increasing speed, while maintaining a constant particle size [31]. The dimensionless number for separation by inertia is the Stokes number St (see equation 1.3).

$$St = \frac{\rho_{particle} d_p^2 u}{18 \eta_{fluid} d_F} \tag{1.3}$$

Herein the influencing parameter are the particle density $\rho_{particle}$, the particle diameter d_p, undisturbed flow velocity u during the loading process, the fiber diameter d_F, the viscosity of fluid η_{Fluid}. In the loading procedure of this work, Stokes numbers between 0.52 and 10.05 were obtained.

Particle bounce
As particle velocity and so kinetic energy increases, particle start to rebound upon

hitting the fiber. This phenomenon is influenced by specific material constants, such as the modulus of elasticity of the fiber and particles. The rebound effect can lead to particle separation further upstream at the side of the fiber where particles have reduced kinetic energy. The separation process results in the formation of three zones for particle separation. The fiber has three particle impact points: one at the stagnation point and two on the right and left sides [70, 86]. This structure resembles a dendritic structure, which is also formed on the fiber array in this work. The impact behavior causes the particle structure to transition from dendritic to compact [70]. If particle velocity increases further, separation no longer occurs during the particles second impact with the fiber.
Löffler and Umhauer [84] first observed the particle bounce from the fiber during the first impact with the fiber.

Electrostatic and gravity
Another mechanism of particle separation is due to electrostatic forces, which can cause interaction between the particle and the fiber. If either the particle or the fiber is electrostatic charged, the separation by mechanism of diffusion or mechanism inertia can be neglected. The attractive electrostatic forces cause the particles to deviate from the usual path of the streamlines and move towards the fiber. In the experiments in this work, electrostatic separation of particles on the fiber was not attempted. In any case, electrostatic separation is more relevant for particles smaller than $1\,\mu m$, which play a minor role in the given particle size distribution of Spheriglass 5000. The impact mechanism of particle separation by gravity is not considered in this work. However, the influence of gravity must be taken into account in the subsequent detachment of the particle structures from the fiber or fiber array.

1.1.2 Setup and methods for the separation of a particle structure on the stretchable fiber and fiber array

To create a particle structure on a single fiber or fiber array, a particle loading procedure is required. The main goal of this procedure was to establish a particle structure on the collector (single fiber or fiber array). No evaluation of the single fiber separation efficiency was conducted. The process diagram for the loading procedure is shown in Figure 1.3. It only displays the components that participated in the loading processes for the single fiber and the fiber array. Specific components, such as the camera technology used to observe the loading of the fiber array, are discussed in their corresponding chapters. The particulate material is dosed by a rotating ring and an ejector nozzle (DIN ISO 5011) using the Topas SAG 410/U. A mass flow rate in the feed flow (direct beyond the aerosol generator) of $4\,g\,h^{-1}$ was determined. A loading flow was discharged from the feed flow. The rest of the feed flow was drained off as an excess flow. The particulate material was removed by a HEPA filter. The excess flow rate was controlled using a Mass Flow Controller (MFC).

Before entering the loading chamber, the aerosol passes through an ^{85}Kr-neutralizer and then a flow rectifier (diameter 16 mm, consisting of a tube bundle). In the loading chamber, the stretchable fiber or fiber array is perpendicular aligned with the loading flow. Downstream of the single fiber and the fiber array, an HEPA filter was used to remove the remaining particulate material. The loading flow rate was controlled using a MFC. The flow velocity can be varied by adjusting the ratio between excess and loading flow. The components were designed based on investigations on the separa-

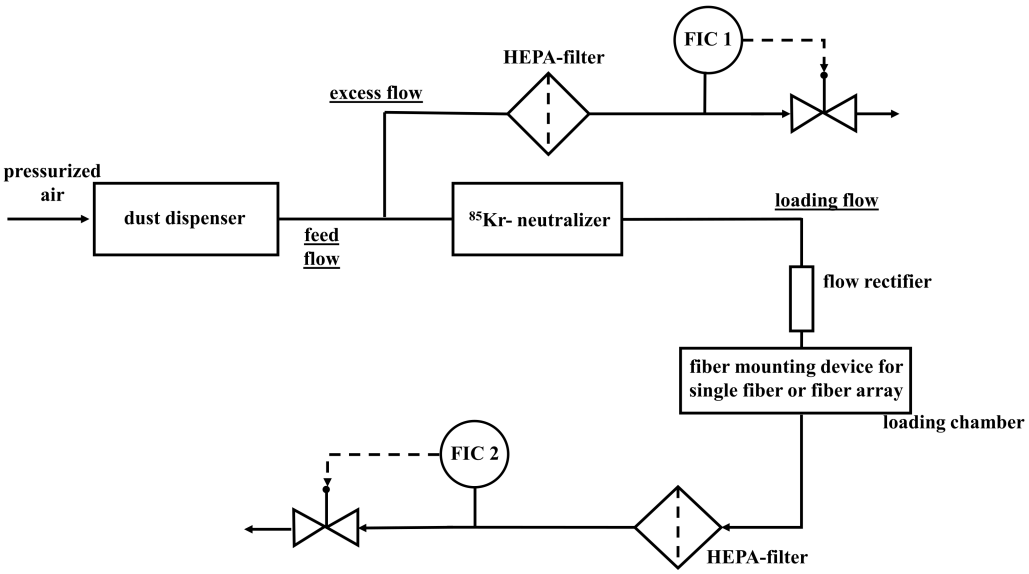


Figure 1.3: *Simple process flow diagram of the loading procedure for the separation of a particle structure in the stretchable single fiber and fiber array.*

tion of particulate material on a single fiber or on a fiber array by Schweers et al. [139], Rembor [118], and Müller [91].

1.1.2.1 Fiber clamping device for single fiber and fiber array

Particle structure separation experiments are conducted using either a single fiber or a fiber array. Further the clamping device should enable the subsequent investigation on the rearrangement and detachment of particle structures from a single fiber and the fiber array. Previous studies have used various methods to clamp fibers when separating individual particles or particle structures onto them. It is crucial to ensure good accessibility of the fibers for vertical flow and loading, as well as to have appropriate measurement technology to evaluate the separation or, in the case of this work, to investigate the detachment of particle structures directly under the fibers. In the investigation by Schweers and Löffler [138] the individual fibers were clamped to allow optical access from all sides above and below. Tubes for aerosol flow or particle-free air were then applied to the fiber(s) from above and below through a 25 *mm* hole. In the investigation by Müller [91], the fibers were mounted in a comb to establish a uniform

distance of 246 μm. This type of mounting was also used for the experiments with an array in this work, but is not shown in the figure. The spacing was chosen for measurement reasons and reflects a representative spacing of fibers in a fibrous filter. Figure 1.4 shows the fiber clamping device utilized for separation of a particle structure on the single fiber and the subsequent stretching process. Each side of the fiber clamping/-mounting is located on a piezo motor which initiates stretching at a defined stretching velocity e of the fiber/fiber array.

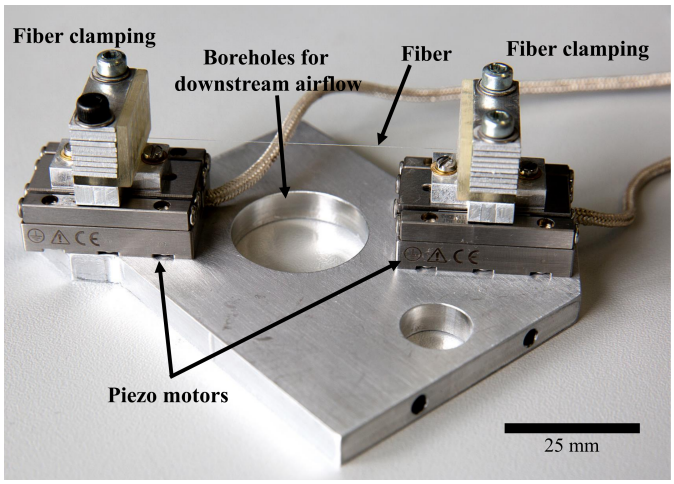


Figure 1.4: *Fiber clamping device for the separation of a particle structure on a single fiber and subsequent stretching procedure. The design of the fiber clamping device for the fiber array is equal, except for the fiber combs, which ensures a constant distance of 246 µm.*

1.1.2.2 Separation of a particle structure on a single fiber

To investigate the rearrangement and detachment of particle structures during stretching experiments, it is necessary to separate structures of different heights, sizes or structure morphology on the fiber during the loading process.

For the stretching experiments with a single fiber, a compact particle structures of varying heights and sizes in the preceding loading processes was separated on the single fiber to investigate influence of structure size/height on the rearrangement and detachment process. The size/height of the particle structure was adjusted by varying the loading time, which was either 5 or 15 min. The prerequisite for this was the use of the same particle material (Spheriglass5000), fiber (stretchable polyurethane fiber), particle concentration in the aerosol, and flow velocity during all loading processes.

1.1.2.3 Calculation of the particles passed the fiber array

To ensure comparability of different particle structures with varying morphologies and size on the fiber array, the calculation of the Time integrated flow (TIF) was done. Pre-

requisite is a constant particle concentration in the loading stream as well as the same particulate material and collector size for all loading processes. The TIF is used to calculate the number of particles (polydisperse particle material) that have passed a defined control area over a given time interval considering the current air flow velocity at a constant particle concentration in the air flow. Therefore, loading was performed until a certain number of particles per cross section had flowed towards the fiber array. The basic considerations for this form of particle and particle count detection are based on the investigations of Raasch and Umhauer [115]. First, the particle flux density (j_i) is calculated using the particle concentration c_p of the aerosol and its velocity u (see eq. 1.4).

$$j_i = c_p \cdot u \tag{1.4}$$

The TIF in particles per mm^2 can be obtained by combining the particle flux density j_i with the respective loading time t for a specific time interval.

$$TIF = J(t) = \int_0^t j_i \, dt \tag{1.5}$$

$$TIF = J(t) = t \cdot j_i \tag{1.6}$$

For a constant j_i:

$$TIF = c_p \cdot u \cdot t \tag{1.7}$$

During particle loading of an array, there are two types of loading state to consider: non-clogged and clogged. Non-clogged arrays have a free flowable area in the fiber interspaces, while for clogged arrays these fiber interspaces are covered with particle material. To quantify the particle loading process of the fiber with particle structures of different morphology, the use of TIF is essential. The investigation conducted by Müller et al. [92] induced comparable loading conditions for the investigation of separation efficiency with a fiber array.

1.2 Fundamentals on the detachment of particle structures from a single fiber or a fiber array

1.2.1 Detachment of particles from single filter fibers due to air flow

First fundamental investigation on the detachment of individual particles and particle structures from a single fiber due to applied air flow have been made by Löffler [81]. In his first studies the detachment of 50 % of quartz particles ($d_p = 10\,\mu m$) from a single fiber were obtained at air flow velocities greater than $10\,m\,s^{-1}$. The forces for particle detachment determined by Löffler [81] are consistent with values obtained from centrifuge experiments.
Löffler [81] demonstrated that the drag force can be estimated using equation 1.8, assuming that the particles and particle structures to be detached are spherical and small. The flow velocity u is estimated from the laminar boundary layer at a distance of $y = d_p/2$ from the fiber surface.

$$F_{Drag} = \frac{\pi}{4} \cdot d_p^2 \frac{\rho_{fluid}}{2} \cdot u^2 C_D(Re_x) \tag{1.8}$$

Here, the drag coefficient $C_D(Re_x)$ was estimated for sphere. Assuming constant fluid density ρ_{fluid} and a fixed ratio of particle diameter to fiber diameter d_p/d_F, the drag force on the particle structure is estimated. The resulting detachment force is induced by the flow. According to Löffler [81], the cross-sectional area A of a sphere in the flow can be calculated as $\frac{\pi}{4}d^2$.

In further investigations, Larsen revealed that air flow velocities of $20\,m\,s^{-1}$ are necessary for the detachment of $16\,\mu m$ particles from a single fiber [75].
To achieve the particle separation ($d_p = 10\,\mu m$), flow velocities below $0.2\,m\,s^{-1}$ are mandatory, otherwise 50 % of the quartz particles will bounce off the fiber and not stick to the fiber [42]. Consequently, there is a large difference in the regime of flow velocities required for particle separation, detachment and bounce.
In Qian's investigations, it was found that particle detachment increases with increasing flow velocity and particle diameter [113]. As observed by Löffler, this is due to the larger face area or increased flow velocity resulting in increased drag force [83]. Furthermore, it was shown that the detachment is time-independent as long the flow velocity is reached. Jankowska and Qian showed that reversing the flow can lead to a slight increase in the detached fraction of particle material [113, 53]. In total, the listed studies summarize the influence of flow on the detachment of particle structure.
Another topic discussed in the literature is the influence of adhesion forces on particle release from the fiber. Specifically, this could be a change in particle material, humidity, particle size, or the electrostatic charge of the filter or each single particle. As shown in Jankowska's studies, less re-entrainment was measured for KCL particles ($d_p = 2.55\,\mu m$ and $d_p = 3.25\,\mu m$) than for fungal spores ($d_p = 3.21\,\mu m$) at the same filtration velocity of $3.00\,m\,s^{-1}$. Less than 1 % of the KCL particles were detached

at this velocity [53]. The increase in re-entrainment for fungal spores is due to the aggregation/deaggregation and different surface structure of the spores. As shown by Qian et al. [112, 113], an increased humidity reduces the fraction of detached particles (bacteria) regardless of the flow velocity. It was also found that the type of particle material (bacteria or solid particles), with its different surface properties, is of course also a factor in detachment. However, this does not play a role in this work as only spherical glass particles are used. Moreover, the fraction of detached particles was greater for charged filters than for neutral filters in the studies performed by Qian et al. [113].

This literature review presents studies where particle structures were detached solely by applied flow forces. The following section provides examples where external excitation has further promoted detachment.

1.2.2 Detachment of particles from single filter fibers due to external excitation and air flow

In the studies in the previous section, the fiber was present as non-stretchable collector. The detachment of particles is related to the achievement of a certain drag force or a change in the adhesion force between the particle and the collector. As aimed in this present work, there are some other studies on the initiated detachment of particles by an external force in filtration technology. Similar to other studies on particle detachment from a substrate, external excitation such as high frequency sonic waves, lasers, and wall vibrations can initiate detachment. The quasi-static model by Tippayawong and Preechawuttipong [156] is based on a moment or force balance, where the particle or particle structure detaches when a threshold value is exceeded. The threshold is determined by the balance between the adhesion force and the aerodynamic lift or drag force caused by the incident flow. In a second approach, a kinetic model is assumed that is based on the accumulation of energy [155].

A study that has investigated the use of external excitation for particle removal in filtration includes, for instance, the research conducted by Szabadi et al. [148]. In their investigations a correlation between magnetization-induced force on metallic fibers and subsequent particle detachment was demonstrated. The external excitation is created by deflecting the single fiber and introducing an additional acceleration of the particle structure.
Zoller [178] showed in his work the composition of different particulate material (in a particle structure on a single fiber) and its changing adherence to the fiber is the initiator of particle detachment. With a reaction of the ash/soot, particulate material detached at flow velocities of 0.5 $m\,s^{-1}$ and an air flow temperature of more than 400°C. Further, calculation in his work showed in a simplified form how tensile strength of the particle structure develops as porosity changes and the adhesion force of parti-

cles to each other varies. In addition, the detachment velocity of the particle structure is determined in an analytical Discrete element method (DEM)-based solution. The experimental results are in partial agreement with the calculations as a function of porosity and contact distance [16].

1.2.3 Tensile stress within particle structures

The detachment of particle structures from a separated particle structure on the fiber, whether with or without external excitation, occurs due to the breakage of particle-particle bonds or the particle-fiber bonds. These are caused by applied tensile stresses due to fiber stretching or applied air flow. The tensile strength of the particle structure and the adhesion force between the particles and the particle and the fiber are crucial for the detachment. Rumpf [125] obtained that the tensile strength of the particle structure depends on three factors: the porosity of the applied particle structure ϵ, the average adhesion force at the contact points of the particles F_{adh}, and the sauter mean diameter $d_{1,2}$ of the particles fraction.

$$\sigma_{break} = \frac{1-\epsilon}{\epsilon} \cdot \frac{F_{adh}}{d_{1,2}^2} \tag{1.9}$$

The main cause of agglomerate breakage is a external forces like the stretching that exceed the tensile strength of the agglomerate at local points or any drag force of an air flow. Figure 1.5 illustrates how external forces, such as air flow (results in drag force F_{Drag}), can cause breakage within a particle structure and how fiber stretching/movement can lead to particle structure fracture due to external tensile stress. The calcu-

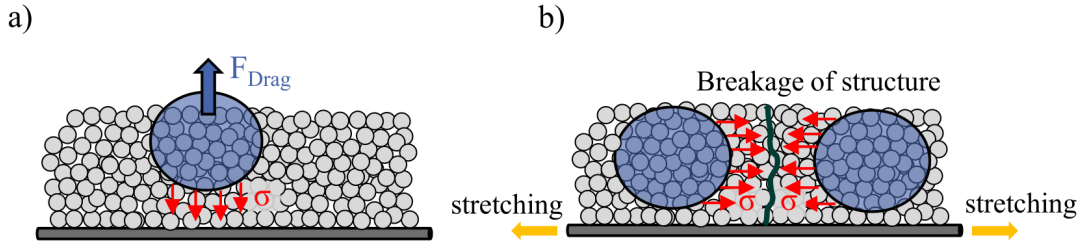


Figure 1.5: *Schematic of the two possible cases for a breakage of an agglomerate on the fiber: a) breakage of a particle structure due to applied drag force, and b) breakage of the particle structure due to fiber stretching.*

lation of tensile stress was initially derived for a monodisperse particle distribution of the particle structure and is only applicable when using sauter mean diameter $d_{1,2}$ and within a porosity range of 0.4 to 0.67 [126]. Despite the distribution of the polydisperse particle material Spheriglass5000, it is uncertain whether the equation can be applied. Currently, there is no better approximation available. Further, as shown in previous studies, the calculation overestimates the tensile strength of the agglomerates. Therefore, Schubert [133] included a correction factor $f_{correct}$ of 10 in his calculations.

1.2.4 Adhesion force between particle-particle and particle-fiber

The basis of all adhesion forces between two objects as particle-particle or particle-fiber, are the intermolecular forces between individual molecules. In addition to van-der-Waals forces F_{vdW}, there are also electrostatic forces $F_{adh,electric}$ and effects that can arise from fluid bridges $F_{adh,liquid}$. The largest components in the category of attractive forces represent the van-der-Waals force between the components particle-particle and particles-fiber. Therefore, they serve as the basis for the description of all phenomena occurring between different objects in this work.

1.2.4.1 Van-der-Waals force

Van-der-Waals forces result from the a dipole interaction between atoms and molecules on the surfaces of the objects. The range of these forces is limited to a short distance from the surface of the object as the fiber and the particles. To calculate the van-der-Waals force F_{vdW} between interacting objects, such as two particles or the fiber and a particle, the potential of the interactions is coupled to a geometry factor Γ and a specific material constant called the Hamaker constant A (see equation 1.11) [40]. The Hamaker constant for a combination of different material can be calculated from the Hamaker constants for the same material using the equation 1.10.

$$A_{1,2} = \sqrt{A_{1,1} \cdot A_{2,2}} \tag{1.10}$$

Herein are the $A_{1,1}$ of material 1 and $A_{2,2}$ of material 2. According to Eichenlaub et al. [33], this results in the Hamaker constant for the desired combination $A_{1,2}$. The Hamaker constants in this work are based on the findings by Wu [166], Tsai et al. [157], and Rimai et al. [122]. The Hamaker model has the same approach as the model according to Derjaguin, Mueller and Toporov (DMT model). The model is valid for contact of object made of hard material that doesn't deform in contact. If there is a reasonable deformation in contact of two objects during contact, the model according to Johnson, Kendall and Roberts (JKR model) is applicable [60]. A categorization can be made according to Tsai et al. [157], but will not be discussed further in this manuscript.

$$F_{vdW} = A \cdot \Gamma \tag{1.11}$$

The design of the geometry factor Γ and thus the size ratio of the objects to each other significantly influences the magnitude of the van-der-Waals force due to the interaction surface. The size ratio of two objects to each other is described in three different cases by Rumpf [124]. The detachment of particle structures from a single fiber or array can be calculated using two of the three cases. For instance, equation 1.12 can be used to calculate the adhesion force between two spheres of equal size based on van-der-Waals force.

$$F_{vdW} = \frac{A_{1,2}}{24} \frac{d_p}{a^2} \tag{1.12}$$

Here, d_p is the diameter of the spheres. The second case is also of great interest when considering the detachment of a particle structure from a stretchable single fiber or the fiber array. This evaluates the contact of a sphere and a plate, for which the adhesion force results in:

$$F_{vdW} = \frac{A_{1,2}}{12}\frac{d_p}{a^2} \tag{1.13}$$

In the third case, two plates are assumed to be in contact, and the geometry factor is determined by the contact area A_{area} of the plates. In all three versions, it is important to consider the characteristic distance a between the two objects, which is typically given a value of 1.65-500 Å[89].

1.2.4.2 Liquid bridge adhesion

Under ambient conditions, liquid bridges may form between the fiber and particle or between particles due to condensed humidity. It is possible that small liquid bridges may form in the micrometer range since the particle material was specifically dried in a drying cabinet during the experiments. Thundat et al. [154] demonstrated that bridges formed at 70 % humidity double the adhesion force F_{adh}. The adhesion force of liquid bridges between particles or a particle and a fiber can be calculated using equation 1.14 by Schubert [134]. Here $\gamma_{1,2}$ is the surface tension of the liquid, p_k is the capillary pressure between the liquid and the environment and r_{min} is the minimal radius of the liquid bridge. In this work, the adhesion forces were not explicitly calculated using liquid bridge adhesion. However, it is important to consider the impact of any deviation between measured and calculated values.

$$F_{adh,liquid} = 2\pi r_{min}\gamma_{1,2} + \pi r_{min}^2 p_k \tag{1.14}$$

1.2.4.3 Electrostatic adhesion

The electrostatic adhesion between two particles can be approximated by considering them as two point charges. The force is determined by Coulomb's law, as shown in the equation 1.15. The point charges of the spherical particles are represented by q_1 and q_2, the distance between the two charges is given by $z_{charges}$ and the electric constant is given by ϵ_0.

$$F_{adh,electric} = \frac{q_1 q_2}{4\pi\epsilon_0 (z_{charges})^2} \tag{1.15}$$

If there is an interaction between the fiber and a particle, a sphere-plate model can be assumed, as with the van-der-Waals force. However, the principle of charge must be applied according to the model by Peart [102] and Zimon [175], in consequence equation 1.15 remains valid for the calculation. In the experiment of this work the electrostatic adhesion is not calculated. Though, it is important to consider this factor when analyzing the adhesion forces and the deviations between the measured and calculated values.

1.2.4.4 Influence of surface roughness

Rabinovich et al. [116] made a further development of the model by Rumpf [127] by including the surface roughness in the calculation of the adhesion force in his models instead of a single asperity. This results in the following equation for the adhesion force according to Rabinovich et al. [116, 117]:

$$F_{ad} = \frac{A_{i,j}r}{6H_0^2}\left[\frac{1}{1+(\frac{32r\,k_1\,rms}{\lambda^2})} + \frac{1}{(1+\frac{k_1\,rms}{H_0})^2}\right] \tag{1.16}$$

Herein parameter k_1 denotes a proportional factor, r the radius of particle, H_0 the distance of closest approach between surfaces, rms the roughness for close-packed hemispherical asperity, $A_{i,j}$ Hamaker constant of material i and j, and λ the peak-to-peak distance. For instance, Beach et al. [10] demonstrated in their experiments a significant increase and decrease in the adhesion force as a result of changes in the surface roughness. Similarly, Schaefer et al. [129] found that the adhesion force between glass beads and a mica-surface can be up to 51 times smaller than models had predicted when surface roughness is not taken into account. Further, Kumar et al. [73] and Miwa et al. [89] revealed in their investigations that adhesion force is reduced and increased with substrate a change in surface roughness.
This present work compares experimental measurements of adhesion force between particles and fibers with calculations made according to Rabinovich's model, which includes surface roughness [116].

1.2.5 Stretching of a polymeric single fiber or a fiber array

This work focus on the cause of rearrangement and detachment of particle structure, which is caused by the stretching of single fibers or fiber arrays. The filter fibers, which are made of polyurethane have a modulus of elasticity of 0.49 MPa [106]. Any macroscopic change in length, regardless of the stretching velocity, results in fiber stretching. Fiber material parameters allow a temporary reversible stretching up to 75% elongation and a maximum elongation of about 300%. In relaxed state, the fiber has an initial diameter of 82 μm in average. Stretching reduces the fiber diameter by approximately 18% at 55% elongation.
External forces below the cohesive forces in the fiber can cause deformation. The deformation of polymers is largely a function of the type of polymer and its composition. If an elastomer, as this kind of polyurethane is present, its property of elastic deformation is characterized by a glass transition temperature below room temperature [63, 3]. The property of elasticity is based on the non-destructive rearrangement of tangled molecular chains, which slide past each other when tensile stress is applied (see Figure 1.6 a)). This phenomenon is known as entropic elasticity, which result from changes in internal order [1]. The normal stress σ generated within the fiber is determined by the effective area and the applied force, which must be perpendicular to the surface. When the force is no longer perpendicular to the reference surface, the

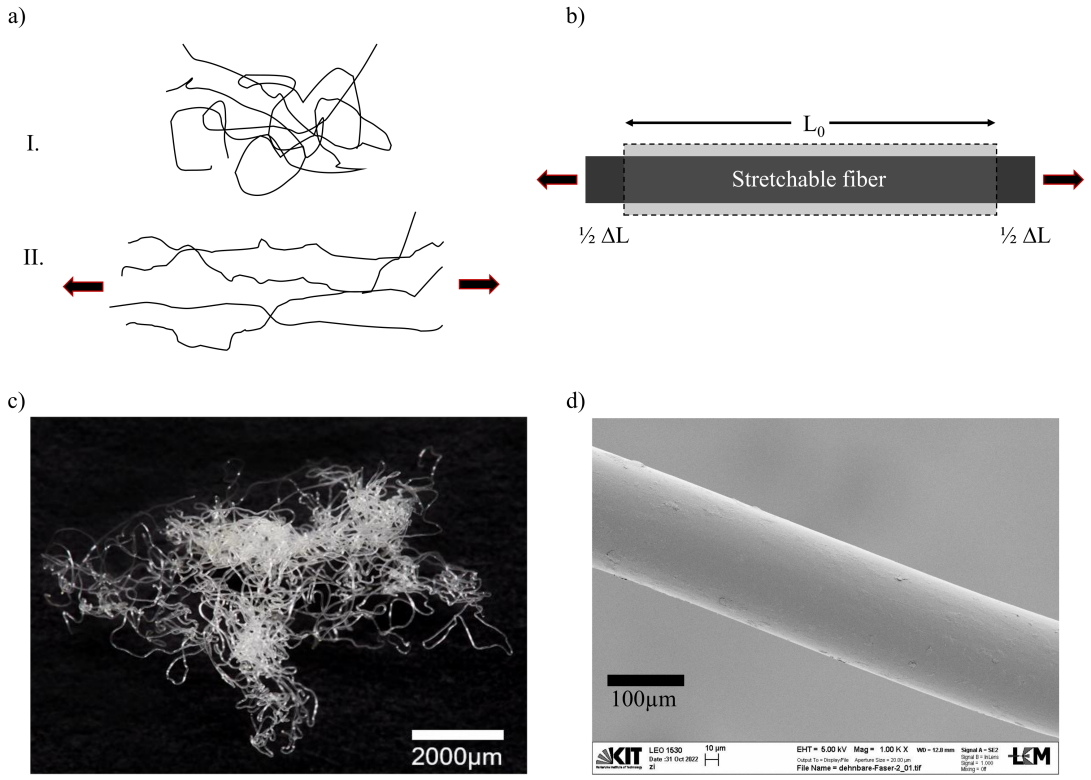


Figure 1.6: *a) Schematic of an elastomer molecule chain in the unstretched (I.) and the stretched state (II.) due to an applied vertical force as shown by Amitay-Sadovsky et al. [3]. b) Schematic of tension of the fiber c) fiber in the oringinal state tangled d) fiber surface entangled in a Scanning electron microscope (SEM) image.*

angle changes γ_{stress}. This is known as shear stress τ_{shear}, which causes deformation or a change in length ΔL, as shown in Figure 1.6 b), regardless of whether it is elastic or plastic deformation. During the stretching experiments, a 22 mm elongation of the clamped fiber(s) in the axial direction is executed during a cycle. The change in length is expressed as elongation $e_{stretch}$, according to the equation 1.17.

$$e_{stretch} = \frac{\Delta L}{L_0} \tag{1.17}$$

Here the change in length ΔL is related to the initial length L_0 of the fiber. Relaxation is defined as the reduction of stress as a function of time. Textbooks assume, a constant strain. However, relaxation also refers to a reduction in strain, which in the context of elastic deformation is accompanied by a simultaneous reduction in stress [9]. When the tensile stress is removed, the molecular chains return to the entangled state and the polymer contracts. A stretching cycle is considered complete only when the fiber has fully relaxed to its starting position.
Due to the elastic deformation of the fiber, structural changes occur inside but also on the surface of the polymer, which results in a significant change in the surface mor-

phology (roughness) as obtained by Amitay-Sadovsky et al. [3] for polyurethane and by Opdahl and Somorjai [96] for polyethylene. The extent of the change in surface structure, like the elasticity, depends on the composition of the polyurethane and, therefore, on the glass transition temperature. The exact chemical composition of this fiber is unclear, as is the estimation of its glass transition temperature.

1.2.6 Setup and methods for measurement of adhesion force between a single particle and a fiber

Atomic Force Microscope (AFM) measurements were conducted to determine the adhesion force between a Spheriglass5000 particle and a stretchable polyurethane fiber in various stretching states, as performed by Opdahl and Somorjai [96]. Figure 1.7 shows a basic schematic of the measurement setup. For observation an additional camera was applied in front of the AFM-measurement head. An accurate positioning and alignment of the particle on the fiber was ensured using camera technique from the front and top view as shown by Hauf-Hartung [39]. A further advantage of measurements with the fiber clamping device is that any elongation of the substrate can be set direct before the measurement without any limits. To keep the fiber in the optimal position during the measuring procedure an additional bracket has been designed and integrated. The bracket prevents the fiber from bending upwards during the measurement procedure. Measurement is performed in ambient conditions. The fiber is

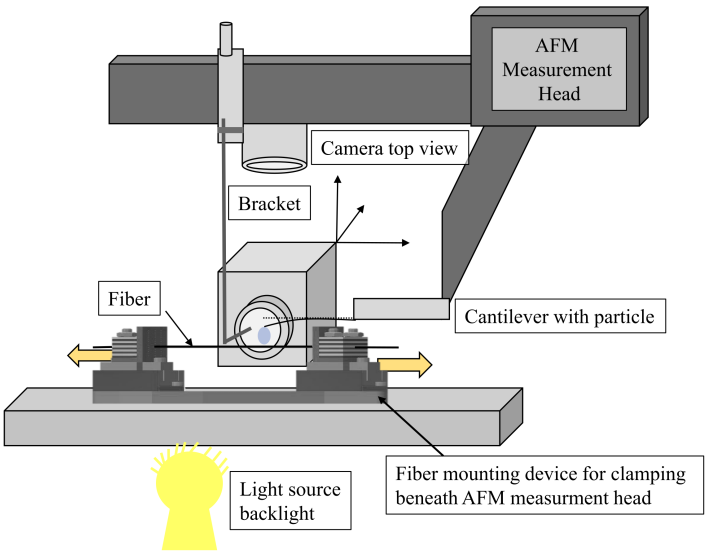


Figure 1.7: *Simple schematic of the AFM measurement setup for the measurement of adhesion force between a particle and the polyurethane fiber in different state of elongation. The illustration is not to scale.*

stretched to four different elongation states using the fiber clamping stretching device. The fiber is elongated up to 7 % (3.976 *mm*) 17 % (9.656 *mm*), 27 % (15.3 *mm*) and 38.7 %

(22 mm). The stretching velocity remained at 12 $mm\,s^{-1}$ for all stretching experiments. In the first step of the measurement procedure the fiber clamping device incl. the fiber is placed beneath the AFM-measurement head. If needed in the experiment, fiber is stretched using the fiber clamping stretching device. After the termination of the fiber elongation, the cantilever is lowered to the zenith of the fiber. Then the bracket is lowered to fix the fiber. The bracket is only lowered to a position, so the fiber position is not changed or influenced by additional pressing. The measurement is then repeated at least 10 times in the tapping mode of the AFM.

1.2.7 Setup and methods for measurement of size and moment of detachment of detached particle structures during fiber stretching

A device based on the laser light sheet technique by Wurster et al. [169] was developed to determine the structure size of detached structures, so they can pass through the fiber interspaces of a future filter. As shown in Figure 1.8 the system detects detached particle structures directly beneath the fibers or fiber array via a laser light sheet and measures their size and the moment of detachment while the fiber or fiber array is being stretched. The moment of detachment during stretching provides information on the busy area during fiber stretching for detachment of particle structures and the level of crack pattern required for structures to detach from the fiber or fiber array. The moment of detachment of particle structures refers in the present work to the elongation of the fiber at the moment of detachment during the elongation process. This presentation was selected for the plots because it is not dependent on the elongation velocity of the fiber during the stretching process. To determine exact size the

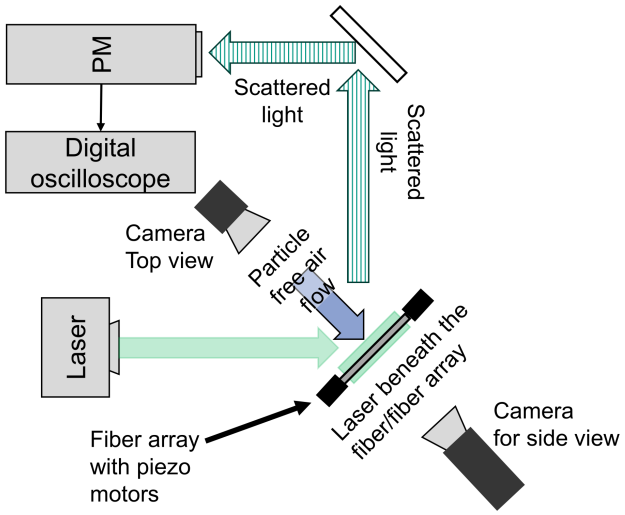


Figure 1.8: *Simple schematic of the measurement setup laser light sheet*

technique uses scattered light of the monochromatic laser ($\lambda_{laser} = 532\,nm$). The system was calibrated with spherical glass beads. Compared to previous studies by Kampa

et al. [64] and Wurster et al. [169], the laser band measurement system includes laser band size of 16x2 mm, detection range between 90 - 2000 μm, sample interval of 100 ns, and illumination. The laser beam profile was assumed to be Gaussian in all direction. Image analysis technique via MATLAB© is used to evaluate the ratio of detached particle material from the particle-loaded fiber or fiber array. This provides an overall impression of the detachment behavior during stretching.
Analysis of side view images during and after each stretching cycle results in the cumulative fraction of the detached particulate structure and the relative particle projection area for experiment with a single fiber. For the experiment with a fiber array analysis of top view images (in direction of flow) results in the relative free projection area of fiber interspaces (RFPI). The RFPI provides information about the flowable area in the fiber interspaces.

2
Thesis outline

2.1 Research Gap and Idea

The research conducted over the past decades has focused on the operation and process parameter of depth filtration. Most filtration processes aim to separate solid particles from an air flow. The primary factors to characterize the operational behavior of depth filters are the separation efficiency, pressure drop and the total loading capacity.
The overall depth filter service life is determined by the development of pressure drop. At the end of the filter service life, when pressure drop reaching a critical value, the filter must be replaced to maintain an energy efficient process [144, 162, 11]. During the filtration process, the particulate material accumulates in the upper layers (first third) of the filter/collector. This phenomenon has been well-studied and is largely understood [76, 35, 51, 46]. The accumulation and clogging of particulate material in the fiber interspaces significantly contributes to the increase in pressure drop and energy consumption of the filter system.[56]. In the classic fibrous filtration the filter fibers are not stretchable.

Based on this, the solution to filter clogging and the associated increase in pressure drop would be to **transfer of particulate material** from the upstream layers of the filter to the void layers downstream using stretching of the collector/filter as an initiator. As discussed in the model by Tippayawong and Preechawuttipong [156], stretching as external excitation should decrease the threshold for particle detachment.
This process idea is intended to create new space for further particulate material in the upstream area facing the flow. The aim is to increase the mass capacity of the filter. Furthermore, the rearrangement and detachment of particle structures should delay the increase in pressure drop as a result of the clogged fiber interspaces.

The following question arises with regard to the research gap and idea. *What factors influence the transfer of particulate material in a future stretchable filter?* The factors that influence the separation process and subsequent stretching should be divided into two sub-categories: **separation of particle structure** on the collector and **stretching of the collector**.

Separation of a particle structure on the collector:	**Stretching of the filtration collector and particle structure:**
• progress (loading height) of the separated particle structure	• stretching velocity of collector
• morphology of the particle structure on the collector	• number of stretching cycle
	• air flow velocity during stretching
	• total length of stretching
	• adhesion force for particle-particle and particle-fiber contact
	• form of stretching (uniaxial or multi-axial)

Since the consideration of these influencing factors (in isolation) on the rearrangement and detachment of particulate material within a fibrous filter is challenging, the **investigations in this work are performed** on **simplified form/model** of the filter. A **single fiber** and a **fiber array** are used. The influencing factors mentioned above remain the same as the **stretchable collector is a single fiber and a fiber array**. This work does not include experiments with a complete filter.

2.2 Research Aim of this Work

In order to answer the question placed above, taking into account the described factors of influence, a fundamental investigation of the *rearrangement and detachment of particle structures from a single fiber or fiber array* is performed in the present work. The aim of this work is defined as follows:

The ultimate goal of this work is to determine and quantify the factors that affect the rearrangement and detachment of particle structures on/from a single fiber or a fiber array.

The separation process and the subsequent rearrangement and detachment of the particle structure due to the stretching process from the single fiber and the fiber array include the formation of cracks, rotation of the particle structures with the fiber in the particle-free flow, displacement of the particle structures on the fiber or fiber array, and ultimately, detachment of the particle structure from the fiber or array. In order to achieve the ultimate goal of this work and address the overall research gap/idea, it is essential to formulate smaller sub-goals:

1. Separation of particle structure on a single fiber or a fiber array with polydisperse particulate material
2. Establishing a measurement technique for determining the size and moment of detached of detached particle structures
3. Determination of the size of detached particle structures from a single fiber or fiber array
4. Determination of the moment of detachment of of particle structures during the stretching process
5. Quantification of the detached particulate material from a fiber or fiber array compared to the initial structure before stretching
6. Qualitative description of the crack pattern of the stretched particle structure
7. Quantification of the ratio of adhesion forces between particles-particles and fiber-particles
8. Establishing of a measuring technique to determine the measure the adhesion force between a particle and the stretchable filter fiber during elongation
9. Determination of the change in the particle loading/filling of the fiber interspaces of the fiber array

2.3 Manuscript Overview

This section provides an overview of the publication-based work (dissertation), as shown in Figure 2.1. As shown above this present work focused on the process of rearrangement and detachment of particle structures from a single fiber (micro level) and a fiber array (meso level). The single stretchable fiber (micro level) and the fiber array (meso level) serve as a simplified model for a future stretchable filter, which was not part of this work. These simplified models are usually used for singular observations of separation processes [138, 119, 70, 91]. However, in this work, the rearrangement and detachment of particle structures is being tested and evaluated. It is not possible to measure pressure loss using these simplified models. Chapter 1 gives a brief introduction into the fundamentals of the separation and morphology of the particle structure as well as the detachment of particle structures from polyurethane single fiber or fiber array. Chapter 2 outlines the main goal of this work and provides an overview of the manuscript. Chapter 3 to 5 focus on the single fiber, while Chapter 6 and 7 concentrate on the fiber array (see Figure 2.1).

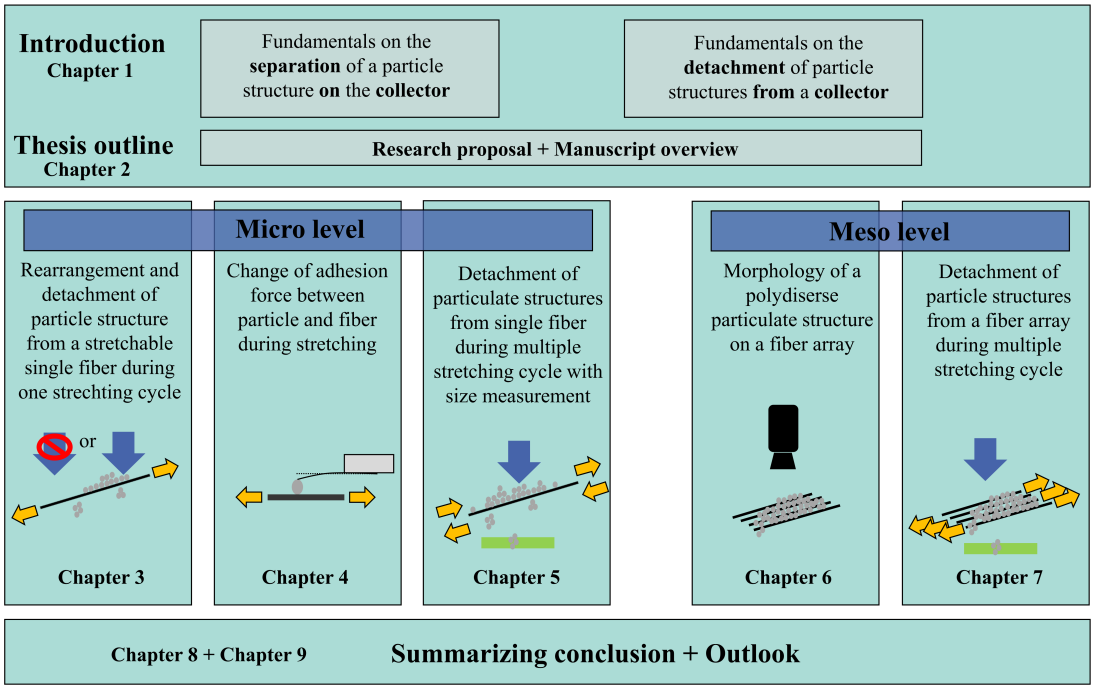


Figure 2.1: *Schematic structure of this work. The publications in this dissertation are categorized into investigation on detachment within the micro- and meso level.*

In **Chapter 3**, the first experiments on the rearrangement and detachment behavior of a compact particle structures during a single stretching and relaxation cycle of a single fiber (micro level) are presented. **Chapter 4** focuses on the change in adhesion force between particle and fiber due to changes in the polymeric surface texture during fiber stretching. **Chapter 5** discusses experiments on the rearrangement and detachment conducted on a single fiber (micro level) during multiple stretching cycles with low and high particle structure on the fiber.
Chapter 6 presents experiments on the separation and growth of compact and dendritic particle structures on a fiber array (meso level) up to the clogging point. **Chapter 7** completes the missing experiments on the rearrangement and detachment from a stretchable fiber array (meso level) with compact and dendritic particle structure beforehand.
All manuscripts have been published in various peer-reviewed journals and have not been used in any other published work.

Chapter 3: A novel method to investigate detachment of particulate structures from an elastic single fiber at low gas flow velocities

Lukas Poggemann, Jörg Meyer, Achim Dittler

Journal of Aerosol Science Vol. 156, (2021), 105785

The objective of the study was to examine the impact of two process parameters, airflow velocity and stretching velocity, on the rearrangement behavior and detachment of particle structures from a stretchable filter fiber (micro level) during one stretching cycle. The study did not extensively examine the process of particle separation onto the fiber. Its sole purpose was to create a particle structure with a defined morphology (St = 3.42) for one subsequent stretching procedure.
The idea was to apply tensile and shear forces to a particle structure by stretching the substrate. To observe the separated particulate structure on the stretched filter fiber, a specialized fiber clamping device and observation setup were developed. The projection area of the particle structure can be used to measure the rearrangement and detachment of the particle structure during the stretching and relaxation process. During fiber stretching, observation of the quantitative change in projection area of the particle structure and the qualitative value of the crack pattern was established using a high-speed camera.
According to initial hypotheses, structural detachment may be associated with the loss of the contact point(s), leading to crack formation. It is believed that the height of the particle structure on the fiber is a contributing factor. This study presents the first experiments of their kind to demonstrate that induced stretching can break up and detach particle structures at airflow velocities of less than $1\,m/s$.

Chapter 4: Experimental investigation on the change of pull-off force between bulk particulate material and an elastic polymeric filter fiber

Lukas Poggemann, Richard Thelen, Jörg Meyer, Achim Dittler

Journal of Colloid and Interface Science Vol. 641, (2023), 903–915

The rearrangement and detachment of the particle structure from the stretchable single fiber depend on the adhesion force between a Spheriglass5000 particle and a filter fiber made of polyurethane during the stretching procedure. The force measurement aims to determine the adhesion force between the particle and the fiber at different states of stretching to evaluate the ratio of adhesion force between particle-particle and particle-fiber. Stretching polymeric fibers causes significant damage to the fiber material and increases surface roughness (RMS). Investigations were conducted using the AFM and the White Light Interferometry (WLI) to investi-

gate changes in adhesion force between particles and fibers at different elongations, while simultaneously examining the fiber surface.
Subsequently, measurements using the AFM showed a decrease in the adhesion force (F_{adh}) between a particle and the fiber with increased stretching. This demonstrated reduction in adhesion force (F_{adh}) is due to the increase in surface roughness and subsequent reduction in contact area. The ratio can be estimated by measuring the adhesion forces between particles and fibers, as well as between particles themselves. These observations can help in explaining the formation of residual structures following the rearrangement and detachment of particle structures.

Chapter 5: Experimental Detection of Particle Structures Detachment from a Stretchable Single Fiber during Multiple Consecutive Stretching Cycles

Lukas Poggemann, Jörg Meyer, Achim Dittler

Separations 9, (2022), 168

This study focuses on determining the size and moment of detachment of complete particle structures resulting from rearrangement and detachment from a single stretchable filter fiber (micro level) during multiple stretching cycles. The size of the detached particle structures will provide an estimate of whether they can pass through the pores of a future filter or remain on a single fiber. Particle measurements were conducted using a self-developed technique that detects scattered light from particles. The air flow velocity (particle-free air) and the stretching velocity are varied to determine their influence on rearrangement and detachment.
In these experiments, the height of the particle structure on the fiber was varied between 78 and 235 μm to evaluate the size of the compact structure on the subsequent size of rearranged and detached particle structures. This study also relates to the theoretical explanations of crack formation in a thin brittle layer on a stretchable substrate from chapter 3. It confirms the observations regarding the formation of a residual structure on the fiber after rearrangement and detachment of particle structures.

Chapter 6: Morphology of Particulate Structures on a Fiber Array before and at Clogging Point of an Aerosol Filtration Process

Lukas Poggemann, Benedikt King, Jörg Meyer, Achim Dittler

Separations 10, (2023), 462

In this study the size of the collector develops from a single fiber (micro level) to a fiber array (meso level). **Chapter 6** focus on the investigation of the development and growth of the particle structure in the interfiber spaces on a fiber array, including its

characteristic features such as pore size, boundary lines of the particle structure, and bridging between fibers. In this chapter the focus is soley on the separation and the morphology of a particle structure.
In chapter 7 these investigations serve as a basis for studying the rearrangement and detachment of particle structures during stretching. In the experiments discussed in this chapter the morphology of the particle structure on the array is varied to evaluate the different growth process. The process of separating compact (maximum St = 10.05) and dendritic (minimum St = 0.52) particle structures on the array is characterized by the TIF until a value of $2.8 \cdot 10^8 \, \# \, mm^{-2}$, where clogging of the array was observed. The separation experiments were examined using polydisperse particulate material only.

Chapter 7: Detachment of particulate structures from a fiber array due to stretching and simultaneous gas flow

Lukas Poggemann, Pablo Längle, Jörg Meyer, Achim Dittler

Separation and Purification Technology, Vol. 351, (2024), 127887

The central objective of the **chapter 7** is to reveal first information about the rearrangement and detachment of particle structures on/from a fiber array (meso level) during 5 consecutive stretching cycles. The chapter includes a quantitative analysis of the size and moment of detachment of detached particle structures, similar to the previous chapters on the rearrangement and detachment of a particle structure on a single fiber. Further, an analysis of the relative free projection area of fiber interspaces was conducted. In addition, a qualitative analysis was performed on the crack patterns and the rearrangement of the particle structures based on their morphology and loading state.
Stretching tests were conducted to determine the rearrangement and detachment behavior at flow velocities of $0.05 \, m s^{-1}$ and $0.8 \, m s^{-1}$. The stretching velocity was varied between $0.6 \, mm s^{-1}$ to $1.2 \; mm s^{-1}$.
In further tests, the direction of stretching was extended from uniaxial to biaxial stretching by increasing or decreasing the distance between the parallel fibers during the stretching process. The change in fiber distance of $27 \, \mu m$ was achieved by rotating the clamp of the paralle fixed fibers during stretching. This results in a multidimensional stress application of shear and tensile forces, also due to the axial shift of the fibers relative to each other. A qualitative comparison was made between the rearrangements and crack patterns with those observed in the experiment with uniaxial stretching of the fiber array and the single fiber was made.

3

Detachment of particulate structures from an elastic single fiber

Title: A novel method to investigate detachment of particulate structures from an elastic single fiber at low gas flow velocities
Authors: Poggemann, Lukas; Meyer, Jörg; Dittler, Achim
Status: Published
Bibliographic data: Journal of Aerosol Science 156 (2021), https://doi.org/10.1016/j.jaerosci.2021.105785

Copyright Journal of Aerosol Science 2021, published by Elsevier. Reprint with permission. The text has been adapted in this thesis to change the citation and figure numbering. Additionally, some symbols have been modified to confirm with the other chapters.

Abstract
The detachment of particle structures from a stiff single fiber exposed to an airflow has been investigated by [75, 83, 113, 53, 110, 180]. In order to detach particle piles from a stiff single fiber, airflow velocities above $1.2\,m\,s^{-1}$ are required. While these values are well above typical operational parameter for depth filters, a shift toward lower velocities for detachment would offer both up and downside for filter operation. One possible application for controlled structure detachment from a filter fiber at lower velocities would be a shift of separated particulate structures from the upper layers of depth filter into lower regions. The result would be additional void space from particle deposition. Currently there is no knowledge available, if fiber stretching could enable such detachment of particle structure fragments at an operation airflow velocity below $1\,m\,s^{-1}$. It is assumed that fiber stretching might introduce shear and tensile stress to the particulate structures. That may lead to first cracks and promote final detachment. This study examines the behavior of particle structure fragments

on an elastic single fiber for the first time. The fiber is loaded with a compact particle structure in a loading chamber. Glass spheres served as inert particulate material. A new customized fiber-mounting device was designed for the stretching procedure of 22 mm (55 %) length. In first experiments, the fiber was stretched without an airflow. Stretching at an elongation rate of 0.4 $mm\,s^{-1}$ caused rearrangement, crack formation and rotation of the fiber. No detachment of particle structure fragments is observed. If the fiber is stretched and exposed to an airflow at 0.8 $m\,s^{-1}$, particles structure fragments re-arranged and subsequently detached. In further experiments at an elongation rate of 1.2 $m\,s^{-1}$, intensive detachment is observed at an increase of superficial airflow velocity from 0.4 $m\,s^{-1}$ to 0.8 $m\,s^{-1}$. In total, this reveals that fiber stretching enables detachment of particle structure fragments from a single fiber exposed to an airflow at superficial velocities below 1 $m\,s^{-1}$. The potential application of elastic fibers in a filter system will have the aim to delay increasing filter backpressure. This effect could be caused by the transport of particulate matter towards areas of lower loading further downstream while maintaining a high level of separation efficiency at operational filtration velocities.

3.1 Introduction:

Depth filtration is commonly used for particulate matter removal in various fields of applications such as air-conditioning and cleanroom technology. The primary factors to characterize the operational behavior of depth filters are separation efficiency, pressure drop and loading capacity [144]. In typical depth filters the pressure drop across the filter system rises at different value with increasing deposited particulate mass in the filter medium [99, 66]. Hence, the energy consumption is increasing, too. Figure 3.1 shows an exemplary evolution of collection efficiency and pressure drop over collected particle mass. The pressure drop is generally developing through three different stages during a filtration procedure. During depth filter stage, the pressure drop is increasing slowly. In this stage, the particles are captured by the different collection mechanisms of individual fibers [101]. Inside a filter, a gradual build-up of particles at the fiber surface takes place. At the end of the depth filter stage, the pressure drop is increasing slightly faster than before.

This is caused by parts of the filter where deposits on neighboring fiber at the upstream side of the filter start to form bridges. In these clogged areas, the deposition moves from the interior fibers of the filter to the deposit structure on the upstream surface. In the transition phase, more and more parts of the surface clog and at the end of this phase, the whole filter area has switched to surface filtration. Subsequently, in the final surface filtration phase, a particle layer grows on the upstream side of the filter, causing a much steeper jet linear increase in pressure drop with increasing thickness of the layer. Further, the collection efficiency reaches very high values close to 100 %. [19, 163]. Once the filter is clogged and transition to surface filtration occurs,

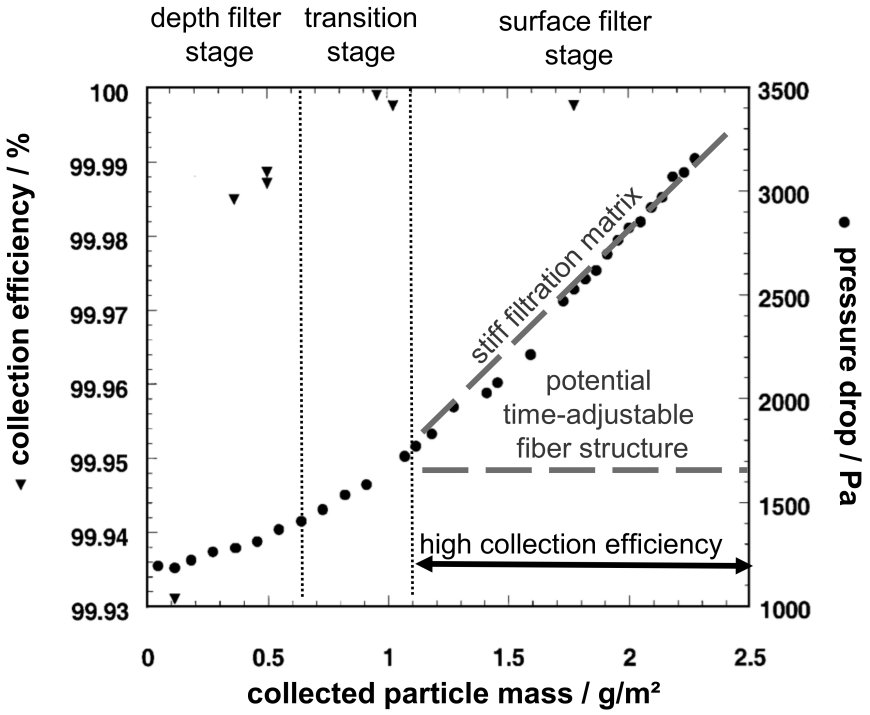


Figure 3.1: *: Collection efficiency and pressure drop over collected particle mass of a stiff filtration matrix and of a potential time adjustable fiber structure. Modified from [152]*

the filter interior is not receiving much particles and thus, no increase in local loading. The filter stays with void space that is not filled with deposit structures, especially at the downstream parts of the filter volume [19].

The overall depth filter service life is determined by the development of pressure drop. In order to delay the steep, the pressure drop increase of the surface filtration stage, more void space especially at the upstream part of in the filter is needed. A chance to clear up space for new particles would be to release blocked pores in the upstream layers of the filter. One way to achieve this would be to stretch the entire filter structure or the individual fibers that make up that structure. It is assumed that stretching of a particle-loaded fiber might induce shear and tensile stress to the particulate structures in these layers. As seen in experiments and calculations by Thouless and Nahta et al., the movement/stretching of an elastic substrate beneath a coating matrix is able to induce cracks. The attached material is exposed to tensile/shear stress in a competitive process between the matrix (coating) and the substrate (fiber, elastic substrate) [153, 94]. Ochai et al. and Lowden et al. have examined exemplary investigation were they observed multiple matrix cracking when subjecting a loaded/-coated fiber to tensile stress [95, 85].

Thus, the introduction of fibers, which are adjustable over the service of the filter,

may lead to these first cracks and promote the transport/removal/detachment of particles to deeper filter layers. Clogging would be delayed. Currently, in common depth filters only stiff fibers are used.

In order to investigate the overall operating behavior of an entire depth filter with stretchable fibers, a basic visual and qualitative, and subsequently, quantitative understanding of effects of fiber stretching on particle structures on an individual stretchable fiber is needed. For this purpose, the collection behavior and detachment behavior of particle agglomerates on an isolated fiber are considered. Only when this knowledge is obtained, the results of basic single fiber experiments can be transferred to the entire fiber matrix in a filter system. An additional step might be the stretching of the entire filter structure to increase the total volume of the filter thus releasing more void space for additional particle deposition. A potential development of pressure drop for a time-adjustable fiber structure is shown in Figure 3.1

In the case of the particle detachment from stiff single fibers, numerous investigations have been carried out. Normally the mechanism of particle detachment and particle bounce occur at higher flow velocity than in the velocity range of depth filer applications [114, 120, 159].

Löffler described first investigations on the limits and conditions for detachment of individual particles and particle structure fragments from a single fiber. One main finding was that inert particles only detach from a filter fiber if flow velocity is significantly higher than common filtration velocities [83]. In detail, Löffler distinguished between single particles with a diameter $d_{particle}$ of $10\,\mu m$ and piles consisting of particles. All particles were deposited on fibers with a diameter of $d_{fibre} = 50\,\mu m$ at a filtration velocity below $0.85\,m\,s^{-1}$. For detachment of 50 % of single particles, an airflow velocity of above $10 m\,s^{-1}$ was necessary. First detachment of piles of particles from the stiff fiber was observed at an airflow velocity of $1.2\,m\,s^{-1}$ [83].

Larsen obtains airflow velocities above $20\,m\,s^{-1}$ for the detachment of $16\,mu$ particles from a stiff fiber [75, 113] investigated the re-entrainment of small particles (pathogens) from loaded filters. The filters were subjected to airflow higher than relevant filtration velocity and in the opposite direction of filtration flow. First detachment of particle with a size of 0.6 to $5.1\,\mu m$ was observed at an airflow velocity of $0.7\,m\,s^{-1}$ [113]. Jankowska et al. determined a lower re-entrainment for of KCL particles ($d_{particle} = 2.55\,\mu m$ and $d_{particle} = 3.25\,\mu m$) than for fungal spores ($d_{particle} = 3.21\,\mu m$ at the same filtration velocity of $3.00\ m\,s^{-1}$. Less than 1 % of KCL particles detached at this velocity [53]. The weakening of adhesive/cohesive strength due to chemical reactions and the followed detachment of particle structures was described by Zoller et al. [180] They observed the detachment of glass spheres and soot from a single fiber after reaction at a flow velocity of $0.5\ m\,s^{-1}$ as opposed to 1.9-2.6 $m\,s^{-1}$ without reaction.

In a simulation Przekop et al. estimated the collection efficiency of particles ($d_{particle}$ = 0.01 to 10 μm) on a single fiber. They calculated that deposition efficiency of particles on the fiber is 10-20 % higher without considering the re-suspension during the filtration process. Filtration velocity/face velocity in these experiments was given as 0.1 ms^{-1} [110]. This found low value in filtration velocity for detachment is an exception, but there is not a single experimental evidence for it.

In all experimental investigations, the velocities for detachment of inert particles/particle structures are rather high compared to common filtration conditions. Further, quoted investigations were focused on detachment of small amounts of particles from a stiff collector. Currently, none of this research projects considered the weakening of particle structures on the fiber due to stretching and movement of the fiber/substrate, which might cause a detachment also at low gas flow velocities.

One important decisive and influencing factor for detachment of particle structure fragments is the morphology and the shape of the particle structure on the fiber. The particle structure on the fiber is formed during the first stage of filtration in a fiber loading process. Starting at this point Kanaoka et al. showed that there is an influence of the filtration velocity on morphology of particulate agglomerates on a cylindrical stiff fiber.

The study examined fundamental dependencies between the filtration velocity and the different collection mechanism. Figure 3.2 shows respectively a schematic of the relationship between the dimensionless numbers and the deposited structure, which were obtained by experimental and theoretical considerations. High Stokes-numbers promote a more compact structure on the front side of the fiber (highlighted in Figure 3.2). Particles have large inertia and move straight to the fiber. [65]
Based on this findings, Kasper et al. [70] investigated the shape of the particle structure on the fiber that are formed under different flow conditions and with different single particle diameters. Here a high Stokes-number and low interception parameter promote rather compact structures, whereas low Stokes-number and increased interception parameters result in dendritic structures with a different/larger cross-sectional area. Finally, the morphology, size and height of particle structure on the fiber have an influence on the drag coefficient [91] and consequently influence on particle detachment.

Usually the filter fiber was operating as a stiff element in the system. In order to decelerate the rise of pressure drop, it might be of high interest to generate knowledge about the detachment and cracking of particle structure fragments and single particles from/on a single filter fiber. In this study, the influence of fiber stretching and low airflow on the behavior of particle structure fragments on an elastic fiber is investigated for the first time. This initial experimental investigation demonstrates that effects like cracking and detachment of inert particle structure during filter fiber stretching can

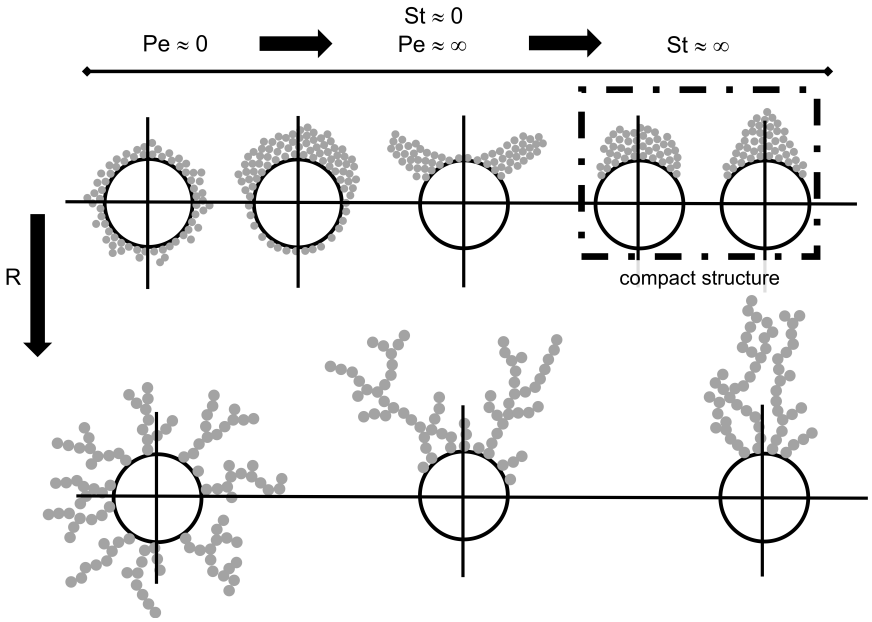


Figure 3.2: *Schematic relationship between the deposit structure and filtration conditions in detail of the dimensionless numbers Peclét, Stokes-number and interception parameter R. Highlighted the compact deposition morphology with higher Stokes-number. Modified from Kanaoka [65]*

occur. Nevertheless, further investigations are needed concerning the detailed process conditions for breakage and detachment of particle structure within/from a fiber matrix. This expertise might then be used in the future to implement a component in the system adjustable over time. The aim is to clear some void space in the upstream areas of the filter, thus slowing down pressure drop increase while maintaining a high collection efficiency, as shown in Figure 3.1.

3.2 Materials and Methods:

3.2.1 Fiber and Aerosol:

For all investigations, polymeric fiber made of polyurethane were used as collector. Fiber material parameters allow a temporary reversible stretching up to 75 % elongation and a maximum elongation of about 300 %. The elastic modulus of the fiber is measured as 0.49 MPa. In relaxed state, the fiber has an initial diameter of 82 μm in average. Stretching reduces the fiber diameter by approximately 18 % at 55 % elongation. A poisson ratio of 0.327 was calculated. To avoid any contamination and surface-charge effects, the fiber was cleaned with ethanol before each loading process. Further, the fiber was handled only with tweezers and gloves during the clamping. As shown in Figure 3.3 a), the fibers are entangled in their original state. Figure 3.3 b) shows an SEM image of an extracted disentangled fiber, as it would be provided for the loading and stretching procedure. The unstretched state of the fiber was established by the same clamping length and the same clamping force for each fiber (here, "unstreched" refers to the initial state of the clamped fiber before particle deposition and stretching of the loaded fiber). Further, a visual inspection using the microscope was performed. Spheriglass 5000 CP00, glass spheres made from solid soda lime A-Glass with a given material and bulk density ($\rho_{material}$= 2.46 $g cm^{-3}$, ρ_{bulk} = 1.28 $g\,cm^{-3}$, $n_{refractive\,index}$ = 1.51), obtained from Potters Industry, served as the inert particulate material in all experiments. Figure 3.4 a) shows the particle size distribution of the glass spheres. The size distribution was determined using laser light scattering (HELOS & RODOS, Sympatec) with a dispersion pressure of 1.0 bar (g). The average diameter was determined as $d_{50.3}$ = 7.73 μm. The particles are mostly spherical as shown in Figure 3.4 b). A similar inert particulate material was used by Zoller et al. [180]

3.3 Experimental Set-up and Procedure:

3.3.1 Set-up for fiber loading process with particulate material

Figure 3.5 depicts the flow diagram of the loading procedure of the fiber. In the loading procedure, the aerosol is generated using a Topas SAG 410/U as used by Zoller et al. [180]. Thereby the particulate material is dosed by a rotating ring and dispersed by an ejector nozzle (DIN ISO 5011). The particulate material was provided in a storage tank.

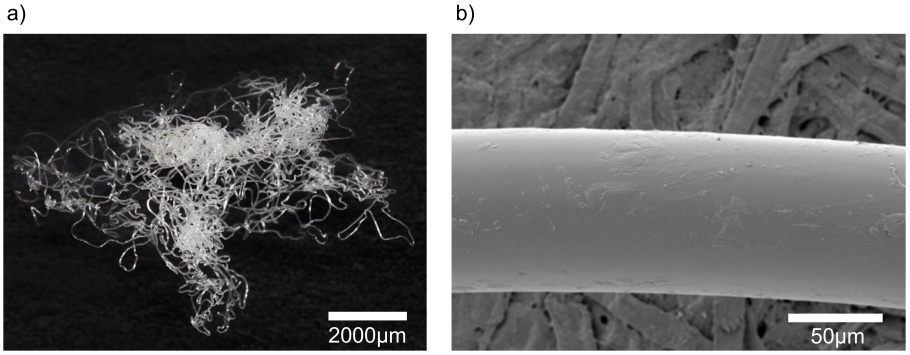


Figure 3.3: *a) Fiber in their original state, entangled, white polymeric structure. b) Fiber disentangled and clamped under the SEM – straightened, unstrechted with initial diameter of around 82 µm*

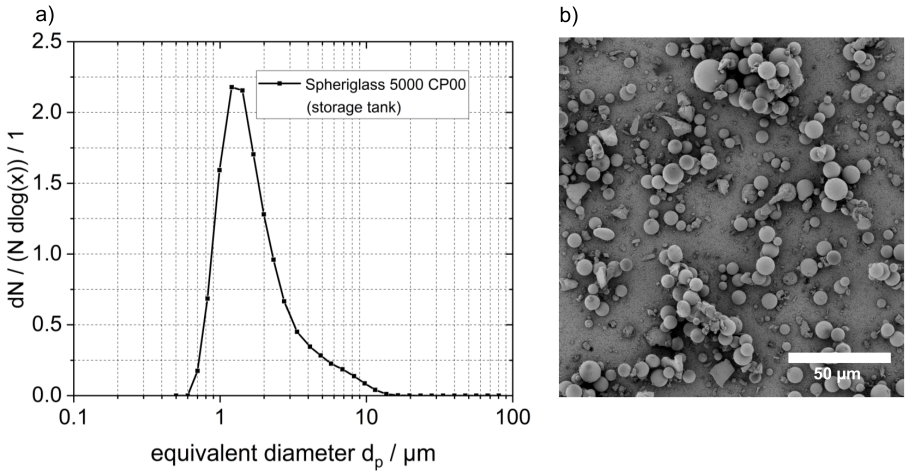


Figure 3.4: *a) Particle size distribution of used Spheriglass 5000 CP00 in the storage tank of the dust generator. Measured offline by HELOS & RODOS, Sympatec b) An according SEM image of the glass particles.*

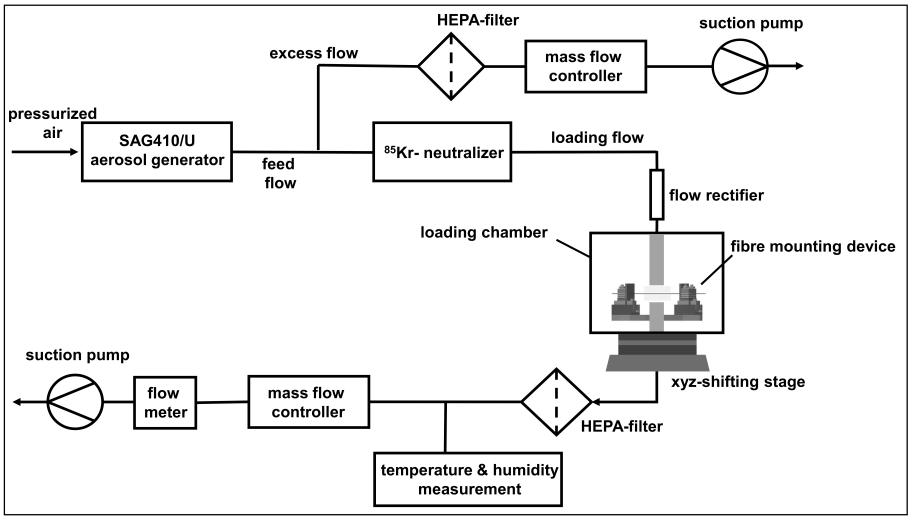


Figure 3.5: *Process flow diagram of the loading procedure including the fiber-mounting device.*

For stable particle mass flow an ejector nozzle pressure of 1.8 bar (g) is necessary. This results in a volume flow of 23 $L\,min^{-1}$ in the feed flow. A mass flow rate of Spheriglass 5000 CP00 in the feed flow (direct beyond the aerosol generator) of 4 $g h^{-1}$ was set for the selected feeding ring speed (5 %of maximum speed) and height of the scraper (5 mm). The loading time was 15 min in all experiments.

The loading equipment includes a section upstream and downstream the loading chamber. The generated aerosol feed flow is divided into loading flow ($V_{loading}$ = 14.28 $L min^{-1}$) for the loading chamber and excess flow (V_{excess} = 8.72 $L min^{-1}$). The excess flow is drained off by a separate suction pump to obtain the correct stable particle mass flow in the loading flow and a stable filtration velocity applied to the fiber. The particulate material is removed by a HEPA-filter following a MFC. The balance of feed flow and loading flow determines the size of excess flow.

After generation, the aerosol passes a ^{85}Kr – neutralizer to reduce the electrical charge of glass spheres. A flow rectifier is placed at the inlet of the loading chamber to establish a laminar plug flow field. The flow rectifier (tube bundle) is located in the inlet pipe, which has a diameter of 16 mm. Subsequently, in the loading chamber the flow forms a short free jet that flows around the fiber allowing particle deposition. After passing the fiber, the flow is approaching the aerosol outlet tube at the exit of the loading chamber. The loading chamber is sealed to avoid any contamination by environmental air and to establish a well-defined volume flow.

The section downstream the loading chamber consists of a HEPA-filter, various devices for flow control, measurement and a suction pump. In order to enable reliable and repeatable results, the humidity, temperature (Sensirion, SHT85) and volume flow

rate (TSI, Flow Meter 4000 series) of the aerosol flow are measured after the HEPA-filter. The volume flow rate of the aerosol and thus the aerosol velocity at the fiber are adjusted by MFC. A calibration of the MFCs was regularly carried out using a bubble flow meter with a precision of 0.03 $L\,min^{-1}$. Loading procedure was performed at about 20-25 °C. Humidity of loading flow was around 10 % There was no extra differential pressure applied across the loading chamber. As written in the introduction several deposition morphologies for particle structure on a single fiber are feasible. To obtain a particle structure on the upstream side top of the fiber a flow velocity of 1.2 $m\,s^{-1}$ corresponding to Stokes-number of 6.52 was selected. Under the given circumstances, the particles mostly deposit due to inertia on the fiber.

3.3.2 Fiber mounting device

For controlled stretching of the elastic fiber a new fiber-mounting device was designed and built, which fits into the existing loading chamber [139]. One challenge for the new fiber-mounting device (shown in Figure 3.6) emerges from the spatial confinement in the loading chamber. Further, the fibers have a maximum length of around 100 mm. The elastic fiber is fixed in the clamping system and positioned by cone-shaped boreholes of 90 µm in the 3D-printed L-section. In order to stretch the fiber, each side of the mounting system is placed on a piezo actuator driven stage (PI, Q-521.230). By using two motors, which move synchronous in opposite directions, the fiber can be kept on the central axis of the flow. This will be realized without displacement relative to the monitoring system during the stretching procedure that is described below. Each piezo actuator achieves a maximum motor velocity of 6 $mm\,s^{-1}$. As a result, the fiber could be elongated with rates between 0.10 – 12 $mm\,s^{-1}$. Furthermore, the maximum linear travel range of each motor is 11 mm with a minimum incremental motion of 8 nm. The maximum drive force is 0.6 N each piezo motor. The length of the clamped fiber between the two clamping points is 40 mm. Combined with the 11 mm travel range of each mounting stage (piezo motor) the fiber could be stretched with a maximum 22 mm (55 % elongation), which is in its elastic range. Operation parameters for the stretching procedure in this study are the elongation rate at the fiber and the velocity of the airflow. In this study stretching and relaxation process were performed in a continuous mode. For further studies, it will be possible to vary the number of stretching cycles and perform a stretching procedure with periodically breaks.

3.3.3 Stretching set-up and Stretching procedure

To observe the stretching of the loaded single fiber, the fiber-mount (see Figure 3.6) was placed under a microscope (Wild Heerbrugg) using a xy-stage for precision positioning. During the stretching procedure, the fiber was exposed to a particle free airflow with a superficial flow velocity of less than 1 $m\,s^{-1}$. Air from the pressurized air supply line, expanded to ambient pressure, was used for the airflow, with a relative humidity of about 10 % and a temperature of 25 °C. The airflow of particle-free air was shifted

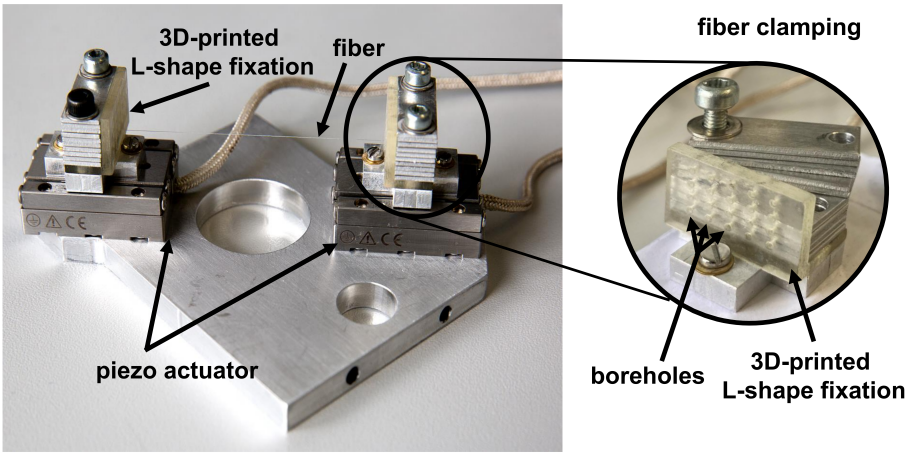


Figure 3.6: *Image of the designed fiber-mounting device for stretching the elastic fiber*

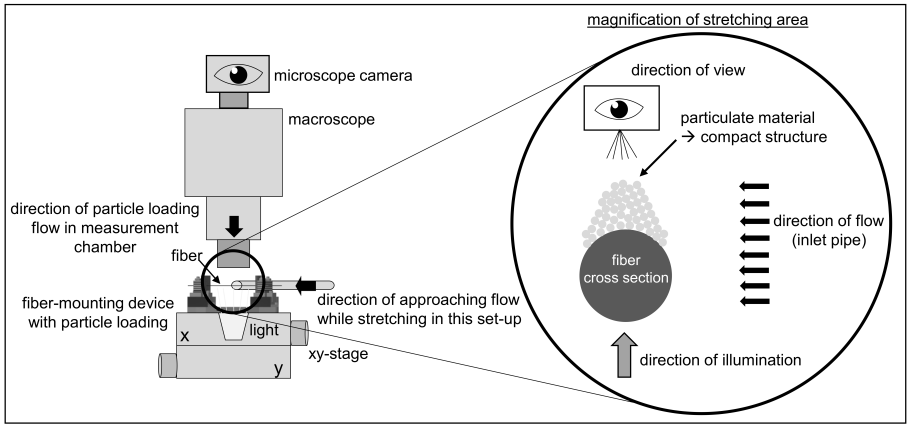


Figure 3.7: *Schematic set-up used for fiber stretching including the fiber-mounting device with loaded fiber and the microscope camera.*

by 90° compared to the particle loading procedure. Direction of loading procedure corresponds to the line of sight during stretching. The fiber had to remain optically accessible from the top for observation. (see Figure 3.7 magnification of stretching area) Illumination of the fiber was installed in the opposite direction.

The loaded part of the fiber remained in the flow axis during the stretching procedure. The inlet pipe had a diameter of 16 mm. The distance between the inlet pipe and the elastic fiber was 10 mm. The flow passes a flow rectifier before reaching the fiber. The superficial flow velocity could be varied between 0.4 and 2 $m\,s^{-1}$. Image acquisition was performed with a microscope camera, a stable frame rate of 10 frames/s and a resolution of 3.1 MPixel. The grayscale of the video images was inverted during recording, resulting in light gray values for the fiber and deposited particle structure and dark gray values for the bright area of the illuminated background. In every experiment with an airflow, the loaded fiber was initially exposed to the airflow for 10 s before the

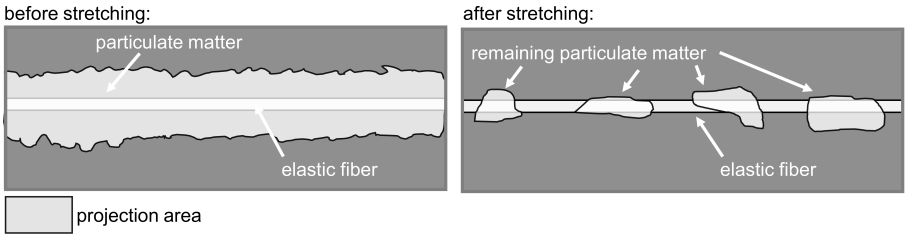


Figure 3.8: *Schematic illustrating the size of projection area of two consecutive frames when stretching the elastic fiber.*

Table 3.1: *Data of stretching procedure*

Step:	Phase:	Duration:
1	Holding phase	10 s
2	Continuous Stretching	55 s (0.4 $mm\,s^{-1}$);18.33 s (1.2 $mm\,s^{-1}$)
3	Holding phase 2	60 s
4	Continuous Relaxation	duration: 55 s (0.4 $mm\,s^{-1}$); 18.33 s (1.2 $mm\,s^{-1}$)
5	Holding phase 3	10 s

stretching procedure started. (holding phase 1) Stretching was performed with an entire elongation of 22 mm (continuous stretching). In the state of maximum elongation, the fiber was retained for 60 s (holding phase 2). The airflow continued. Afterwards the fiber was relaxed back to the starting position applying the same movement parameters (continuous relaxation). After continuous relaxation, the fiber remained in the initial position for 10 s (holding phase 3).

Table 3.1 shows a detailed overview of stretching procedure data. All stretching procedures were performed under ambient pressure and temperature and without any housing of the fiber-mounting device.

3.3.4 Evaluation of experimental results and method of frame fitting

Stretching of the elastic filter fiber shall promote the formation of cracks and detachment of the particle structure fragments from the fiber. Besides the visual/qualitative observation of the fiber and the detachment of particulate material during the stretching process, a more quantitative analysis for different experiments can be established by comparing the projection area of successive frames in a video of critical section of the fiber [180]. An example is shown in Figure 3.9. The projection area of bright pixels representing the particles on the fiber is reduced from one frame to the next. The progression of particle projection area is used as a measure for the effects that appear during fiber stretching. As the detection area of the microscope camera is limited to the central section of the fiber, a part of the loaded fiber is moving out of the field of view while stretching the fiber. Consequently, there would be a loss of data during the stretching and relaxation process. This loss is eliminated by adapting the Region of Interest (ROI) of each frame according to the grabbed frame data respective fiber

length.

This procedure is named “frame fitting”. During the holding phases, the size of ROI is constant between the frames within this phase. During the stretching or relaxation procedure, the ROI is increasing or decreasing among the frames. Figure 3.9 shows an exemplary recorded frame including the frame fitting method. For the maximum elongation of the fiber, the length of the ROI in x-direction corresponds to the maximum length of the detected image of 2048 px. With the start of the stretching procedure, the ROI_{Start} is 1430 px. 440 px correspond to a length of one millimeter. Depending on the elongation length and the clamped length of the fiber, the increment ROI_{add} of the ROI has to be calculated. The size of the ROI is changed by adding gradually about the size of ROI_{add} on both side of the ROI of previous frame. (see Figure 3.9) When starting the relaxation of the fiber, the ROI is reduced again gradually in direction of x-axis down to 1430 px. Thus, for each frame, the ROI is fitted for the current stretching length. Each frame of the obtained video material was processed with a MATLAB© procedure illustrated in Figure 3.10. With the implemented image analysis, the projection area of loaded fiber for each moment of the experiment was calculated.

First, each frame is grabbed with its timestamp/frame data. Based on the frame data (stretching time, relaxing time or holding time) the size of ROI is determined. For a more accurate processing, each frame is converted to a MATLAB© grayscale image. Subsequently the image is binarized using the known method of Otsu [97]. Within the binarized image, the bright pixels are counted. Those represent the absolute projection area of fiber and particulate material on the fiber (PPA_i) on an initial fiber length of 4.65 mm. For each experiment, the elastic fiber is newly loaded with particulate material. To observe repeatable behavior of the stretching process, a uniform compact deposition pattern was aspired. [65, 72]. Nevertheless, there are random variations of the particle projection area that result from small fluctuations during the particle deposition procedure in the measurement chamber. Therefore, the Relative particle projection area (rPPA) was used to evaluate the change in particle projection area. For the $rPPA$ value of each frame, the current particle projection area of each frame PPA_i is set in relation to the initial particle projection area PPA_{Start} at the start of the stretching process. (see Eq. 3.1)

$$rPPA = \frac{PPA_i}{PPA_{Start}} \tag{3.1}$$

Effects such as the rearrangement and rotation of the particle structures on the fiber can also contribute to changes – and generate artifacts – in the particle projection area (indirect $rPPA$). The rotation of the particulate structure is initiated by the internal twist and thus, torsion of the fiber. However, these events are detected by qualitative visual observation. The size of detached agglomerates cannot be determined due to the

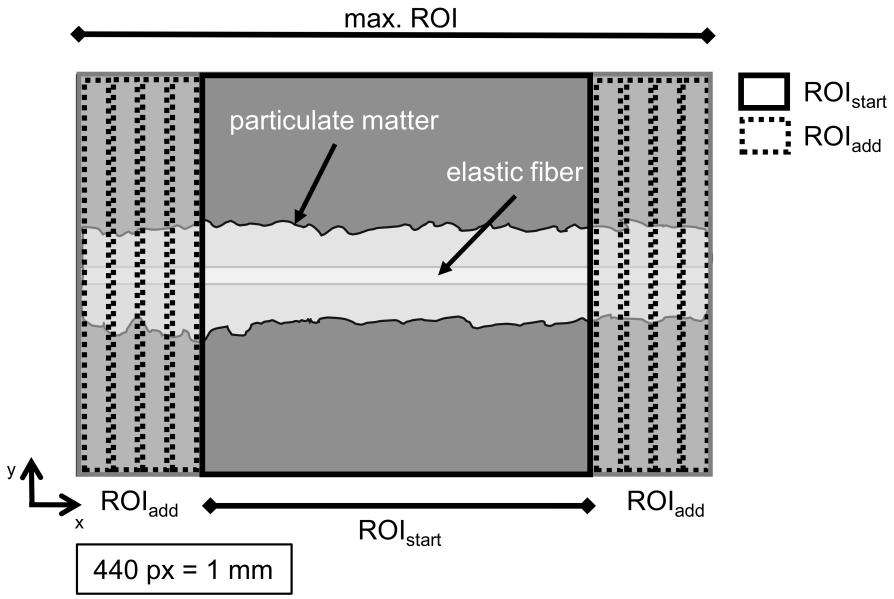


Figure 3.9: *Schematic of the changing size of the ROI. ROI is adapted for each frame separately before the image analysis.*

low frame-rate of the camera. A future step is to perform a more quantitative analysis of detached particle agglomerates by using an accurate measurement technique. This might gain more knowledge about the thickness/height of the particulate structures released from the fiber.

3.4 Results and discussion

3.4.1 Details on qualitative and quantitative data/combination with supplementary data

The results shown in the following will give a qualitative and a semi-quantitative overview of the effects occurring within the particle structure on the elastic fiber during the stretching process. Each of the experiments were performed threefold, including two replicate runs. The complete data is available in the supplement data section. Currently, no exact quantification of the detached particle material is possible, so the analysis is limited to a descriptive report of the events on the fiber, as well as a partial quantification of the (residual) particle structure on the fiber by analyzing the particle projection area including rPPA. The size and height of detached particle fragments could give insight into the exact stress needed for first and multiple crack initiation [93]. An exact prediction based on time or elongation is currently not possible. Therefore, a first description of those effects based on repeated trials and a representative example seems reasonable.

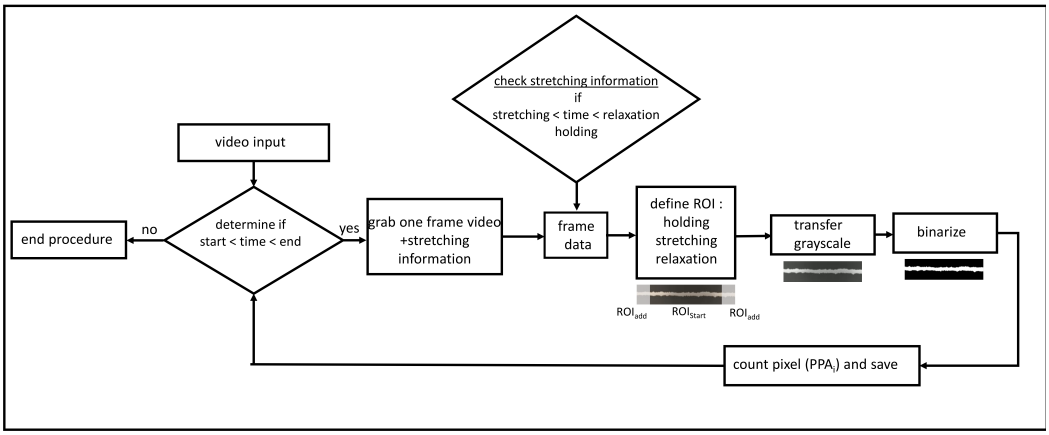


Figure 3.10: *Procedure for image analysis of the recorded data. Determine of PPA as an indicator for detachment and change in structure of the particle loading on the fiber.*

3.4.2 Stretching without airflow

At first, the influence of fiber stretching on the behavior particle structure is investigated without an airflow ($u_s = 0\,m\,s^{-1}$) to the fiber. Figure 3.11 and Figure 3.12 depict representative images of a loaded fiber during the stretching, holding and relaxing phases. Due to the used airflow velocity during the loading process, the particle structure on each fiber has a compact shape during the first holding phase and at the start of the stretching phase (see Figure 3.11 I. and Figure 3.12 I.).

Figure 3.11 shows the fiber, which is stretched with an elongation rate of $0.4\,mm\,s^{-1}$. At the beginning of the stretching phase, the particle structure start to move and slide along with the fiber in direction of stretching. First crack formation within the compact particle structure is obtained at a total stretching length of $8\,mm$ (36% stretching). (see Figure 3.11 III.) In detail, the deposited particulate material starts to separate into structures on the fiber (inter-particle contact cracking) as supposed in Table 3.2. These structures have a size between $550\,\mu m$ to $800\,\mu m$ (in visible length). Due to the continuing stretching, the cracks between the separated particle structure fragments are increasing (see Figure 3.11 IV.). Besides the crack formation, the fiber is rotating including the particle structure on the fiber, so the contact line between particle structure and fiber becomes visible (see Figure 3.11 V.).

In addition, the rotation of the fiber is shown schematically above the corresponding image of the fiber. At the end of the continuous stretching phase the crack formation and rearrangement reaches its maximum (see Figure 3.11 V.). During the second holding phase, the fiber stays elongated at $22\,mm$ (55% stretching) for $6\,s$. Within the particle structure on the fiber, no change is visible in this phase (see Figure 3.11 VI.). As the continuous relaxation starts, the emerged cracks start to vanish. The relaxation of the fiber is performed at a contraction rate of $0.4\,mm\,s^{-1}$. At the end of the relaxation process, the fiber is slightly crimped. The structure/form of the fiber

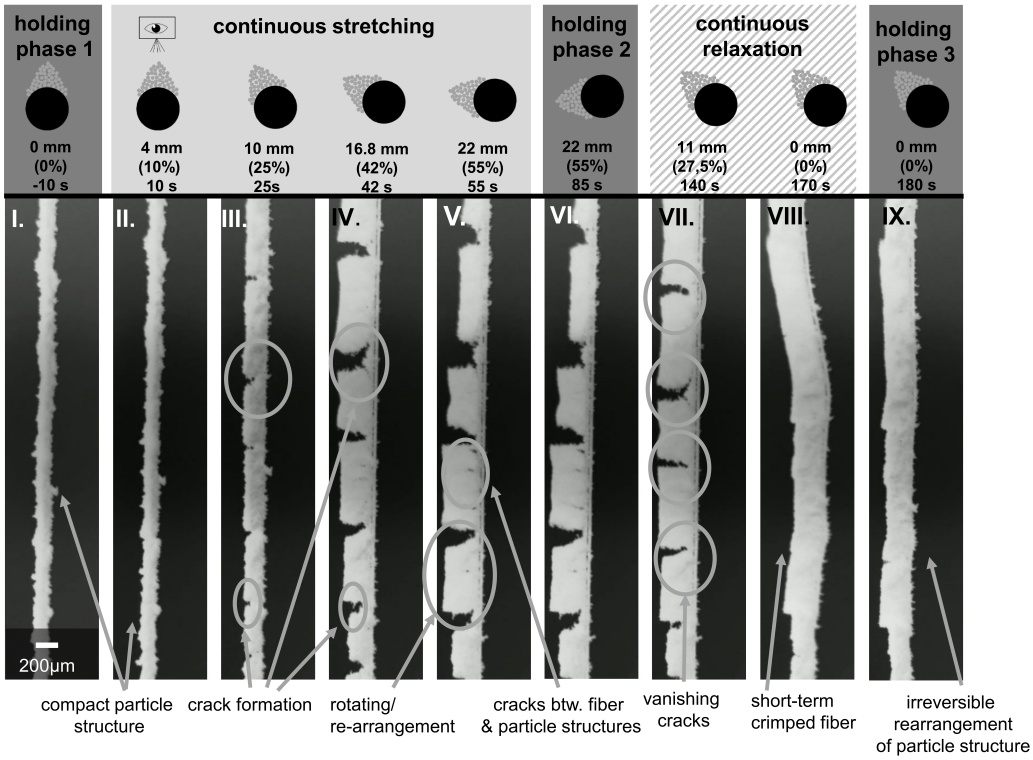


Figure 3.11: *Photographs (inverted) of the deposited particulates structure during one stretching and relaxation cycle of a particle loaded fiber. Without a superficial airflow. Elongation/-contraction rate of 0.4 mm s^{-1}. Compact structure at the beginning. Above the images denoted: the elongation length of the fiber, the time of stretching experiment. Pictograms of the loaded fiber indicate the rotation of the fiber and the change in particle loading. No frame-fitting within this images.*

regenerates gradually to straight cylinder line within 10 s after the end of the relaxation phase. As Figure 3.11 IX. shows, the particle material on the fiber is in a compact shape again after the stretching procedure. The rearrangement of the particle structure on the fiber and rotating of the fiber seems to be at least partially irreversible (see Figure 3.11 IX). In total, fiber stretching at this elongation rate without airflow causes only rearrangement and formation of cracks (see Table 3.2). Detachment of particle structure fragments was not observed. Further, the fiber is rotating around its axis. The rotation of the fiber is caused by the internal twist within the fiber.

To emphasize the first effects of the elongation rate, Figure 3.12 shows representative images of the fiber that is stretched with a tripled elongation rate of 1.2 $mm\,s^{-1}$ without an airflow. As seen before, the particle structure on the fiber has a compact shape in the beginning. First crack formation is obtained between a fiber elongation of 4 mm (10 % stretching) to 10 mm (25% stretching). The broken up structures between the cracks have the same size as in the experiment with an elongation rate of 0.4 $mm\,s^{-1}$. With continuing stretching, the separate structures start re-arranging and the fiber, including the particle structure on the fiber, rotates around its axis. The presumed rotation of the fiber is shown in schematic images above each photograph of the fiber. During the second holding phase, particle structure fragments on the fiber re-arrange without stretching which is visible by the reduced bright area of the upper two particle structure segments in Figure 3.12 VI. Further, within the separated particle structure fragments on the fiber, cracks emerged during the last millimeter of the continuous stretching phase. In comparison to the experiment with the elongation rate of 0.4 $mm\,s^{-1}$ rearrangement and fiber rotation is more distinctive with an elongation rate of 1.2 $mm\,s^{-1}$. At the start of the continuous relaxation phase, the fiber including the particle structure fragments seem to rotate back to their initial position. As shown in Figure 3.12 VII. the cracks start vanishing with decreasing fiber elongation. As a single event, detachment of a small particle structure could be observed in Figure 3.12 VIII. Back to initial fiber length, the cracks within the total particle structure on the fiber have vanished.

However, it becomes obvious that an irreversible rearrangement of particle structure fragments on the fiber took place. Some rotation of the particle structure segments is still visible at the upstream contour of the particle structure on the fiber. Comparing to the experiment with the elongation rate of 0.4 $mm\,s^{-1}$ the fiber is less crimped. During the third holding phase, the slight crimp of the fiber is slowly vanishing. As Figure 3.12 IX. shows, the particle material on the fiber is still in the compact shape after the stretching procedure. Similar to in the experiment with a lower elongation rate of 0.4 $mm\,s^{-1}$, the fiber stretching mainly promote crack formation and rotation of the fiber including the particle structure on the fiber. However, during the relaxation phase, first detachment of particle structure has been observed. The stretching of the fiber might weaken the particle structure and their contact to the fiber, so small parts

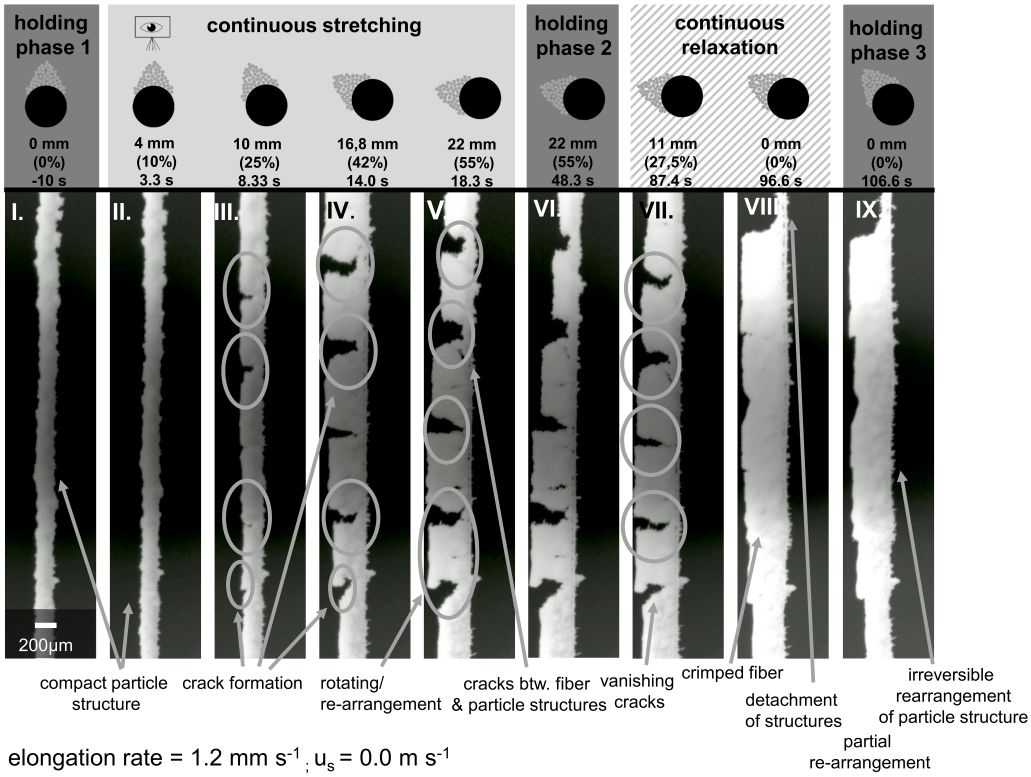


Figure 3.12: *Photographs (inverted) of the deposited particulates structure during one stretching and relaxation cycle of a particle loaded fiber. Without a superficial airflow. Elongation/-contractions rate of 1.2 $mm\,s^{-1}$. Compact structure at the beginning. Above the images denoted: the elongation length of the fiber, the time of stretching experiment. Pictograms of the loaded fiber indicate the rotation of the fiber and the change in particle loading. No frame-fitting within this images.*

detach during the relaxation procedure. A schematically overview of this mechanism was given in Table 3.2.

3.4.3 Stretching with airflow

In the experiment without an airflow, detachment of particle structure fragments does not occur by just stretching a single fiber slowly. Hence, the fiber is exposed to an additional airflow (as indicated in the images from the left side) at a superficial velocity of 0.8 $m\,s^{-1}$ while beginning stretching at an elongation rate of 0.4 $mm\,s^{-1}$. Figure 3.13 depicts representative images of the fiber during the different phases. During the first holding phase, the loaded fiber is just exposed to an airflow of 0.8 $m\,s^{-1}$ for 10 s. Figure 3.13 I. shows no particle detachment or rearrangement occurs during this phase. As shown in Figure 13 II. the particle structure on the fiber maintains in a compact shape during the first 4 mm (10% stretching) of elongation. After 6 mm (15% stretching) of continuous stretching first cracks emerge in the particle structure on the fiber. The

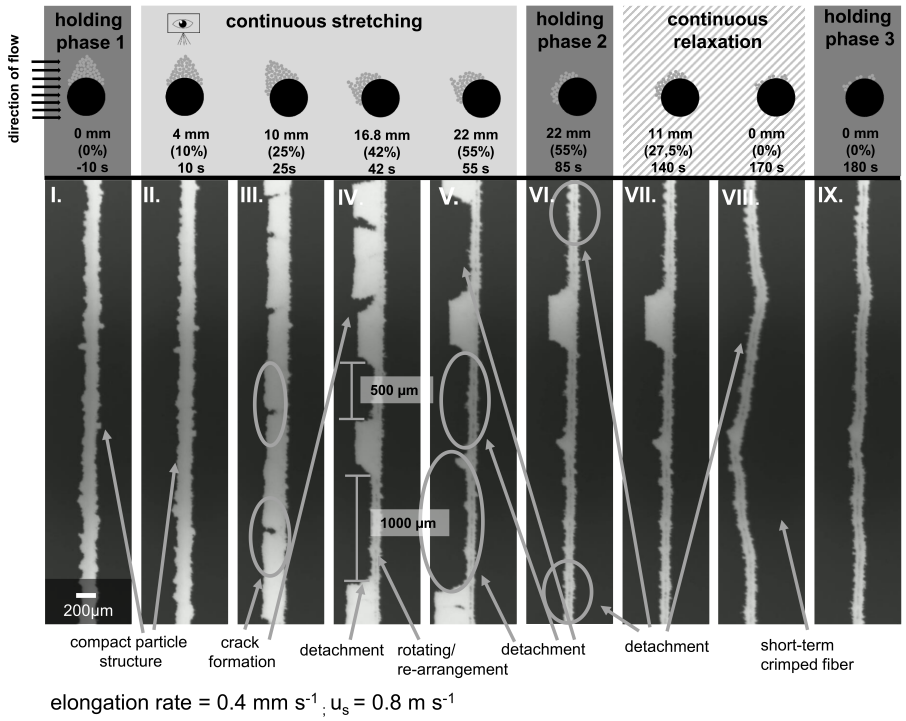


Figure 3.13: *Photographs (inverted) of the deposited particulate structure during one stretching and relaxation cycle of a particle loaded fiber. With a superficial airflow of 0.8 m s^{-1}. Compact particle structure on the fiber at the beginning. Above the images denoted: the elongation length of the fiber, the time of stretching experiment. Pictograms of the loaded fiber indicate the rotation of the fiber and the change in particle loading. No frame-fitting within this images.*

formation of cracks increases with the increasing elongation length (see Figure 3.13 III. after 10 mm (25% stretching) of stretching). The whole particle structure might slide on the fiber. In addition, the fiber is rotating and the particle structure re-arrange on the fiber as already observed in experiments without an airflow. In this experiment the rotation of the fiber was in the same direction that had been observed in the experiment before without an airflow. The emerging cracks seem to have the same size and spacing as well. The residual obtained particle structure fragments are rotated into the direction of airflow (luv side of the fiber). First detachment of particle structure fragments from the fiber occurred at an elongation of 10.8 mm (27% stretching). At once the rotation of the fiber and the rearrangement of particle structure fragments on the fiber proceeds. The first detached particle structure fragments have a size between 500 – 1000 μm. At the end of the stretching phase (after 18.33 s), a large part of the particle structure is already detached from the fiber (see Figure 3.13 V.). The fiber rotating and rearrangement/orientation of agglomerates to the luv side of the fiber does not inhibit detachment. As Löffler obtained, particulate material is more likely to detach in bigger particle structure fragments (piles) from the fiber than just single particles [83]. Starting the second holding phase between the continuous stretching and continuous relaxations procedure some particle structure fragments detach from the fiber (see at the side of the photographs). Figure 3.13 VI. shows that some residual single particles remained on the fiber in areas where big particle structure fragments detached. During the second holding phase, the fiber is still rotated as seen in the schematics above the images of the fiber. Within the continuous relaxation phase, the remaining part of particle structure detached from the fiber. The fiber starts crimping as depicted in Figure 3.14 VIII. During the third holding phase, the short-term crimped fiber is straightened back to initial state.

In order to quantify the phenomena on the fiber, the rPPA, instead of qualitative images of the stretching experiments, were investigated. Figure 3.14 shows the recorded rPPA during the stretching processes without and with a superficial airflow to the fiber. The elongation rate in both cases was 0.4 $m\,s^{-1}$. The continuous data is divided in five sections in accordance to the steps during the stretching procedure as described in section 3.3.3. In both experiments without and with an airflow, the rPPA remains on a constant level during the first holding phase of 10 s. No particle structure fragments re-arrange or detach. The fiber including the particle structure is not rotated yet, as indicated by the pictograms. For the experiment without an airflow (black line) the rPPA starts increasing after 5 mm (12.5% stretching) of stretching. rPPA increases continuously because the fiber is rotating around its axis (as indicated by pictogram) in combination with rearrangement and sliding of the particle structure fragments on the fiber. Maximum of rPPA is reached almost at the end of the elongation. A decrease of rPPA is based on the rotating particle structure fragments that are leaving the observation level. During the second holding phase of 60 s the rPPA is decreasing slightly due to the rearrangement of particle structure fragments. In general, the rPPA is remaining

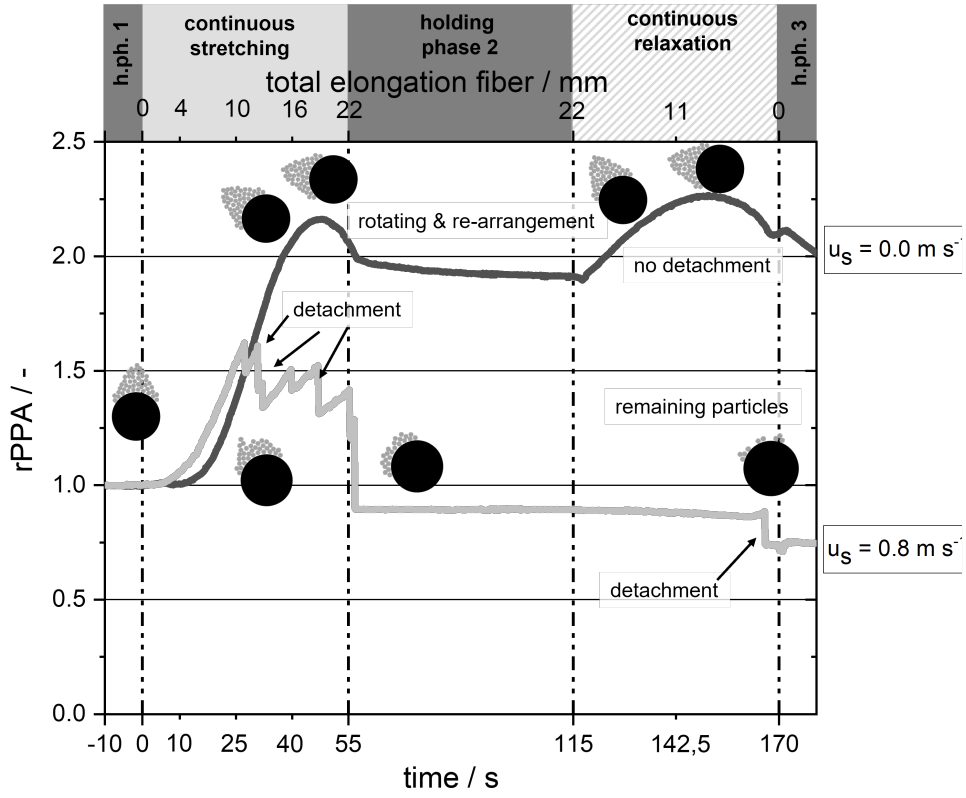


Figure 3.14: *rPPA plotted versus elongation and time during the stretching and relaxing procedure without and with an airflow. Constant elongation/contraction rate of 0.4 mm s^{-1}. The pictograms indicate the rotation of the fiber and detachment phenomena occurring on the fiber like in Figure 3.11 & Figure 3.13.*

on a value of almost twice the initial value. Starting the relaxation phase after the second holding phase, the rPPA is increasing again because the cracks within the particle structure on the fiber start vanishing. By reaching the initial state of the fiber length, the rPPA is still on a level way above the starting level. The elastic fiber is crimped at the end of the relaxation process. (see Figure 3.11 XII.) Remaining particle structure fragments on the fiber have been re-arranged irreversible and remain in the position they had during the second holding phase. These appearances are reasons for the rPPA above 1. During the holding third holding phase the crimp of the fiber is vanishing, but the rearrangement of particle structure fragments on the fiber remains. In total, the rPPA of the fiber is increasing above the initial level of 1 during the five phases of the experiment. There was no significant and sudden decrease of the rPPA during the whole experiment, which would be an indicator for detachment of particles.
In the experiment with an airflow of 0.8 $m s^{-1}$ (see Figure 3.14 gray line) the rPPA starts increasing after 2.5 *mm* (6.25 % stretching) of stretching. rPPA is rising continuously with the continuing elongation of the fiber. The fiber is rotating around its axis and

the particle structure is re-arranging to the luv side of the fiber. The rPPA reaches its maximum almost in the middle of the stretching phase. First detachment of particles is indicated by a sudden decrease of rPPA at an elongation of 10.8 mm (27 % stretching). Moreover, up to the maximum stretching length of the fiber the rPPA is decreasing significantly multiple times. These events are linked to further detachment of particle structure fragments from the fiber (see Figure 3.13 IV. and V.). Reaching the maximum of the elongation length the rPPA is below the initial level at the start of the experiment. During the second holding phase between stretching and relaxation phase, there is no change in the rPPA. The fiber including the residual particle structure on the fiber is remaining in the rotated state as indicated by the pictogram. During the continuous relaxation phase, the rPPA is remaining on the same level as during the holding phase, except a small decrease at the end, which is linked to detachment of particle structure fragments from the fiber. The fiber is crimped after reaching the initial elongation. The rPPA level is remaining constant because there are no more particle structure fragments on the fiber that could rotate or influence the particle projection area. Comparing the experiments with and without an airflow it was obtained that particle structure fragments just detach in the combination of stretching of 0.4 $mm\,s^{-1}$ and an airflow. The stretching procedure might induce shear and tensile stress leading to cracking within particle-structures and between fiber and particle-structures (see Table 3.2). Thus, the particle structure fragments are more likely to re-arrange and finally detach if exposed to an airflow. In all corresponding repeated experiments, the same phenomena of re-arrangement, rotation and detachment could be observed (see supplementary data). In both cases, the particle structure fragments might slide and rotate on/with the fiber before the cracking.

3.4.4 Impact of different airflow velocities on the detachment behavior of particle structures on the fiber

To illustrate the influence of the superficial airflow velocity on the behavior of particle structure on the fiber, Figure 3.15 shows representative images of the loaded fiber exposed to three different airflow velocities. The applied airflow velocities are 0.4 $m\,s^{-1}$, 0.6 $m\,s^{-1}$ and 0.8 $m\,s^{-1}$ respectively. For reasons of comparisons, one of the airflow velocities is the same as in the experiments above. Direction of airflow is from the left side as indicated in each figure. In every experiment, the elongation rate was 1.2 $mm\,s^{-1}$. The fiber is exposed to the airflow (at its velocity u_s) during the entire experiment. All experiments were repeated two times. The video material of each individual experimental run can be found in the supplementary data. During the first holding phase of each experiment, the particle loaded fiber is just exposed to the airflow. As shown in the images in Figure 3.15 a) b) c) I., the particle structure on the fiber has the desired compact shape at the begin of the experiments. Further, no detachment occurs in any experiment during the first 10 s without stretching the fiber (see Figure 3.15 a) b) c) II.). This confirms the findings of [83] that no detachment

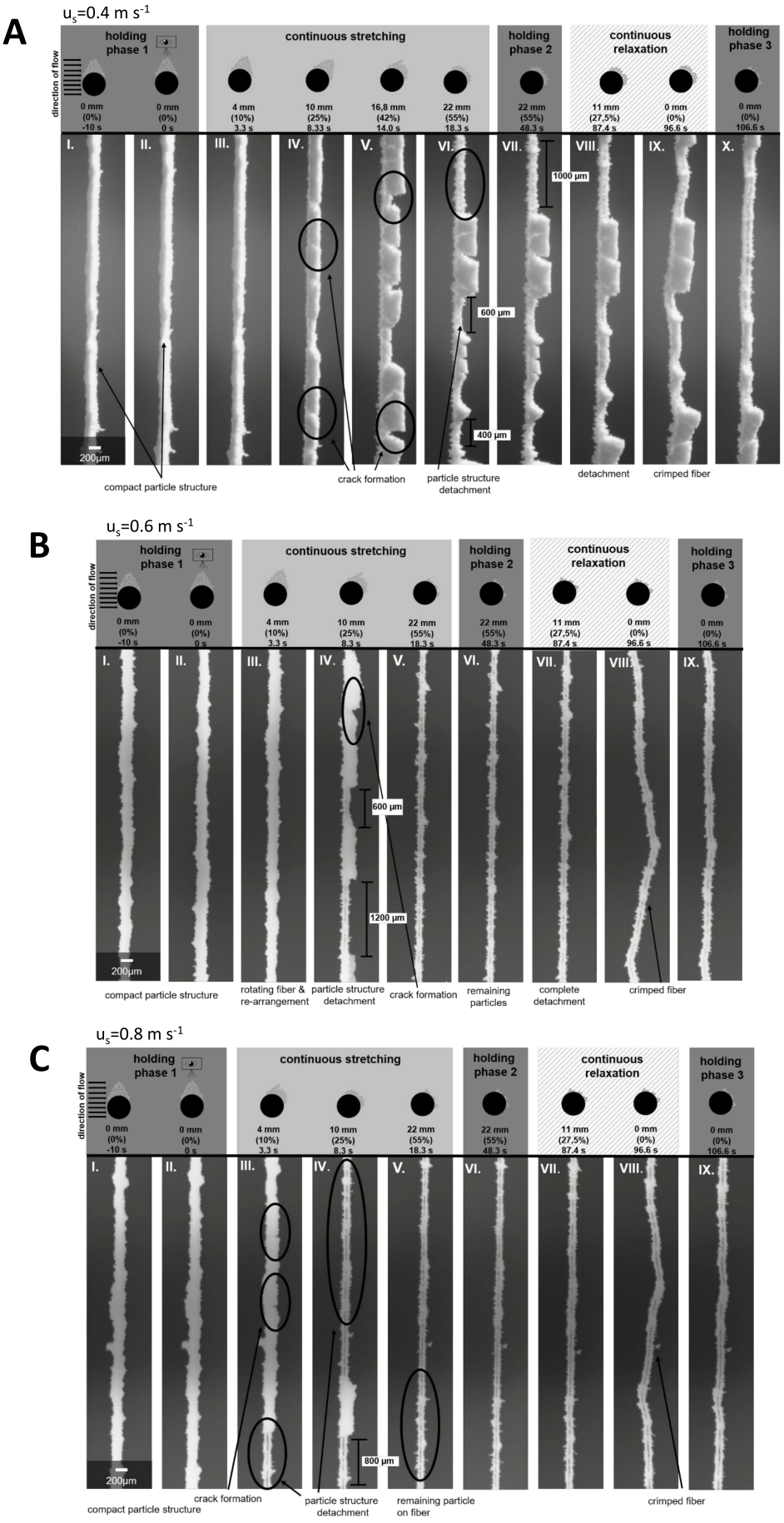


Figure 3.15: *Photographs (inverted) of the loaded fiber during detachment experiments with a constant elongation/contraction rate of 1.2 mm s^{-1} and various superficial velocities of the airflow. a) 0.4 m s^{-1}, b) 0.6 m s^{-1}, c) 0.8 m s^{-1}*

of particle structure fragments occurs at these airflow velocities below $1\,m\,s^{-1}$. Figure 3.15 a) depicts representative images of a fiber during one stretching procedure at an airflow velocity of $0.4\,m\,s^{-1}$. First crack formation and rearrangement of the particle structure fragments is observed at a fiber elongation of $9\,mm$ (22.5% stretching) (see Figure 3.15 a) IV.). Formation of cracks is intensifying during the continuous stretching phase. Starting the stretching process the fiber also begins to rotate around its axis. The rotation of the fiber is indicated by the pictogram above the fiber images. The fiber rotates to the far side of the airflow (lee side of the fiber). As shown in the images, the particulate structures follow the movement of the fiber. First detachment of particle structure fragments was observed at a fiber elongation of $19.2\,mm$ (48% stretching).

The detached particle structure fragments have a size between $400\,\mu m$ and $1000\,\mu m$. During the second holding phase, no further particle structure fragments detached from the fiber. During the relaxation phase of the fiber, the cracks within the particle structure on the fiber start vanishing. The particle structure fragments re-arrange on the fiber. As shown in Figure 3.15 a) X. the shape of the visible projected particle structure is completely changed comparing to the start of fiber stretching (see Figure 3.15 a) II.). A layer of residual particles is left on the fiber. Further, the fiber is crimped at the end of the relaxation phase. During the third holding phase, some big particle structure fragments detach from the fiber. The particle structure fragments might have been loosened by the stretching and relaxation procedure. As observed before some residual particle remained on the fiber at the end of the third holding phase. (see Table 3.2, detachment with residual particle)

Increasing the airflow velocity up to $0.6\,m\,s^{-1}$ first detachment of particle structure fragments occurred at a fiber elongation of $9.6\,mm$ (24% stretching). As shown in Figure 3.15 b) IV. the formation of cracks and rearrangement was not that pronounced as at airflow velocities of $0.4\,m\,s^{-1}$. The first detached particle structure fragments have a size up to $1200\,\mu m$. In Figure 3.15 b) IV. crack formation and rotation of the fiber is visible. At the end of the continuous stretching phase, a huge amount of particle structure fragments detached from the fiber. Single particles and small residual particle structure fragments are remaining on the fiber (see Figure 3.15 b) V.). During second holding phase and the relaxation phase, no further particle detachment is observed. As shown in Figure 3.15 b) VIII. the fiber is crimped after the relaxation phase. No particles detach during the disappearing of fiber crimp in holding phase 3. (see Figure 3.15 b) IX.)

Figure 3.15 c) depicts representative images of the fiber during the stretching procedure exposed to an airflow of $0.8\,m\,s^{-1}$. First detachment of particle structure fragments was observed at a fiber elongation of $3.6\,mm$ (9%). Crack formation and rotation of the fiber preceded the detachment of particle structure fragments. The rotation of the fiber is shown by the pictograms. The piles on the fiber seem to orientate

to the lee side of the fiber. As observed before, the fiber is rotating around its axis, too. At an elongation of 10 mm (25% stretching) almost the complete particle structure is detached from the fiber. As indicated in Figure 3.15 c) IV. the size of the particle structure fragment is around 800 μm. At the end of the continuous stretching phase, there are just single particles and small agglomerates remaining on the fiber. No detachment of small particle structure fragments occurred during the second holding phase and the relaxation phase. The bond between single particles and the fiber appears to be more resilient than the adhesion force within the particle structure. As observed before during the experiments at different superficial airflow velocities, the crimp of the fiber disappears within the 10 s after the end of the relaxation phase.

For a more quantitative and continuously analysis of the phenomena on the fiber, instead of qualitative single images of the representative stretching experiments, the rPPA could be investigated. Figure 3.16 shows the recorded rPPA during the stretching processes for the experiments at three different superficial airflow velocities including an experiment without an airflow (light grey dotted line, $u_s = 0\,m\,s^{-1}$). The fiber is elongated in all experiments with an elongation rate of $1.2\,mm\,s^{-1}$.

In all experiments, the rPPA is remaining at the initial level in holding phase 1. No particle structure fragments re-arrange or detach on/from the fiber just by the airflow without stretching. During the first 1 mm (2.5 % stretching) of stretching, the rPPA of all experiments is remaining at the initial level. After an elongation of 1 mm (2.5% stretching) the rPPA in the experiment with superficial airflow velocity of $0.6\,m\,s^{-1}$ and $0.8\,m\,s^{-1}$ respectively are increasing until the first particle structure fragments detached from the fiber. The increase of rPPA is based on the rearrangement of particle structure fragments and the rotation of the fiber that is depicted by the pictograms. The largest increase of rPPA is observed at an airflow velocity of $0.4\,m\,s^{-1}$ and in the experiment with no airflow ($u_s = 0\,m\,s^{-1}$). particle structure fragments have more time to re-arrange on the fiber and the formation of cracks is more distinctive (see representative images Figure 3.15 a) and Figure 3.16). Detachment of particle structure fragments is characterized by a sudden decrease of rPPA. For all experiments, the rPPA is increasing above 1 during the first seconds of stretching phase. By detachment of agglomerates during the continuous stretching phase, the rPPA is decreasing below 1 for the experiment at superficial airflow velocities of $0.6\,m\,s^{-1}$ and $0.8\,m\,s^{-1}$. In both experiments, not further significant change in rPPA could be observed because all particles detached from the fiber. In the experiment with an airflow velocity of $0.8\,m\,s^{-1}$ first detachment occurs at an elongation of 4 mm (18 % stretching). In the experiments with lower airflow velocity ($0.6\,m\,s^{-1}$ and $0.4\,m\,s^{-1}$), first detachment occurs only at an elongation of 9.6 mm (24% stretching) and 19.2 mm (48% stretching) respectively. In the experiment with $u_s = 0.8\ m\,s^{-1}$ and $u_s = 0.6\,m\,s^{-1}$ almost all particle detach during the first half of the continuous stretching phase. The rPPA of the experiment at a superficial airflow velocity of $0.4\,m\,s^{-1}$ is remaining on a constant

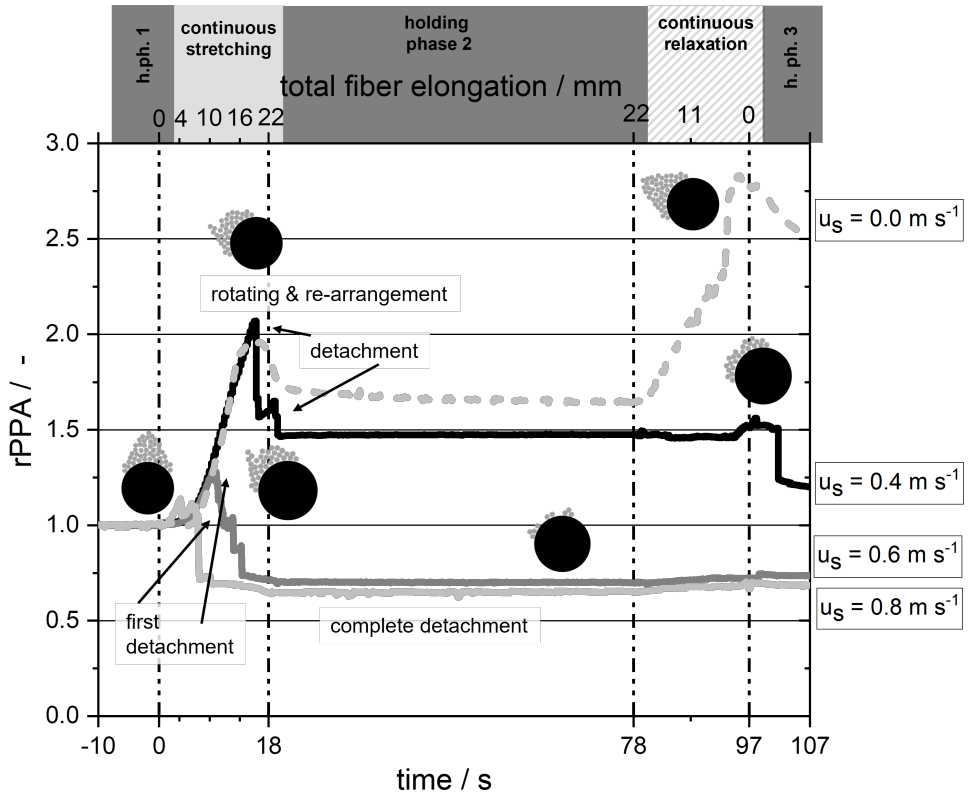
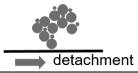


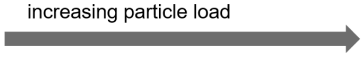
Figure 3.16: *rPPA of stretching experiments with different superficial airflow velocities and one elongation/contraction rate of 1.2 mms^{-1}.*

level above 1 in the second holding phase. This is caused by increased irreversible rearrangement of particle structure fragments and rotation of the fiber. Further, a large part of particle structure is remaining on the fiber. The slight change in rPPA during the relaxation phase is based on fiber rotation and rearrangement of the particle structure on the fiber. During the third holding phase, there is a sudden decrease, which is linked to detachment of particle structure fragments. The connection between particle structure on the fiber and the fiber might degrade by the stretching and relaxation procedure, so particle structure detachment gets more likely (see Table 3.2).

In the experiment without an airflow, the decrease of rPPA at the end of continuous stretching phase is less abrupt. particle structure fragments re-arrange and rotate on the fiber. During the second holding phase, this process continues without any external influences. By the start of the relaxation, the rPPA is increasing again due to the rollback of crack formation. A sudden decrease of rPPA at the beginning of the third holding phase is linked to more intensified rotation/rearrangement and detachment of small particle structure fragments. In comparison to the experiment with an airflow, the rPPA is above the initial level that results from an irreversible change in particle

Table 3.2: *Schematic of hypothesis on behavior of agglomerates and particles during fiber stretching.*

mechanism	1. adhesion	2. slide	3. cracking	
			interparticle contact	particle contact to fiber
number of contact points to fiber	1	≥ 2		
1. fiber initial length				
2. fiber stretched		slipping/sliding 	agglomerate breaks 	contact point to fiber breaks  detachment
3. return to fiber initial length	remaining – no effects due stretching	remaining structure 	re-arrangement 	with residual particles



structure on the fiber and almost no detachment of particle structure fragments.

3.4.5 Hypothesis concerning behavior of particle structures on elastic single fiber during stretching based on the observation/crack formation in matrix on elastic substrate

Resulting from the qualitative observations during the stretching experiments, Table 3.2 summarizes potential applicable mechanisms for the sliding, rearrangement, cracking and detachment of spherical particles and agglomerates under fiber-stretching conditions. There are three potential mechanisms of behavior of particle structure fragments on an elastic fiber based on the fundamental idea of the movement of the substrate beneath a particulate structure [143]. All of them depend on the geometry of the contact and the cohesive/adhesive forces of the particulate deposit.

One determining parameter for the different mechanisms is the number of contact points to the fiber. A single spherical particle has only one fiber contact point whereas agglomerates of particles have higher numbers of fiber contact points. Single particles with one contact point to the fiber might adhere to the fiber while it is stretched. For agglomerates or a contiguous area, fiber stretching induces stress to the particle structure and thus, can result in sliding and cracking of structures. Detachment is a result of complete contact point breakage between agglomerates and the elastic fiber or/and between neighboring agglomerates/particles. Based on the first observations in the experiments shown, residual particles always remain on the fiber, after detachment of agglomerates from the fiber. The theoretical breaking stress of a particle structure can be calculated according to Rumpf and Hamaker [40, 123]. For the determination of the force between fiber and particle structure, normally the deformation of the substrate must be taken into account. According to Schütz and Schubert, this contribution is negligible in case of calculation of adhesion force for e.g. limestone

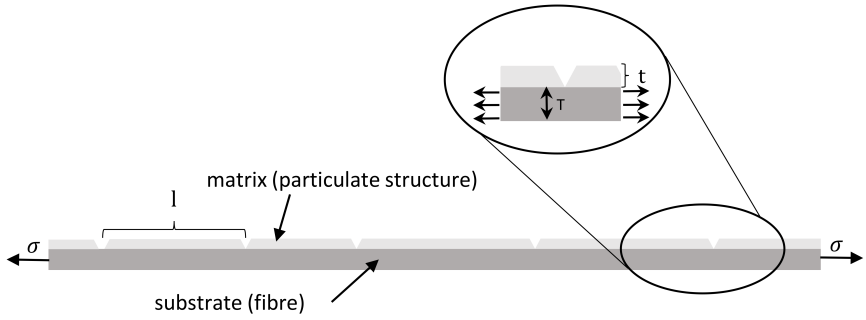


Figure 3.17: *Schematic of the stress model on a plane substrate covered with a matrix layer. Applied stress to the substrate. Modified from [93].*

particle and silver steel plate [135, 132]. In the case of elastic materials, discarding this deformation might not be valid and could give an explanation for the residual particles. All mentioned processes are potentially preceded by a change in number of contact points. Further, a crossover of mechanisms of particle structure fragments behavior is imaginable.

A relevant factor for detachment and cracking effects is the analysis of the applied tension on the fiber (substrate) and the matrix on the fiber. If the induced stress σ exceeds a critical value σ^*, the first fracture occurs within the matrix on the elastic substrate [93]. Cracking of the particle structure on the fiber was observed in all shown experiments. Schematic of filter substrate system with cracking is shown in Figure 3.17. Thouless and Beuth have carried out fundamental investigations on the factors influencing this initiation stress for crack [153, 12]. The height t of the thin film (particle structure) is crucial. Further, the length l of the particle fragments is characteristic for the applied or induced stress of the substrate beneath. This results in an energy release rate at the tip of each crack, which is able to grow further in the matrix/film. The rate is given in Eq 3.2.

$$G_m(l/t, \sigma) = \frac{\sigma^2 \pi z (1-\nu^2)}{E} F(s)^2 \tag{3.2}$$

The correlation of G_m includes the Young's modulus E of the substrate (fiber), as well as the applied stress σ during initial cracking and the Poisson's ratio ν of the substrate. Moreover, the exact depth z and length of the cracks is needed for the function F(s) shown by Thouless [153]. In addition to the influencing factors mentioned, a distinction is also made between the two cases of cracking without and with detachment of the matrix from the substrate [93]. Further accurate measurements of the height of the particle structure and the size of detached agglomerates will provide more information about the factors influencing detachment and cracking of the matrix (particle structure on the fiber). So far, the insights gained on the cracking process are the first introductory step to the understanding of the weakening of particle structure adhesion on the fiber, which ultimately leads to the detachment of the particle structures from

the fiber. In addition to that, the applied airflow has a considerable influence on the detachment of particulate structures from the fiber, as drag forces create additional stress in the fracture zone. In each experiment with an applied airflow, particle structures detached from the fiber. The orientation of the particle structure, whether lee or luv to the fiber may have an influence on the detachment behavior as the exposed area of the particle structure is changed. Besides cracking of the particulate matrix, the stretching of the fiber is causing a tension in the fiber. The rotation of the fiber including the particulate material is caused by a torsion of the fiber. The torsion of the fiber is a result of the applied tension by stretching the fiber. However, due to a number of influencing variables which are currently unclear (e.g. the angle of fiber rotation), a precise estimation and modeling is difficult and not feasible yet.

3.5 Conclusion and Outlook

The fundamental influence of the fiber stretching process on rearrangement and detachment behavior of particle structure fragments on/from an elastic single fiber while exposure to gas flow is presented in this study. Before the stretching process, the fiber was loaded in a loading chamber with a defined compact particle structure. The compact morphology was obtained by a filtration velocity of $1.2\,ms^{-1}$ under the given parameters of particle size distribution and fiber diameter, based on the findings of Kanaoka and Kasper et al. [65, 70]. To separate of the influence of the process parameters during stretching, some initial fiber stretching experiments were examined without an airflow. In subsequent experiments, the particle-loaded fiber was exposed to a particle free airflow during stretching. The observation and evaluation of the loaded fiber was examined with a microscope. Subsequent offline image analysis was realized by a MATLAB© routine. The main results are:

- A custom-designed fiber-mounting for investigations on loaded elastic filter fibers was constructed and applied for the first time.
- A method for image analysis of particle-projection area with an implemented frame fitting method to compensate for ROI growth during stretching was developed.
- At experiments with a low elongation rate below $1.2\,mms^{-1}$ and no airflow, no detachment of particle structure fragments from the fiber occurred in these experiments.
- particle structure fragments detach with the combination of a superficial airflow velocity below $1\,ms^{-1}$ and an elongation rate of the fiber of at least $0.4\,mms^{-1}$.
- Comparing to results for ‘conventional’ fibers by Löffler [83] the dynamic/elastic fiber initiates particle structure detachment at reduced superficial airflow velocities below $1\,ms^{-1}$.

- Comparing to results of Zoller et al., piles of glass particles detached at velocities of 0.4 $m\,s^{-1}$ with previous mechanical weakening of the particle structure instead of weakening by reaction [180].
- Comparing to results of Jankowska et al. the surface and structure has a huge influence on the detachment/re-entrainment of particle and particle structure [53].
- particle structure rearrangement combined with increasing rPPA occurred more frequently at lower elongation rates below 1.2 $mm\,s^{-1}$ and without airflow.
- particle structure detachment is getting more likely with increasing airflow velocity at a constant elongation rate of 1.2 $mm\,s^{-1}$.
- Uncontrolled rotation/torsion of the fiber while stretching the fiber was observed independent of airflow.
- Rotation of the fiber causes re-orientation of piles luv and lee of the fiber .

A more precise method for particle structure fragments analysis will be part of our future work in this field. A laser-sheet measurement technique in combination with an image analysis will be applied for detection and accurate size measurement of detached particle structure fragments. These investigations might result in more detailed analysis of the correlations between particle load, the applied process parameters and the probability of detachment. Moreover, an investigation of various multi-fiber configurations using a 3D-printed L-shaped fixation is possible, e.g. an arrangement of several fibers stacked or parallel.

The use of elastic fibers in filter media might be an enabler for adaptive filter systems in the future. These potential adaptive systems will have the aim to delay increasing filter backpressure while maintaining a high level of separation efficiency. Consequently, this could extend the loading capacity and life span of the filter.

Declaration of competing interest: The authors declare that they have no known competing financial interests or personal relationships that could have appeared to influence the work reported in this paper.

Acknowledgement: We gratefully acknowledge that this project was funded by the Deutsche Forschungsgemeinschaft (DFG, German Research Foundation) – 427981860.

We kindly thank Prof. Dr.-Ing. Peter Elsner, Dr.-Ing. Wilfried Liebig and Dr. -Ing. Jonas Huether from the Institute for Applied Materials (IAM), KIT, for use of their single fiber tensile test stand. We also kindly thank Freudenberg Filtration Technologies SE & Co. KG for donating fiber material to this research.

Appendix A. Supplementary material: Supplementary data to this article can be found online at https://doi.org/10.1016/j.jaerosci.2021.105785 .

Graphics program: PowerPoint, Gimp.

4

Investigation on the change of pull-off force between particulate material and an elastic fiber

Title: Experimental investigation on the change of pull-off force between bulk particulate material and an elastic polymeric filter fiber
Authors: Lukas Poggemann, Richard Thelen, Jörg Meyer, Achim Dittler
Status: published
Bibliographic data: Journal of Colloid and Interface Science 641 (2023), 903-915, https://doi.org/10.1016/j.jcis.2023.03.051

Copyright: Journal of Colloid and Interface Science 2023, published by Elsevier. Reprint with permission. The text has been adapted in this thesis to change the citation and figure numbering. Additionally, some symbols have been modified to confirm with the other chapters.

Abstract
Hypothesis
Adhesion between particles and a filter fiber is an important process of the filtration as it dictates the process of separation and in the following the detachment process of particles during filter regeneration. In addition to the shear stress that a new polymeric stretchable filter fiber implements into the particulate structure, the elongation of the substrate (fiber) is also expected to cause a structural change in the surface of the polymer. Thus, the changed contact area and surface energy could affect the adhesion force between particles and fibers.

Experiments
Systematic measurements of adhesion forces between a single particle and the stretchable substrate were performed using AFM. The substrate surface characteris-

tics (roughness) was changed directly beneath the modified measurement head using piezo-motors to achieve stepless elongation state. Polystyrene particles and particles made of Spheriglass were applied.

Findings
In the experiments, a reduced adhesion force between the particles and the filter fiber was found for a new high range of substrate roughness and peak-to-peak distance, in which the Rabinovich model has not been used before [116]. Further, the influence of high and low energy surface particulate material was evaluated to understand the detachment process in the new real adaptive filter and in DEM-simulation.

4.1 Introduction

Depth filtration systems are used in a wide range of applications to remove particulate matter from the air ensuring reliable operating conditions for process plants or guaranteeing safe air quality when air conditioning systems are in use. During the filtration process the particulate material is accumulated within the filter matrix. In the advanced filtration process, more particulate material remains in the upstream layer of the filter. As a consequence, the lifetime of a depth filter is often determined by the pressure drop, which determines the moment the filter must be replaced. The increase in pressure drop is largely determined by the deposited particle mass in the upstream area of the filter, which accumulates in this filter layers during the transition phase and the surface-filter phase of a depth filtration process. In the downstream layers, less particle material is deposited. In order to extend lifetime of a filter medium, a possibility might be to initiate detachment of particle structures in the upstream areas of the filter and transport the particulate material into deeper layers of the filter matrix [106]. This would enable the deposition of further particulate material in the upstream layers of the same filter medium. The most important mechanisms in this new type of filter are the fracturing/rearrangement of the particle layer on the filter and as a consequence the detachment of particle structures from the upstream layers to the downstream layers of the filter. The rearrangement and detachment of particle material within the accumulated filter layer releases larger pores during the filtration process. These transport processes shall be initiated by stretching of the upper layers of the fiber matrix though inducing mechanical stress to the particle structure. rearrangement or detachment of particle material by gas flow exclusive requires high flow velocities, as shown by the investigations of Löffler et al., Qian et al., Jankowska et al., Przekop et al. and Zoller et al. [81, 113, 53, 111, 179].
To gain more basic knowledge about the mechanism within the fibrous filter, systematic experiments at a single fiber are examined. Using this information from the microscopic level (single fiber), filtration behavior of fibrous filters can be modeled more precisely. In experiments with stiff fibers (without mechanical excitation) first detachment of particle piles from a fiber into the gas flow occurred at air flow veloci-

ties of $1.2\,m\,s^{-1}$ [81]. Moreover, extensive detachment experiments with a stretchable single fiber (with mechanical excitation) have already been realized to determine the influencing parameter on moment of detachment and the size of detached particle agglomerates. Further, the fraction of detached particle structure from total particle structure on the fiber after various stretching cycle was determined [107].

For a more detailed understanding of the rearrangement and detachment process of particle agglomerates within a filter on a microscopic level, a characterization of adhesion force between single particles and a polymeric filter fiber at different stretching conditions is required. Detailed insights on how the change (elongation, surface structure) of the fiber properties as process component affect the adhesion and detachment process of single particles. Experimental studies on the detachment of particle material have already be performed. External influencing factors such as flow velocity in the filtration process are characterized [106, 107]. In addition, this the detachment process is not only investigated experimentally on a macroscope and microscopic level, the obtained data (adhesion force, surface data of the fiber) is further implemented in a DEM-simulation. For the particle-resolved simulation it is essential to know the adhesion force between fiber and particle body in different strain states of the fiber. First approaches for a detachment process resolved from literature data have already been shown in Braschke et al. [16]. Thus, this type of calibration for the DEM-simulation is an extension of the usual calibration types as performed by Coetzee [23]. In specific, the shown measurements of adhesion force take consider the direct interaction of adhesion between the fiber and the particle material.

For the determination of adhesion force between a particle and a substrate (fiber), there are several possibilities such as the centrifuge or ultracentrifuge method. The centrifuge method was used by Schmidt et al., Petean et al. and Haarmann et al. [130, 104, 37]. In this study, AFM was used to determine the adhesion force and surface properties between a solid body (particle) fixed at the cantilever and the substrate beneath. As a stationary and highly sensitive method, it offers sufficient space to integrate any setup for testing the change particle-surface interaction due to change of surface properties.
An alternative use of AFM is the characterisation of the wetting ability of different low or high energy surfaces. In those cases a droplet is attached to a cantilever or capillary tube and is brought into contact with the substrate. For the interaction between the liquid phase and solid (substrate), Daniel et al. was able to replace the well known measurement of the contact angle of a droplet. The measurements with the AFM result in a characterization of the wetting properties of the superhydrophobic surface [24]. Similarly, Hokkanen et al. and Liimatainen et al. were able to use Scanning droplet adhesion microscopy (SDAM) to show how the wettability of different superhydrophobic coatings and surfaces [80, 44]. These measurements replace a classic characterisation with the Contact angle goniometry (CAG). The investigated surfaces were coatings with a low energy surface.

As shown by Daniel et al., Jiang et al. and Shyam et al. there is a dependence between the surface energy and some inhomogeneity of the surface. This consequently results in a measureable change of adhesion force or friction of the droplet. [24, 58, 141]. Shyam et al. was able to show a more general approach on the interaction between a droplet (depinning and droplet pull-off) and the surface of a substrate. This technique is considered for the determination of wetting properties or adhesion strength [141]. Nevertheless, in this study a contact between a solid particle and a solid substrate is under investigation.

For this study the change of substrate (fiber stretching) can be realized directly in the AFM measurement housing. A stepless stretching results in a continuous change of surface state/surface energy previous to the measurement of adhesion force. This prompt type of measurement has not been performed yet.

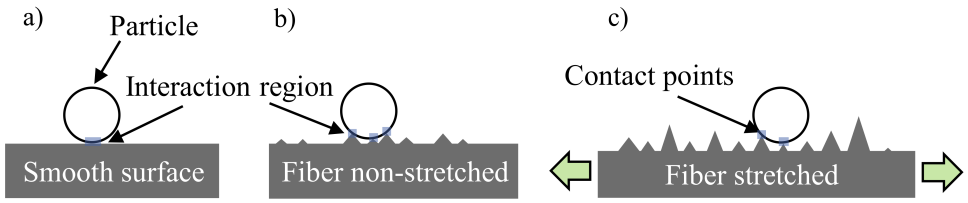


Figure 4.1: *Schematic of a contact between a) An ideal smooth surface and ideal spherical particle. b) A Rough surface of a non-stretched fiber and spherical particle. c) The surface of a stretched fiber with increased surface roughness. The interaction area (blue) is reduced to contact points by the increase of surface roughness.*

Figure 4.1 shows different states of the substrate in the contact with a particle. For instance, in Figure 4.1a) depicts a particle on a smooth ideal surface. The contact area is small according to the ideal state. If there is no ideal smooth surface, the number of contact points between the particle and the substrate is increased. The interaction region is increased. Thus, Figure 4.1b) shows the contact between a particle and a real surface with given roughness. This case represents the fiber surface in the non-stretched state. Due to the stretching, the surface roughness is changed. As a result, the contact area between the stretched fiber and a single particle differs from the condition between a non-stretched surface and a spherical particle (see Figure 4.1c)). The number of contact points is changed due to the change in surface structure. In the shown case the number of contact points/interaction area is decreased. As shown in various studies, depending on the surface roughness, the adhesion force can either decrease or increase depending on the magnitude of surface change [96, 10, 34, 71, 109].

Table 4.1 summarizes different material combinations that have already been investigated in pull-off measurement studies in connection with the roughness of the substrate so far. Further, table 4.1 shows the order of magnitude of the particle material and roughness in the corresponding investigations. Miwa et al. revealed that the

Table 4.1: *Pull-off force measurements in combination with roughness. The applied method was either theoretical (theo.) or theoretical&experimental (theo.&exp.).*

Reference	**particle size & material**	**substrate material**	H_0	**roughness substrate**	**method**
Ali Ata et al. 2000 [6]	glass sphere 10 μm, roughness 0,2 nm	alumina, silver, titanium-coated Si	0.3 nm	0,2 - 1,2 nm	theo. & exp.
Beach et al. 2002 [10]	10 μm glass particle, 9 μm polystrene particle	polypropylene coatings	0.3 nm	0-400 nm	theo. & exp.
Götzinger et al. 2004 [34]	Gold particle	silica & stainless steel	0.3-0.4 nm	$rms < 0.3\,nm$	theo. & exp.
Kataiunen [71]	blunt silicon tips	TiO_2	0.3 nm	0.65-11 nm	theo. & exp.
Kappl et al. 2002 [69]	1-50μm glass beads	silicon		1.6-10.5 nm	theo. & exp.
Kumar et al. 2013 [73]	1.45-10.25 μm glass sphere	DLC silicon wafer	0.3 nm	0.23-24 nm	theo. & exp.
Miwa et al. 2020 [89]	silica particle 1.6-5 μm	silicon wafer	0.4 nm	0.6-1.9 nm	theo. & exp.
Rabinovich et al. [116] 2000	10μm glass beads	—	0.3 nm	0.1-20 nm	theo.
Rabinovich et al. [117] 2000b	10μm glass beads	silicon nitride silica	0.3 nm	0.17-10.5 nm	theo.&exp.
Schaefer et al. 2020 [129]	8μm glass beads polystyrene, tin	mica, pyrolitic graphite	–	0.17-10.5 nm	exp.
Tsukada et al. 2004 [158]	1-3 μm	Lactose smooth, Lactose rough stainless steel plate	0.4 nm	—	theo.
Wanka et al. 2013 [164]	PS particle 3-13 μm silica particle	PS surface on steel		0.55±10 nm	theo. & exp.
Yang et al. 2007 [172]	glass sphere	silicon surface	0.3 nm	0.5 nm	theo. & exp.

change in pull-off force is influenced by the interplay of the particle size and surface roughness or number of asperities. In the studies pull-off force between silica particles and a wafer surface was determined [89]. The adhesion force of glass particles on substrates of different materials was investigated by Schaefer et al., Ali Ata et al, Kappl et al and Kumar et al.[129, 6, 69, 73]. In particular Ali Ata et al. identified a reinforcing influence of increased humidity on the results of the adhesion force measurement at different roughness of the substrate and the contact pressure (load) [6]. Schaefer et al. measured the adhesion force between small particles of several materials with an atomically flat surface. Discovering a reduced deviation between theory and experiment by the factor 3 [129]. Kumar et al. considered the influence of different particle sizes in relation to the change in surface roughness in theory and experiment. Extending the model of Rabinovich et al. by considering different combination of radius of asperities to the radius of adherent particles in the system. [116, 73]. Yang et al. developed a multiscale model for the description of adhesion considering the elastic and the plastic deformation in the contact zone of the particle. Exceptions have to be made for surfaces with sharp angular features and for limited spherical asperities [172]. Tsukada et al. determined the adhesion between fine drug particles smaller than 3 μm and a static plate of lactose. In the findings, the mean value for adhesion between particles and lactose plate was reduced for a qualitative increase of surface roughness. Moreover the distribution of measured values was spread more widely [158].

Wanka et al. presented results for the measurement of adhesion force with a Hopkinson bar for particle with a diameter between 3-13 μm. In general, a good agreement with theoretical calculation according to Rabinovich in the size range of particle diameter 4-7 μm was observed [116]. For the experiments with particle size between 8-13 μm a strong increase is determined. This increase might be due to the increased movement of large particle by their inertia after their first contact. Whereas small particle remained at the same point of contact [164].

In this study, adhesion force was determined between the polymeric fiber (polyurethane) and two type of large particles for a magnitude of size that have not been studied so far. Spherical monodisperse research particles of PS and bulk particles of spherical polydisperse Spheriglass 5000CP00 powder were used as particle material. The pull-off force measurements are compared with a model developed by Rabinovich et al.[116, 117]. The model relates the change in pull-off force to the change in surface roughness for a new combination of material. Moreover the designed AFM setup enables measurement of pull-off force direct on the stretchable thin filter fiber as real world sample by using a 2D video navigation.

4.2 Material and Methods

4.2.1 Materials and sample preparation

In all investigations polymeric fibers made of polyurethane were used as stretchable substrate. The fiber has reversible stretching properties up to 75 % elongation. The fiber diameter is 82 μm in non-stretched state. Stretching reduces the fiber diameter by approximately 18 % at 55 % elongation. The elastic modulus of the fiber is measured as 0.49 MPa [106].
In his experiments, Jiang et al. assigns the used polyurethane coatings to the "low energy surfaces". Polyurethane in this form is thus considered to be hydrophobic. In tests, Jiang et al. determined contact angles between polyurethane (different material compositions) and a liquid phase of around 92.9°-117.8° [58]. Since no exact material composition of the fiber material is available yet, a hydrophobic behaviour is suspected. Though no liquid phase is present on the fiber during the experiments in the study.

Monodisperse particles for research purposes made of Polystyrene (PS) (microParticles GmbH, Berlin) were used in the pull-off experiments. Furthermore, exemplary selected particles from polydisperse powder of Spheriglass 5000CP00 were under investigation. The spheres are placed on the bottom side, opposite to the reflective AL coating of the cantilever. As shown in the images of the cantilever tip in the Supporting Information (SI) material, the spheres are positioned in the middle of the tip. (see Figure 1 SI) The Spheriglass particle were randomly picked from the top of the glass side. Before the Spheriglass particles are dispersed and washed in acetone. Afterwards a few drops of the suspension was spread on the glas slide. The acetone was evaporated before the gluing process. From polystyrene, particles of size 9.88 μm, 12.3 μm were used. For Spheriglass 5000CP00 particles with the size 10.37 μm, 17.13 μm and 23.78 μm were picked. The randomly selected Spheriglass particles were sized after the gluing process with the WLI.

The particles are mounted on the bottom side, opposite to the reflective AL coating of of the tipless cantilevers (AiO Al-Tl, BudgetSensors Ltd.). The mounting procedure was inspired by the protocol of Mak et al. [88]. A thin glue layer (UHU Plus Endfest 300, UHU GmbH & Co. KG Bühl, Germany) was placed on the top of a glass slide. By touching the layer with the cantilever the glue is transferred to the tip of the cantilever. Spare glue was striped off on a clean glass slide. All particles were picked upline with the cantilever tip regardless the size and material. All movements during the gluing procedure were performed with the xy-stage beneath the cantilever carrier and traced by the AFM video camera that supports 3D-navigation. The glue was allowed to harden for 24h. This rearranged method for the application of colloidal probes to the cantilever enables a fast and clean attachment. A hard sapphire (Sapphire 12M, Bruker Corporation) was used to assign the deflection sensitivity for each cantilever with the glued particle. Images of attached particles on the cantilevers can be found in the Figure 3

SI.

4.2.2 Experimental Setup and Measurement Procedure of Adhesion Force

AFM-measurements were performed with a Bruker Dimension Icon (USA) with an integrated xy-axis table. For observation an additional camera was applied in front of the AFM-measurement head. Figure 4.2 a) shows the overall measurement setup including the fiber mounting device for stretching and the integrated camera for the top view. Figure 4.2b) shows a detailed view of the arrangement of fiber and the cantilever. By using a 12x-magnification lens in the front view and backlight illumination, the contact point between sphere and fiber was depicted in a high-resolution image. The resolution of the images was 7.71 px per μm with an numerical aperture (NA) of 0.038 - 0.202. The advantage of the new designed measurement setup is the possibility of visualizing the contact approach between the particle and the fiber from two different perspectives including possibility for video. This enables an accurate positioning and alignment of the particle on the fiber. A further advantage of measurements with the fiber clamping device is that any elongation of the substrate can be set direct before the measurement without any limits.

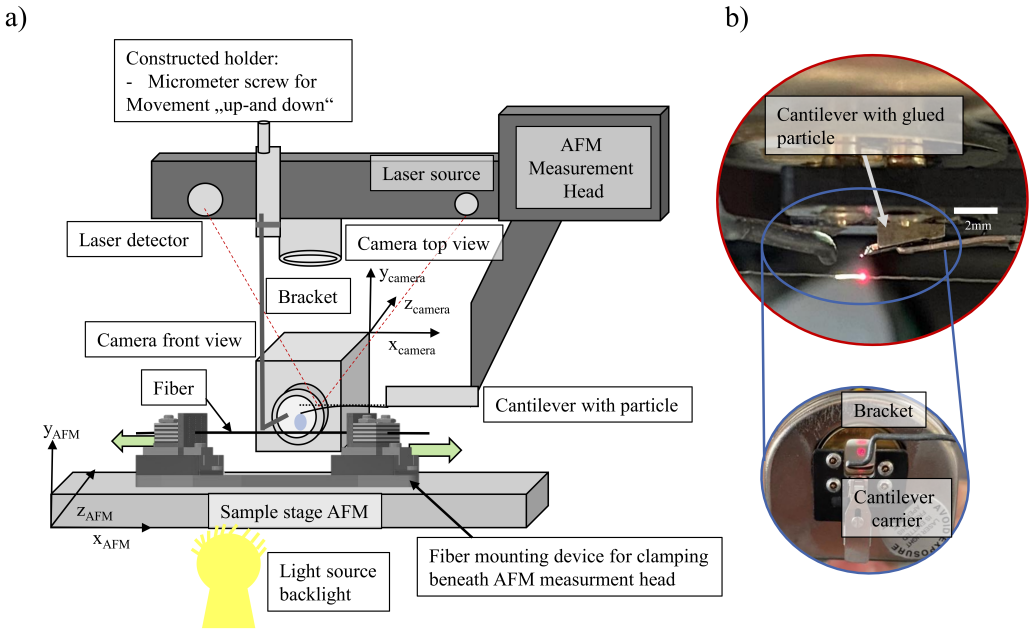


Figure 4.2: *a) Schematic of the experimental measurement setup placed beneath the AFM-measurement head. Showing the key components and the adjustment axis. The front camera is mounted on a long lever connected to the AFM base. b) Front view image of the clamped fiber beneath the cantilever and the bracket. Magnification of the cantilever carrier with the bracket in the notch.*

In combination with the integrated (camera top view) of the AFM a two dimensional navigation of sphere at the cantilever tip on the fiber was enabled. To keep the

fiber in the optimal position during the measuring procedure an additional bracket has been designed and integrated. The bracket prevents the fiber from bending upwards during the measurement procedure. It is manufactured from metal wire and can precisely be raised and lowered with a micrometer screw. The micrometer screw is fixed at the AFM-measurement head. To get close to the breakage point between fiber and particle, the bracket was fitted into the notch of the cantilever carrier (see Figure 4.2b)).
Measurement is performed in ambient conditions. The temperature was at 25 ± 2°C (air-conditioning) and a relative air humidity of 25 ± 5 %. The fiber is stretched to four different elongation states using the fiber clamping stretching device designed by Poggemann et al. [106]. The fiber is precisely elongated up to 7 % (3.976 mm) 17 % (9.656 mm), 27 % (15.3 mm) and 38.7 % (22 mm) by using the motorized piezo-actuator Q-521 (Physik Instrumente GmbH, Germany). The stretching velocity remained at 12 mms^{-1} for all stretching experiments.

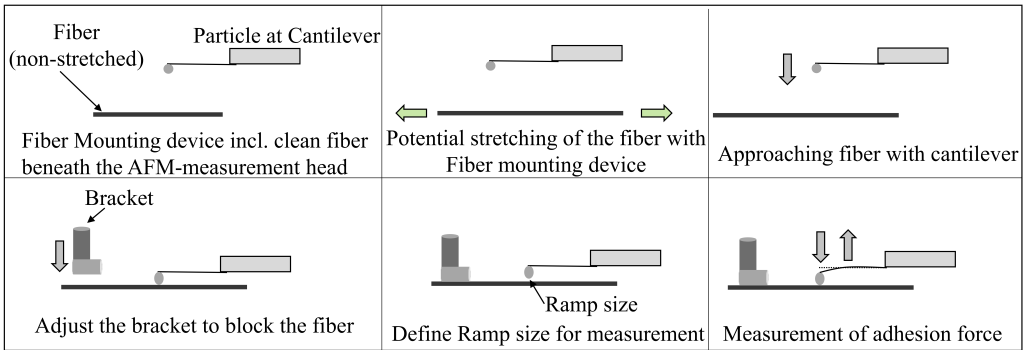


Figure 4.3: *Procedure for adhesion measurement on the non-stretched and stretched fiber*

Figure 4.3 shows the procedure for measuring the adhesion force with the AFM. Starting at the top left of the schematic, the non-stretched fiber is first placed beneath the AFM-measurement head. If needed the in the experiment, fiber is stretched using the fiber clamping stretching device. After the termination of the fiber elongation, the cantilever is lowered to the zenith of the fiber. In the following the bracket is lowered to fix the fiber position. The bracket is only lowered to a position where it touches the fiber surface (see Figure 4.3 second picture from bottom left and Figure 2 SI), so the fiber position is not changed or influenced by additional pressing. To measure the adhesion force between the fiber and the particle, the cantilever is placed in the ramp position (ramp size = 3 μm). The measurement is then repeated at least 10 times in the tapping mode of the AFM.

4.2.3 Evaluation of the measurement in direct contact to the polymeric fiber in the stretching device

The measurement of the adhesion force between the particle and the fiber is to be carried out immediately after the stretching on the stretched fiber. In preliminary tests, it

Table 4.2: *Median of pull-off force between Spheriglass particle with diameter 10.37 µm and polymeric fiber clamped in different specimen device.*

specimen device	pull-off force [nN]	
	non-stretched	stretched
fiber clamping & stretching device	592 ± 30	385 ± 43
glass slide	543 ± 179	385 ± 67

was found that the adhesion force between the fiber and the test particle is so huge that the fiber follows the movement of the sphere during the retraction of the cantilever. Upward deflection of the fiber occurs, resulting in delayed detachment of the particles from the fiber.
Due to the mobility of the fiber in the pull-off direction of the cantilever (upwards), the stall point between the fiber and the cantilever is shifted in the direction of the cantilever ramp. Due to the fact that the cantilever ramp is performed by a piezo motor, the maximum distance is z_{travel} 11 μm. To prevent the unwanted z-movement of the fiber, it is necessary to fix the fiber. The previously described bracket was developed to stabilize the fiber, allowing the measurement procedure to take place directly in the process. To validate the measurement results with the designed bracket (adjusting/fixing the fiber), measurement of pull-off force was performed between a particle and a glued fiber on a glass slide and between a particle and a fiber that is clamped in the fiber clamping device. The measurement of adhesion force between the glued fiber on glass slide and the particle represents an approximation to standardized conditions. For example, the substrates are usually in the form of a large-area preparation (see Table 4.1), which does not have the shape of the actual application in the real world. In the experiments with the clamping device, the designed bracket for fiber adjustment was used. The adhesion force was measured in for each setup in the non-stretched and stretched state (elongation: 22 mm, 38.7 %). Table 4.2 shows the measured pull-off forces for a Spheriglass particle from a polymeric fiber for both type of specimen device. The pull-off force was determined with a non-stretched and a stretched fiber fixed in/on each specimen device. The shown measurements of the pull-off force is performed with a substrate whose dimensions and shape correspond to the real application.

4.2.4 Experimental Setup for Surface Characterization

For the characterization of the fiber surface, the roughness at different elongation states was determined using the WLI (ContourGT-X, Bruker Corporation, USA) and the AFM Bruker Dimension Icon. Both methods are common known techniques for the charakterisation of a substrate surface [32]. For WLI the fiber was fixed on a glass slide in the unstretched, as well as in the different stretched states. The fiber clamping device could not be placed beneath the WLI due to spatial restrictions. However, the elongation of the fiber was precisely realized using the fiber holder. Imaging was per-

formed on the zenith of the fiber, where adhesion force is determined with the AFM. Bruker software Vision64 (Bruker Corporation, USA) was used to analyze the WLI images. The images of the fiber were subjected to a cylinder fit. The mathematical fit unifies the geometric shape, which interferes with the calculation surface roughness parameter. For each elongation state, images were recorded at six randomly selected positions on the fiber.

The recorded area covered at least 20x120 μm (height x width). The images of all the fiber sections can be found in the supplementary data (Figure 6-15 SI). Root Mean Square (RMS) and the peak to peak distance λ were obtained for each elongation state of the fiber. Measurement of peak-to-peak distance and RMS followed the protocol by Rabinovich et al. and Beach et al. [116, 10]. The analysis of peak-to-peak distance was realized for different section of the the WLI images. The RMS is a common value for surface roughness. Regardless of the measurement method, the RMS is defined as the local deviation of the height position from the mean of the surface measured from a mean line (see eq. 7.1). The value is the geometrical average of ordinates of the profile about the mean line. Thus, it is assumed that the sum of areas above the mean line is approximately equal to the areas below [4, 29].

$$RMS = \left[(1/L_{sampling}) \int_{L_{sampling}}^{O} Z(x)^2 dx \right]^{1/2} \tag{4.1}$$

$L_{sampling}$ marks the sampling length of the sampled probe. The x represents the position on the ordinate whereas the function $Z(x)$ considers the profile height function of the sampling surface. For a more detailed analysis of the fiber surface, a characterization with the AFM was performed at min. 3 different locations of the fiber zenith at the different elongations states. The covered area sized 25x25µm. The R_a for surface roughness was measured using cantilevers All-In-One-Al (Budget Sensors) with dimensions of 150x30x2.7µm, tip radius 10 nm(length, width, and thickness). For the the calculation of roughness values the data was fitted with a cylinder fit. All images of the characterisation with AFM are shown in Figure 11-15 SI.

4.3 Theory

Calculation of adhesion force between a particle and a smooth surface is executed by the model of Johnson-Kendall-Roberts (JKR) [60] and the model of Derjagiun-Muller-Toprov (DMT) [26]. For the calculation $\gamma_{1,2}$ is the surface adhesion energy of two different surfaces and the particle diameter d_p are relevant. In these models the deformation of particle in contact is included.

$$F_{DMT}(r) = 2\pi\gamma_{1,2}r \tag{4.2}$$

$$F_{JKR}(r) = \frac{3}{2}\pi\gamma_{1,2}r \tag{4.3}$$

In this calculation any information about the distance between particles and the surface is neglected, although this parameter has a major influence on the interaction force. A specific material constant A and a specific distance a between the surface and the particle are added in the calculation of adhesion force according to Hamaker et al. [40]. For the calculation a typical value for contact distance a of 0.3 nm was used. An early model for the calculation of adhesion force between a rough surface with a single asperity and a smooth particle was developed by Rumpf et al. [123].

$$F_{Hamaker} = \frac{A_{i,j}r}{12a^2} \tag{4.4}$$

$$F_{Rumpf} = \frac{A_{i,j}}{6}\left[\frac{r}{a^2} + \frac{d}{s(a+r)^2}\right] \tag{4.5}$$

A further development of this model is the model by Rabinovich that considers the RMS of the surface instead a single asperity [116, 117]. Further the peak-to-peak λ distance is added as a parameter to the calculation of the adhesion force.

$$F_{ad} = \frac{A_{i,j}\,r}{6H_0^2}\left[\frac{1}{1+(\frac{32\,r\,k_1\,rms}{\lambda^2})} + \frac{1}{(1+\frac{k_1\,rms}{H_0})^2}\right] \tag{4.6}$$

Herein parameter k_1 denotes a proportional factor which is obtained from the parameter roughness and peak-to-peak distance. For its given peak-to-peak distance, Rabinovich calculates a proportional factor k_1 of 1.817 for the peak radius and gives in his calculation a valid range for roughness in the range of at 0.1 < RMS < 20 nm. Nevertheless the model is open for different types of surface with a multiple scale of roughness, if the peak-to-peak distance increases. An extended validity for larger multiples of roughness is expected for a larger peak-to-peak distance [116, 117]. An example for the use of Rabinovich model in the range of high peak-to-peak distance and higher roughness are the calculations by Beach et al. [10].
The proposed model by Rabinovich does not consider any deformation of the surface, so the modeling tends to underestimate the puff-off force [116]. Furthermore, any polar forces in the composition of the adhesion force are not considered, although they contribute to total adhesion. If there are two different materials present in the system, the Hamaker constant is calculated as shown in Eq.4.4 referring to Israelachvili et al. [50]. The constants of materials i and j must be combined. The calculation of the Hamaker constant for calculation is based on findings by Wu et al., Tsai et al. and Rimai et al. [166, 157, 122]. The cut-off distance was 0.1 nm. The used parameter RMS and peak-to-peak distance for calculation of adhesion force are shown in Table 4.3 and in Figure 4.6.

ht

Table 4.3: *Data used for the calculation of the Rabinovich Model [116]*

Material	Form	Hamaker constant A (10^{-19} J)
Spheriglass 5000	particle	0.853 [157]
Polystyrene	particle	0.637 [157]
Polyurethan	substrate	0.64 [166] [89]

4.4 Results and Discussion

In this section, the experimental results of roughness measurement and of the adhesion force measurement between a particle and fiber (in different elongation states) are described and compared to a model of Rabinovich et al. [116]. Rabinovichs model is valid, if λ is comparable to the particle size [117]. Further, the results of surface roughness measurements are shown in the corresponding elongation states of the fiber. The determined values of surface roughness and peak-to-peak distance were used in the calculations of the pull-off force between particle and fiber.

4.4.1 Measurement of surface roughness and Peak-to-Peak distance

The change in the surface roughness of the fibers was determined in different elongation states of the fiber with the WLI and the AFM. Figure 4.4 depicts sections of the fiber surfaces in the non-stretched and the stretched state (22 mm, 38.7 %) using the WLI and the AFM for characterization. For investigation of each stretching state (non-stretched, stretched), 6 fibers were randomly picked from a batch. Figure 4.4 shows one out of six fibers for the non-stretched and for the stretched state (stretching 22 mm, 38.7 %) investigated with AFM on the left hand side and WLI on the right hand side. All fibers originate from one batch. All images of all fibers are shown in the SI, Figure 6 to 15.

For each experiment of each stretching state, a unused fiber was investigated. The images are depicted as gray-scale images using the Bruker software. The location for measurement were picked randomly on the zenith of the fiber. The presented values for RMS and peak-to-peak distance are an average based on the measurement of 6 fibers. The parameter RMS and peak-to-peak distance of the fiber surface were determined for different stretching states at least for an area of 120 x 20 μm^2 using the WLI images. The mean R_a value for each stretching state is determined using all the AFM images of the fiber.

In the non-stretched state of the fiber (0 mm, 0 % stretching), the surface is almost completely smooth and only small flakings/blocks in the surface are visible. There are islands/blocks where the skinlike surface layer on the fiber is slightly torn away. In the AFM-image of the non-stretched state some small closed cracks (lines) are visible. This

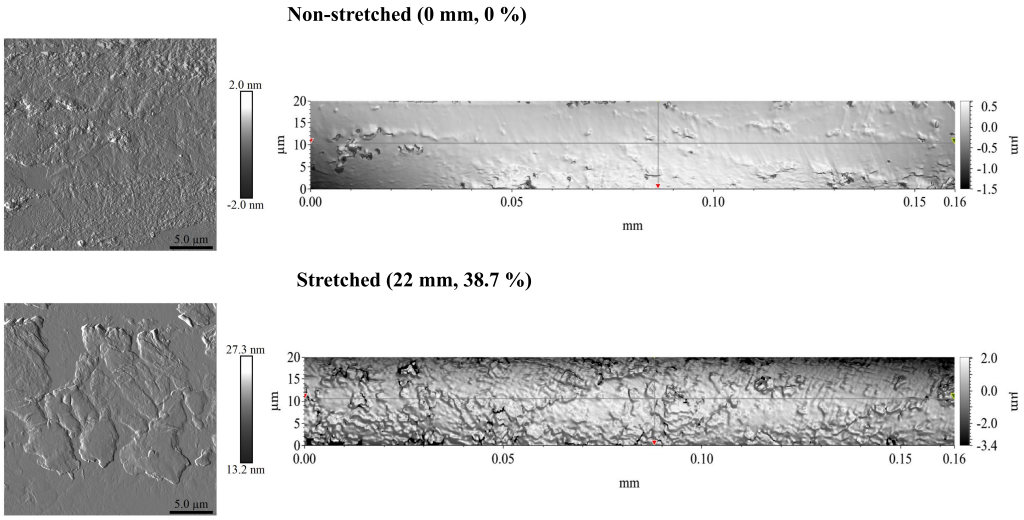


Figure 4.4: *Images (Cutout) of the fiber surface in the non-stretched state (TOP) (0 %, 0 mm) and after stretching (BOTTOM) (22 mm, 38.7 %). Images generated with AFM (LEFT) and WLI (RIGHT) including the respective Height-Scale.*

type of surface structure can be seen in both the AFM and WLI generated images. As seen in the cutaway image with the AFM, the height difference over an area of 625 μm^2 is 4 nm. Irregular irregularities can be seen in the surface of the fiber. In addition, slight cracks can already be seen in the outer skin under the surface layer, which will form islands on the skin layer.

A change of the fiber surface is visible in the images (WLI and AFM) of the fiber surface at an elongation of 22 mm (38.7 % elongation). In the stretched state, the surface clearly has cracks and rifts all over the shown sample area. A different layer beneath the upper layer becomes visible. The underlying layer appears to have a smooth surface like the surface of a non-stretched fiber. This becomes visible between the cracks and clods of the upper layer. Some blocks are peeling off from the outermost layer of the fiber. Thus, the number of fractured areas increases, but it seems that just the layer beneath the top layer changes its structure. This creates new asperities with a height of 2 to 3 μm which results in an increase of RMS. There might be a layered composition of the fiber, where the outermost layer (skinlayer) of the fiber is ripped off by the induced shear stress.

The change in the surface is visible both qualitatively in the images, but also in the quantitative data of the surface roughness measurements. Figure 4.6 shows the resulting values of roughness measurements at different stretching states of the substrate. An increase in RMS of about 80 nm is observed with an increase of elongation of the substrate. The measured data shows that roughness increases already at an elongation of 3.976 mm (7 %). With the increase of fiber elongation from 3.976 mm (7 %) up to 9.656 mm (17 %) there is only a additional rise of roughness. The rise of roughness increases the surface energy of the substrate which causes a change in the ability of wet-

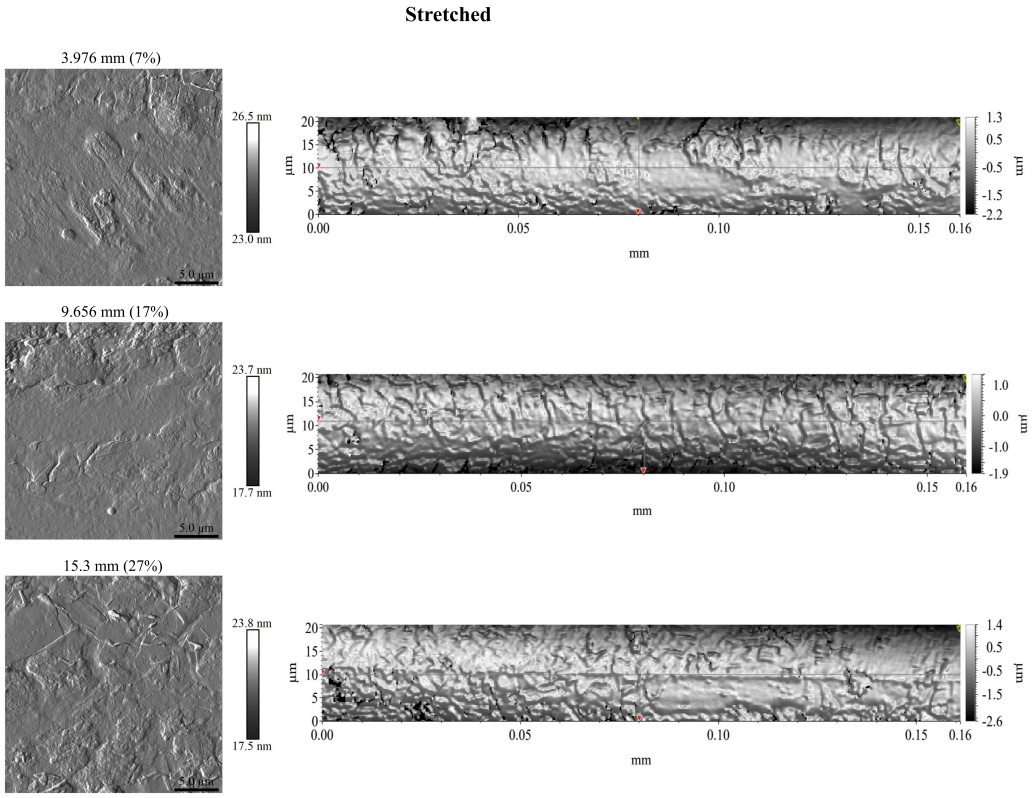


Figure 4.5: *Images (Cutout) of the fiber surface at different stretching states 3.976 mm (7%), 9.656 mm (17%) and 15.3 mm (27%). Three different fiber are shown. For each investigation of a stretching state, a new fiber was used. The images were generated using AFM (LEFT) and WLI (RIGHT).*

ting. With a further increase of stretching up to 22 *mm* (38.7 %), the measured values for the roughness of a fiber shows a major increase. The high standard deviation of the surface roughness is due to the 6 different fibers from one batch. The corresponding image of exemplary fiber surfaces are depicted in Figure 4.5. All images in Figure 4.5 shows a WLI-image (Right) of the fiber with the dimensions of 160 x 20 μm^2. On the left hand side a mapped AFM image (25 μm x 25 μm) of each elongation state of the fiber is depicted. In the image of the fiber stretched with 7 % (3.976 *mm*), parts of the smooth fiber surface of the unstretched state (range 0.05 *mm* - 0.10 *mm*) are still visible. There are already clear changes in the fiber surface, which is expressed by slight elevations of approx. 1 μm. Thus, the first scores in the non-axial direction can be seen in the fiber in the 0.10-0.15 *mm* section. This change in the fiber surface produces the first increase in roughness discussed above. The number of non-axial grooves increases massively with the increase in elongation to 9.656 *mm*, which, viewed over a number of 6 fibers, does not bring about any further significant change in roughness. In the images (WLI and AFM) of the fiber stretched by 15.3 *mm*, cracks and grooves in the axial direction can then be seen in addition to the cracks in the non-axial direction. In addition, in the section between 0.05 *mm* and 0.10 *mm* (WLI-image) and in the section 0.10-0.15 *mm* a kind of scale bulges from the fiber, which raises the roughness again by 16 *nm*. As shown in the WLI image, the resulting shed structure in the skin layer is recognized in the AFM images, too. By the increase of roughness the of surface energy of the low-energy surface (polyurethane) is increased here in contrast to the non-stretched state. A discussion about the change of wetting properties and the change of surface energy is placed in section 4.4.3.

The model of Rabinovich considers the nanoscale roughness as a strong influence on the adhesion force between two surfaces, though changes in the macroscale roughness might also have an influence as Beach et al. showed in his studies [116, 10]. Opdahl et al. showed that an elongation of polymer specimens can increase the roughness by about 25 *nm* [96]. As shown in the studies of Amitay-Sadovsky et al, applied elongation in this range below 100 % leads to an increase in surface roughness of this order of magnitude [3].

As already seen in the calculation of Rabinovich et al., the surface roughness can be divided into macroscale roughness and nanoscale roughness [116]. In this study we are considering the macroscale roughness due to the used particle-fiber ratio. However, it can be assumed that the increase in surface roughness of 80 *nm* in the macroscale area might result in an increase in nanoscale surface roughness, too. Due to such a large change in surface roughness, it was necessary to resort to a measurement methodology like WLI that fully maps the surface change in image and quantitative values. For a more detailed view the fiber was analyzed with the AFM, too. Another factor, which is related to the calculation of pull-off force, is the peak-to-peak distance of the substrate. The peak-to-peak distance is shown as a function of fiber elongation in Figure 4.6. As shown in the data, the value of the peak-to-peak distance ranges from 9000-1200 *nm*. With the increase of roughness from 112 *nm* to 161 *nm*,

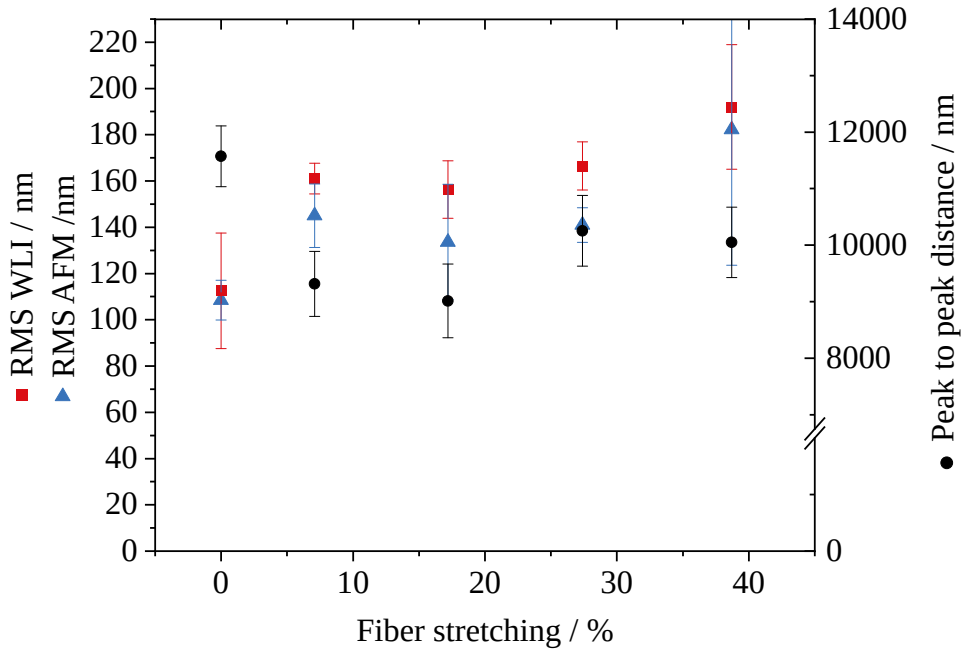


Figure 4.6: *Calculated roughness index RMS from WLI (red squares) and R_a (blue triangle) from AFM as a function of fiber stretching. Measured peak-to-peak distance (black circles) using WLI.*

the peak-to-peak distance decreases slightly. By breakage of the upper layer of the fiber surface, some corrugations develop, which represent new peaks on the surface. Comparable to the roughening and breaking up of a dried river bed. Further fiber stretching results in a slight increase of peak to peak distance up to 10050 nm. As shown in the Figure 4.6 this effect is based on the gradual movement of peaks apart. Rabinovich's model includes the peak-to-peak distance, which was determined manually from the surface analysis with the WLI or the AFM. Depending on the resolution of the performed surface analysis, the peak-to-peak distance can vary. The direction in which the analysis is done is an influencing factor. The present peak-to-peak distances was determined for 25 μm pieces over a total distance of minimum 120 μm fiber length.

4.4.2 Measurement of pull-off-force

Pull-off force between a single particle and the fiber was determined with the AFM technique. Spheriglass particle material and PS particles were selected for measuring the pull-off force. The PS particles serve as a reference. Spheriglass particles were used in single fiber experiments to determine the detachment behaviour of particle structures from a stretching single fiber [106]. These investigations are not part of this study.

Each AFM-experiment was executed threefold. For each repetition the measurement of adhesion was performed at least 10 times at the same spot. Figure 4.7 shows the measured pull-off force between Spheriglass particles and the fiber as a function of RMS of the substrate. Additionally a polynomial fit 2nd order is shown to emphasize the resulting trend of the discrete values. Further, Figures 4.7 shows the modeled discrete values based on Rabinovich's model for the adhesion force between spheriglass particle and the fiber [116]. The discussion for these calculated values and its fits is found in section 4.4.3. During the experiment, fiber stretching was realized immediately before the measurement of the pull-off force. The discrete measured values for the adhesion force are marked as unfilled symbols. As shown in section 4.4.1, by stretching the fiber (as substrate) the surface roughness RMS is increased.

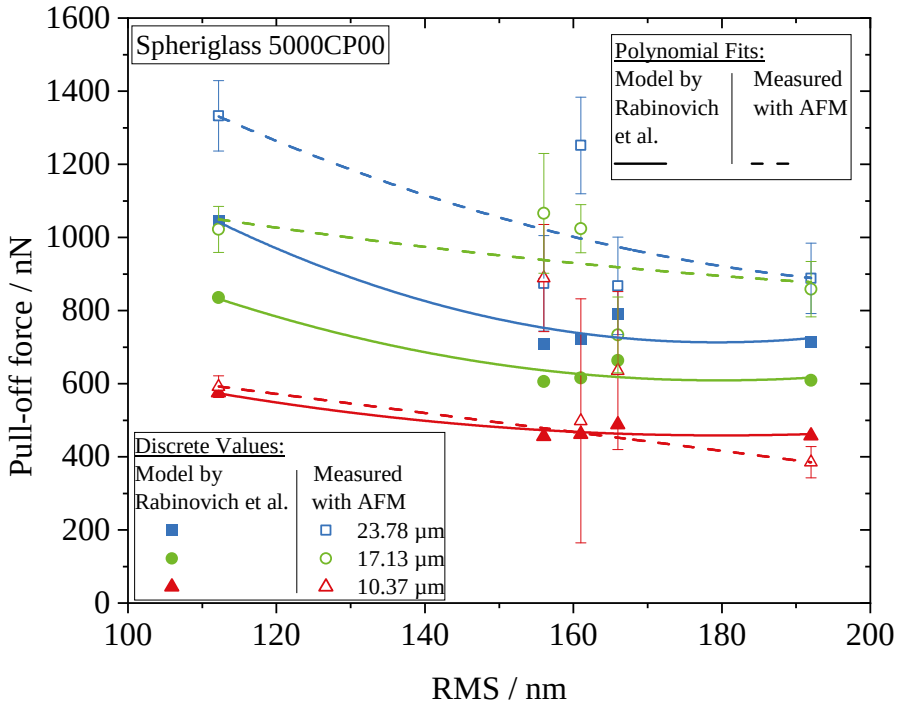


Figure 4.7: *Pull-off force as a function of RMS of the elongated fiber - measured with AFM (blank symbols). Calculated adhesion force based on the model of Rabinovich et al. using the measured RMS and Peak-to-Peak distance at each elongation state (filled symbols) [116]. Polynomial fit for measured and calculated values (including measured roughness values).*

The initial values for the measured adhesion force are distributed according to the size of the particles. The measured adhesion force is in the range of 592 nN to 1332 nN. As shown in the data, the measurements with the smallest particle result in the lowest adhesion force and the experiment with the largest particle in the highest adhesion force to the fiber. With the increase of the surface roughness of the fiber up to 161 nm, the adhesion force between particle and substrate increases in the experiments with

the particle size of 17.13 μm and 10.37 μm. For the experiments with the particle size of 23.78 μm, there is a reduction in the adhesion force. Further increase in surface roughness, triggered by further fiber elongation, causes a reduction in adhesion force for the experiments with particle diameter smaller than 23.78 μm. In the experiment with the particle size of 23.78 μm, the adhesion force almost reaches the level at the initial surface roughness of 112 nm. With the last two increases in surface roughness, a reduction to the minimum of each particle size is observed regardless the used particle size. Since the adhesion force between fiber and particle is a result of the contact area between particle and fiber, it is the particle size, and consequently the available contact area of this side, that is decisive for the adhesion force in the case of a uniform change in roughness. This is an explanation for the significant reduction of the adhesion force in the experiments of 23.78 μm.

Basically for each particle size the measured pull-off force between a single particle and the fiber is lowered by the increase of the surface roughness up to 192 nm. This increase is based on stretching the substrate by 38 %. The trend is shown by the polynomial fit of the discrete measured values. (dashed line). In the experiments with Spheriglass particles with the size of 23.78 μm a maximum reduction of about 33 % is visible. As Beach et al. and Ditscherlein showed adhesion force is affected by the change of roughness hence the number of contact points is changed [10, 30].

Figure 4.8 shows the measured pull-off forces of PS particle with the AFM as a function of the surface roughness of the fiber. Two different sizes of particles (PS) were used to determine the adhesion force at different elongation states of the fiber. The discrete measured values for the adhesion force are marked as unfilled symbols. Further, Figures 4.8 shows the modeled discrete values based on Rabinovich's model [116]. The discussion for these calculated values and its fit is found in section 4.4.3.

The initial values of adhesion between PS particles and the fiber (substrate) are between 522 nN and 743 nN and are thus correspondingly in the range according to their size. As the surface roughness is increased, the adhesion force between the particle and the substrate is reduced for both particle sizes. Likewise, for both particle sizes, the adhesion force increases again for a further increase in roughness to 161 nm caused by fiber elongation. For a substrate roughness of 166 nm and 192 nm the pull-off force remains almost at a constant level for both particle size. The deviation of both value overlap for these roughness parameter.

In total in the experiments with PS particles a gradual decrease of pull-off force is observed or both sizes 12.30 μm and 9.88 μm, respectively. For the experiments with the particle size of 12.30 μm a reduction of 373 nN results from a change of the surface structure. In the experiments with the particles of the size 9.88 μm this reduction 215 nN was determined. A polynomial fit was applied to the measured values for adhesion force. The fit is shown as a dashed line. The parameter for the given fits are listed in Table 4.4. In addition to the reduction of the absolute values of the adhesion force for both used particle size, the difference between the two forces is also reduced

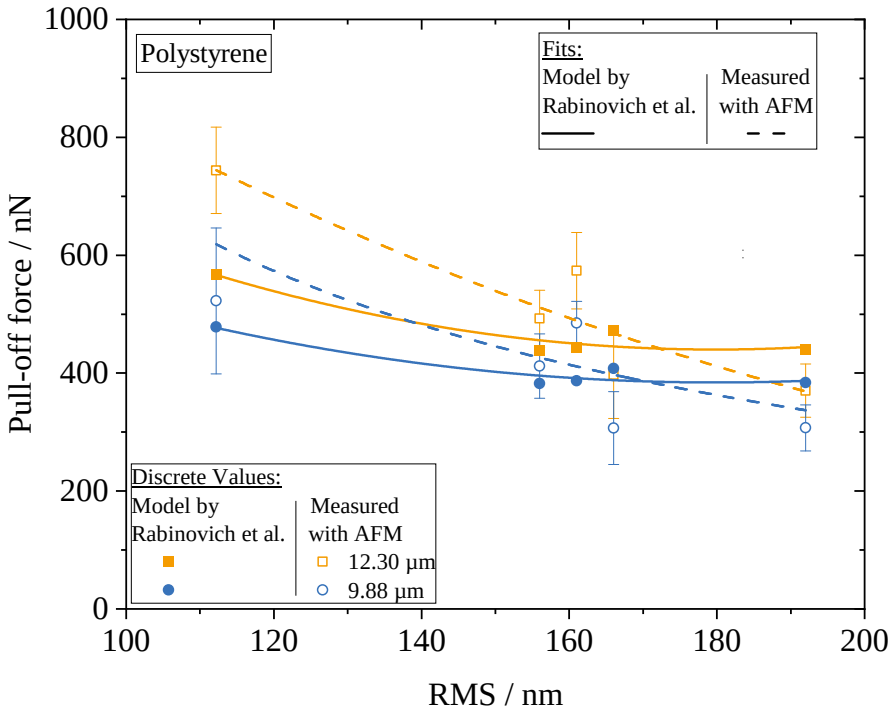


Figure 4.8: *Pull-off force as a function of RMS of the elongated fiber - measured with AFM. Calculated adhesion force (including measured roughness values and peak-to-peak values) according to Rabinovich model. [116]*

Table 4.4: *Parameter of polynominal fit for the measured data for a given function of* $y = Intercept + B1 * x^1 + B2 * x^2$

Material & Size	B1	B2	Intercept	R^2
Spheriglass				
measured				
23.78 μm	-18.38	0.04	2861.56	0.35
17.13 μm	-5.41	0.01	1522.06	0.99
10.37 μm	-2.67	0.0002	888.84	0.99
modeled				
23.78 μm	-26.15	0.073	3057.91	0.92
17.13 μm	-17.64	0.05	2193.42	0.92
10.37 μm	-9.02	0.025	1270.08	0.91
Polystyrol				
measured				
12.30 μm	-9.88	0.017	1638.74	0.75
9.88 μm	-8.55	0.019	1262.67	0.42
modeled				
12.30 μm	-9.94	0.027	1333.9	0.91
9.88 μm	-7.26	0.020	1037.48	0.91

by the change in the surface area of the substrate. For the large particles, there is an increased change in the adhesion force, since the reduction of the contact points is larger compared to the total contact area. This trend was also found in the studies of Kumar et al. where the same change in surface structure results in a larger reduction of adhesion force for large particles (10.25 μm) than it was observed for particles of size 7.59 μm. [73]

The reduction of pull-off force between the particle and the fiber results from the change of surface roughness of the fiber. In the studies by Beach et al., for spherical polystyrene particles with the diameter of 8.14 μm a reduction in adhesion force of about 90 nN was found. The change in surface roughness was found similar. However, the material of is not the same as used in this study.

Comparing the deviation between experiments with PS and Spheriglass, the deviation of experiments with PS particles deliver a much better repeatability than the experiments with particle from Spheriglass. To emphasize a key-information of this study, Figure 4-5 SI and Figure 16-19 SI show pill-off curves of single AFM measurements with spheriglass particles and polystyrene particles. The curves of the same particles size show a qualitatively similar course in the stretched and unstretched state of the fiber.
There is no abnormal snap-in or pill-off behavior detected, that could indicate fiber movement, during the measurement process on stretched fiber (with increased roughness). In the measurements with the stretched fiber, the point of pill-off shifts due to the tapering of the fiber during the stretching process. In the snap-in curves of the measurements with spheriglass particles, a small up and down movement of the curve is observed at the moment of particle snap-in. This phenomen might emerges from any devation in the sphericity of the particles. Spheriglass is a bulk material and not a monodisperse research particle.

4.4.3 Discussion of the findings concerning the interaction of surface properties and adhesion force

In Figure 4.7 and Figure 4.8 the median of the measured pull-off forces between single particle and fiber is shown, as well as the calculated values for adhesion force according to Rabinovich's model [116]. The roughness on x-axis is based on the elongation state of the fiber during the stretching experiment. Measured data for roughness and peak-to-peak distance were also used to calculate the adhesion force according to Rabinovich [116]. As described in Section 4.4.1, these values are based on the measurement of the fiber surface with the WLI and have standard deviations due to the repeat measurements on six different fibers. These standard deviations around the corresponding median were not considered in the modeling of the discrete data points and fits in Figure 4.7 and Figure 4.8. For the calculation the contact distance was estimated here with 0.3 nm. The chosen contact distance in the calculation corresponds to the condition at an approach of two smooth surfaces. A change of the contact distance due

to a change in surface roughness is conceivable. Consequently this change would have an influence on the magnitude of the adhesion force [129, 34]. In these calculations, a change due to surface change is not considered. A polynomial fit 2nd degree was performed for the measured and the modeled data.

In the investigations with Spheriglass (see Figure 4.7), a reducing influence on the pull-off force due to the change/increase of the surface roughness is also shown for the modeled data. The calculated discrete values for the experiments with sphere diameter of 23.78 μm and 17.13 μm are clearly below the measured surface roughness, especially for low surface roughness. This difference is partly reduced with increasing roughness as in the experiments with 23.78 μm. For the roughness of 158 nm and 166 nm, the deviations of the measured discrete adhesion forces overlap with the fitted curve for the experiments with particle size of 23.78 μm. The fitted curve for the discrete values of the experiments ($d_p = 23.78\,\mu m$) and the curve for corresponding modeled data show an similar course in the same order of magnitude of the adhesion force. For the experiments with a spherical glass particle of 17.13 μm, the difference between the measured adhesion force with the AFM and the calculated data remains constant over the entire range of the surface roughness of the substrate. Nevertheless, a similar decreasing trend can also be seen in these calculations due to the polynomial fits. The slope of the fit for measured data is less high than for the modeled data.
For the experiments with a particle of size 10.37 μm a very good agreement between discrete values of the adhesion force is shown for the extreme values of the roughness of 112 and 192 nm. For a surface roughness of 158 nm a large deviation is observed. These deviation could originate from local inhomogenities of the surface which influence the measured adhesion force. Beach et al. revealed that surface roughness causes up to a 120 % error from one spot to another on the surface. The increase of deviation of the mean value between the minimum and the maximum value of roughness is clearly visible. The calculation by Rabinovich et al. does not consider any deformation of the particle or the substrate [116]. A potential increase of adhesion force in the measurement results could originate from the deformation of the substrate. The first layer might be deformed by pressure of the particles during the measurement procedure with the AFM. The glass particles (Spheriglass 5000) have an increased hardness with an Young's modulus of 4100-6500 $N\,mm^{-2}$. The following increase of contact area during the measurement procedure results in higher pull-off forces. These uncontrolled deformation of the polymeric substrate could explain the high adhesion force of glass particle.

Figure 4.8 shows the measured and the calculated data (according to Rabinovich's model see section 4.3) of the adhesion force between a PS particle and the fiber with the corresponding surface roughness. As already observed in the experiments with Spheriglass particles, the difference between the model and the measured value is the largest for the smallest measured surface roughness. As shown in the experiments

with Spheriglass, the calculated values for the adhesion force are below the measured values for both particle sizes. In addition, a large standard deviation is obtained in the measurement with the particle size of 9.88 μm.
With an increase in surface roughness due to further fiber elongation, the calculated adhesion force decreases for both particle sizes. When a roughness of 166 nm is reached, the discrete values for calculated adhesion force are larger than the adhesion force measured with AFM. As observed in the measurement with glass particles the deviation between the minimum and the maximum roughness is higher, which is caused by local inhomogenities in the surface structure. As shown in the images of the surface (Figure 4.5 and Figure 6 and Figure 11 SI) the surface structure is not this distinct as in the maximum of surface roughness.
For experiments with PS particle, Beach et al. mentioned a deformation of the particles during the loading process in the AFM-experiments. This could be a further explanation for increase of adhesion force in the measurements.

In general the modeled values of adhesion force for PS particle display a good agreement with the measured values by the AFM for high surface roughness. In the range of low surface roughness the measured pull-off force is higher than the modeled. In addition, in the investigation with Spheriglass there is a good accordance between measured data and calculated data for smaller particle size. The calculation of adhesion force for both particulate materials is influenced by precision of surface measurement of the surface roughness and the peak-to-peak distance. Especially the manual determination of peak-to-peak distance is a crucial factor that must be considered. An example of determination is given in Beach et al. [10].

The influence of moisture and electrostatic forces are neglected in the shown model by Rabinovich et al. [116]. Moisture could induce capillary forces between the particle (fixed at the cantilever) and the substrate [61]. The formation of capillary forces between the particle and the rough surface can increase the measured adhesive forces [109]. For low humidity range Ata et al. revealed a weak adhesion force between a glass sphere and a metallic substrate [6]. Heim et al. observed an influence of capillary forces on adhesion forces only from a moisture content of 20-40 % [41]. This effect is not considered in the calculated model and could affect the difference between calculated data and the measured values for experiment with Spheriglass and PS, respectively. Further the influence of the nanoscale roughness of the particles is not considered in the calculation. Thus, the PS-particles are very smooth particles, since they are extracted from research material. The particles made of glass are particle material used for the filtration experiments, which was taken from a bulk. As seen in Figure 1 SI, the particles may exhibit bumps or potential deviations from spherical geometry.

In analogy to the results given in this manuscript and in other studies on the change of the adhesive force by changing the surface, the change of the wetting properties of a hydrophilic or hydrophobic surface can be seen. The wetting mechanics

of surfaces describes the interaction between a water droplet and a rough surface. A contact angle is formed between the surface and the water droplet on the surface depending on the surface energy of the substrate. The size of the contact angle can be divided into two different categories. A contact angle of less than 90° is referred to a hydrophilic surface, and a contact angle of 90-180° is referred to a hydrophobic surface [21]. Depending on the contact angle, a characteristic adhesion force is formed between the droplet and the surface. According to the model of Cassie-Baxter, when the roughness is increased, the hydrophilicity or hydrophobicity is increased [21]. Thus, an increase of surface roughness for a hydrophobic surface such as polyurethane could reduce the adhesion force between a droplet and the surface. Increasing the roughness of the hydrophobic fiber substrate would reduce the adhesion force to a water droplet or any moisture at the interface. The particle materials used in this study are PS and glass, whereas the first is a hydrophobic material and the second material is a hydrophilic material. Polystyrene has a surface energy of $0.0375\,J\,m^{-2}$, whereas glass has a surface energy of $0.0834\,J\,m^{-2}$ [167, 121]. Polyurethane has a surface energy of $0.02715\,J\,m^{-2}$ [87].

4.5 Conclusion

For a more detailed understanding of the detachment process of particles within a new stretchable filter, knowledge of the adhesion force between individual particles and the polymeric stretchable fiber at different stretching conditions would be beneficial. Based on the results and methodologies of the studies by Opdahl et al., Tsukada et al. and Miwa et al. the idea was developed to measure the pull-off force between a single particle and a filter fiber at different surface conditions directly after stretching [96, 158, 89]. Previous work characterized the dependence of the adhesion force between colloid material of different dimensions and in different combinations of materials, as well as partially abstracted shapes of the substrate (see Table 4.1). Roughness in those investigations was mostly lower than $25\,nm$ (Root Mean Square (RMS)).

The study presented here complement the previous results with the results for polyurethane as substrate and glass and Polystyrene (PS) as particulate material. In addition the shown investigations revealed the direct relationship between a variable surface structure (fiber stepless stretchable) and the pull-off force for a surface roughness and particle size of a magnitude that have not been studied before. The fiber as substrate is present in the shape/dimension as it is found in filtration process.

The setup around the Atomic Force Microscope (AFM) was redesigned to allow observation of particle contact with the substrate from two perspectives. A more precise operation and navigation on the zenith of the real filter fiber (substrate) was possible. In addition an innovative adjustable bracket above the fiber was developed to fix the fiber as a flexible substrates during the AFM measurements. It represents

an extension of the setup design of Bamberg et al. with a different level of application [8]. The AFM measurements are performed with the exact form and size of substrate as found in the real-world application (in the filter). To validate the new direct form of measurement with the AFM, a comparative measurement was performed using a standardized process setup in which the fiber was attached to a fixed glass slide. Comparing to studies by Schaefer et al. and Katainen et al. a stepless change of substrate surface property is possible using the fiber stretching device [129, 71]. This results in a non-limited level of application which has not reach its limits yet.

The experimental results indicate a decrease of pull-off force between the spherical particles and the polymeric fiber by the increase of surface roughness from 112 nm to 192 nm broadly similar to what was observed by Beach et al. and Amitay-Sadovsky et al. and Miwa et al. with different material as substrate [3, 10, 89]. In general this effect is based on the decrease of contact points/area as described in the mentioned studies. The maximum decrease of adhesion force was revealed for a size of 12.30 μm for PS particles. For glass particles the maximum decrease of 440 nN was found the particle size of 23.78 μm. This result corresponds to the results of Kumar et al. who also observed the largest reduction for rather large particles with the size of 10.25 μm. For smaller particles up to a diameter of 7.59 μm, the agreement with Rabinovich's model is higher as well as in the results in this study[116, 73]. The RMS of 192 nm was found to be the maximum roughness that was obtained by stretching the fiber within the possible range of 22 mm (38.4 %) elongation.

The increased surface roughness causes an decrease in the number of contact points between the spherical shaped particle and the substrate (fiber) as described by Miwa et al. [89]. In the given range of roughness this effect is obtained in the extreme case of large particles for both particulate material. As shown in the study of Kumar et al. and Wanka et al., the Rabinovich model underestimates the pull-off force between particle and substrate in this magnitude of particle size [116, 73, 164]. In general the calculated and the measured values in this study show a similar trend. Rabinovich's model is suitable for a description of the qualitative progression of adhesion during a simulation of the stretching process for the used combination of material [116]. An analogous case to the reduction of the adhesion force by a change of the surface structure can be found in the interaction of water drops and hydrophobic or hydrophilic surfaces. This is caused by a change in surface energy. Consequently, the adhesive force between a hydrophobic surface such as polyurethane and a water droplet can be reduced by increasing the roughness [80].

In the future, the trend of the measured data will be used in a Discrete element method (DEM) simulation. The simulation might reproduce the a detailed image of rearrangement and detachment process within the filter matrix as shown by Dong et al. and Braschke et al. [31, 16], as well as the change in number of contacts during

the stretching process. Furthermore, studies of the adhesion force between spherical particles of different size are under way to characterize in detail the detachment of particle agglomerates in a new stretchable filter matrix.

Data availability: Data will be made available on request.

Declaration of competing interest: The authors declare that they have no known competing financial interests or personal relationships that could have appeared to influence the work reported in this paper.

Acknowledgement: We thank Hendrik Hölscher and KNMF (Karlsruhe Nano and Micro Facility, www.knmf.kit.edu), KIT, for support and lab use. A Helmholtz Research Infrastructure at Karlsruhe Institute of Technology (KIT, www.kit.edu).

We also kindly thank Freudenberg Filtration Technologies SE & Co. KG for donating fiber material.

We gratefully acknowledge that this project was funded by the Deutsche Forschungsgemeinschaft (DFG, German Research Foundation) - 427981860.

Appendix A. Supplementary material: Supplementary data associated with this article can be found, in the online version, at https://doi.org/10.1016/j .jcis.2023.03.051.

5

Detachment of particulate structures during multiple stretching cycle of the single filter fiber

Title: Experimental Detection of Particle Structures Detachment from a Stretchable Single Fiber during Multiple Consecutive Stretching Cycles
Authors: Poggemann, Lukas; Meyer, Jörg; Dittler, Achim
Status: Published
Bibliographic data: Separations 2022, 9; 168; https://doi.org/10.3390/separations9070168

Copyright in Separations 2022, published by Multidisciplinary Digital Publishing Institute. Reprint with permission. The text has been adapted in this thesis to change the citation and figure numbering. Additionally, some symbols have been modified to confirm with the other chapters.

Abstract
The deposited particulate material within a fibrous filter affects the pressure drop which develops through three different stages. The implementation of a time-adjustable matrix is intended to cause detachment of particle structures from fibers within the upstream layers at low flow velocities. The deposited particle structures are transported further within the filter and clear up void space for an extension of filter service life. As in previous studies observed fiber stretching initiate cracks and following detachment of particle structures with a simultaneously applied airflow. For complete detachment of the particle structure, five consecutive stretching cycles are performed in this study. The elongation velocity, the flow velocity and the particle loading are varied. Using an image analysis technique and a laser-light measurement technique simultaneously, the cumulative fraction of detached particle structures and the size of detached particle structures are determined. A high initial particle loading on the fiber induces early detachment of larger structures from the fiber. The size of

detached structures is increased by the increase of the elongation velocity. The mean value remains almost constant whether the elongation velocity or superficial velocity are increased. For small initial structures on the fiber, a decrease in superficial velocity causes detachment of larger particle fragments.

5.1 Introduction

Fibrous filters are mostly used in filter systems with low particle concentration. High collection efficiency is needed at low pressure drop during the entire filtration process. The primary factors to characterize the operational behavior of depth filters are the separation efficiency, pressure drop and the total loading capacity [144]. The overall depth filter service life is determined by the development of pressure drop. Typically, the pressure drop develops through three different steps. First particles are collected within the upstream layers of the fibrous filter matrix. Particulate material is collected at the surface of each single bare fiber across the depth of the filter matrix. During this depth filter step, pressure drop increases slowly [101]. As more particulate material is collected by the filter matrix, particle deposits on neighboring fibers start to from bridges. The separated particle material starts to clog. Deposition and, thus, clogging occurs mainly at the upstream section of the filter matrix. Pressure drop is increasing slightly faster at the end of the depth filter step [13, 14]. During the transition step, the particulate material is collected either by the loaded fiber or within/on the surface of a clogged area. Pressure drop strongly depends on collected particle mass within the filter matrix [152]. At the end of this phase, the whole filter is switched to surface filtration. Subsequently at this surface filtration step, more particulate material accumulates on the upstream side of the filter forming a particle layer with high flow resistance. Based on the processes, the filter interior is not receiving any more particle mass. As shown in Figure 5.1 (LEFT), the filter remains with void space in the downstream layers that is not filled with particulate material [19]. Pressure drop is increasing linear in the surface filtration step with the deposited particle mass until critical pressure drop. At the end of the filter service life, whether in the transition step or in the surface filtration step, the filter must be replaced.

In order to extend the filter service life, a chance might be to free up some blocked space within the upstream layer. As a result, it should be possible to delay the steep increase of pressure drop at the end of the transition step. The intended trigger to remove/detach particulate material from the fiber and within the clogged areas in the upstream layers is stretching of the fiber matrix or individual fibers within the filter [52]. By stretching the collector, shear and tensile stress are applied to the deposited particulate mass on the fiber. As depicted in Figure 5.1 (RIGHT) the particulate material shall be transported further downstream the filter matrix to clear up void space at the upstream part of the filter. In investigations by Tippayawong, an external excitation such as vibration in addition to the applied airflow, act as a trigger for detachment of particle. The external excitation influences the threshold for removal

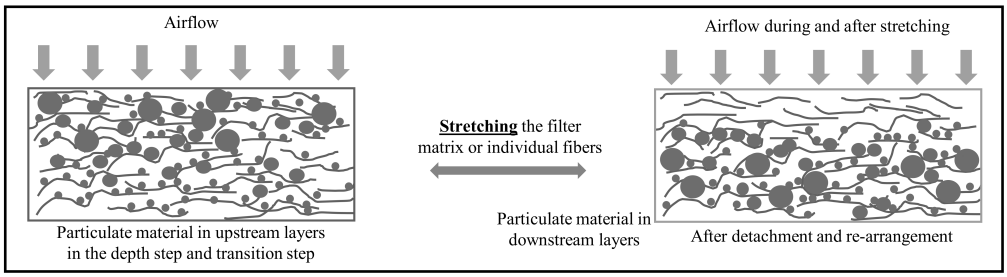


Figure 5.1: *Schematic of the filter matrix, in a cross section. LEFT: Normal mass accumulation matrix during the first (depth filter step) and the second filter step (transition step). [14] RIGHT: Potential distribution of particulate material after detachment and rearrangement of particles within the filter matrix. Fiber stretching was used to initiate detachment to clear up some void space. Modified from VDI 3677 [27].*

between surface adhesion and the aerodynamic lift [156].
So far, the aspect pressure drop describes the behavior of a depth filter at the macroscopic level. To gain more detailed/fundamental information about the processes within the fibrous filter, systematic experiments at an isolated fiber are examined. Using this information from the microscopic level (single fiber), filtration behavior of fibrous filters can be modeled more precisely. As shown by Poggemann et al. [106] a mechanical elongation of individual single fibers induce shear and tensile stress to the compact particulate structure on the fiber resulting in rearrangement and detachment of particle structures during the process. Compared to other investigations [75, 83, 113, 53, 111, 179], which focused on detachment of particle or particle structures from stiff collectors, the necessary gas velocity (superficial velocity) for particle detachment at stretchable fibers have been quite low. As already shown by Beuth and Thouless, the cracking process and the size of the detached fragments on a moving substrate can be described as a function of the height of the matrix on the substrate (fiber) [153, 12]. In the case of single fiber experiments, the amount of collected particulate material on the fiber is parameter for the development of filtration process. To estimate the amount of separated particulate material in the experiments, the level of fiber loading is evaluated in these investigations. The level of the particulate structure on the fiber affects the average distance between the cracks. This fact results in different sizes of the detached particle structures. A detailed view on the effects (cracking/detachment) on one filter fiber neglects the cross effects/influence of the neighboring fibers as in a filtration matrix. These bridging effects mainly occur at the end of the depth filter step and in the transition step [79].

The measurement technique to characterize the size and moment of detachment of particle structures was constructed based on the measurement method designed by Wurster et al. for continuous online detection of entrained oil droplets [169, 170]. Moreover, the size of the detached particle structures gives a rough estimation of whether the structures will remain somewhere on the surface of the filter, re-deposit in the subsequent filter matrix of the filter or penetrate through the whole filter medium.

Since the particle structures have to pass through the gaps between fibers during the detachment process, the distance between several individual fibers is important for the transportation of particulate material into downstream layers. Based on the definition for depth filters, the filters have a packing density in the range of 0.1 - 0.02 and subsequently a porosity of up to 99.8 %. This results in a distance between the individual fibers that is usually a multiple of the fiber diameter [56, 27]. By the use of imaging techniques for filter characterization, the distance between individual fibers was validated [7, 139, 46].

For a reliable characterization of the properties and phenomena of/at a filter, process parameters and materials parameter (fibers and particulate material) were specifically varied in previous studies. The aim of these studies was to evaluate the development of pressure drop, the separation behavior of particles at the collector, the flow field or the material parameter of the used particulate material. To obtain a realistic insight of the filtration process as well as to control any influencing variable, a defined fiber distance was used in the studies. Müller et al. studied the separation behavior of particles at parallel fibers. The 25 parallel fibers had a distance of 246 μm [91]. Kanaoka et al. investigated the development of pressure loss during particle separation on fibers of a model filter with a distance of 130 μm and 190 μm [66]. The fiber diameter in the corresponding studies were at most one fifth of the distance between the fibers that are used in the model filter.

In the simulation studies, the distance between the fibers is obtained by the packing density and also the fiber diameter. Mostly, the calculation of the flow field was based on the approach by Kuwabara et al. Junction points are neglected in these studies [74, 68, 7].

This investigation focuses on the detachment process of particle structures from a single filter fiber. Thus, the fact that any stretching of fibers in an entire filter inevitably changes the spacing between the fibers is currently neglected. The overall objective of this study is to gain basic knowledge about the impact of applied process conditions on the structure size, on the amount of detached particulate material and the kinetics in the stretching experiments. During multiple stretching cycles a low gas flow is applied to the fiber. Small structures can pass through the gaps more easily, whereas huge structures releases more space, but can be recollected effectively in downstream layers. A detailed prediction of where the particle structures migrate in a complete filter after detachment from the fiber is not possible yet, as there are no multiple parallel or stacked fibers in this study. The knowledge about the influence and interaction of the applied process parameters helps to built a base for the layout of a prospective stretchable depth filter. Construction parameters are, e.g., the space requirements for elongation the size and thickness of the filter.

5.2 Materials and Methods

5.2.1 Fibre and Particulate Material

As in the previous study, polymeric fibers made of polyurethane were used as stretchable collector for all investigations [106]. The fiber has reversible stretching behavior up to 75%, so it can be used for multiple stretching cycle up to 39.3% stretching. Isopropyl alcohol was used to clean the fiber before each loading process. For protection, the fiber was handled with tweezers and gloves during clamping only. Each fiber was replaced after nine stretching procedures. The fiber is a prototype for an application in an potential adaptive filter.

The particulate material is made from solid soda lime (A-Glass with a given material density and refractive index; $\rho_{material} = 2.46\,\mathrm{g\,cm^{-3}}$, $n_{refractive\,index} = 1.51$). The inert particulate material was obtained from Potters Industry and was used in all experiments in this study. The same material was used by Zoller et al. and Poggemann et al. in previous studies [180, 106]. Particle size distribution is measured by laser light scattering (Helos & Rodos, Sympatec) with a dispersion pressure of 1.0 bar (g). Volume based median diameter of the particle size distribution is given with $d_{50,3} = 7.73\,\mu\mathrm{m}$.

5.2.2 Aerosol Generation and Loading Procedure

Similar to a previous study by Poggemann et al., an experimental setup was used, which is depicted in Figure 5.2 [106]. Before this loading procedure, the stretchable fiber is mounted on the designed fiber-mounting device that fits into the loading chamber and the measurement chamber of Laser Structure Detection System (LSDS) (see Section **??**).

The aerosol used in this study contained glass spheres as a disperse phase and pressurized air as a continuous phase. The particulate material is dosed by a rotating ring and an ejector nozzle (DIN ISO 5011) using the Topas SAG 410/U. The disperser worked at an ejector nozzle pressure of 2.0 bar (g). This results in a volume flow of $25\,\mathrm{L\,min^{-1}}$ in the feed flow. To obtain a constant humidity level in the storage tank of SAG 410/U, a sheath air flow with an indicated pressure of 1.3 bar (g) was applied. As in Poggemann et al. the mass flow rate of $4\,\mathrm{g\,h^{-1}}$ in the feed flow was set for the selected ring velocity (5 % of the maximum velocity) in the setup of the disperser [106]. The loading procedure includes two sections upstream and downstream the loading chamber, where the fiber mounting device is placed. Upstream the loading chamber, the feed flow is split into loading flow ($V_{loading} = 14.28\,\mathrm{L\,min^{-1}}$) and excess flow ($V_{excess} = 10.72\,\mathrm{L\,min^{-1}}$). To ensure a stable loading flow, a constant excess flow is drained of by a suction pump. The excess particulate material is removed by a HEPA-filter upstream a Mass Flow Controller (MFC). After the separation of excess flow, the loading flow consecutively passes a ^{85}Kr—neutralizer to reduce the electrical charge of glass spheres. A following flow rectifier (consisting of a tube bundle) ensures a laminar plug flow field. The volume flow rate of loading flow is established using a MFC and a

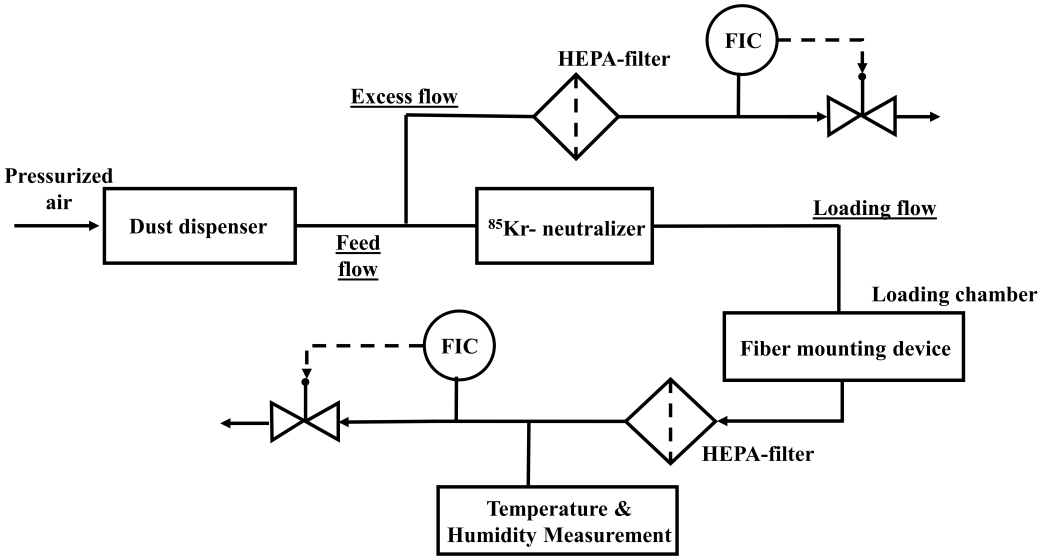


Figure 5.2: *Schematic setup to produce an aerosol containing glass spheres and the deposition on a single fibre that is clamped at the fiber mounting device [106].*

suction pump downstream the loading chamber. For a precise flow control, the MFCs were regularly calibrated using a bubble flow meter with a precision of 0.03 L min^{-1}. Downstream, the loading chamber all particles were separated from the gas stream using a HEPA-filter. The humidity and temperature (Sensirion, SHT85) are monitored downstream the loading chamber. The humidity of the loading flow was approximately 10%. The experiments are conducted between 20 ° C and 28 ° C and atmospheric pressure.

The loading procedure of the bare fiber takes place in a short free jet flow inside the loading chamber, which is sealed to avoid contamination by leak air. There was no extra differential pressure applied or measured across the loading chamber. Inlet and

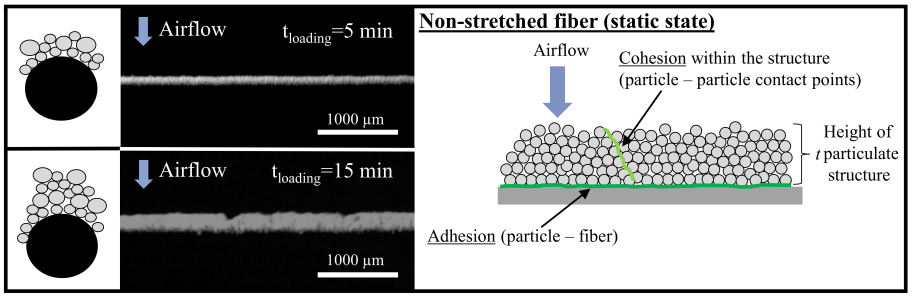


Figure 5.3: *(**LEFT**): Images (in the side view) of the loaded fiber after 5 min loading time (TOP) and after 15 min loading time (BOTTOM).Direction of airflow from the top to the bottom. Illumination from the front. (**RIGHT**): Schematic of the loaded fiber in the non-stretched state. Marked is the state of the interfacial layer and the condition of stress.*

outlet pipe of the loading chamber had a diameter of 16 mm, which results in a flow velocity of $u_a = 1.2\,\mathrm{m\,s^{-1}}$ at the given volume flow. The superficial velocity for generation of the particle loading is in the range of filtration velocity for fibrous filter systems [27] A Stokes-number of 6.52 was obtained. Two different loading times (5 min and 15 min) at constant raw gas concentration were applied. Figure 5.3 (LEFT) shows two different particulate structures on the fiber in the non-stretched state. The heights of the particulate structures varies between approximately 103 μm for 5 min loading time and approximately 332 μm for 15 min loading time. The different heights of particle structures on the fiber are intended to represent different loading stages of the total filter during the transition filtration phase. In a filter matrix a linear increase of the deposited mass was observed by Thomas et al. [152]. The resulting structures (shown in Figure 5.3 LEFT) on the fiber are mainly located on the upstream side of the fibers. A compact structural shape has developed according to the process conditions which favor separation due to inertia [65]. As Kasper et al. described, the separated structure on the fiber can exceed the fiber diameter in height several times. The separated structures were representative for separation in a fibrous medium [70, 180]. However, in a real filtration process different types of structures such as compact and diffusive with dendrites might overlap. In this study, only compact structures on the fiber are considered.

Figure 5.3 (RIGHT) shows the state of the interfacial layer between the fiber and the particulate structure in the non-stretched state of the fiber. The particle structure and the fiber are in a static state. In this static state, no shear stress acts within the particle structure or between the fiber and the particle structure. The indicated cohesion within the particulate structure and adhesion between the particulate structure and the fiber are significant for the behaviour of the structure on the fiber during the stretching process. For detachment of particle structures from the fiber, either the cohesion between the particles or the adhesion between the particle structure and the fiber must be eliminated. The adhesion between fibers and particles and cohesion between particles, respectively, are mainly based on intermoleculare forces. As observed during the detachment/regeneration of a filter cakes, the detachment behaviour is influenced by the properties of the particle structure (e.g., porosity ϵ and height t), the properties of the filter medium, and the filtration parameters.

5.2.3 Multiple Stretching Cycle

As described in Poggemann et al. at stretching velocities of $1.2\,\mathrm{mm\,s^{-1}}$ and superficial velocities of $0.4\,\mathrm{m\,s^{-1}}$, the compact and huge particulate structure on the fiber did not detach completely within the first cycle of stretching [106].

In this study five stretching cycles are performed consecutively. The elongation velocity and relaxation velocity are the same. Figure 5.4 shows the process diagram of one stretching experiment. All experiments were performed threefold. The fiber was replaced after 45 stretching cycles. This number of stretching cycles is based on

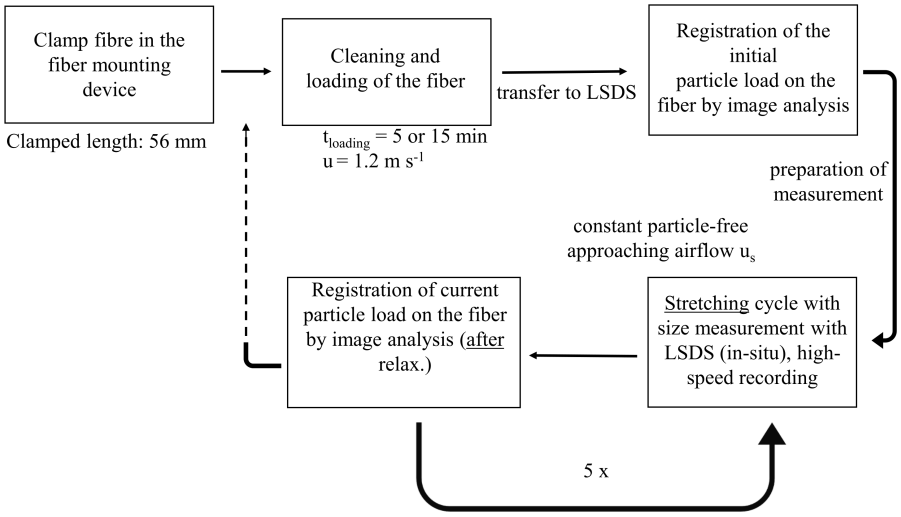


Figure 5.4: *Procedure of a stretching experiment including the multiple stretching cycles (5 times).*

values of the tensile tests. In total, 6 fibres were used in the shown experiments. The fibers did not show any macroscopic changes before and after multiple particle loading. The size of particle structure fragments are measured with the LSDS (quasi in-situ) during each stretching cycle. The airflow is approaching the fiber during the whole stretching cycle. The percentage of detached particle structure is analyzed at the end of each stretching cycle via image analysis (see Section 5.2.5). The images after individual stretching cycles are found in the supplementary data. Table 5.1 summarizes the experimental parameter for the loading and the stretching process. As shown in Poggemann et al. fiber stretching is established by two synchronous moving piezo actuators placed on the fiber- mounting device [106]. The elongation velocity is varied between 0.05 mm s^{-1} and 12 mm s^{-1}. Fiber stretching was operated with an entire elongation of 22 mm. With a distance of 56 mm between the clamping points of the fiber, this results in a maximum elongation of 39.3%.

Table 5.1: *Variation of loading time, average flow velocity, superficial velocity and elongation velocity*

Fibre Loading Time / min	**Average Flow Velocity During Loading Procedure/m s^{-1}**	**Superficial Velocity (u_s) During the Stretching/Relaxation Process/m s^{-1}**	**Elongation Velocity (e)/mm s^{-1}**
5;15	1.2	0.05; 0.2; 0.8	0.6; 1.2; 2.0; 12.0

5.2.4 Large Structure Detection System

For the continuous counting and sizing of detached particle structures from a single fiber a dedicated measurement system was developed. Because those particle structures move very rapidly within the particle-free airflow once they are detached from the stretched fiber, it was necessary to detect and size them immediately. In addition, the structures start to disintegrate following the airflow below the fiber. A novel device based on the laser light sheet technique by Wurster et al. [169] was developed. Figure 5.5B shows the overall optical measurement concept of the LSDS. A thin laser sheet is placed at a distance of a few millimeter below the fiber, so detached particle falling through the light sheet directly after the detachment from the fiber. The light sheet was produced by expanding a Gaussian TEM00 laser (MGL-FN-532) of $1\,W$ cw solid state and a wavelength of $532\,nm$. For this expansion in horizontal direction two cylindrical lenses are used. First the laser is expanded by a plano-convex lens with a focal length of $5\,mm$. The second plano-convex lens with a focal length of $200\,mm$ has a distance of $200.5\,mm$ to the first lens and focuses the laser on the aperture. The aperture (dimensions: $16 \times 2 \times 0.150\,mm$) was applied to sharp edges of the laser-sheet. The Photomultiplier (PM) captures the scattered light against a background of stray scattered light in an angle of $90° \pm 13°$ [17, 78]. For the perpendicular optical access, the clamping points of the fiber-mounting device are arranged diagonal. The detached particle structures (detachment events) produce pulse of scattered light while passing through the light sheet. These pulses of scattered light (emitted at an angle of $90° \pm 13°$) are focused onto the PM (P30CW5, Sens-Tech Limited). At the photocathode of the PM, the photons release initial electrons. These generated electrons are exponentially amplified at dynodes and result in a measurable electrical voltage signal at the anode of the PM [38]. The generated electrical impulses are filtered (low pass filter with cutoff frequency of 100 kHz) and digitized using a digital oscilloscope (Picoscope 4224, Pico Technology). Using a MATLAB© routine the separated online-signals are recorded and classified individually according to the pulse height and the time stamp.

The high-speed camera (AOS Promon 1000/U) is mounted outside of the measurement chamber perpendicular to the clamped fiber. Online observation and analysis of the remaining particle material on the fiber after the measurement procedure is performed. Further, observation of the rearrangement process of the particle structure is possible. The used objective lens (Navitar 1-60135, 1-61387, 1-60110, 1-6010) allows a resolution of (up to) $5.2\,\mu\mathrm{m\,px}^{-1}$. The necessary illumination for a high-speed record was provided by using a red LED-stripe ($620\,nm$) and a diffuser plate. The fiber including the particle structure was illuminated from the back, creating a shadow profile of the fiber and the particulate structure on the fiber. In front of the PM, a dichromatic filter (DT-green filter) culled the red light, so simultaneous LSDS measurement and high-speed recording with illumination is performed. As depicted in Figure 5.5A,B, a ring-light RL2 (StarLight Opto-Electronics GmbH & Co. KG, Nürnberg) was installed for photography and filming with illumination from the front (same direction as camera) during and after stretching cycle.

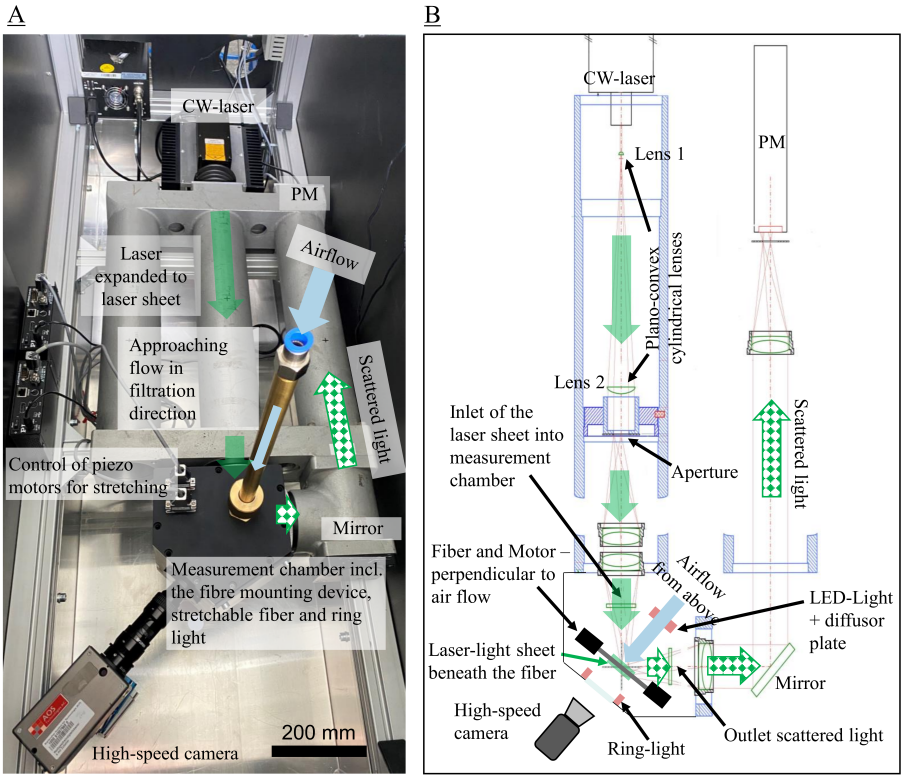


Figure 5.5: *Image (**A**) and schematic diagram (**B**) of the laser-light sheet measurement system. An expanded laser beam (thin sheet) runs below the fiber (shown in Figure 5.6B). The scattered light within the measurement area is captured focused onto a PM and transferred into electrical impulses.*

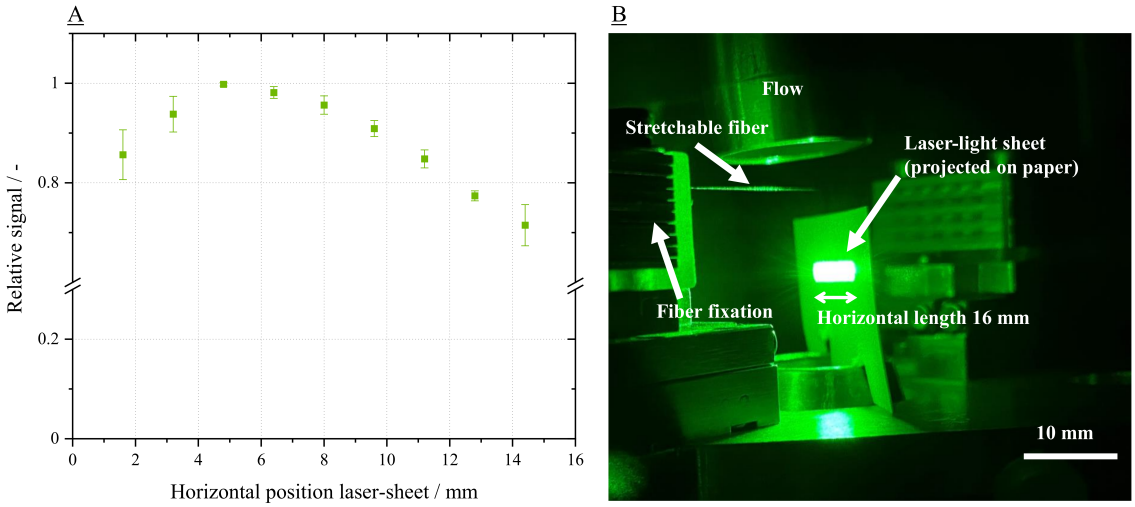


Figure 5.6: *(**A**): Relative signal of beam intensity profile, measured in horizontal direction of laser sheet (below the fiber), total horizontal length of laser sheet 16 mm. (**B**): Image of laser sheet in the measurement chamber. Here the laser light sheet is projected onto a piece of paper below the stretchable fiber. Distorted view due to viewing angle.*

The laser-light system was calibrated with glass spheres in a size range of 90 μm to 2000 μm. The resulting signal for each size class showed a x^2-dependence with a factor of 0.765 mV μm^{-2}. The upper detection limit was at 4279 μm due to the saturation of the oscilloscope. Larger structures are still counted, but not sized correctly. The lower detection limit is 90 μm given by a minimum signal-to-noise ratio of 2. Samples are collected with a sample interval of 100 ns. The average amplifier voltage for the PM was 360 V. The measured signals are sorted into several channels. The LSDS provides number concentrations in 129 channels within the detection limits. Number based distribution (e.g., Q_0; q_0) was calculated assuming a uniform shape of detached particle structures. The calibration results in a function between photomultiplier signal (electrical signal captured with the digital oscilloscope) to projected structure size which is equivalent to scattered light as shown in Zoller et al. [181].

The laser beam profile was assumed to be Gaussian in all direction. To evaluate the described measurement technique, the intensity profile in the horizontal axis were probed with monodisperse glass bead of 1 mm fixed on a piezo motor for stepwise movement. The beam intensity registered (by the LSDS) is shown in Figure 5.6A. As depicted here, the intensity varies by a maximum of about 33% across the horizontal coordinate. This results in a variation of 16.5% in assigned size.

5.2.5 Determination of Cumulative Fraction of Detached Particle Structure from Total Structure and Residual Structure on Fiber

The projection area (pro. a.) of the remaining particle material is determined using a MATLAB© routine. For each cycle, the image is cropped and converted to grayscale.

Before each experiment, a reference frame is created using only the bare fiber. All images are binarised according to Otsu [97]. Within the binarised images, the bright pixels are counted. Those represent the pro. a. of particulate material and fiber. In the side view, the pro. a. combine both the fiber and the compact particle structure. For the final pro. a. of the particulate structure, the pro. a. of the reference frame (only the bare fiber) is subtracted. As shown in Equation (5.1) the ratio of the current pro. a and the initial pro. a. at the beginning of the experiment gives the cumulative fraction of the detached particulate structure. To eliminate the influence of fiber rotation during the stretching process, image analyses is executed at the end of each stretching cycle 2 min after reaching the initial position. The residual structure on the fiber was determined using the recorded images after the fifth stretching cycle. The grayscale images were subjected to qualitative analysis.

$$\frac{Cummulative\,fraction\,of\,detached\,particle\,structure\,from\,total\,structure}{} = \frac{c-r}{i-r} \tag{5.1}$$

With c as the current pro. a. of the fiber plus the particulate material on the fiber, r as the reference pro. a. of a bare fiber, i denotes the initial pro. a. of the fiber plus the particulate material.

5.3 Results and Discussion

In all experiments, a compact particle structure on the fiber was accomplished. In previous studies, a high particle loading on the fiber was used showing the basic effects of rearrangement and detachment of particle structures [106]. As described in Section 5.2.2, evaluation of detachment behavior of particle structures at different loading height/stages is necessary to gain knowledge about an optimal time for external excitation of the fiber and the filter, respectively. Therefore, results of fibers with reduced particle loading (5 min) are compared with those of high particle loading (15 min) on the fiber (see Section 5.2.2). The initial particle structure on the fiber at the beginning of the experiments is shown in each diagram by schematic drawings.

The detached particle structures are divided into two categories which are based on the time of detachment. The detached structures during the first elongation cycle are represented by filled symbols in the following graphs. The particle structures, which detach in the 2nd to 5th elongation cycle, are represented by hollow symbols. The cumulative number of detached particle structures during the five stretching cycles is plotted on the right y-axis. The figures depicted in the following, contain all structures, that detached during the three experiments (two replicate tests) of 5 stretching cycles each.

5.3.1 Variation of Particle Loading Time

Figure 5.7 (TOP, LEFT and RIGHT) shows the measured size of the detached particle structures as a function of the fiber elongation. The fiber was stretched with an elon-

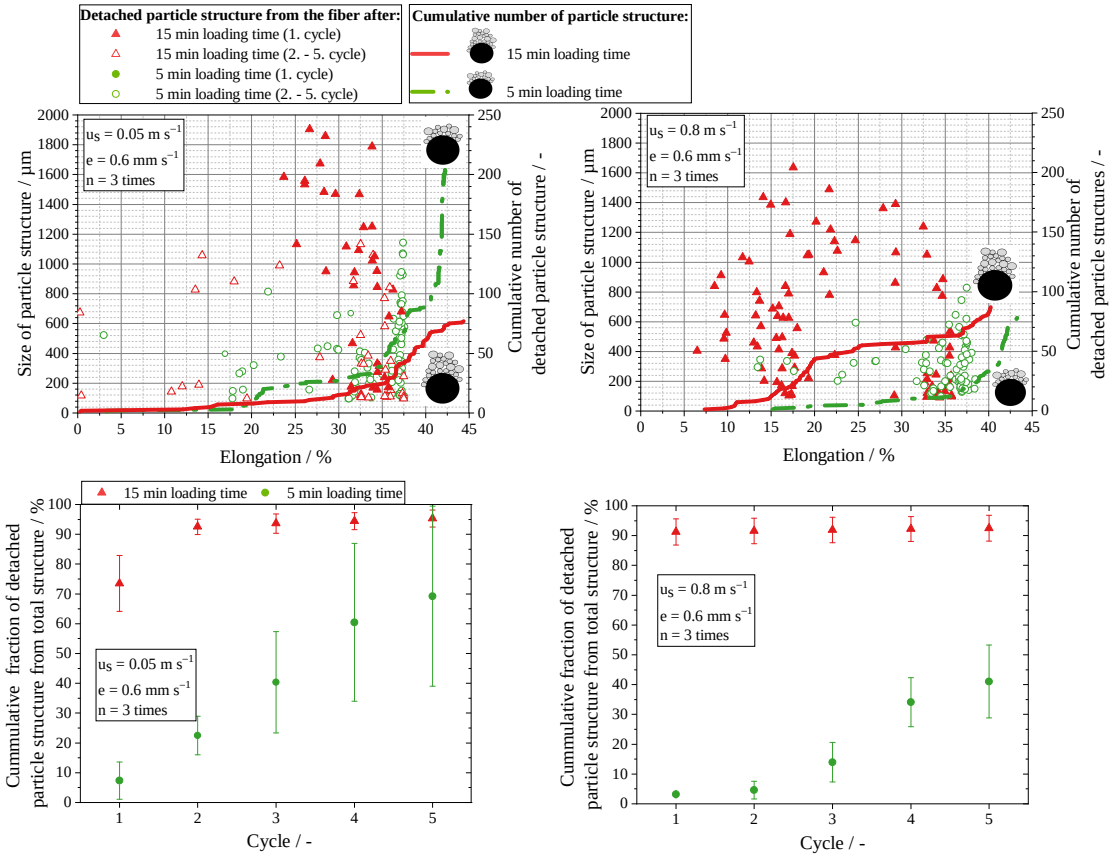


Figure 5.7: *(**TOP**) Size and cumulative number of detached particle structures measured with the LSDS during the five cycles of fiber stretching, comparing low (5 min loading time, green) and high (15 min loading time, red) particle loading of the fiber for two superficial velocities (u_s = 0.05 m s^{-1}, left and u_s = 0.8 m s^{-1}, right, respectively). (**BOTTOM**) Cumulative fraction of the detached particle structures from total particle structure determined with image analysis during the 5 cycles of fiber stretching.*

gation velocity of 0.6 mm s^{-1}. The airflow was orientated in the same direction as in the loading procedure. In all experiments, detachment of particle structures was observed regardless of the particle loading of the fiber.

Focusing on the experiments with a high fiber loading, the number of particle structures that detached during the first stretching cycle are significantly increased by the increase of superficial velocity. This fact results from the increase of drag force during the first weakening (from 0.05 m s^{-1} to 0.8 m s^{-1}). However, the total number of detached structures after five cycles remains almost the same regardless the increase of superficial velocity. The increase of the superficial velocity causes a shift of the main area for detachment from 25-35% fiber elongation to 10-25% fiber elongation. For a higher superficial velocity of 0.8 m s^{-1} and a high fiber loading, detachment of particle structures occurred at a lower fiber elongation. Regardless the applied flow velocity the fiber rotates during the stretching procedure as described in previous experiments

[106]. Thus, the face area of the particle structure and the lever arm are changing significantly due to the height of particle structure during the stretching process. Moreover, the flow velocity is included in the drag force with the power of 2, so the influence is much more pronounced.

Fiber elongation acts as a weakening factor in these experiments. In the experiments with a low fiber loading, no structure detachment during the first stretching cycle was determined. The structures are weakened by the first elongation cycle. In the following stretching cycles, particle structures detach from the fiber due to the combination of drag force and weakening by crack formation.

The main area for detachment during the 2nd to 5th stretching cycle was only slightly shifted by the increase of applied superficial velocity from $0.05\,m\ s^{-1}$ to $0.8\,m\,s^{-1}$. The main area for detachment in the experiments with low fiber loading and an elongation velocity of $0.6\,mm\ s^{-1}$ remains at a fiber elongation of 30-38 % for both superficial velocities.

Regardless of the superficial velocity, the size of detached particle structures is not changed significantly compared to the experiments with the high fiber loading. On the contrary, the number of detached structures decreases by increasing the superficial velocity. The maximum structure size remains below $1200\,\mu m$ in the experiments with low fiber loading. A reason for a lower number of detected structures could be that a majority of structures in these experiments were below the detection limit of the LSDS. For the experiments with a high particle loading, the structure size is almost up to $1600\,\mu m$ or $2000\,\mu m$ in the experiments for the respective superficial velocities. A reason for the large size of detached particle structures is the difference in the distance of cracks within the particle structure on the fiber. As mentioned in Poggemann et al., the average distance of cracks l that are formed within the particle structure during stretching is a function of the height t of the particle structure on the fiber [153, 106]. A more overall picture of the crack formation due to substrate/fiber stretching, might emerge from experiments with different particle materials with other surface properties.

Figure 5.8 (LEFT) shows the crack formation during stretching experiments for two different particle loadings on the fiber (elongation = 8%). Regardless of elongation velocity and the superficial velocity, the average distance between the cracks l differs between $515.1 \pm 118.4\,\mu m$ for high particle loading and $203.3 \pm 55.5\,\mu m$ for low particle loading. Cracks are formed from the surface of the particle structure to the lowest layer of particle structure on the fiber. The slope of cracks is very steep. The slope of the cracks during the breakage process of the total structure on the fiber is characteristic for the used particle material. Different particulate material may have a different fracture angle due to their properties. The size of the structures and the breakage process could be influenced. In addition, Figure 5.8 (RIGHT) shows schematically the state of the interfacial layer between the particle structure and the fiber during the elongation procedure. Fiber stretching introduces shear stress to the interface between particle structure and fiber. Crack formation rises from the failure of cohesion within the parti-

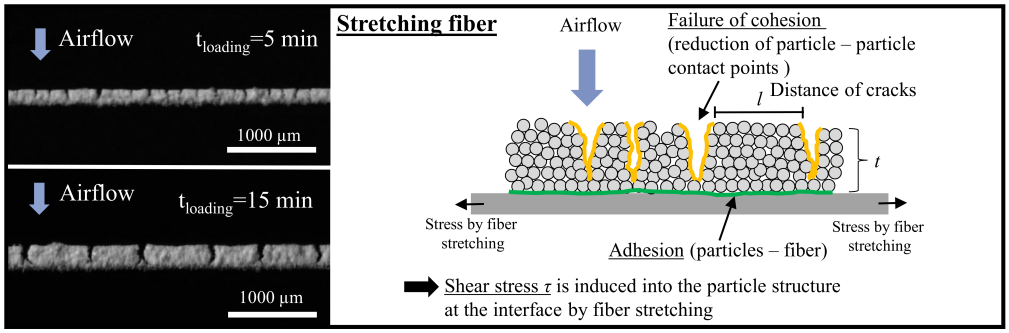


Figure 5.8: *(**LEFT**): Images (side view) of the loaded fiber after 5 min loading time (TOP) and after 15 min loading time (BOTTOM) at 8 % fiber elongation during the first stretching cycle. Same elongation velocity of 0.6 mm s^{-1}. Illumination of the structure from the front. (**RIGHT**): Schematic of the loaded fiber in the stretched state. Marked the physical state of the interfacial layer.*

cle structure at weak points within the particle structure/at the surface of the structure. The distance of cracks is determined by the ratio of applied stress due to fiber elongation and the corresponding cross-sectional area of the structure on the fiber. The applied elongation velocity of the fiber and the tensile strength of the particle structure affect the breakup behavior of the structure on the fiber.

Figure 5.7 (BOTTOM, LEFT and RIGHT) shows the cumulative fraction of detached particle structure as a function of the number of stretching cycle. Standard deviations of the mean value result from three experiments with the same process conditions. In experiments with high particle loading, the cumulative fraction of detached particle structures after the first cycle is increased by the increase of superficial velocity. After the 2nd stretching cycle, the cumulative fraction of detached particle structures is in the range of complete detachment, regardless the superficial velocity. The missing fraction up to 100% represents the amount of residual structures on the fiber (see Figure 5.9). These structures can be observed by analyzing the fiber separately in all experiments with high fiber loading as described in Section 5.2.2. The corresponding images can be found in the supplement data.

In the experiments with a low fiber loading (5 *min*), a small, yet non-negligible cumulative fraction of missing detached structure is observed after the first and second elongation cycle, although no detached structures were registered by the LSDS in these cycles. Two possible reasons are given here: either the detached particle structures must have been smaller than the lower detection limit (90 μm) of LSDS or the fiber including the particle structure did not rotate back to the initial position and projection size within the field of view.

Regardless the applied superficial velocity in the experiment with low particle fiber loading, the cumulative fraction of detached particles is increasing less steep than with higher particle loading.

As shown in the Figure 5.7 (BOTTOM) the standard deviation of the fraction is re-

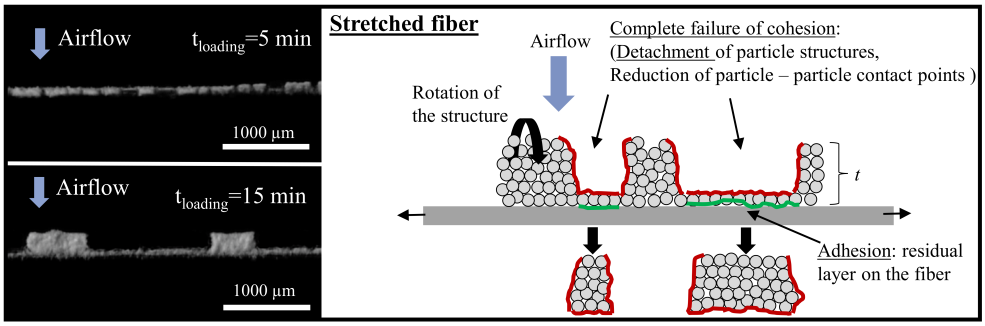


Figure 5.9: *(**LEFT**): Images (side view) of the loaded fiber after 5 min loading time (TOP) and after 15 min loading time (BOTTOM) at 20 % fiber elongation during the second stretching cycle. Same elongation velocity of 0.6 mm s^{-1}. Illumination of structure from the front. (**RIGHT**): Schematic of the loaded fiber in the stretched state. Marked the physical state at the interfacial layer.*

duced by increasing the superficial velocity from 0.05 $m\,s^{-1}$ to 0.8 $m\,s^{-1}$.

The experiments demonstrate that large particle structures are more likely to detach earlier during the elongation process with the same applied process conditions. As a proposal for a potential complete stretchable filter system, it can be beneficial to separate a high amount of particulate material in the filter before the start of the stretching process. For detachment of particle structures from a fiber with a low particle loading, multiple elongation cycles are required to achieve the same level of particle detachment from the fiber. This fact can be transferred to a complete filter system. The influence of neighboring fibers in a fiber array or a total filter has not been clarified yet.

Figure 5.9 (LEFT) shows the continued stretching procedure with proceed crack formation and first void spaces due to detachment of particle structures from the fiber. In addition, a rotation of the remaining particle structures on the fiber is observed. As in Figures 5.3 and 5.8, a fiber with low and high particle loading are depicted. Figure 5.9 (RIGHT) shows a schematic of the fiber in the stretched state and the interfacial layer between the fiber and the particulate structure. As depicted in the images, a residual layer of particulate material is marked at the position of void spaces where structures detached. A complete failure of cohesion within the structure results in detachment of particle structures. Adhesion between the lowest layer of the particle structure and the fiber maintains mostly in the first stretching cycles. This could lead to information about the magnitude between cohesion and adhesion forces of the particle structure on the fiber. Repeated elongation of the fiber outcomes in application of shear stress, which increases the chance for detachment of particle structures.

5.3.2 Influence of Elongation Velocity

The influence of the elongation velocity on particle structure detachment was investigated in more detail by applying two more elongation velocities, namely 1.2 $mm\,s^{-1}$ and 12 $mm\,s^{-1}$. The elongation velocity of 12 $mm\,s^{-1}$ represents the maximum elonga-

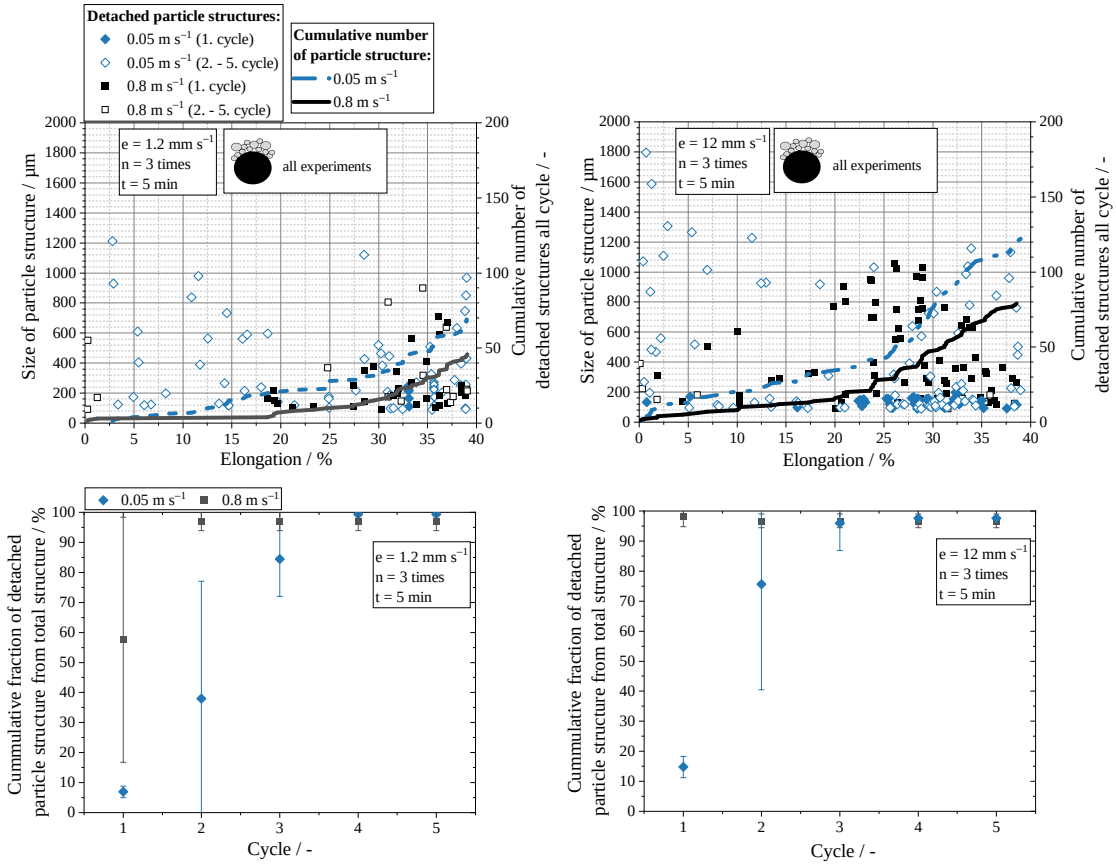


Figure 5.10: *(**TOP**) Size and cumulative number of detached particle structures measured with the LSDS during the 5 cycles of fiber stretching. Comparing two different elongation velocities (1.2 mm s^{-1}, left; 12 mm s^{-1}, right) for two different superficial velocities during the stretching procedure (0.8 m s^{-1} and 0.05 m s^{-1}, respectively). (**BOTTOM**) Cumulative fraction of the detached particle structures from total particle structure.*

tion velocity of the setup. As in Section 5.3.1, the set of superficial velocities remained constant at 0.05 m s^{-1} and 0.8 m s^{-1}, respectively. As in the previous Section 5.3.1, a compact particle structure was deposited on the stretchable fiber. All experiments (in Figure 5.10) were conducted with a low particle load on the fiber (5 min) to probe the effect of external excitation at the beginning of the transition phase with a low particle structure on the fiber. The size of detached particle structures was determined using LSDS. The corresponding elongation is shown on the x-axis to provide comparability between experiments with different elongation velocities. The cumulative fraction of detached particle structure was analyzed via image analysis after each finished stretching cycle.

Figure 5.10 (TOP, LEFT and RIGHT) shows the measured size of the detached particle structures in the experiments with an elongation velocity of 1.2 mm s^{-1} and 12 mm s^{-1}, respectively. As shown in the diagrams, the number of detached particle structures during the first stretching cycle is increasing with the increase of the

elongation velocity. Comparing to the results with the lowest elongation velocity of $0.6\,mm\,s^{-1}$ (see Figure 5.7) this trend becomes even more clearly. Focusing on all experiments with a superficial velocity of $0.8\,m\,s^{-1}$, early detachment of structures during the first stretching cycle appears in the experiment with an elongation velocity of $1.2\,mm\,s^{-1}$. The tenfold increase in elongation velocity reinforces this trend. Due to the increase of the aspired elongation velocity, the acceleration of the motors for fiber elongation increases. This results in larger shear stress between the fiber and the particle structure on the fiber. As a consequence the cohesive bonds within the structure on the fiber dissolve as shown in Figures 5.8 and 5.9.

By increasing the elongation velocity, a slight increase in the size of the detached structures is also noticeable. Moreover, a shift of the moment for first detachment to lower fiber elongation by increasing the elongation velocity is clearly visible. This is due to the velocity of crack formation which is increased by the elongation velocity.

As shown in Figure 5.10 (TOP) the actual elongation when the first particle structures detach from the fiber is reduced from 18% to 2% fiber elongation. For an elongation velocity of $0.6\,mm\,s^{-1}$, no detachment at all is detected during the first cycle. For experiments with a superficial velocity of $0.05\,m\ s^{-1}$ this trend is less noticeable for structure detachment during the first cycle. However, a shift towards lower fiber elongation is visible during 2nd to 5th cycle detachment. The main range of elongation for detachment is shifted from 5-20 % to 0-10% in these experiments by increasing the elongation velocity. As shown in the experiments the increase in elongation velocity enables detachment at lower elongation of the fiber. Thus, in a potential stretchable filter system less space is needed at a constant filtration velocity.

Comparing the mean size of detached particle structures during the first stretching cycle between the experiments with $0.05\,m\,s^{-1}$ and $0.8\,m\ s^{-1}$, respectively (see Figure 5.10), the detected size of structures in experiments with $0.8\,m\,s^{-1}$ is always larger than with a superficial velocity of $0.05\,m\,s^{-1}$. A high drag force at the particulate structure can overrule the cohesion within the structure during stretching process. Comparing to Ibrahim et al., with external excitation (here stretching) detachment of glass particle structures smaller than $100\,\mu m$ was observed at flow velocities of $0.05\,mm\,s^{-1}$ [49].

Evaluating the size of the detached structures in the 2nd to 5th stretching cycle and the same elongation velocity, this trend is reversed, and detached structures become smaller with increasing superficial velocity. The detached structures in these stretching cycles could be structures that remained on the fiber after the first detachment of big structures. For a potential total filter system this might result in particle structures that do not move into downstream layers, but remain on the surface or at the raw gas side of the filter.

Figure 5.10 (BOTTOM, RIGHT and LEFT) depicts the cumulative fraction of detached particle structure as a function of the number of stretching cycle for the experiments with an elongation velocity of $1.2\,mm\,s^{-1}$ and $12\,mm\ s^{-1}$, respectively. The superficial velocity remained constant at $0.05\,m\,s^{-1}$. Compared to the experiments with

low elongation velocity (0.6 $mm\ s^{-1}$, see Figure 5.7 (BOTTOM)), the cumulative fraction of detached particulate structure increases in each stretching cycle if the elongation velocity rises to 1.2 mm s^{-1} and to 12 $mm\,s^{-1}$, respectively. For high superficial velocities, this trend (0.8 $m\,s^{-1}$) is valid for all cycles including the first elongation cycle. For lower superficial velocities, this increase is more pronounced for the subsequent 2nd-5th cycle.

Considering the experiments with a superficial velocity of 0.05 $m\,s^{-1}$, the number of stretching cycles that are necessary for complete detachment of the initial particle structure is reduced by the increase of elongation velocity. This trend is also observed in the experiments with a superficial flow velocity of 0.8 $m\,s^{-1}$. A reason for this enhanced detachment of particle structure is the accelerated crack building due to higher shear stress which results in more energy at the crack tips [93]. The crack formation causes weakening of the structure by reducing cohesive bond between particle structures on the fiber. If the applied drag force remains the constant, particle structures detach more likely.

5.3.3 Development of Structure Size

Besides the initial height of the particle structure on the fiber, the applied process parameters as elongation velocity of the fiber and superficial velocity during the fiber stretching procedure have an influence on the rearrangement and detachment process. For a rough estimation of the released particulate material that can be transported into downstream layers, the size of detached particle structures is measured immediately after detachment from one single fiber. In the following, the $d_{50,0}$-values (hollow symbols) and the $d_{90,0}$-values (filled symbols) are shown as characteristic values for the entire Q_0-distribution of the detached particle structures. The characteristic values are defined as the particle size below 50 % or 90 % of the remaining number based particle distribution is placed.

The data in Figure 5.11 underlines the trends in structure size caused by varying the process parameters. The complete Q_0-distributions of all experiments are given in the supplementary data. Figure 5.11 (LEFT) shows the measured size of particle structure as a function of the applied elongation velocity. Linear fits for the $d_{90,0}$-values were calculated. For the experiment with a low particle loading on the fiber with an increase of elongation velocity the $d_{90,0}$-values are increased. This clear trend is given for a small increase of elongation velocity from 0.6 $mm\,s^{-1}$ to 1.2 $mm\,s^{-1}$ and for a much bigger increase from 1.2 $mm\,s^{-1}$ to 12 $mm\,s^{-1}$. The largest increase of $d_{90,0}$ is observed in the experiment with a superficial velocity of 0.8 $m\,s^{-1}$. The smallest reduction occurs at a flow velocity of 0.05 $m\,s^{-1}$. A high elongation velocity favors fast emerging of cracks within the particle structure on the fiber due to the high energy at the tip of cracks. The stress for formation of cracks is induced by the acceleration of substrate (see Figure 5.8 and Figure 5.9). In combination with a high drag force on the agglomerates due to the higher flow, large structures detach earlier during the stretching cycle. [94]

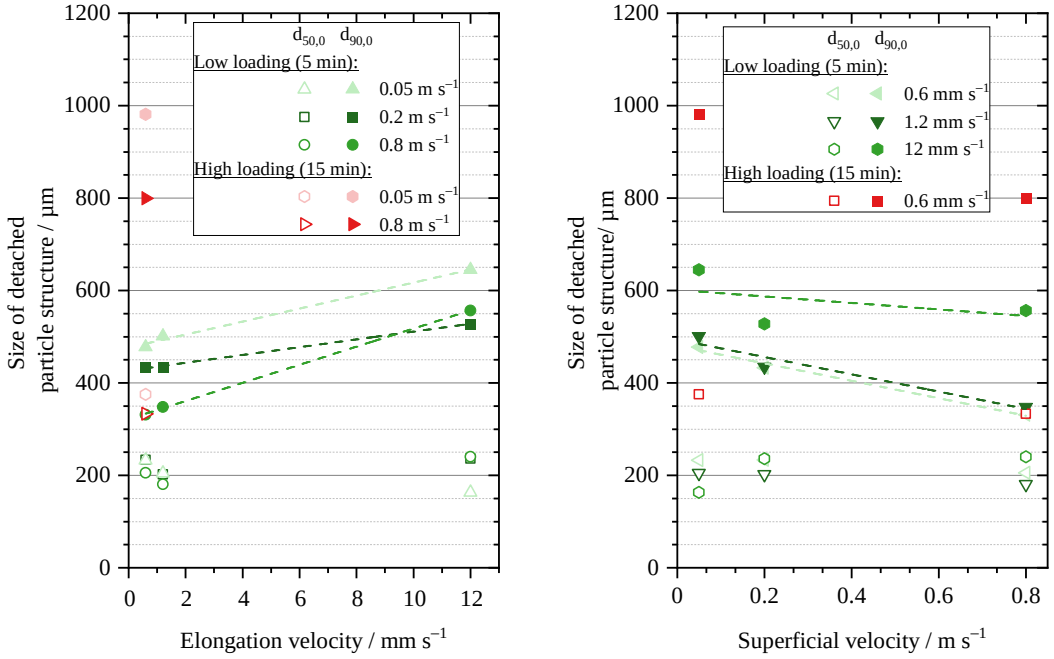


Figure 5.11: *$d_{50,0}$ and $d_{90,0}$ values of detached particle structures as function of elongation velocity (LEFT) and superficial velocity (RIGHT). All structures detached within 5 cycles of fiber stretching with the given parameters. Linear fits of the development of $d_{90,0}$ values.*

The $d_{50,0}$-value is slightly decreasing with increasing elongation velocity from $0.6\,mm\,s^{-1}$ to $1.2\,mm\,s^{-1}$ for all three values of superficial flow velocity. In the Q_0-distributions (see supplementary data) of the corresponding experiments, this can be observed by a constant trend in the region below the 50 % value. For the experiments with a high particle structure on the fiber, the characteristic structure sizes extracted from the Q_0-distribution are larger than in the experiments with an low loading on the fiber. One reason for this is that the total height of the structure which is larger than with a low loading on the fiber (see Figure 5.8). However, as visible on the images, the average length l between the cracks of the high structures is larger than with a small structure on the fiber. This is based on the height on the matrix (particulate structure) on the stretchable substrate (fiber). A change of structure size as a function of elongation velocity is not detected yet for high structure on the fiber at the beginning of the experiment.

Figure 5.11 (RIGHT) shows the measured size values as a function of applied superficial velocity during the fiber stretching experiment. As mentioned before, the number median values $d_{50,0}$ do not differ much regardless the superficial velocity, except for the values for an elongation velocity of $12\,mm\ s^{-1}$, where a slight increase of the flow velocity is observed. The $d_{50,0}$ values are mainly below $250\,\mu m$, so agglomerates

of this size could pass through a fiber gap, which has a size 3-times the fiber diameter. The values of $d_{90,0}$ are decreasing with increasing superficial velocity for the experiments with low elongation velocities of 0.6 $mm\ s^{-1}$ and 1.2 $mm\ s^{-1}$, respectively. For the $d_{90,0}$-value of the experiments with an elongation velocity of 12 $mm\ s^{-1}$ this trend is not visible for the highest flow velocity in the experiments. Furthermore, the difference between the $d_{90,0}$-values for the experiments with 0.6 $mm\ s^{-1}$ and 1.2 $mm\ s^{-1}$ is very small. This fact proposes that the influence of elongation velocity on size of detached structures is less pronounced. Nevertheless, there is a clear impact on the timing for detachment, which was revealed in Sections 5.3.1 and 5.3.2.
In total, the size recordings show a clear trend for the experiments including the different elongation velocities and flow velocities. The largest detached structures are found in the experiments with low flow velocities and high elongation velocities. In addition to this, the structures at the mentioned range of settings already detach during low fiber elongations. As a consequence, little installation space is needed for a potential filter system.
However, due to the fiber distance, which has been mentioned in Section 5.1, some of the particle structures might be to large to pass through gaps between fibers. As a result, the structures might re-arrange on the filter surface in the area of raw gas.

5.4 Conclusions and Outlook

In this study, a detailed view on the influence of process parameters such as particle loading time of the fiber (height of particle structure), elongation velocity and superficial velocity on the detachment behavior of particle structures is shown. In detail, the size of the structures and the time of detachment from an elastic fiber are of interest, whether the particles are able to pass between fibers into the lower layers of the filter.

For the first time a measurement technique for online characterization of the detached particle structures during the entire stretching process of a loaded stretchable single fiber was constructed. Furthermore, a developed method to characterize the fiber loading by image analysis during five consecutive stretching cycle was applied. The size of the detached structures was measured using a laser sheet technique, which also provides information on the respective point in time of the detachment. The fiber loading time was varied between 5 min and 15 min. The elongation velocity and the superficial velocity were systematically varied between 0.6-12 $mm\ s^{-1}$ and (0.05-0.8 $m\ s^{-1}$). The main results are:

- The application of multiple excitation cycle induces shear stress multiple times to the particle structure therefore enables complete detachment of the huge and compact particle structure from the stretchable filter fiber at low gas flow velocities of 0.05 $m\ s^{-1}$.
- High initial particle loading (15 min) on the fiber induces detachment of larger particle structures from the fiber than for small initial particle loading (5 min)

due to development of larger crack distances l during the stretching procedure and more particulate material on the fiber. The detected particle structures will be able to pass gaps between fibers in a total fibrous filter.

- For high initial particle loading on the fiber, the detachment of structures starts at lower fiber elongation than for small particle structures on the fiber, regardless the superficial velocity. This fact suggests with a higher loading within the total filter, less stretching distance is required for the same detachment success.
- For small initial structures on the fiber, an increase in elongation velocity causes earlier detachment of particle fragments during the first and the 2nd-5th stretching cycle due to faster development of cracks within the particulate structure.
- Detachment of particle structures occurs more likely after failure of cohesion A small residual layer of particles remains on the fiber after the first stretching cycle due to adhesion.
- The number of required stretching cycles for "complete detachment" is reduced by the increase of the elongation velocity.
- The combination of low elongation velocity and low superficial velocity favours detachment of small particle structures from the fiber that can move into downstream layers of a potential filter.
- For the experiments with an elongation velocity of $0.6\,mm\,s^{-1}$ and a small initial structure on the fiber, detachment only is detected in the 2nd-5th cycle, regardless of the superficial velocity.
- Regardless the superficial velocity during the fiber stretching procedure, the size of $d_{90,0}$ is increased by an increase of elongation velocity.
- With an external excitation, detachment of glass particle structures smaller than $100\,\mu$m are observed at flow velocities of $0.05\,m\ s^{-1}$.
- Detachment of particle structures (piles of particles) is initiated at a superficial velocity below $1.2\,m\,s^{-1}$ due to the multiple external excitation (fiber stretching) which causes emerging cracks and the break up of the initial structure on the fiber.
- Detachment of particle fragments is increased due to external excitation within the range of operation filtration velocity. The size of detached structures presumes that detachment within a filter is possible, but probably no penetration through the entire filter will occur.

Based on these findings, investigations on the detachment behavior of particle structures from a loaded fiber array during stretching and simultaneous flow will be

carried out in the future. Online observations of the loading procedure and the detachment of particle structure from the fiber array during the elongation are pending. A more detailed investigation of the adhesion and cohesion forces between fiber and particles is planned to gain more knowledge about the magnitude of these forces. Furthermore, clogging effects (bridging effects) during the loading procedure of a parallel fiber array will be investigated. The application of elastic fibers in filter media is an initiator for adaptive filter systems in the future.

Author Contributions: Conceptualization, A.D., J.M. and L.P.; methodology, L.P.; software, L.P.; validation, A.D. and J.M.; formal analysis, L.P.; investigation, A.D.; resources, A.D.; data curation, L.P.; writing—review and editing, A.D., J.M. and L.P.; visualization, L.P.; supervision, A.D. and J.M.; project administration, A.D. and J.M.; funding acquisition, A.D. All authors have read and agreed to the published version of the manuscript.

Funding: We gratefully acknowledge that this project was funded by the Deutsche Forschungsgemeinschaft (DFG, German Research Foundation) – 427981860.

Data availability: Poggemann, Lukas (2022), “Detachment of Particle Structures From a Stretchable Single Fiber During Multiple Consecutive Stretching Cycles”, Mendeley Data, V1, doi:10.17632/242dvfx9h8.1

Acknowledgments: We kindly thank Freudenberg Filtration Technologies SE & Co. KG for donating fiber material to this research. We also kindly thank Friedhelm Klingel for his expertise and help in designing the optical system of the laser light sheet technique.

Conflicts of interest: The authors follow no commercial interest with this study.

6

Morphology of particulate structures on a fiber array before and at clogging point in gas-particle-filtration process

Title: Morphology of Particulate Structures on a Fiber Array before and at Clogging Point of an Aerosol Filtration Process
Authors: Poggemann, Lukas; King, Benedikt; Meyer, Jörg; Dittler, Achim
Status: Published
Bibliographic data: Separations 2023, 10, 462.
https://doi.org/10.3390/separations10090462

Copyright in Separations 2023, published by Multidisciplinary Digital Publishing Institute. Reprint with permission. The text has been adapted in this thesis to change the citation and figure numbering. Additionally, some symbols have been modified to confirm with the other chapters.

Abstract
Fundamental microscopic investigations are based on the interaction between filter fiber and particles. The fibrous filter theory is based on a single fiber of a fiber array, and experiments focus either on a single fiber or a fiber array. This study investigates the particle loading process of a fiber array and focuses on the microscopic development of particle structures on the fiber array. Gravimetric measurements and image analysis of the array were used to study the development of the particle structure and morphology. Microscopic analysis of the video data focused on the evolution of particle accumulation within the fiber spacing, the development of boundary lines of the particle structure, and the number/size of bridges and pores within the particle structure. For the tested flow velocities, an increase in mass was observed to increase

the duration of the filtration process. An extreme increase in deposited mass was observed at the moment of complete blocking (clogging) of the fiber spacing at flow velocities of $0.65\,m\,s^{-1}$. The size of pores (hydraulic diameter) increased with the flow velocity during the loading procedure. However, the total number of pores was higher in tests with lower Stokes numbers due to the dendritic and more porous structure. This work provides insights into the growth kinetics and structural setup of the particle structure (on a microscopic level). This will improve the understanding of the change of the filtration process from the transition phase to the clogging phase in fibrous filters.

6.1 Introduction

Fibrous filters are applied for various purposes, including the removal of particles from gases in process plants or maintaining the safe air quality of air-conditioning systems. The behavior of pressure drop, separation efficiency, and total loading capacity is critical for characterizing a filtration process with depth filters and the filter lifetime. The characteristic trend of the pressure drop can be divided into three stages during the filtration process. Filter hardware parameters that affect the duration of these stages include the porosity of the filter medium in the initial state (fiber diameter and spacing) and the thickness of the filter medium. The characteristics of the concentration of aerosol, such as particle size/distribution, particle material density, aerosol flow velocity, and viscosity of the continuous phase, also play a role in influencing the different stages of the pressure drop. The pressure drop across the filter is caused by the clogging of particulate material in the unobstructed area between the fibers. The kinetics of the clogging process, which is dependent on the morphology of the particle structure, directly affects the development of the pressure drop. The morphology of particle structures within a filter may vary with the applied filtration parameter. At the beginning of the filtration process, a unique particle structure forms on each individual fiber. Later on, structures on neighboring fibers may interact and even merge.

In the initial phase of filtration, particles are deposited on the unoccupied fibers of the filter, resulting in a slow increase in pressure drop with the deposited mass. The progression of the pressure drop in the depth filtration phase and subsequent phases is shown in Figure 6.1 on the left. If the particle size and density are constant, the morphology of the particle structure on each fiber is primarily influenced by the flow velocity. Figure 6.1 right (a) illustrates the deposition process on the unoccupied fibers during this first phase, assuming a constant density and size of the particles. In the second phase (Figure 6.1 right (b)), particles continue to separate on already existing structures, causing changes in the flow field around the fibers. The previously deposited structures reduce the free space between fibers, resulting in an increase in pressure drop [152, 67]. This non-linear increase in pressure drop is visible in the transition phase in Figure 6.1 on the left.

Particle structures built at positions on the fiber with a large angle to the stagnation

point are more likely to grow into the fiber spacing. As shown by Kanaoka et al., Müller et al., and Zoller et al., a dendritic type of structure develops at low Stokes numbers [65, 92, 180]. Structures deposited by inertia when flow stagnates may also grow into the spacings.

In addition to the increase in pressure drop in the second stage (transition phase), the area for separation at the collector increases, too. The transition stage is between the depth filtration stage and the subsequent surface phase.

In the third phase (surface filter phase), the particles start to build a filter cake on the surface of the filter (see Figure 6.1 right (c)). The pressure drop increases proportionally to the deposited particle mass and filtration time (see Figure 6.1 left) [56, 152, 14]. The deposition of particles on the filter surface comes along with a complete closing (clogging) of fiber interspaces. This produces a gradient in the deposited mass along the filter depth because further particulate material cannot travel deeper/downstream into void filter layers [45].

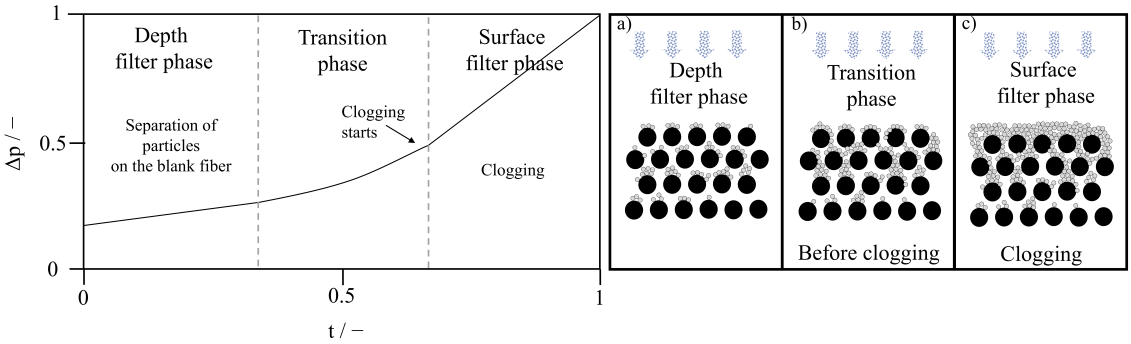


Figure 6.1: *LEFT: Pressure drop as a function of particle mass during the filtration time. RIGHT: Schematic of the filtration phases during a depth filtration process. a) Depth filter phase, b) Transition phase, c) Surface filter phase.*

A possible solution to open closed interspaces within a filter is to introduce stress into the separated particulate material by stretching the filter matrix. Previous studies have shown that particles can be detached by vibration or magnetic excitation of the collector [110, 156]. Experiments with a single fiber collector have demonstrated that stretching up to 39% can initiate the re-arrangement and detachment of particle structures from the surface of the collector [106, 107]. During stretching, the elongation of the substrate generates shear and tensile stresses within the particle structure, resulting in cracking and a reduction of contact points that weakens the particle structure. As the polymer substrate is stretched, the fiber's surface changes, reducing the adhesion forces between individual particles and the fiber [108]. In experiments with a single fiber, only one-dimensional stress states have been investigated so far. Stretching of arrays of stretchable fibers is expected to result in a multiple stress state. However, to ensure the best knowledge about the initial state of the particle structure on the array, it is necessary to generate and characterize particle structures of different mor-

phologies before the stretching experiments. Furthermore, it is crucial to understand the detailed development of structure morphology on the collector before and at the Clopgging Point (CP), which is the primary cause of pressure drop and filter cake formation. While pressure drop analysis is often sufficient to evaluate the performance of the filtration system, it is important to recognize the role of particle structure development on the collectors and its influence on pressure drop development. In addition, understanding the timing and conditions under which particle structures build up, as well as their stability and fragility during tests (before or at the clogging point), is important when applying shear stress to detach structures. As previously mentioned, the clogging point represents a changing point where the structures in the filter close upstream pores, and the structure may change. Consequently, this study investigates the evolution of various particle structures on a fiber array. The fibers have a defined spacing representing a simplified version of the overall filter system, similar to the studies by Müller et al. [137, 91].

Clogging Point and Characteristic Morphology of Structures on a Collector

Clogging of particulate material on or in a collector matrix occurs when the continuous accumulation of particle mass causes a transition from depth filtration to surface filtration [54]. This transition point, also known as the upper transition point, is the point at which the pressure loss vs. mass curve returns to a linear slope [152]. Alternatively, it may be identified as the intersection of tangents at the beginning (depth filter phase) and during the surface filter phase [55]. ASHRAE 52-76 defines the clogging point as the point where mass accumulation occurs at the end of the pressure drop curve [5]. Kanaoka et al. describe the clogging point where particles start to separate on the filter cake or by particles that have already been separated, resulting in a continuous linear increase in pressure drop across the filter [67]. DEM simulations have shown closure of spaces between fibers starts in the transition phase and is completed by the end of this phase [151]. Similarly, Valdes et al. demonstrated that there is a critical gap distance for bridge formation, above which a bridge is well-formed and difficult to dissolve. They used the force chain model to describe the forces of particle contacts [160]. Some studies refer to the second phase as the clogging phase, representing the change from depth filtration to surface filtration. Zhang et al. note the lack of a clear definition of the clogging point with regard to particle separation on the collector [173].

The velocity rate for the filling of fiber interspaces during the filtration process is a function of the development of morphology of the particle structure on the collector, which is influenced by the applied process conditions [65]. The pressure drop is a function of the unobstructed area in the filter.

A lateral dendritic structure on the fibers promotes the formation and merging of numerous small bridges in the interspaces of the fiber, while a compact structure is likely to grow in the direction of flow and may never merge with neighboring particle structures. Tao et al. investigated this angle-dependent behavior in their calculations

[151]. To consider these effects, dendritic structures, structures in transitional state, and pure compact morphologies are examined in this study.

To understand the deposition process of particles in a complete filter, investigations and observations on a single fiber or a fiber array are a common research method in the field of depth filtration [139, 92]. Hardly any studies in the literature have been published on the particulate accumulation process prior to and during clogging at a single fiber array containing polydisperse materials. Previous studies focused on the overall filtration performance in a complete filter [25, 59, 118, 77, 47]. To conduct these observations, the focus should shift from a whole filter medium to a fiber array or a single fiber collector, as Zhang et al. suggested [173]. Particle separation on the microscopic level can be observed and quantified better in these arrangements. An interesting aspect on the microscopic level is the evolution of the number and size of individual pores and bridges as a function of the morphology within a certain range of Stokes numbers (0.52–10.05). Further aspects for research are the development kinetics of single structures and their shape and appearance on the fiber array.

6.2 Experimental Methods

6.2.1 Fiber Array and Particulate Material

In previous investigations, experiments concerning the behavior of separation and detachment were conducted on a single fiber [106, 107]. To investigate the influence of the neighboring fibers as in a real filter medium, in this paper, all experiments were performed on an array consisting of five equally spaced parallel fibers in a plane perpendicular to the flow. For uniform spacing of the fibers, they were tightly clamped in combs with a spacing (center-to-center) of exactly 246 μm [91]. The fibers were made of polyurethane and had a diameter of 82 μm. The material composition enabled reversible stretching up to 75% [106]. Prior to clamping, the fibers were in a crimped state. Figure 6.2 depicts the clamping device with the five parallel fibers. The fibers had a clamped length of 53 mm. Before each gravimetric detection of the collected mass and growth analysis, the fiber clamping device was cleaned with isopropanol and compressed air to obtain a blank mass for each test. Any contamination by fat or particulate material was avoided.

The fibers were loaded with polydisperse and inert particle material (Spheriglass 5000CP00, soda lime A-glass). The $d_{50,3} = 7.73$ μm of the distribution were used to calculate the characteristic Stokes, Péclet, and Reynolds numbers and the interception parameter. The particulate material had a material density and a bulk density ($\rho_{material} = 2.46\,\mathrm{g\,cm^{-3}}$, $\rho_{bulk} = 1.28\,\mathrm{g\,cm^{-3}}$, $n_{refractive\,index} = 1.51$) and was obtained from Potters Industry [106].

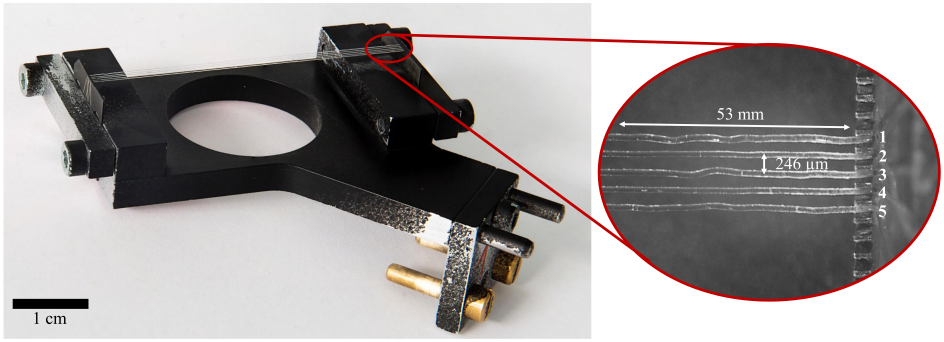


Figure 6.2: *Fiber clamping device with five fibers. Enlarged view on the right: The fibers fixed to the comb have a spacing of 246 µm [90].*

6.2.2 Particulate Loading and Gravimetric Measurements of Particle Structure on the Fiber Array

The particle loading process of the array was performed in a 16 mm free jet airflow at different flow velocities.

Figure 6.3 shows the flow diagram of the loading procedure. The aerosol with a volume flow of 26.3 L min^{-1} (feed flow) was generated with the SAG 410/U by Topas, which was already used in the studies of Zoller et al., Wang et al., and Papapostolou et al. [161, 98, 180]. Particle dispersion is achieved by sucking the particulate material from a steel ring using a venturi nozzle. Any interruptions or irregularities in the particle loading of the ring can lead to irregular dispersion. Because of that, continuous monitoring and a constant scraper height are necessary. Further, the aerosol is neutralized using an ^{85}Kr-neutralizer.

A loading flow was discharged from the feed flow. The rest of the feed flow was drained off as an excess flow. The particulate material was removed by a HEPA filter. The loading flow was directed through the inlet pipe, which includes a flow rectifier (diameter 16 mm), and passed into the loading chamber where it approached the array. The camera and optical equipment were positioned at the top of the inlet pipe, where an air junction provided optical access for observation (see Figure 6.3). Downstream of the fiber array, an HEPA filter was used to remove the remaining particulate material. The loading flow rate was controlled using a MFC.

Table 6.1 shows the volume flow of the corresponding airflow velocity, the characteristic numbers Reynolds Re, Stokes St, Péclet Pe, the interception parameter R, and the bounce parameter β. The particle bounce parameter β introduced by Kasper et al. is proportional to the ratio of Stokes St and interception parameter R for a constant combination of materials (see Equation (6.1)). The calculation of the onset of the bounce of particles is based on the diameter of the particle d (in μm) and the velocity of air flow u (in $m\,s^{-1}$). The parameter enables a categorization of the morphology of particle structures (consisting of monodisperse particles) on the fiber [70]. A description of this relationship has also been shown by Hiller et al. and Brach and Dunn [42,

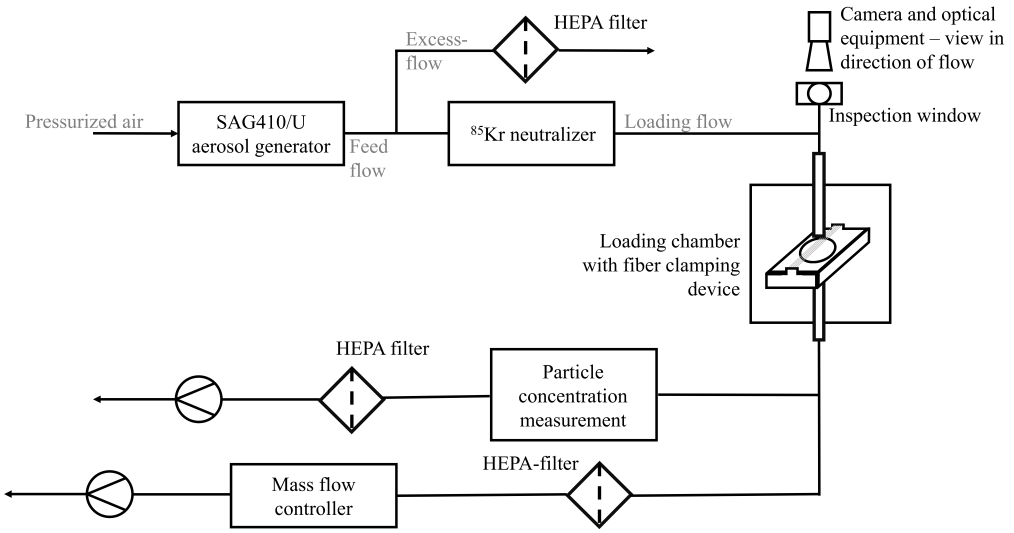


Figure 6.3: *Process flow diagram of the array loading procedure, including the optical equipment at the top of the inlet pipe for the observation of the clogging process on the fiber array.*

15].

$$\frac{St}{R} = \beta \frac{\rho_{material}}{18\mu} \tag{6.1}$$

$$\beta = d \cdot u \tag{6.2}$$

To compare experiments with different airflow velocities, a characteristic Time integrated flow (TIF) is defined, which serves as the independent variable, describing the evolution of the fiber loading process. This enables comparison of experiments with different particle concentrations and airflow velocities.

To calculate the TIF for the respective airflow velocity, the particle number concentration was measured at different airflow rates and particle feed rates in the loading chamber using an Optical particle counter (OPC). The particle flux density j is determined from the particle concentration c_p and the mean airflow velocity u.

$$j = c_p \cdot u \tag{6.3}$$

The time-integrated flux density TIF in particles per mm^2 can be obtained by combining the particle flux density j with the respective loading time t for a specific time interval.

$$TIF = J(t) = \int_0^t j \, dt \tag{6.4}$$

For a constant j:

Table 6.1: *Characteristic numbers for the tested flow velocities.*

Flow Velocity u /$m\,\mathrm{s}^{-1}$	Volume Rate (Loading Flow) /$\mathrm{L}\cdot\mathrm{min}^{-1}$	Re/-	Stokes St/-	Pe/-	R/-	β/-
0.1	1.21	0.54	0.51	2.72×10^{6}	0.09	0.773
0.15	1.76	0.78	0.82	3.97×10^{6}	0.09	1.12858
0.25	3.05	1.35	1.30	6.88×10^{6}	0.09	0.95569
0.65	7.84	3.48	3.62	1.77×10^{7}	0.09	5.0245
1.2	14.48	6.42	6.70	3.26×10^{7}	0.09	9.276
1.8	21.71	9.63	10.05	4.90×10^{7}	0.09	13.914

$$TIF = J(t) = j \cdot t \tag{6.5}$$

Gravimetric methods were used to measure particle accumulation on the fiber array directly after the experiments. The clamping device and fibers (including particulate material) were weighed after the loading process using a METTLER TOLEDO XR205DU balance (0.01 mg readability; 81 g capacity). Before weighing, the mass of separated particulate material on the fiber array, the surface of the fiber clamping device was cleaned with a cotton pad. Two replica tests per airflow velocity were conducted. After the weighing procedure of the loaded fiber array, the complete fiber clamping device and the fiber array were cleaned and reinstalled in the loading chamber for a new experiment.

6.2.3 In Situ Observation of Particulate Structure Development

To quantify the progress of the loading process and the associated formation of pores, it was necessary to observe the array through an inspection glass in the direction of aerosol flow as described in Section 6.2.2. The whole loading process was recorded by video. A Basler acA4024 29uc USB 3.0 camera and Navitar lens system (1-6010, 1-6020, 1-50330, 1-50011) were used to observe the accumulation process of particulate material on the fiber array. The camera had a resolution of 4024 × 3036 pixels, and the optical equipment provided a working distance of 341 mm with a magnification of 3.5. The observation was conducted in the direction of flow. During all experiments, a video was recorded at a frame rate of 4 frames per second, and the observation area covered a total length of 16 mm of the fiber.

The recorded video was analyzed using a MATLAB procedure. A complete progress diagram of the MATLAB program can be found in Support Material.

As observations took place in the direction of flow, parameters on the horizontal level were detected only. The MATLAB analysis was performed in the central section of the recorded fiber length at 5.8 mm. Image processing provided information about the image scale and the average spacing of the fibers. For the characterization of the morphology of the particle structure, the following parameters were recorded:

- Particulate mass on the whole fiber array and relative projection area of the particulate material in the spacing between the fibers (accumulation of particulate material on the whole fiber array and in the spacing between the fibers; see Figure 6.4);
- Length of borderline (see Figure 6.5);
- Number and size of bridges;
- Number and size of pores.

6.2.3.1 Accumulation of particulate material

Figure 6.4 (top) shows images of the non-loaded fiber array at the beginning of the experiment (left) and loaded fiber array at the end of the experiment (right). The MATLAB-processed images are presented below. As filling of the inner fiber spaces only was considered, the non-shaded areas were used for analysis.

In the left image, the free space between the fibers is marked red. In the right image, the particulate material in the free-space area is marked bluish/turquoise. The fraction of those marked areas describes the ratio between the area coated/occupied by accumulated particulate material in the fiber spacing at time i (Figure 6.4, turquoise) and the uncoated area. This parameter (relative accumulated particulate material in the spacing between the fiber; see Equation (6.6)) is a measure of the degree of openness of the fibrous structure. Thus, the fraction of accumulated particulate material is 0 at the beginning of the experiment and approaches 1 as the (complete) accumulation of particle material in the interspaces increases (see Equation (6.6)).

$$\frac{\text{Area particulate material between the fibers at time } i}{\text{Free space at the beginning of the experiment}} = \text{Relative accumulated particulate material in the spacing between the fibers} \tag{6.6}$$

6.2.3.2 Borderline

The length of the borderline is given by the summarized pixels at the border between the particulate structure and an open space between the fibers. Its length depends

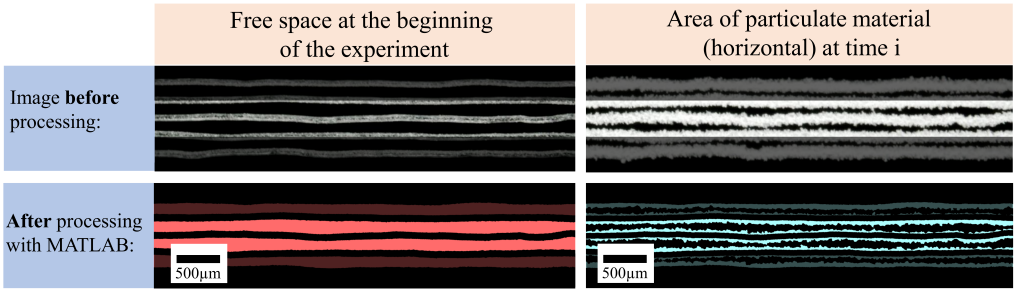


Figure 6.4: *Images of the non-loaded and loaded fiber before (**top**) and after processing (**bottom**) with MATLAB. (**right**) The free space is marked red. (**left**) The accumulated particle material in the spacing is marked turquoise.*

on the shape of the particulate structure on the fiber array. The structure of particle loading is between compact and dendritic. For a dendritic structure, a ragged and long borderline is expected. For a compact structure, a short and straight borderline is expected. To classify the experiments, a quotient is calculated by dividing the length of the current borderline by the length of the borderline of the unloaded fibers. Figure 6.5 illustrates a section of the borderline of both an unloaded fiber (orange) and a fiber with a dendritic structure (white lines). Only the middle two fiber interspaces are considered for evaluations. The quotient is calculated from the colored lines, and if a dendritic structure is present as shown in the figure, the quotient is greater than 1. If the structure is more compact, the quotient is close to 1.

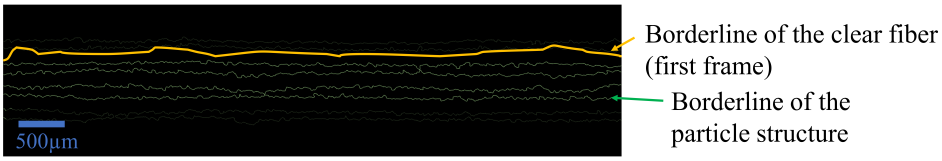


Figure 6.5: *Borderline of a loaded fiber after processing with MATLAB. The orange line symbolizes a single borderline of an unloaded fiber. bottom: Equation for the calculation of the ratio between the borderline of the particle structure to the borderline of the initial structure. Only the two inner fiber spacings are considered.*

$$\frac{\text{Current borderline of the particle structure}}{\text{Borderline of the clear fiber} \cdot 4} = \text{Relative length of borderline of the current particle structure compared to borderline of the clear fiber} \tag{6.7}$$

6.2.3.3 Pores and bridges

The left of Figure 6.6 depicts an original image of the loaded fiber array captured by the camera system. In the schematic representation on the right (processed with MATLAB) of this frame, the blue-purple object represents the fiber position at the start of the

experiment, which allows precise tracking of the growth of particulate material. The particulate material is marked white. The red objects are detected bridges. The black areas between the two bridges are identified to be pores.

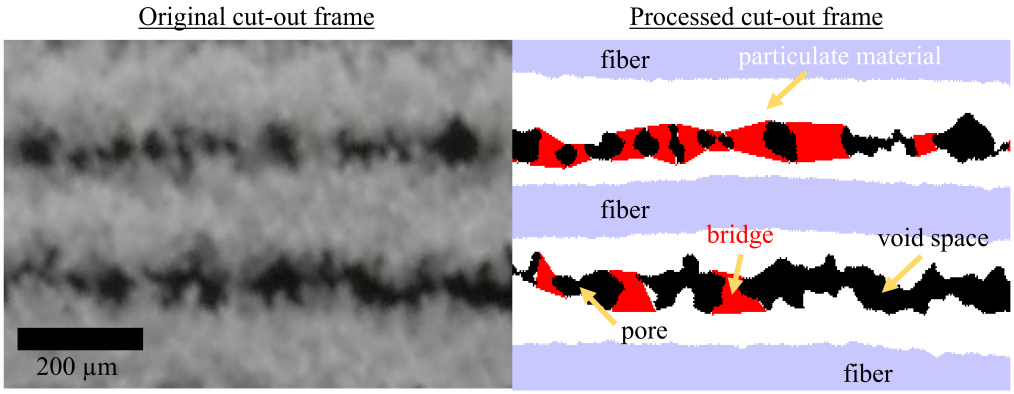


Figure 6.6: *(**left**) Cut-out of a frame—original image. (**right**) Cut-out of a frame/schematic with bridges (red) in the interspaces between the fibers. Particulate material is colored white. The fiber is purple.*

The two inner fiber spacings can be viewed as large pores without bridges. A pore is identified as a closed object (black) and can be characterized using the MATLAB function "regionprops", which gives the area A, perimeter P, diameter of the equivalent circle d_{equi}, and size in the direction of x and y x_i. The hydraulic diameter of the pores can be calculated using the area (A) and circumference (P) of the pore, as shown in Equation (6.8).

$$d_h = 4\frac{A}{P} \tag{6.8}$$

When bridges are formed, a pore is turned into two or more objects. This enables the detection of the number of bridges in the space between the fibers. The algorithm assumes that a bridge (red) has formed between two adjacent pores (black) and detects it accordingly.

The detection of the size of bridges between fibers of the array requires a more complex algorithm, since the edges of a bridge are not firmly fixed. The left side of one pore corresponds to the right side of a bridge. The variables x and y indicate the position in the image. To detect a bridge and determine its size, the left side of a single pore is approached and checked whether it meets the bridge requirement.

Figure 6.7 shows a bridge (black) and white-colored pores on the right and left sides. First, the left side of a pore (black object) is marked (indicated here by the red arrow). Then, starting from this position, the left side of the white pore is scanned upwards and downwards to check whether it meets the bridge requirement. If the difference $\Delta x = x(y-1) - x(y)$ is greater than 4 pixels (threshold), the coordinates x and $x(y)$ are saved as the upper right corner of the bridge. The same procedure is performed for all three remaining corners of the potential bridge. The found coordinates

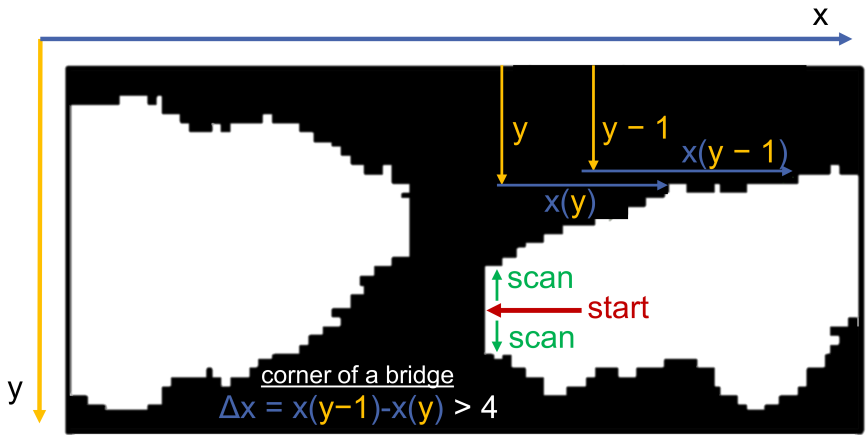


Figure 6.7: *Schematic detection procedure of a bridge within the emerging particle structure on the array. The bridges are formed in the interspace between two fibers. A bridge divides one pore into two pores.*

are connected and saved as the corners of the bridge. The area between the corners and the scanned edges gives the area of the bridge. If a bridge is located at the border of an image, the upper and lower borders of the nearest pore are drawn horizontally to the border of the image. The detected positions and sizes of bridges are saved in a separate black-and-white image. The "regionprops" function in MATLAB is used to process the numbers and horizontal sizes of the bridges.

6.3 Results and Discussion

6.3.1 Gravimetric Measurements of the Particulate Material

To characterize the deposited particle mass on the fibers, experiments were terminated at a pre-defined TIF. Subsequently, a gravimetric analysis was conducted. Then, a new experiment was started. Experiment times varied between 3 and 210 min, depending on the flow velocity and feed rate of the aerosol generator (see Section 6.2.2). All experiments shown were carried out with the aerosol generator described in Section 6.2.2, whose dispersion technology is based on VDI 491-3 and ISO 5011. Continuous control of the ring loading is intended to exclude the possibility of ring loading failure and thus inconstant dispersion conditions. Any deviations in the deposited mass can thus also be attributed to inconsistencies in the dispersion or to the occurrence of electrostatic effects, whereas the latter is counteracted by neutralizing the aerosol with an ^{85}Kr.

Gravimetric analysis of the particle material on the 16 mm long array (5 fibers) is presented in Figure 6.8. For experiments executed at a face velocity of 0.15 $m\,s^{-1}$, no deposition was detected below a TIF of 10^8 particles $\cdot$ mm^{-2}. Similarly, for experiments conducted at airflow velocities of 0.25 $m\,s^{-1}$ and 0.1 $m\,s^{-1}$, no loading was de-

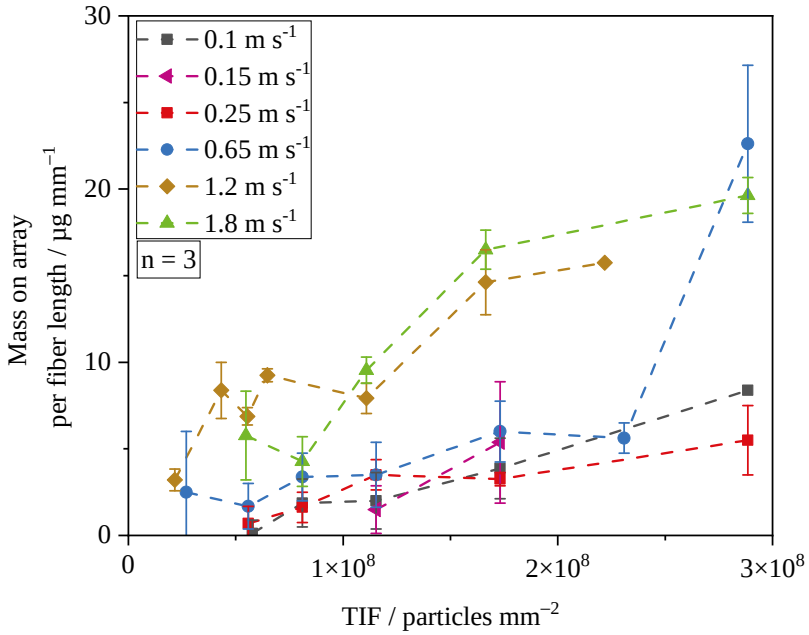


Figure 6.8: *Development of mass on the array over fiber length (5 equally spaced fibers) as a function of TIF.*

tected below 6×10^7 particles $\cdot$ mm^{-2}. At high TIF, however, the mass on the fiber array increases continuously with increasing TIF at airflow velocity below 0.25 $m\,s^{-1}$, reaching a maximum of 5.5 $\mu g \cdot mm^{-1}$ in the experiments at 0.1 $m\,s^{-1}$.

The investigation revealed particle deposition on the fibers in experiments with compact morphology. Increased deposition occurred at airflow velocities greater than 1 $m\,s^{-1}$ (Stokes greater than 5.1). Particles with large diameters, which represent the high-mass fraction of the Particle distribution (PD), were most probably deposited by inertia. After reaching a TIF of 1.73×10^8 particles $\cdot$ mm^{-2}, the increase in mass slowed down because of the poor growth of compact-shaped structures. The structure likely grows in the direction of flow and is compacted by incoming particles. Hence, the collector size increases slightly only. In the experiments with the compact structures (1.8 $m\,s^{-1}$ and 1.2 $m\,s^{-1}$), increases in particle mass on the array are observed at similar TIF. Given that the TIF is a time-dependent metric and each data point is a result of three measurements, the probability of a random increase in mass due to discontinuous dispersion is negligible with the duration of the experiments.

In the experiments at 0.65 $m\,s^{-1}$, the deposited mass increased considerably above TIF 2.3×10^8 particles $\cdot$ mm^{-2}. First, the deposited mass was below that of experiments with a complete compact structure. Shortly after the TIF 1.73×10^8 particles $\cdot$ mm^{-2}, a sharp increase in the deposited mass on the fiber array is observed, indicating the complete closure of the structure and the resulting enlargement of the collector area.

The increasing collector area increased the probability of separation, which might increase the impact coefficient. The steep increase in mass with increasing TIF was observed in all replicate experiments. The deposited mass was nearly 22.6 $\mu g \cdot mm^{-1}$ fiber length (five times 16 mm loaded fiber length) in the experiments at 0.65 $m\,s^{-1}$. At TIF greater than 2.3×10^8 particles $\cdot\, mm^{-2}$, the interspaces between the fibers were blocked. Unfortunately, measuring the pressure drop in a fiber array is not feasible. To gain a better understanding of the phenomena, different factors, such as accumulation of particulate material, size, and number of bridges and pores, were considered.

6.3.2 Accumulation of Particulate Material before Clogging

To distinguish the different phases of the separation process on the fiber array and to quantify the deposition kinetics during classical filtration, evaluation points were introduced at selected TIF. The position of the evaluation points is based on the overall course of an experiment with an airflow velocity of 0.65 $m\,s^{-1}$. In such an experiment the fiber interspaces are completely clogged, and no bridges are detected at a TIF of 2.8×10^8 particles$\cdot$mm^{-2} (relative accumulated particulate material in the spacing ≈ 1). The TIFs corresponding to the evaluation points are shown in Table 6.2.

Table 6.2: *TIF at the evaluation points for video-based analysis of the fiber array.*

	TIF at Evaluation Point/particle$\cdot$mm^{-2}			
Feedrate Aerosol Generator	**1**	**2**	**3**	**4**
10	5.5×10^7	1.15×10^8	1.73×10^8	2.8×10^8

Image analysis was used to quantify the growth kinetics of particle structures in the fiber interspaces by measuring the increase in particle material in the inner fiber interspaces of the array. Figure 6.9 shows the relative accumulated particle material in the fiber interspaces over the increase in TIF up to a TIF of 1.75×10^8 particles $\cdot\, mm^{-2}$ at different airflow velocities. None of the experiments revealed complete blocking at these TIF values. The airflow velocities ranged from 0.1 to 1.8 $m\,s^{-1}$. The development of accumulated particle material in the interspaces remained constant over the entire experiment. The evaluation started at the smallest TIF where the fibers became visible. The growth rate represents the rate at which the fiber interspace was occupied by particulate material. The fiber array first was in the depth filter phase, followed by the transition phase as in normal filters.

The average growth rates between the second and the third evaluation points were

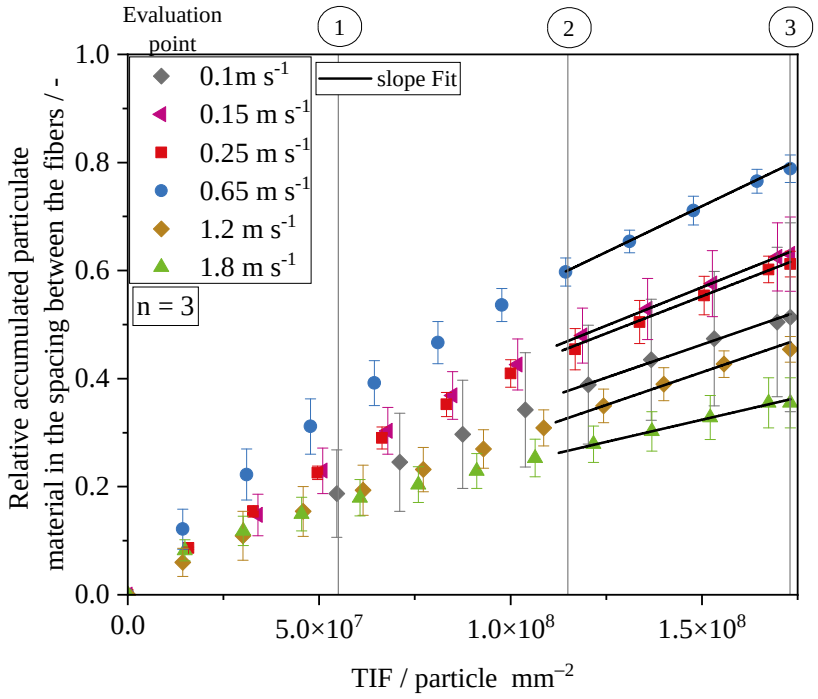


Figure 6.9: *Relative accumulated particulate material in the spacing at the initial three evaluation points of the experiment, representing the depth filter phase and transition phase. A growth rate analysis was conducted for each curve to determine particle accumulation in the interspaces of the fiber array.*

determined by using a linear fit (black fit) for each curve, with a coefficient of determination above 0.99. Regardless of the applied airflow velocity, the experiments passed the run-in phase and were in the surface phase or at the beginning of the transition phase.

Analysis of experimental conditions revealed trends and mechanisms in particle growth kinetics within the fiber interspaces. Dendritic particle growth was observed at flow velocities ranging from 0.1 to 0.65 $m\,s^{-1}$. As shown in Figure 6.10, dendritic structures develop in the region of interception in the experiment at a flow velocity of 0.15 $m\,s^{-1}$.

The same phenomenon had been found before in a computational simulation by Payatakes and Tien [100]. Figure 6.11 shows the rate for particle accumulation on an array plotted against the flow velocity and Stokes number, which is extracted from linear fit in Figure 6.9. The rate reflects structure growth in the interspaces and on the fibers. An increase in the particle structure within or outside of the image plane cannot be detected. Compact structures formed in the experiments at 1.2 and 1.8 $m\,s^{-1}$ result in a low growth rate compared to the low airflow velocity experiments. The smallest growth rate of dendritic structures was observed at 0.1 $m\,s^{-1}$, while growth at 0.15 and

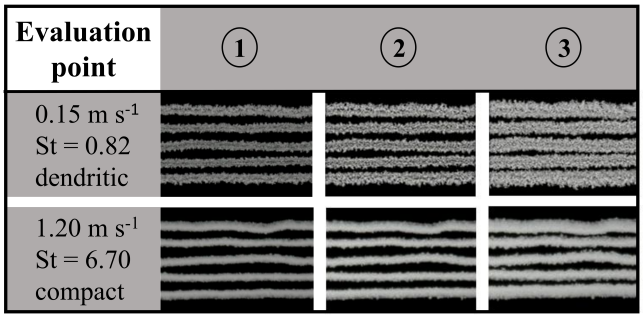


Figure 6.10: *Particulate material on the fiber for two different flow velocities. All experiments were performed three times.*

0.25 $m\,s^{-1}$ was 27% higher than in the experiments with an airflow velocity of 0.1 $m\,s^{-1}$. In the experiment with a flow velocity of 0.65 $m\,s^{-1}$, the growth was 49% higher. The particle loading rate in Figure 6.11 is on a higher level because particles accumulated opposite to the direction of flow.

Kanaoka et al. (1986) observed a change in the orientation of particle deposition from upstream to cross-stream on the side of each fiber as the Stokes number decreased towards zero and the Péclet number increased towards infinity [65]. The masses deposited on the fiber at flow velocities 0.1 $m\,s^{-1}$, 0.15 $m\,s^{-1}$, and 0.25 $m\,s^{-1}$ were approximately the same at the same value of TIF (see Figure 6.8). Therefore, the higher growth rate at 0.15 $m\,s^{-1}$ and 0.25 $m\,s^{-1}$ compared to 0.1 $m\,s^{-1}$ in Figure 6.9 cannot be attributed to an increased deposition rate.

Instead, the particle bounce parameter β defined by Kasper et al. may explain the observed horizontal widening of structures in the direction of the image plane [70]. As particle velocity or diameter increases, the rebound parameter β increases, leading to re-arrangement and eventually to bouncing and dislodging of previously deposited particles [131]. In addition to the effect of interception, re-arrangement might occur, initiated by the accumulation of particles that widen the structures at the horizontal level.

While previous studies cited in this work have used a narrow particle size distribution or monodisperse material, whereas this study used a polydisperse particle size distribution, which leads to overlapping deposition effects.

Therefore, the interception effect for small particles and the inertia effect for large particles overlap. When considering the rebound parameter, the effects for impinging particles and particles that detach before deposition overlap at the same flow rate for each particle size. The predominantly dendritic particle deposition observed at flow rates below 0.65 $m\,s^{-1}$ changes to a compact deposition on the fiber surface at flow rates of 0.65 $m\,s^{-1}$ and higher. The loading rate between the fibers decreases with increasing flow rate above 0.65 $m\,s^{-1}$. This indicates that particles hardly adhere in cross-stream or detach after adhesion at the highest Stokes numbers.

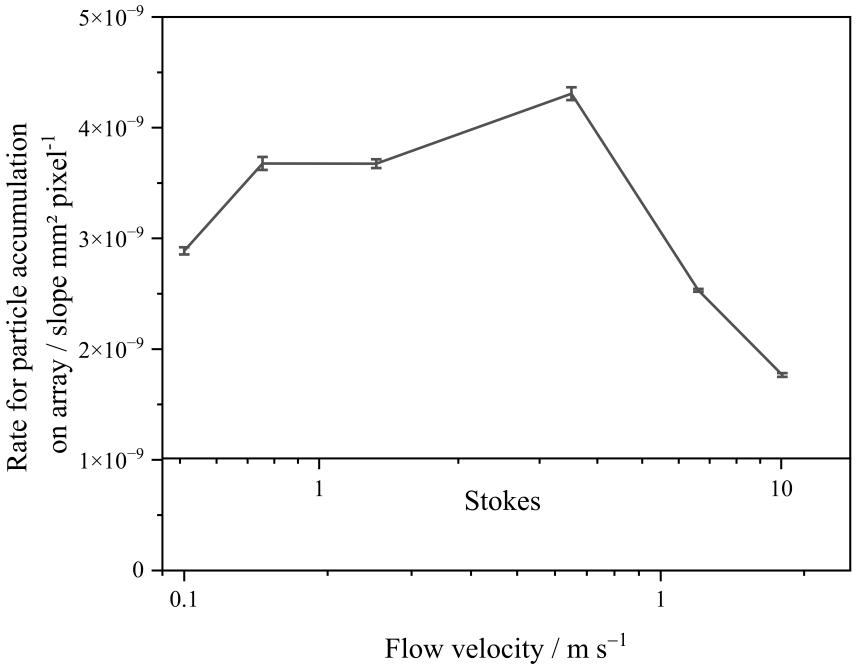


Figure 6.11: *Rate of particle accumulation as a function of Stokes before CP.*

6.3.3 Development of Structures before and in the Clogging Phase

It is outlined in Section 6.3.2 that as the TIF increases, more particles accumulate in the interspaces between the fibers. The complete closure of the interspaces between fibers was not observed at values of TIF up to 1.75×10^8 particles $\cdot$ mm^{-2}. To analyze bridge growth up to the CP, three experiments were conducted with different flow velocities at higher terminal TIF values. The flow velocity covered the range of deposition patterns (dendritic, transition, and compact morphology). The final TIF value reached 2.8×10^8 particles $\cdot$ mm^{-2} after a long experimental time. For one set of parameters, complete clogging was achieved. Figure 6.12 displays the complete evolution of the structures up to the predefined evaluation points.

In all experiments, a particle layer was initially visible on the fiber at Evaluation Point 1. In the tests an incident flow velocity of 1.8 $m\,s^{-1}$, deposition at the stagnation point of the fiber was clearly visible. At Evaluation Point 2, the characteristic separation of particles was observed in all experiments. The morphology of the particle structure was a function of airflow velocity. In the experiments with a flow velocity of 0.25 $m\,s^{-1}$, dendritic structures with small arms appeared in the interspaces between the fibers. In the experiments with an airflow velocity of 0.65 $m\,s^{-1}$, growth of dendritic structures was observed, too. However, more particulate material is separated at the stagnation point of the fiber, as shown by the presence of a thick layer of particle ma-

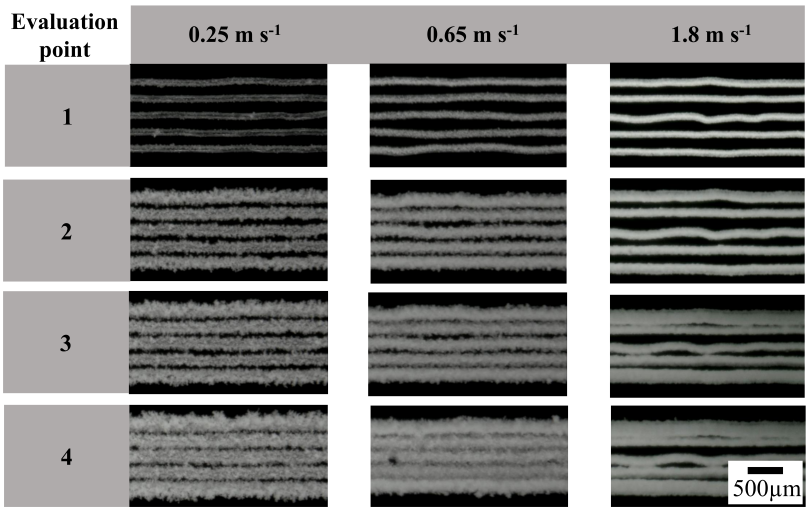


Figure 6.12: *Particle structures in experiments with three different superficial velocities at 4 evaluation points.*

terial. In the experiment with an airflow velocity of $1.8\,m\,s^{-1}$, the unobstructed fiber interspaces were clearly visible. The particulate material just separated on the zenith/-top of the fiber. At the third evaluation point, deposition of particulate material in the interspaces of the fiber was visible though the compact structure seems to bend into the interspaces. Merging particle structures across the interspaces were found at the sites where the fiber bends.

In the experiments with airflow velocities of $0.65\,m\,s^{-1}$, and $0.25\,m\,s^{-1}$, increased growth of the dendritic structures into the interspaces of the fiber was observed at this evaluation point. The images of the experiments at $0.65\,m\,s^{-1}$ reveal a few gaps in the particle structure visible at Evaluation Point 3, where the fibers have dents and are slightly separate from each other. These gaps only close as the number of bridges decreased towards Evaluation Point 4. In addition, impacts on the already clogged particle structure were found and attributed to large particles which hit the particulate structure. Compared to the total area, these impacts are small in size. In the experiments with an airflow velocity of $0.25\,m\,s^{-1}$, the dendritic structure grew into the interspaces of the fiber. The dendritic arms were much more pronounced compared to the experiments with an airflow velocity of $0.65\,m\,s^{-1}$. The compact structure of the fiber merged (formation of bridges) across the interspaces of the fibers. The contact points of merging particle structures from different fibers were found to be much wider for the compact structures than for the dendritic structures. The clogging point will be reached soon when the free interspaces between the fiber are closed completely. For all experiments with different airflow velocities, an increased separation of particles at the outer fibers of the array is observed with increasing loading at Evaluation Point 4. Thus, in the experiments with the airflow velocity of $1.8\,m\,s^{-1}$, the structure at the outer fiber becomes a little bit bulky. The edges of the structure remain sharp and

smooth. However, the growth of the structure on the outer two fibers is observed in the tests with incident flow velocities of 0.25 $m\,s^{-1}$ and 0.65 $m\,s^{-1}$, too. Due to the separation mechanism, the structure has more small arms and dendrites on the outer fiber surface. The reason for this increased separation is the change of the flow around the fiber which is a result of particle separation in the interspaces of the fibers. This effect was predicted in the calculations of Müller et al. [92]. As described in Section 6.2.3, only the inner interspaces of the array are considered during evaluation. The limit on using just 5 parallel fibers is because the used motors are not able to stretch more polymer fibers at once due to the restrain force that the fibers encounter.

In Figure 6.13, the fraction of accumulated particulate material and the total number of bridges are plotted as a function of TIF for each flow velocity. The experiment was conducted three times, and the data were analyzed using MATLAB.

For the highest flow velocity ($u = 1.8\,m\,s^{-1}$), the graph shows a continuous growth of the fraction of accumulated material in the transition phase, with a small decrease in growth rate for a TIF above 2.0×10^8 particle $\cdot\,mm^{-2}$. This section comes with an increase in the standard deviation. At the same time, the number of bridges levels off at around 10 for the experiments with a flow velocity of 1.8 $m\,s^{-1}$. In contrast, the experiments with a flow velocity of 0.25 $m\,s^{-1}$ and the dendritic structure on the fibers show a continuous increase in the number of bridges starting at a TIF of approximately 7.5×10^7 particles $\cdot\,mm^{-2}$. This effect is due to the growth of the structure vertical to the flow direction, which tends to close the interspaces between the fibers. In these experiments, the fraction of accumulated material increases from the start of the experiment with a steeper slope than in the experiments with a compact deposit at a flow velocity of 1.8 $m\,s^{-1}$. The relative accumulated particulate material starts to decrease slightly as bridge growth becomes dominant at a TIF of 1.25×10^8 particles $\cdot\,mm^{-2}$. In the experiments conducted at an airflow velocity of 0.65 $m\,s^{-1}$, the relative accumulation of particulate material within the fiber spacing displayed the most rapid increase. The accumulation continuously increased from the start of the experiment until complete closure of the filter occurred with minimal pore sizes.

Significantly, the experimental conditions that involved an airflow velocity of 0.65 $m\,s^{-1}$ exhibited the lowest standard deviation among the observed results. With increasing TIF, the number of bridges increases continuously at TIF of 1.6×10^8 particles $\cdot\,mm^{-2}$ to a maximum of approximately 100 bridges. Initially, dendritic growth is observed with well-developed bridge formation and the maximum number of bridges. The maximum value of bridges occurs just before Evaluation Point 3. It is important to note that the generation of bridges and the separation of particles at the fiber generally are processes that involve a certain random component. This fact is highlighted by the high standard deviations. Once the maximum is reached, the number of bridges decreases as the array becomes more clogged and the pores and interspaces between the fibers continue to fill and multiple small bridges merge into broader structures. A cake of particulate material forms on the array, as illustrated in Figure 6.12.

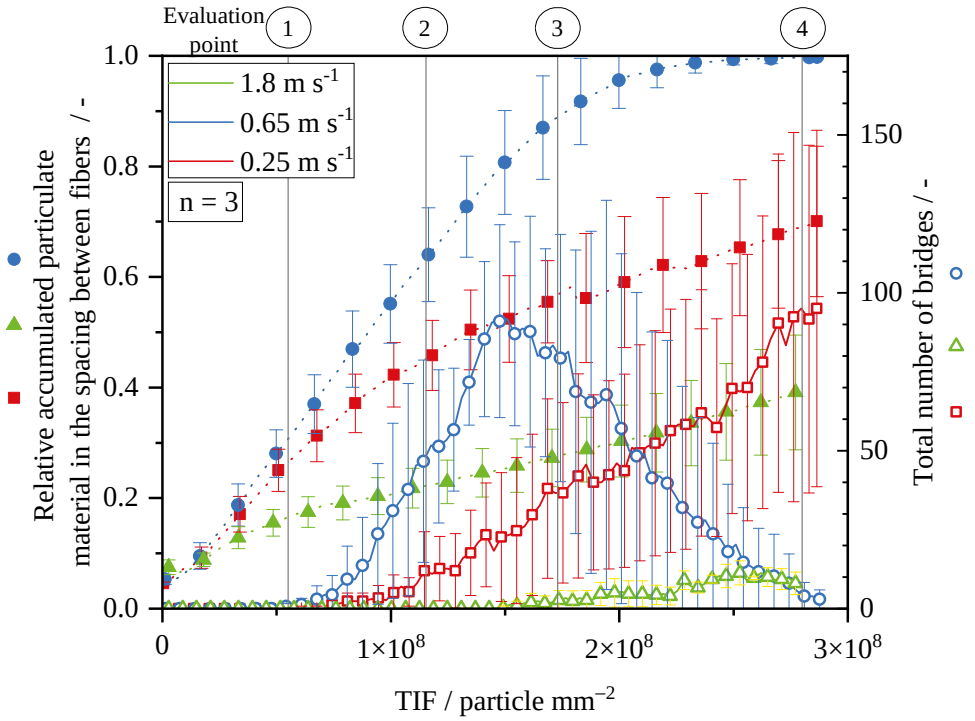


Figure 6.13: *Particulate material on the array and the corresponding total number of bridges. All experiments were performed three times.*

The boundary line reflecting the deposition pattern is presented in Figure 6.14. The boundary line is characteristic of the respective type of deposition morphology or mechanism. For the dendritic structures in the experiments with airflow velocities of 0.25 $m\,s^{-1}$ and 0.65 $m\,s^{-1}$, a jagged and long boundary line can be observed. The boundary line of the experiments with a compact deposit is similar to the original fiber. The boundary line of the experiment at 0.65 $m\,s^{-1}$ is initially jagged but becomes straighter with increasing TIF. In comparison, the boundary line of the experiment at 0.25 $m\,s^{-1}$ is more jagged. Once complete closure of the interspaces is achieved, the boundary line disappears, as shown here by the experiments at airflow velocity 0.65 $m\,s^{-1}$.

Figure 6.15 presents a quantitative analysis of the length of the boundary line (horizontal, parallel to fiber axis) relative to the initial boundary line of the fiber for the three different morphologies (dendritic, transition from dendritic to compact, compact) of particulate structures. At an airflow velocity of 0.65 $m\,s^{-1}$, the ratio first increases slightly above 1 due to the dendritic separation of particles. Just before the second evaluation point, the ratio starts to decrease due to the formation of the first bridges. After the second evaluation point, the curve continues to decrease due to the formation of bridges and clogging of the interspace between the fibers. At the end of the experiment, the ratio reaches the value of 0 for the experiment with 0.65 $m\,s^{-1}$. At an airflow velocity of 1.8 $m\,s^{-1}$, by contrast, the ratio of the boundary lines remains

constant at almost 1 due to the horizontal increase in compact structure. However, a reduction below 1 is observed between Evaluation Points 3 and 4, caused by the formation of bridges and the subsequent shortening of the boundary line at the end of the experiment (see Section 6.3.4). As observed earlier, the boundary line of the dendritic structure is more jagged, resulting in a larger ratio than for the compact and transition structures. The ratio remains above one after the third evaluation point.

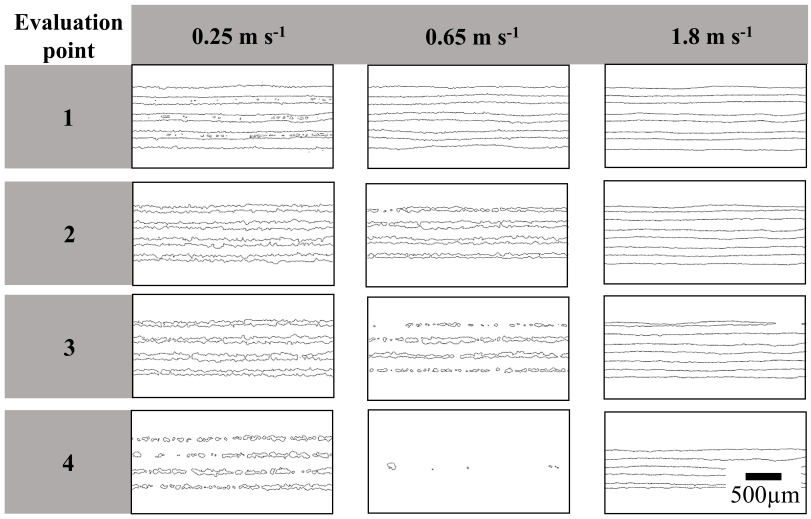


Figure 6.14: *Images of the development of particle structure of the array in experiments with three different superficial velocities.*

6.3.4 Size of Pores and Bridges

The pressure in a filter drops due to friction between gas molecules and fibers or deposited particle structures. Particle structure growth on the collector can lead to an increased blockage area (fiber + particulate material) and reduced free cross-sectional area for flow. Section 6.3.2 emphasized that particle structures grow at varying rates and extend into interspaces of the fibers. While previous studies focused on the pressure drop as a function of process parameters, the impact of structural morphology on particle separation/accumulation and the CP has yet to be investigated in sufficient detail. Observing particle deposition on a single fiber or array of fibers is not sufficient to characterize pressure loss in the filtration process. The particulate material is deposited on the fibers. The fiber interspaces start to clog when more particulate material is separated onto a pre-existing particulate structure under a large angle to the stagnation point (refer to Section 6.3.3). Particle bridges as illustrated in Figure 6.12, develop with progressing filtration time between/across the fiber interspaces due to the growing of particle structures on neighboring fibers. As described above, the formation of bridges reduces the unobstructed flow area of the initial "pore" between the two fibers and generates two new pores on either side of the bridge. The number and dimensions

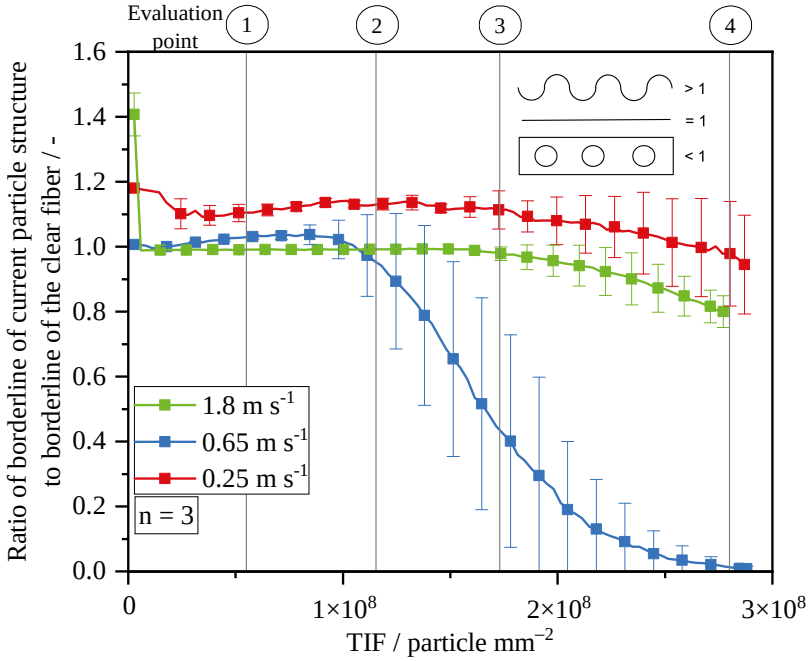


Figure 6.15: *Development of boundary line for the three representative flow velocities over the complete duration of the experiments. The particle concentration in the feed flow was* 1.6×10^5 *#/cm*^{3}*. All experiments were performed three times.*

of formed bridges depend on airflow velocity and the deposition mechanism as well as on the fiber's structural morphology.

Figure 6.16 shows the development of maximal size (parallel to fiber axis) and number of bridges with three characteristic airflow velocities as a function of the TIF. This figure follows the principle of a heatmap. The total number of bridges (in the following pores) in each section is visualized using a grayscale code.

At a flow velocity of 0.25 $m\,s^{-1}$, the first small bridges (71–81 μm) develop just before the second evaluation point. At first, the number of bridges simply increases to an average size of 50 μm. Then, starting at TIF of 1.6×10^8 particle $\cdot$ mm^{-2}, more small bridges are formed while existing bridges grow together to form larger ones. At Evaluation Points 3 and 4, the number of medium-sized bridges (50–60 μm) does not increase any further, while the large bridges continue to grow.

As shown in Figure 6.13, the curve for the increase in particulate material in the interstitial spaces flattens somewhat at a TIF of 1.6×10^8 particle $\cdot$ mm^{-2}. At Evaluation Points 3 and 4, the structures are not fully closed yet (see Figures 6.12 and 6.17). The size of bridges reaches a maximum of 281 μm.

At an airflow velocity of 0.65 $m\,s^{-1}$, bridge formation occurred earlier that at 0.25 $m\,s^{-1}$. The size of the first bridges formed in the two sets of experiments was similar. There was a significant growth of bridges between Evaluation Point 2 and

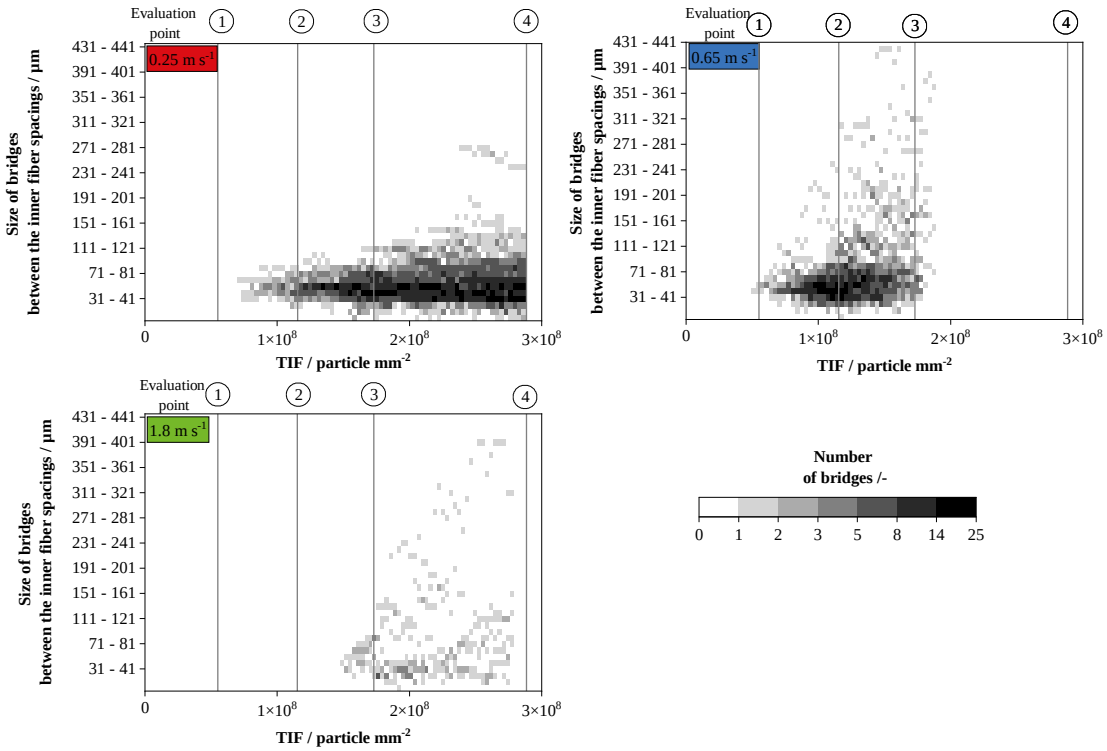


Figure 6.16: *Size and number of bridges between the fibers in the experiments up to CP. At 1.8 m s^{-1}, 0.65 m s^{-1}, and 0.25 m s^{-1}. Scaling of colors (number) is logarithmic. Size of bridges parallel to the axis of the fiber.*

Evaluation Point 3, with a considerable number of large bridges (larger than 121 μm) and small bridges (ranging between 41 and 71 μm) being formed. The bridges continued to grow towards Evaluation Point 3, reaching a maximum size of 441 μm. The number of bridges, however, was smaller than that at 0.25 m s^{-1}. The number of small bridges continued to decrease towards Evaluation Point 4, while bridges of medium size (between 121 and 201 μm) increased in size due to particle accumulation.

In the experiments at an airflow velocity of 1.8 m s^{-1}, the formation of bridges sized 41–81 μm occurred shortly before Evaluation Point 3 and continued to increase with increasing TIF. The total number of bridges in this size range increased, too. The maximum bridge size reached 401 μm before Evaluation Point 4, which is twice the size of the bridge observed at 0.25 m s^{-1}. The total number of bridges ranged from 8 to 14 and was lower than in the other experiments. This might be due to the fact that the structure between and on the fiber is growing more in the direction of the airflow. As a dendritic structure has more side arms in the horizontal direction that can reach structures on other fibers, the chance of bridge formation is higher.

As discussed in Section 6.2.3, bridges typically result in the formation of new pores. At the beginning of the filtration process, there are empty spaces between

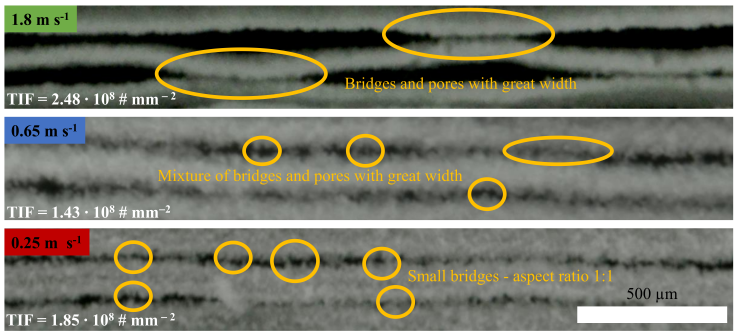


Figure 6.17: *Images of the characteristic pores and bridges at three different airflow velocities during the loading procedure at the corresponding TIF.*

neighboring fibers that gradually become filled with deposited particles. Figure 6.18 presents the size and number of those pores at the corresponding TIF for three different airflow velocities. They are measured using the hydraulic diameter as a metric for pore size. The free fiber interspaces are detected at the start of each experiment and appear as a single large pore per fiber pair. At a TIF of 0 particle $\cdot$ mm^{-2} are the unobstructed interspaces between the fibers. As the loading process continues, the size of the interspaces between the fibers narrows. Subsequently, the hydrodynamic diameter starts to decrease. A newly created bridge splits into a large pore into two new pores. The experiments at an airflow velocity of 0.25 m s^{-1} exhibit an initial steady decrease in pore size with a constant number of pores from the beginning of the experiment. This indicates a stable growth of the particle structure within the interspace of the fibers. Immediately after Evaluation Point 1, corresponding to a TIF of 1.5×10^7 particle $\cdot$ mm^{-2}, the number of pores increases steadily. After the evaluation point, there is a marked increase in the number of smaller and medium-sized pores, particularly in the size range of 21–41 μm, which may include small holes within the dendritic structure (observed in Figure 6.12). After Evaluation Point 4, mainly small pores are formed, while large pores above 100 μm become less frequent. Just before the fourth evaluation point, additional large pores may form in the deposited structure due to small demolition and fracturing. Moreover, it is possible that formed dendritic arms of the structures may detach and expose void areas between the fibers.

Further particle loading would lead to clogging in the interspaces of the fiber array. The number of small pores continues to increase, which suggests further growth and clogging of already existing pores. The exact TIF at which clogging occurs at this airflow velocity is not known. Figure 6.12 presents images of the growing structure including pore formation. Figure 6.17 illustrates the pores and bridges and their aspect ratios. In fiber sections with a slightly smaller fiber spacing the structure recedes more quickly with large pores/spaces and closing fast and almost completely.

At an incident flow velocity of 0.65 m s^{-1}, an initial linear decrease in pore diameter at a constant pore number is observed again. The deposited structure, as shown in Figure 6.12, exhibits a morphology transitioning from dendritic to compact. Pore

growth in the size ranges of 41–61 μm and 21–41 μm starts just before the second evaluation point. Further development of smaller pores and simultaneous reduction of larger pores indicates the gradual closure of large pores and growth of the structure between the second and third evaluation points. After Evaluation Point 3, the number of small pores continues to increase as the structure slowly closes completely.

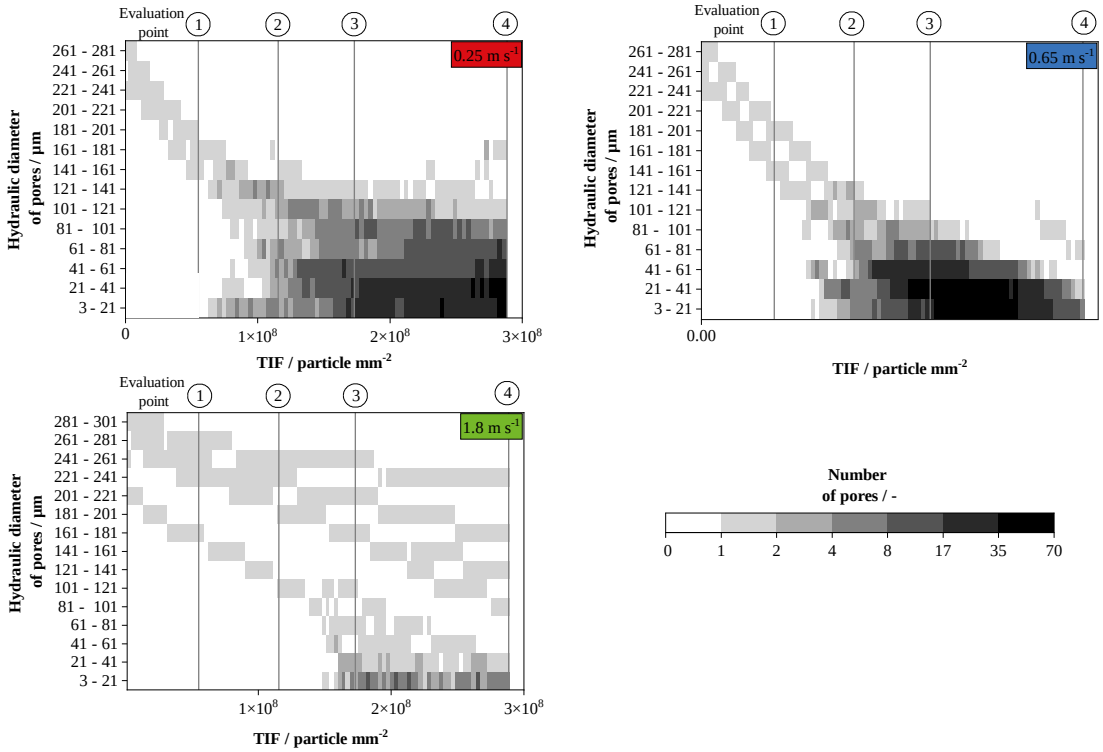


Figure 6.18: *Hydraulic diameter of the pores between the fibers in the experiments before reaching CP. At 1.8 m s^{-1}, 0.65 m s^{-1}, and 0.25 m s^{-1}. Grayscale (total number) is logarithmic. The pores at TIF = 0 are the interspaces between the fibers. Plot for 0.65 m s^{-1}: Hole in the clogged particle structure.*

Large pores with hydrodynamic diameters of 81–121 μm occur before Evaluation Point 4. These are actually holes in the previously closed particle structure, which were created by larger particles. The holes are closed by particulate material as the filtration process continues (see Figure 6.18). Although some pores are still present at the end of the loading process, the combination of different results (accumulated particulate material, number of bridges, and pores) shows that the structure has reached the clogging phase.

When the airflow velocity increases by 1.8 m s^{-1}, a compact particle structure is formed on the fiber array in agreement with the investigation by Kanaoka et al. [65]. As depicted in Figure 6.18 on the lower left, the pores persist up to large values of TIF. The hydraulic diameter decreases to 241–261 μm because the structure grows in the di-

rection of the stagnation point, rather than horizontally. Large pores form right after the start of the experiment and exist up until Evaluation Point 4. Before the third evaluation point, additional pores develop in the range below 100 μm. They are formed parallel to the bridges (see Figure 6.16). The number of individual pores remains very low in the experiment with 1.8 $m\,s^{-1}$ compared to 0.65 $m\,s^{-1}$ and 0.25 $m\,s^{-1}$. Pores in the size range of 3–21 μm are found in all experiments. The presence of pores until the end of the experiment, along with the observation of large elongated pores between the fibers, suggests that the structure is not fully closed. These results, together with the findings presented in Section 6.3.3, support the notion that the structure is not in a completely clogged state. The structures merge due to their length, as reflected by the horizontal bridge size data.

6.4 Conclusions and Outlook

In this study, the impact of airflow velocity on the formation and development of particulate structures on an array of elastic filter fibers was investigated. The experimental results revealed new details about the morphology of the particulate structures. It depends on the airflow velocity, with dendritic structures forming at low velocities and compact structures at higher velocities.

Visual observation took place in the airflow direction using a special camera that allowed for a comprehensive analysis of the whole deposition process. This technique facilitated the determination of the number and size of pores and bridges between individual fibers or within the structure and of the relationship between the boundary line and the relative accumulated particulate material in the spacing between the fibers. Those investigations of the mass on the fiber array revealed a steeper increase when the fiber structure's clogging point was exceeded. The ratio of boundary lines for dendritic structures was found to be larger than that for compact structures, indicating a more jagged boundary line in the former case. The technique was also used to determine the size of pores within and between the individual particle structures. The hydraulic diameter of the pores increased the size with an increasing Stokes number. The size of bridges decreased as the Stokes number decreased. The number of bridges was significantly higher for dendritic structures on the fiber than for compact structures, where long bridges are formed during the experiment. The growth rate of the particle structure passes through a maximum at a Stokes number of 3.62. In these experiments, the CP was reached.

Based on the above results, future investigation will focus on the behavior of the separated particle structure (with different morphologies and growth progress) on the fiber array during the stretching (up to 39% of the filter fibers). The elongation of the fibers causes stresses in the deposited particle structure, which might result in re-arrangement and detachment. The size and effects of particle structure rearrangement and detachment will be examined and predicted as precisely as possible. It is uncertain how much elongation of the fiber structure is necessary/is possible with

an entire filter medium, but it has already been shown in previous experiments that even at small elongations of 5% the first detachment occurs during the first elongation cycle [107]. Overall, the use of elastic fibers in filter media has the potential of paving the way towards the development of adaptive filter systems in the future.

Author contributions: Conceptualization, A.D., J.M., and L.P.; methodology, L.P.; software, L.P.; validation, A.D. and J.M.; formal analysis, L.P.; investigation, A.D.; resources, A.D.; data curation, L.P. and B.K.; writing—review and editing, A.D., J.M. and L.P.; visualization, L.P., B.K.; supervision, A.D. and J.M.; project administration, A.D. and J.M.; funding acquisition, A.D. All authors have read and agreed to the published version of the manuscript.

Funding: We gratefully acknowledge funding of this project by the Deutsche Forschungsgemeinschaft (DFG, German Research Foundation)–427981860.

Data availability: Poggemann, Lukas (2023), "Morphology of Particulate Structures on a Fiber Array before and at Clogging Point of an Aerosol Filtration Process", Mendeley Data, V1, doi:10.17632/g7wthghkh9.1

Acknowledgments: Kindly thank Freudenberg Filtration Technologies SE & Co. KG for donating fiber material. We acknowledge support by the KIT Publication Fund of Karlsruhe Institute of Technology.

Conflicts of interest: The authors follow no commercial interest with this study.

7

Rearrangement and detachment of particle structure from a fiber array

Title: Detachment of particulate structures from a fiber array due to stretching and simultaneous gas flow
Authors: Poggemann, Lukas; Längle, Pablo; Meyer, Jörg; Dittler, Achim
Status: Published
Bibliographic data: Separation and Purification Technology 351 (2024), p. 127887, ISSN: 1383-5866,
https://doi.org/10.1016/j.seppur.2024.127887

Copyright Separation and Purification Technology 2024, published by Elsevier. Reprint with permission. The text has been adapted in this thesis to change the citation and figure numbering. Additionally, some symbols have been modified to confirm with the other chapters.

Abstract
The main cause of high pressure drop and increased energy consumption in a filtration process is the clogging of particulate material in the upstream layers of a depth filter. To alleviate this issue, stress can be introduced into the particulate structure through stretching, which promotes rearrangement and detachment of particle structures, allowing for transfer of some of the clogged particulate material from the upstream layers to downstream void regions. This study aims to extend previous findings from experiments with single fibers to the level of an array. The goal is to analyze the introduction of a multiple stress state by performing stretching experiments with a particle-structure on a fiber array.
The stretching tests investigate the influence of different process parameters such as stretching velocity and air flow velocity during stretching on the rearrangement

and detachment behavior of a separated particle structures from the fiber array. Rearrangement and detachment of the particle structure are a direct consequences of the stress induced by stretching. The experiments showed a significant increase in relative free projection area of fiber interspaces (RFPI) of up to 160 % and thus a large-scale removal of particle material from the fiber interspaces when the flow velocity was increased from $0.05\,m\,s^{-1}$ to $0.8\,m\,s^{-1}$. Surprisingly, the radial rearrangement of the compact particle structures during stretching resulted in a clogging and blockage of the interfiber spaces (negative RFPI in the range of minimum -54 % after the first stretching cycle) and not in a total release of the interfiber spaces. The size of the particle structures in the experiments decreased by about $331\,\mu m$ with the number of stretching cycles, indirectly confirming the presence of residual structures. Preliminary experiments also confirmed an increased influence on the rearrangement and detachment (removed particulate material of about 30 %) of particle structures by further increasing the fiber distance of $27\,\mu m$ and thus introducing a biaxial stretching into the particle structure.

7.1 Introduction

Depth filtration is a widely utilized technique in gas-particle technology, aiming to separate a dispersed phase from a continuous one. Its applications span various fields, including air conditioning systems and the purification of process gases. Key parameters for assessing the operation's effectiveness include separation efficiency and pressure drop. The latter signifies the energy consumption of the filtration process. As particles accumulate on top of individual filter fibers and in the void space of the fiber, the pressure drop at the filter rises. Throughout the filtration process, a gradient of deposited particle material forms over the depth of the filter with highest particle loadings on the upstream fibers [46, 47]. Ultimately the filter clogs on the inlet side leaving void space without particulate material in the downstream layers of the filter. The clogging marks the transition to cake filtration with a steep increase in pressure drop [152]. When pressure drop reaches a critical point, necessitating filter replacement, it becomes evident that in-depth filtration, cleaning or re-cleaning of used filter media is not a common practice.

With the increasing demand for more energy efficient and sustainable processes, there is a growing need to reduce the consumption of filter media and energy. One possible solution to open up clogged fiber interspaces and initiate detachment of particle material within the upstream area of the filter is to apply stress to the separated particulate material. The stresses that cause the particle structures to rearrange and detach can be induced by stretching the fibers.

Experiments with a particle loaded single fiber collector have shown that stretching of the fiber can initiate the desired rearrangement and detachment of particle structures from the collector surface [106, 107]. During stretching, the elongation of the substrate creates shear and tensile stresses within the particle structure, resulting in

cracking of the particle structure. Szabadi et al. and Zoller were able to show that the detachment of particle structures from spheriglass by magnetic deflection of a fiber or the effects of a reaction in the particle structure are possible [148, 178]. In addition separate studies on the microscopic fiber surface during stretching showed that due to the change surface roughness of the fiber, the adhesion force between a individual particle and the fiber is reducing by about 33 % [108].
To gain a more comprehensive understanding of the rearrangement and breakage of the particle structures within the filtration collector, the size of the model need to move from a single fiber to a fiber array. Previous investigations of rearrangement and detachment effects were limited to the observation model of a particle loaded single fiber. Single fiber stretching creates stress state within the structure. In advanced filtration processes close to the clogging point, the development of bridges between individual filter fibers within the filter are crucial for increasing pressure loss. Typically, fibers are arranged randomly or in a tangled manner, but parallel fiber arrangements occur in infinitesimal sections. For simplification and to reduce side effects, these parallel arrangements are also replicated in the fiber array (see [91]). In the fiber array, as well as throughout the entire filter medium, particles form structures between adjacent fibers. The impact of the applied process variables such as stretching velocity and flow velocity on the rearrangement and detachment of particle structures have never been under investigation at the observation level of a fiber array. The range for the applied process variables is based on previous investigations of individual fibers, as listed above. Based on the performed investigations on a single fiber, it has been determined that an air flow velocity of $0.05\,m\,s^{-1}$ to $0.8\,m\,s^{-1}$ is necessary to causes particle structures to break up and detach, which is promoted by fiber stretching and the applied stress. In the previous experiments with a single fiber only one-dimensional stress-state have been investigated so far [106]. In the fiber array experiments, multidimensional stress states are expected to occur within the separated particle structure due to the neighboring fibers. This idea of influencing the cracking and rearrangement of a separated particle structure has not yet been investigated. Understanding the underlying mechanisms is crucial for the effective implementation of these innovative process approaches and ideas. The knowledge of micromechanics and influencing factors can help to understand the overall process of rearrangement and detachment.

With regard to the previous investigations conducted with a single fiber, the fiber array represents a simplified form/model of an entire fibrous filter. This simplified form allows the observation of processes that normally take place within an entire filter and cannot be observed in isolation. The diameter of the fibers, the distance between them and the arrangement of the fibers have been deliberately simplified in order to enable the observation and quantification of individual processes and effects, such as rearrangement, growth and break-up of pores as well as the detachment of particle structures.

However, this simplification also involves some compromises that neglect certain effects and interactions during the loading process, but also during the stretching of the filter fibers. For example, the fibers are prototypes of a stretchable filter fiber, which is why the fiber diameter is slightly larger than the standard size. Further as previously stated, the fiber spacing is based on the published as in Müller's experiments on the separation of particles on a fiber array [91].
Another point that is different and far more complex with a complete filter than with a fiber array is the loading behavior of the filters, as well as the structural changes of the filters during the stretch. As demonstrated in a simple numerical model by Siena et al. the influence of a single (one-dimensional) layer in a random generated fiber mesh and the influence of the distribution and arrangement parameters of the fibers on the porosity and local flow velocity at and between the fibers [142]. Virtual samples were created for each porous medium, which differed in their porosity and pore-structure topology. Furthermore, specific investigations were conducted to ascertain the manner in which flow trajectories within the pores develop as a consequence of the tortuosity of the filter. Further, Alim et al. were able to demonstrate how neighboring pores develop in a porous filter medium using an analytical two-dimensional model, which was then compared to experimental data [2]. With regard to the arrangement of parallel fibers used in this study, this approach showed that with a parallel arrangement of fibers, only the presumably simplest case is considered.
Focusing on the influence of the arrangement of the filter fibers, Griffiths et al. studied the link between the tortuosity of a filter and its resulting performance. A general network model was presented to describe a filter structure comprising a random network of interconnected pores and the tortuosity of a filter and its resulting performance. It was found that that the studies allow a simple scaling allows the performance curves over a wide range of the filter material properties to be mapped onto a single master curve [36]. In this context, an attempt was made to provide the deposition with a uniform framework through the parallel fibers of the fiber array.
In experimental studies using X-ray techniques, Song et al. have shown how the structure in the spaces between the fibres and the deposition of dendritic structures in the porous structure of a fibrous filter develop until clogging occurs [145]. It was found that clogging within the filter and fiber interspaces affects the particle loading characteristics of the entire filter media. The largest proportion of particles is deposited in the face regions of the filter structure (in the depth of 0-200 μm), which also affects the further deposition process. In further experimental studies, Song et al. conducted in-depth investigations into the clogging of particle structures within a filter [146]. These investigations involved the development and build-up of particle structures in the various phases of the filtration process, which were again performed using a X-ray micro-computed technique. In further studies Song et al. investigated the effects of particle bouncing and sliding on the collector during particle separation [147]. The results demonstrated that the separation of particle structures within the interspaces of the fiber changes during the entire process. Additionally, the study

examines the structural alterations to the filter medium during loading. In contrast to previous studies in this overview, which employed a stiff fiber matrix, the present study utilizes a stretchable filter fiber array. This approach enables the prediction of fluid flow and permeability behavior in such a medium.
With regard to this fact, Shi et al. developed a machine learning process for predicting permeability in a deformable porous medium [140]. This process was trained on data obtained from a stretching experiment. It was demonstrated in previous studies that the permeability of the filter medium changes with stretching, depending on the orientation and previous alignment of the fibers. This is important for analyzing the processes inside the filter. The focus on a deformable and changeable medium represents a novel approach.

The starting point for the stretching experiments in this studie is always a separated particle structure consisting of polydisperse particle material on the fiber array. At the beginning of the stretching experiments, the fiber array is loaded with a particle structure in either the unclogged or clogged state. The unclogged state has unfilled fiber interspaces, allowing airflow to pass through. In contrast, the clogged state has completely filled fiber interspaces with particulate material. These loading conditions represent the filter's states before and after clogging of the upstream filter layers. The morphology of the particle structure was examined in both compact and dendritic forms, both in unclogged and clogged states. The loading conditions of the fiber array were defined based on previous investigations by Müller et al. and the investigations on the unique development of the particle structure on a stretchable fiber array [92, 91, 105]. Szabadi et al. and Zoller et al. have already demonstrated dendritic structures on a single fiber [180, 148].
During the subsequent stretching tests, a fiber array was stretched for the first time in five stretching cycles. The stretching velocity is varied between $0.6\,mm\,s^{-1}$ or $1.2\,mm\,s^{-1}$ as in previous studies with the single fiber [107]. During all stretching tests the particle loaded fiber is approached by a particle-free air flow with a velocity of $0.05\,m\,s^{-1}$ or $0.8\,m\,s^{-1}$.gate this simplified type of stress Similar to the single fiber experiments conducted by Poggemann et al., the fibers in this study were initially stretched only in the axial direction to invest its application [107]. The study recorded the size and moment of detachment during the stretching process to quantify the rearrangement and detachment of particle structures, as in previous studies. Experiments will also be conducted to obtain a qualitative understanding of the fracture process and rearrangement on the fiber array for the first time. The aim of this analysis is to complement the thorough investigation of structural modifications presented in [105]. Further, the size analysis of the detached particle structures and their moment of detachment is particle structure. To evaluate the overall effect of stretching on the amount of deposited particle material on the fiber array, the total relative particle occupancy of the array is calculated after each stretching cycle.
In addition to the stretching tests with a fixed fiber distance and axial stretching, for

the first time preliminary tests with a flexible fiber distance have been investigated. In this experiments the fiber distance can be flexibly changed by at least 27 μm during the elongation process by means of a variable angle of the fiber clamping. This biaxial stretching is intended to show the change in pore size during the stretching of an overall filter. As a result a multidimensional stress state is generated in the deposited particle structure due to the elongation and simultaneous change in fiber distance. Cracks can emerge within the due to stretching of substrate as shown by Beuth et al., Natha et al. and Thouless et al. [153, 12, 93, 94]. Theoretical considerations of stress distribution have been made by Jia et al. and Ochai et al. [95, 57]. The fibers are not only stretch in the direction of the fiber axis, but also shift relative to each other in the axial direction with different deflections. The rearrangement and breakage of the particle structure on the fiber array were analyzed using only qualitative image analysis in the direction of the particle-free airflow. This study aims to investigate the influence of different process parameters, such as stretching velocity and air flow velocity during stretching, on the rearrangement and detachment behavior of particle structures from the fiber array. The rearrangement and detachment of particle structures are direct consequences of multidimensional stress induced by stretching.

7.2 Material and Methods

7.2.1 Fibers and particulate material

All studies were conducted using stretchable polyurethane filter fibers that can be stretched up to 75 %. The fibers have an average diameter of 82 μm and exhibit a crimped shape in their initial state. Stretching the fibers to 55% elongation results in a diameter reduction of approximately 18%. The elastic modulus of the fiber is measured at 0.49 MPa.
As in previous studies, inert polydisperse Spheriglass 5000 CP00 particles (Potters Industries LLC) was used in all experiments [180, 107, 148]. The particle size distribution shown in Figure 7.1 was determined by light scattering analysis using Helos, Sympatec. All analyses refer to the $x_{50,3}$ = 7.82 μm of the particle size distribution. Prior to use in the loading procedure, the particulate material was dried in an oven for a minimum of 48 hours to facilitate dispersion.

7.2.2 Stretching device

A specially designed fiber clamping device (Figure 7.2 a)) is used to hold the fibers during the loading and subsequent stretching of the fiber array. The device allows the clamping of five parallel filter fibers between two opposing combs with a defined tooth spacing of 246 μm and a distance of 51.9 mm. In this respect, the clamping device is similar to the one used by Poggemann et al. to study the development of morphology [108]. As in previous studies, a desired fiber elongation of 38.5% is achieved by stretching 22 mm. In contrast to the previous study, the holder shown here has a piezoelec-

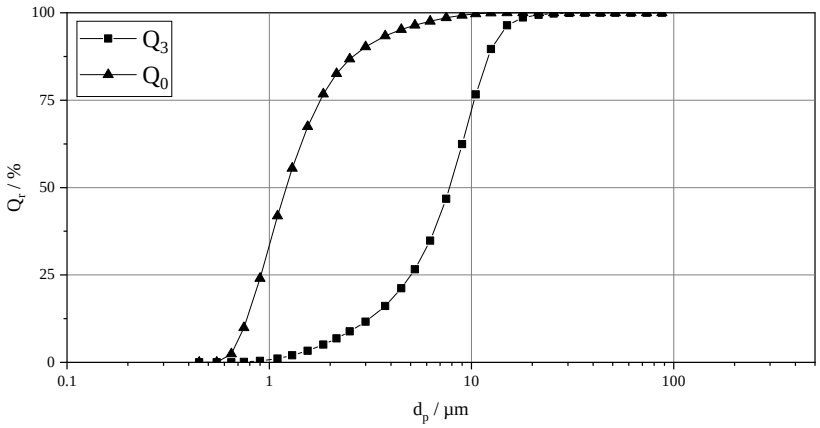


Figure 7.1: *Cummulative number based (Q_0) and volume based (Q_3) size distribution of the used polydisperse particulate material Spheriglass5000CP.*

tric motor (PI, Q521-230) under each of the two clamping blocks to allow a maximum movement of 11 *mm* per side. Due to the strength of the five elastic fibers, the maximum stretching velocity is limited to a maximum of 1.2 $mm\,s^{-1}$. In order to change the

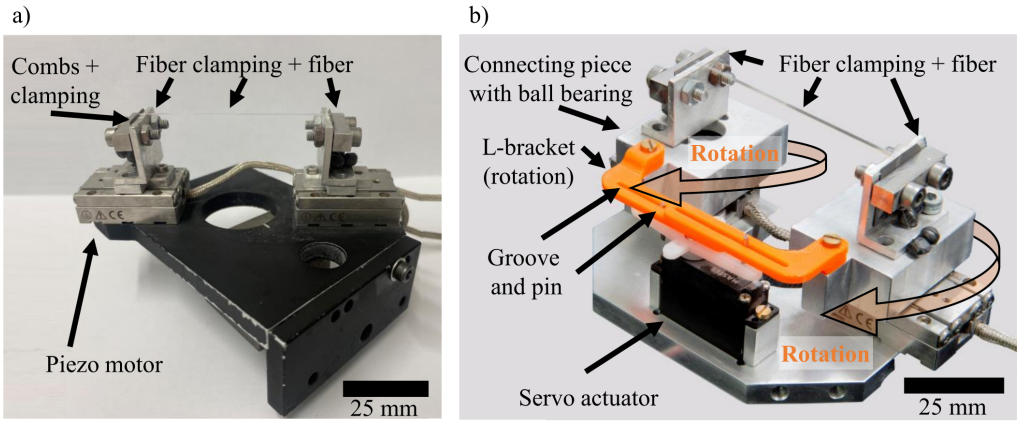


Figure 7.2: *a) Clamping device for just stretching the fiber array b) Clamping device for simultaneous stretching and changing the fiber distance by rotating the clamping combs.*

fiber distance during the stretching process, there is a second fiber clamping device (see Figure 7.2 b)) in which the clamping of the fibers is rotatably mounted. The objective is to achieve simultaneous strain by changing the fiber spacing, creating a biaxial stretching and multidimensional stress state in the particle structure. Piezo motors are used for the linear movement of the fiber clamping device for uniaxial stretching. To enable rotation of the fiber clamp around the vertical axis, horizontal ball bearings are mounted between the motors and the fiber clamp. The clamps are affixed to the side of a model servo using a 3D-printed L-bracket (see Figure 7.2 b)). The servo gearing

enables various rotation angles of the attached fiber clamp. The fiber clamp's rotation and linear movement are achieved by connecting a pin in a groove. The fiber distance can be reduced or increased by up to 27 μm by rotating by up to 45 degrees. Figure 7.3 shows the main principle of enlargement of fiber distance using rotation of parallel fibers. This principle has already been used in a simplified ans static form by Müller et al. Both clamping constructions are mounted on aluminum plates for easy handling [91]. Prior to each load, the fiber array is cleaned with compressed air and isopropanol. All five fibers are replaced after three experiments.

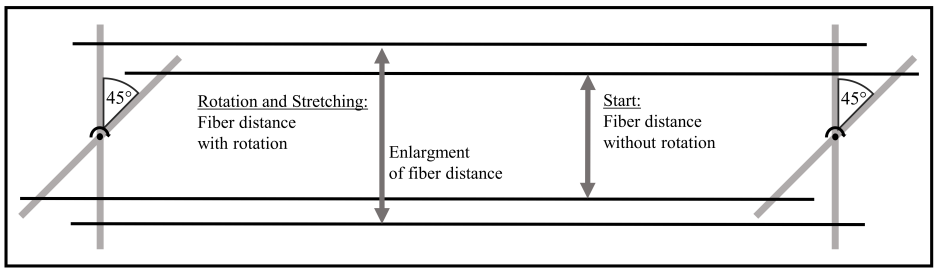


Figure 7.3: *Schematic representation of two clamped fibers. It is possible to enlarge and reduce the fiber distance by rotation of the fiber clamp. Here the increase in the fiber spacing.*

7.2.3 Aerosol Generation and Loading Procedure

The aerosol, with a volume flow of 26.3 $l\,min^{-1}$ (feed flow), was generated using the SAG 410/U by Topas, a system previously employed in studies by Zoller et al., Wang et al., and Papapostolou et al.[163, 98, 180]. Figure 7.4 shows the Particle dispersion was achieved by sucking particulate material from a steel ring through a venturi nozzle. Additionally, the aerosol underwent neutralization using an 85Kr-neutralizer. A part of the generated aerosol was discarded after particle removal through a HEPA filter. The remaining loading flow passed through the inlet pipe equipped with a flow rectifier (diameter 16 mm) and entered the loading chamber, approaching the fiber array. The particle loading process for the array was executed within a 16 mm free jet airflow at varying flow velocities. Downstream of the fiber array, another HEPA filter was employed to remove any remaining particulate material. The mass flow was controlled using a MFC. This detailed process ensured precise control and monitoring of the loading flow throughout the experiment.
Aim of the experiments is to compare different particle structure/loading conditions at different airflow velocities at the same particle concentration in the aerosol during the loading procedure.
The TIF is used to calculate the number of particles (polydisperse particle material) that have passed a defined control area over a given time interval considering the current air flow velocity. Therefore, loading was performed until a certain number of particles per cross section had flowed towards the array. The basic considerations for this form of particle and particle count detection are based on the investigations of

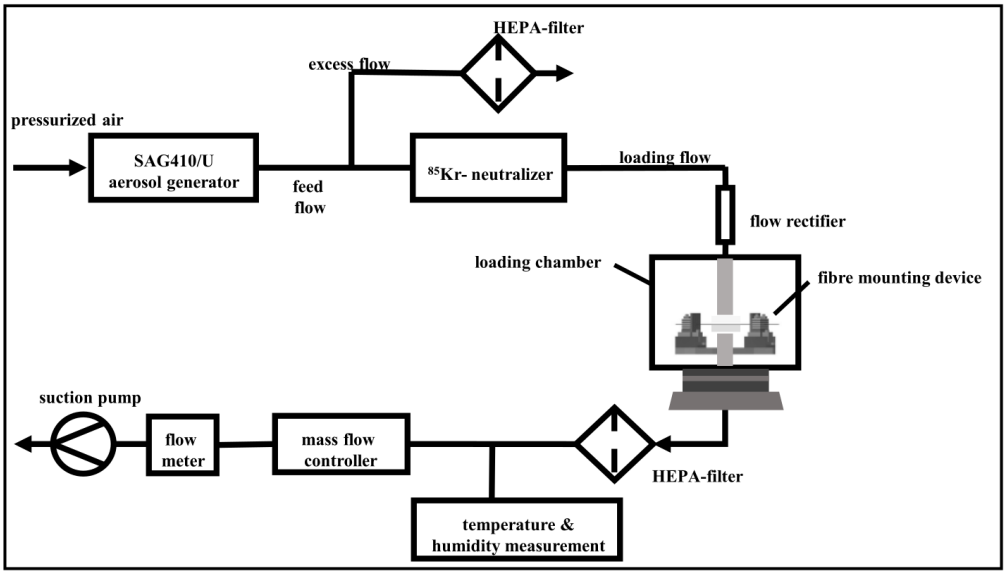


Figure 7.4: *Schematic setup to produce an aerosol containing glass spheres and the deposition on an fiber array that is clamped at the fiber mounting device [107].*

Raasch et al.[115]. First, the particle flux density (j_i) is calculated using the particle concentration c_p of the aerosol and its velocity u (see eq. 7.1).

$$j_i = c_p \cdot u \tag{7.1}$$

The TIF in $particles\,per\,mm^2$ can be obtained by combining the particle flux density j_i with the respective loading time t for a specific time interval.

$$TIF = J(t) = \int_0^t j_i \, dt \tag{7.2}$$

$$TIF = J(t) = t \cdot j_i \tag{7.3}$$

For a constant j_i:

$$TIF = c_p \cdot u \cdot t \tag{7.4}$$

In earlier studies by Poggemann et al., the progression and clogging of the fiber interspaces of the array by particles was investigated in detail [108]. This process, also known as clogging, is of great interest as it marks the start of the transition phase and the increase in the pressure loss curve of a filtration process. It divides the usual filtration process of depth filtration into a first section in which further aerosol can still flow through the fiber inerspaces. In the second stage of the advanced filtration process, the spaces between the fibers are blocked by particle material. The particle structures on the individual fibers grown together to form a clogged structure. This is followed by a

steep increase in pressure drop due to the formation of a layer of dust inside the filter and on the surface of the upstream side.
In order to adequately characterize the rearrangement and detachment behavior of particle structures, it is necessary to study different types of particle structures. Therefore, the morphology of the particle structure on the array is varied. Either dendritic or compact structures are deposited on the fiber array, depending on the Stokes number. For each of these structures of different morphology (compact and dendritic), a distinction is then made between a non-clogged and a clogged structure depending on the TIF. The corresponding deposition parameters for all states are listed in Table 7.1.

Flow velocity m/s	Volume rate L/min	Re -	St -	Pe -	TIF $10^8 \# \, mm^{-2}$ (non-clogged structure)	TIF $10^8 \# \, mm^{-2}$ (clogged structure)	Morphology
0.146	1.76	0.78	0.82	3.9	1.73	4.06	dendritic
0.65	7.84	3.48	3.62	17.3	1.73	4.06	dendritic
1.2	14.48	6.42	6.70	32	1.73	4.37	compact
1.8	21.78	9.64	10.05	47.9	1.73	6.05	compact

Table 7.1: *Dimensionless numbers of the loading procedure*

7.2.4 Stretching Procedure

All uniaxial stretching experiments without changing the fiber distance are performed with a non-clogged and a clogged particle structure on the fiber array. In addition, a further set of experiments was performed on the fiber array blocked by a particle structure in which the fiber distance is reduced or increased by 27 μm. In the present investigation, a sequence of five consecutive stretching cycles was performed. Elongation velocity and airflow velocity remained constant throughout the stretching and relaxation process of the fiber. All experimental procedures were performed in triplicate. Throughout the stretching cycle, a particle free airflow was directed towards the fiber. Table 7.2 summarizes the experimental parameters for the stretching experiments. The unblocked area within/in the fiber interspaces was analyzed at the end of each stretching cycle using image analysis techniques as described in Section 7.2.6. The size of particle structure fragments are measured with the LSDS (quasi in situ) during each stretching cycle.

7.2.5 Experimental Setup for Size Characterization

For the measurement of the scattered light equivalent size of the detached particle structures, the specially constructed laser light measurement technique is available [64, 168, 107, 182] (see Figure 7.5). In the setup of the measurement technique, a laser with the wavelength 532 nm is expanded to a 16 mm wide and 2 mm high laser-light sheet. During stretching a particle-free airflow is approaching the fiber array. Further

stretching velocity / $mm\,s^{-2}$	air flow velocity / $m\,s^{-1}$	stretching length / mm	change of fiber distance / μm
0.6; 1.2	0.05; 0.8	22	0; ±27

Table 7.2: *Parameters for the stretching process. All parameters were combined and applied in each range of particle structure morphology. Experiments are performed, both with and without changing the fiber distance.*

a camera is used in direction of airflow to determine the RFPI. When the detached structures from the array pass the laser band, light is scattered accordingly and converted into an electrical signal using a photomultiplier. The assignment of the signal height to the corresponding scattered light equivalent size of the particle structures is done by a previously performed calibration with glass spheres. For the measure-

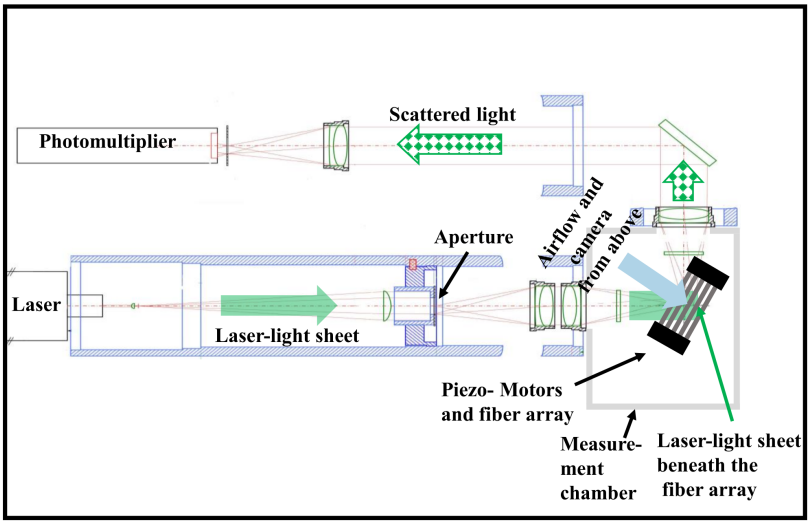


Figure 7.5: *Schematic diagram of the laser thin film measurement system. An expanded laser beam (thin sheet) passes beneath the fiber array. The scattered light within the measurement area is focused onto a photomultiplier and converted into electrical pulses.*

ment of structures detached consecutively from a fiber array in rapid succession, the measurement technique was improved with respect to the counting rate and the identification of superimposed signals using software. By analytically approximating the acquired signal structure, superimposed signals from two particle structures following each other quickly can be identified and considered individually. This case was expected for a fiber array with a significantly larger amount of deposited particle material. The measurement range of the laser light measurement technique is from 90 μm to 2000 μm. The sampling interval is $1 \cdot 10^6\,s$, which means that even structures deposited in rapid succession can be detected with a minimal signal length of around $1 \cdot 10^{-4}\,s$.

7.2.6 Determination of relative projection area of free space in the fiber interspaces

To capture the rearrangement and detachment of the particle structure on the fiber array during the stretching process, a Basler camera acA4024 29uc for video recording is used in direction of airflow. The camera has a resolution of 4024 x 3036 pixels and a variable frame rate up to 31 fps in full resolution.
By using a camera system mounted in the direction of flow, it is possible to observe the stretching process and thus quantify the rearrangement of the particle structure on the fiber and in the inner interspaces of the fiber by image analysis. The perspective is the same as in the array loading studies [108]. The illumination takes place via red ring light, which illuminates in the direction of flow. To quantify the fractured structure and the free flow area within the particle-loaded array, the relative free projection area in the interspaces of the fiber is calculated. The calculation of RFPI can be found in equation 7.5.

$$RFPI = \frac{1-A_{particle,i}}{A_{particle,0}} = \frac{1-A_{total}-A_{pore,i}}{A_{total}-A_{pore,0}} = \frac{A_{pore,i}-A_{pore,0}}{A_{total}-A_{pore,0}} \tag{7.5}$$

Herein A_{total} denotes the overall area of the fiber array interspaces in the non-loaded stage, $A_{pore,0}$ is the area of pores at the beginning of the stretching process (after the loading process) and $A_{pore,i}$ the area of pores after the i-te stretching cycle. Figure 7.6 further shows the processing steps from the preparation of the projection images to the calculation of the cleaning efficiency or the RFPI in the inner fiber interspaces in a flow chart. The image section at the time directly after loading can be seen at the top, whereby the fiber environment was removed with a Matlab routine. The correct section of the image was cropped, rotated and binarized. As shown in the second image from the top in Figure 7.6 the particulate material is colored white. In the next step/image the image was inverted in order to be able to analyze the unoccupied area within the fiber interspaces. In the third image, the white area then represents the unblocked area in the particle-loaded fiber array A_{pores}. The size of this area is determined by counting the pixels. The fourth image from the top (Figure 7.6 shows the same section of the fiber array after 5 stretching cycles. The processing steps cropping, binarizing and inverting have already been carried out. The fiber environment was also hidden using the Matlab routine. During the 5 stretching cycle, particle material was clearly detached from the fiber array, which increased the unblocked regions on the fiber array ($A_{pore,5}$. This can be seen as the white area in the cropped image. The RFPI provides insight into the changes that occur within the fiber array interspaces after each stretching cycle in the initial load. The following interpretations can be made:

- $RFPI > 0$: release of clogged inner pores (complete release if RFPI=1)
- $RFPI = 0$: No changes in the free inner pores
- $RFPI < 0$: Clogging of the inner interspaces of fiber array due to rearrangement

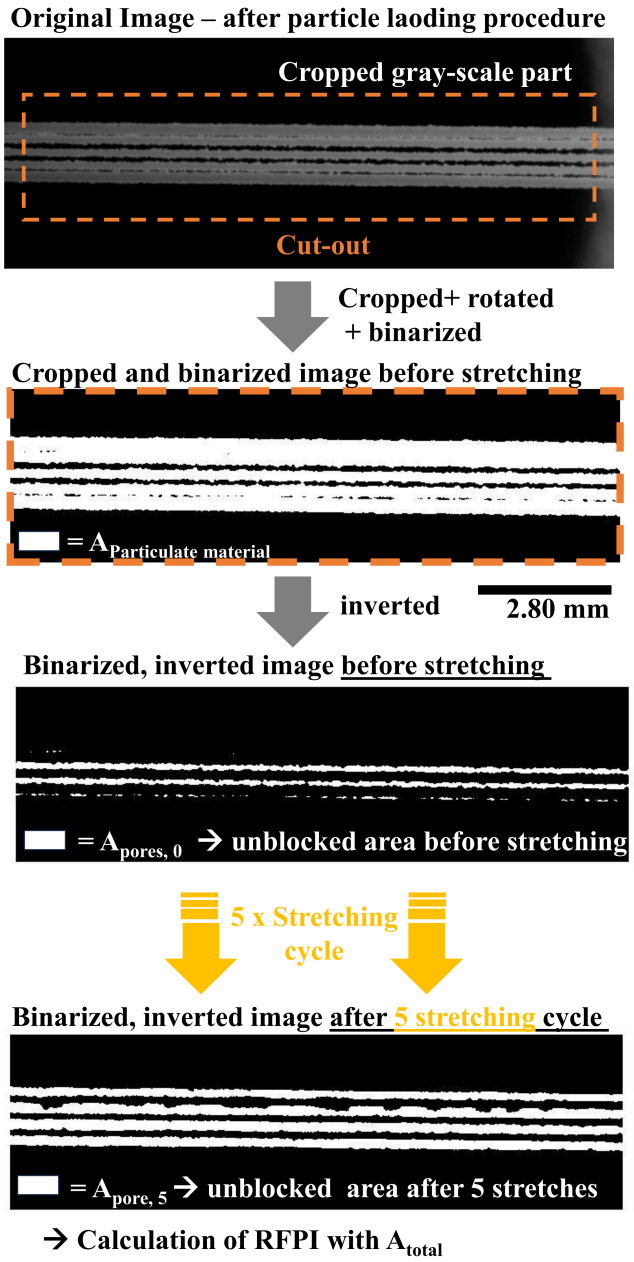


Figure 7.6: *Schematic procedure for determining the proportion of unblocked area in the fiber interspaces of the array.*

The evaluation process involves the usage of a custom-developed MATLAB routine which is given in the Supporting Information (SI). The application of tensile forces to the fibers in the experiment did not result in any significant alterations to the measured RFPI values for the fiber array. To illustrate this, five consecutive strains were performed without the addition of particle material. There were no significant changes in the projection area. The corresponding images of the experiments can be viewed in the SI.

7.3 Results and Discussion

7.3.1 Morphology of particulate structure on the fiber array before clogging

Figure 7.7 depicts macroscopic images of the generated particle structure with non-clogged fiber interspaces (TIF=$1.73 \cdot 10^8 \, \# \, mm^{-2}$). The structures on the fiber are not yet fully clogged or grown together and represent the non-clogged structures which are used for the first set of stretching experiment.

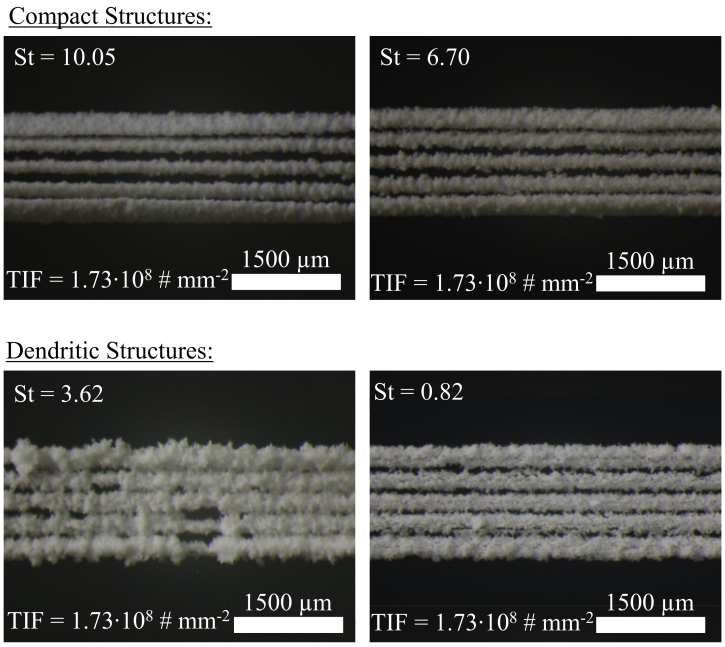


Figure 7.7: *Morphology of the non-clogged particle structures on the fiber array as a function of the Stokes number.*

The morphology of the non-clogged particle structures on the fiber array is a function of the Stokes number. All structures shown here were taken from the particle loading process of the TIF listed in Table 7.1. The preliminary investigations on the development of the structures on the fiber array for high stokes numbers can be found in the studies by Poggemann et al [108]. Compact structures (Figure 7.7, TOP) show minimal particle bridging, which leads to large horizontal pores between the fibers. These

compact structures tend to form at the stagnation point of the fiber.
In contrast, irregular dendritic structures (Figure 7.7, BOTTOM) show increased bridging due to their increased contribution to diffusive deposition, which leads to the formation of numerous small interspaces between the fibers. The particle structures show an increased number of small dendritic branches growing into the fiber interspaces as observed in the investigation by Szabadi et al. [150]. In addition, a increased porosity of the particle structure is clearly recognizable.

7.3.2 Detachment of particle structures from a fiber array before clogging

7.3.2.1 Development of structures during uniaxial stretching

Compact and dendritic structures exhibit distinct differences in their detachment behavior during stretching. For a compact structures, the detachment process from the fiber array can be divided into three steps. These steps are illustrated in Figure 7.8 on the left. In the first phase, the compact particle structure moves in sync with the

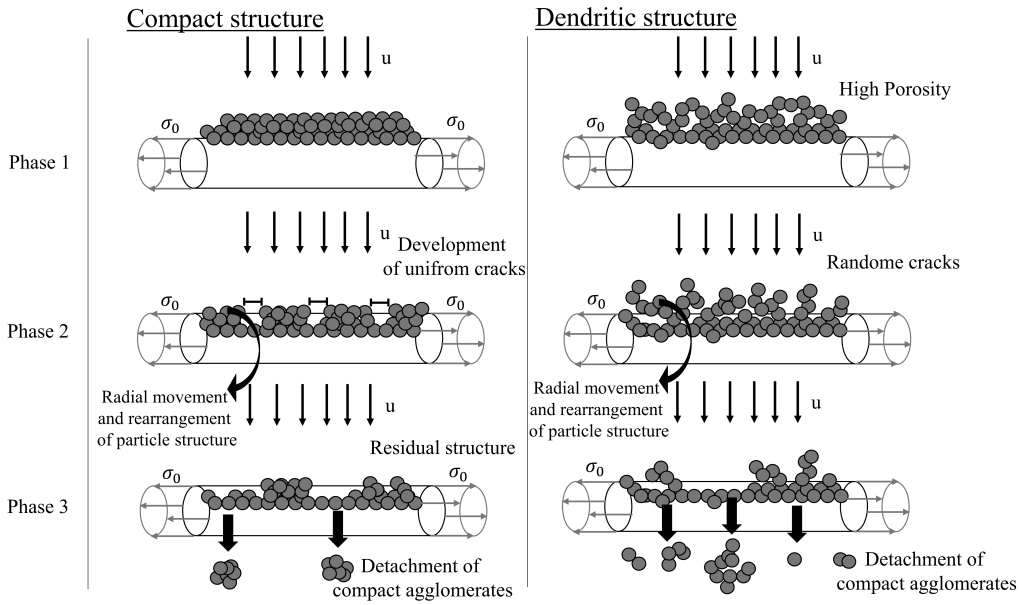


Figure 7.8: *Schematic of the three phases of detachment. Left: compact structures, Right: dendritic structures. Crack building, radial rearrangement of particle structures and detachment are visible.*

fiber experiencing elongation, without any formation of cracks. The deposited particle structure remains attached. During this phase, the adhesive forces between particles dominate over the forces induced by fiber stretching. This prevents the formation of cracks within the particle structure.
Usually at one-third of the desired fiber elongation, cracks begin to develop within the particle structure, although no particle agglomerates have yet separated from the structure. From the camera perspective in this investigation, it is not entirely clear

where the crack occurs within the particle structure. However, since the individual particle structures on the neighboring fibers of the array are still without any real connections, it cannot be assumed that the cracks of the parallel structures are influencing each other. However, the structure is slightly loosened from the fiber surface and individual particles are rearranged.
The second phase is marked by the growing of cracks. As the fiber stretching continues, the cracks expand and generate multiple small particle structures on the fiber. Due to the lack of contact to neighboring structures, these small particle agglomerates have significantly less stability than the initially formed particle structure before stretching. As stretching proceeds, the small particle structures start to rearrange in radial direction gradually with each fiber of the array. The particle structures can move into the interspaces of the fiber array (not shown here for the sake of clarity). Regardless of the direction of radial rearrangement, and regardless of whether the structures move into the fiber interspaces, this results in an increase in the face area of the particle structure. This leads to an increase in stress due to flow forces. In addition, the angle of attack of the external force caused by the flow changes. The movement of particle structure is mainly due to the stretching of the fiber which might induce a slight rotation of the fiber that is finally transferred to the particle structure that rearrange in radial direction in the following. The third phase of the stretching process starts with the detachment of the first particle structures.
The detachment behavior of dendritic structures can also be divided into three phases, similar to compact structures. Due to the increased contribution of diffusive deposition mechanisms, dendritic structures tend to deposit uniformly on the flow-facing side of the fiber while the compact structures at high stokes numbers grow mostly towards the upstream direction in a narrow range around the stagnation point. In addition, the typical small dendritic branches are formed on the sides of each fiber and are thus automatically perpendicular to the air flow during stretching procedure.
In the case of dendritic particle structure on the array, the stretching process starts in phase 1 with the movement of the particle structure with the stretched fiber.
In the following cracks are formed within the particle structure (phase 2). However, the resulting cracks do not emerge throughout the entire particle structure as they just occur more local due to higher porosity of the particle structure. In addition, particle structure start to move slightly perpendicular to the fiber axis. This radial rearrangement of the structures is not nearly as pronounced as with the compact structures. Presumably, there is also a difference in the overall adhesion between the fiber and the particle structure, which can also be explained by the lower porosity and fewer contact points.
With further fiber stretching, only the outermost dendrites of the particle structure detach, which marks the start of phase 3. After the first detachment of the dendrites, larger structures start to detach and peel off from each fiber.
In all experiments with compact and dendritic particle structure, a residual structure remains on the fiber surface after detachment of particle structures during stretching.

This indicates disruption of particle-to-particle bonds rather than particle-to-fiber bonds.
If there are remaining particle material on the fiber after the stretching, during relaxation of the fiber the individual structures may move radial back to the position before stretching. The cracks within the dendritic structures are clogged if there are locally neighboring particle structures on the fiber. In the case of compact structures small agglomerates may do not detach during the stretching, compact structures can remain suspended in the spaces between the fibers and are slightly compressed due to the relaxation of the fiber. Further they move in in radial direction during the relaxation process. If particle structure remain in the fiber interspace they are partially supported by the neighboring fibers. Though the cracks are mostly closed, but the changed surface structure clearly shows that a rearrangement has taken place.
In experiments with compact and dendritic structures, the previously formed cracks are closed during relaxation, and during subsequent stretching, the structure tends to fracture again preferentially at the same locations as before. Considering the number of detached agglomerates, significantly fewer particle agglomerates separate during relaxation than during stretching. Therefore, the following analysis focuses only on the agglomerates detached during stretching.

7.3.2.2 Development of Moment of Detachment during uniaxial stretching

In the following plots, the moment of detachment of particle structures refers to the corresponding elongation of the fiber at the moment of detachment during the elongation process. A plot over elongation was chosen for this plots because it is independent of the elongation rate of the fiber during the stretching process. The same form of illustration was chosen in the previous publication for the detachment of particle structures from a single fiber [107]. From the data, patterns can be extracted that provide information on how often and at what elongation the collector must be stretched to detach particle structures. In addition to the morphology described above, the stretching speed and the air flow velocity are varied in experiments.

The graphic in Figure 7.9 plot the size of the released particle structure over the fiber elongation at the moment of detachment for each detachment event. Detachment events during the first stretching cycle are represented by solid symbols, while events in the 2.-5. cycle are consolidated marked by outlined symbols. Delayed release of particle structures after the end of fiber stretching may result in the detection of particle structures beyond the intended and advertised range of fiber elongation. These particle structures were assigned an elongation of 38.5 % (maximum elongation) in the application.
Regardless of the morphology (St=3.62; St=10.05) of the particle structure on the fiber and the stretching velocity, during the first cycle almost no particle detach in the first

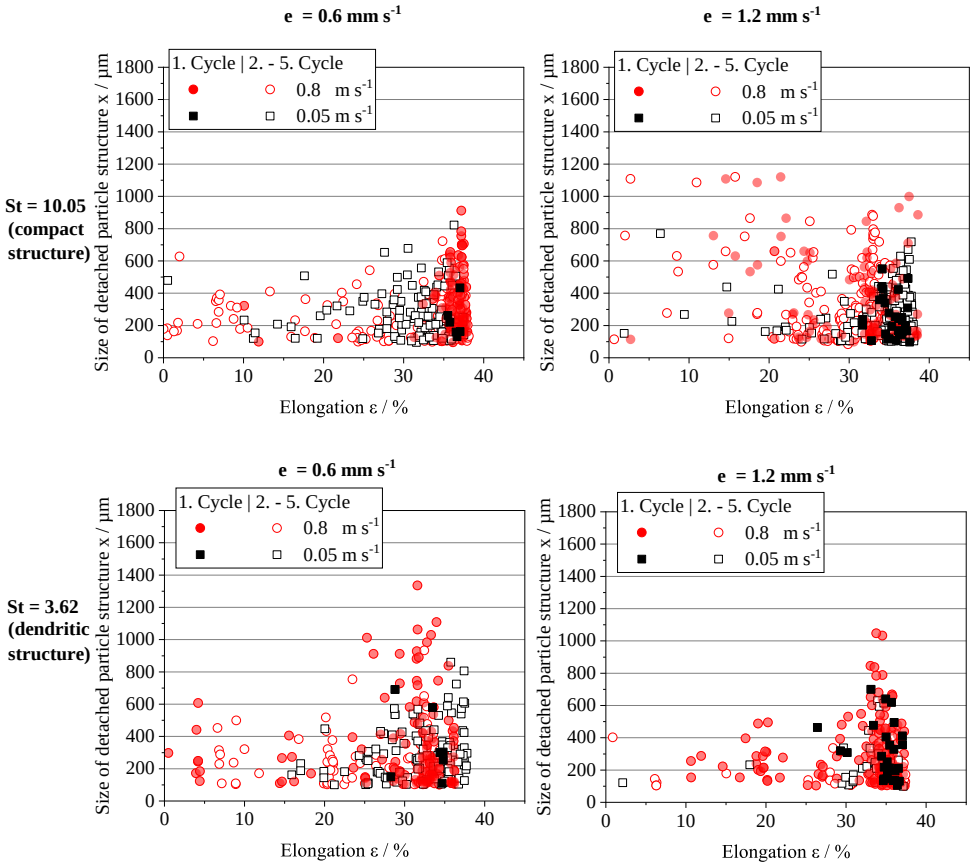


Figure 7.9: *Size of the detached particle structures as a function of the structural morphology (TOP: St = 10.05; BOTTOM: St = 3.62; Left: 0.6 mms^{-1}; Right: 1.2 mms^{-1}), as well as the elongation and flow velocity.*

25 % of stretching at low airflow velocities of 0.05 $m\,s^{-1}$. It is assumed that the force of the airflow is not strong enough to detach the particle structure from the fiber in individual agglomerates. In all experiments regardless the morphology (St=3.62; St=10.05) the most frequent area for detachment is the area of 20-38.5 % of stretching which is independent from the corresponding stretching cycle. Looking at all experiments with high air velocity (0.8 $m\,s^{-1}$), there is a first detachment of particle structures at stretching of 5 - 10 %. The detached particle structure in the 0.8 $m\,s^{-1}$ experiments (St=3.62; St=10.05) is on average larger than the structures detached within the experiments
In the second to fifth stretching cycle some particle structure detach at less than 5 % of stretching. This observation is independent of the morphology of the particle structure on the fiber. The successive stretching causes a loosening of the deposited particle structure due to induced cracking, which also leads to detachment at lower flow velocities.
In the experiments with low stretching velocities the majority of particle structures detaches in the 2.-5. cycle. In the experiments with a high stretching velocity of 1.2 $mm\,s^{-1}$

most particle structures detach at the end of the first stretching cycle in the range of 25-28 % of fiber stretching. For a possible application in filtration, this means that the collector only needs to be stretched slightly faster in order to achieve improved particle detachment at the end of the first cycle, but the flow velocity can be kept constant at 0.05 $m\,s^{-1}$. In general, the effect of stretching velocity on the moment of detachment is less pronounced for dendritic (St=3.62) structures than for compact (St=10.05) structures.

7.3.3 Development of relative free projection area

Observation of the RFPI allows quantitative statements about the state of the interfiber spaces and pores after the stretching processes. The results presented here discuss the effects of flow velocity, stretching velocity, and initial morphology of the deposited particle structure. The data provides a more holistic view of the detachment process.

Figure 7.10 shows the RFPI as a function of the number of stretching cycles for the compact structures at a Stokes number of 10.05 and 6.70, respectively. As a result of detachment of particle strucuture due to stretching, the RFPI increases with high air velocities of 0.8 $m\,s^{-1}$ for all stretching velocities. The reached RFPI values after 5 stretching cycle are regardless of the morphology (St=10.05; St=6.70) of the initial structure.

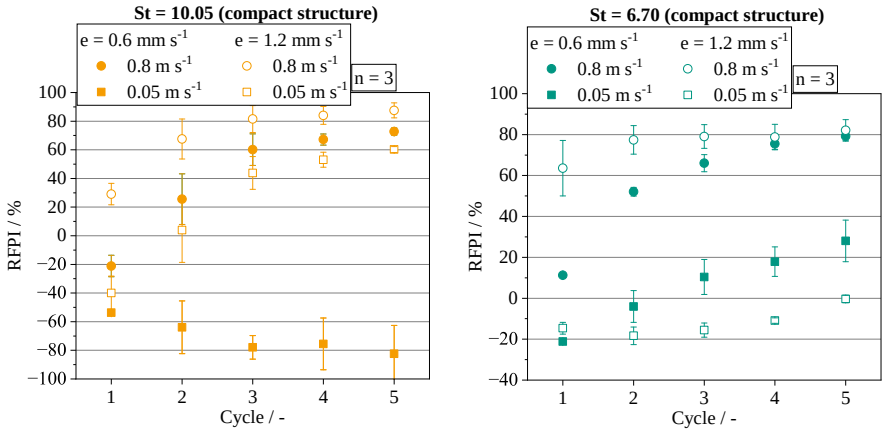


Figure 7.10: *RFPI of the stretching experiments with a compact particle structure on the fiber array.*

An increase in stretching velocity also enhances the RFPI, except in the experiment with a particle structure generated at a Stokes number of 6.70 and an airflow velocity of 0.05 $m\,s^{-1}$ during stretching. This single experiment show exactly the opposite. In general, an increase in the RFPI is always associated with a release of the interfiber spaces and a detachment of particle structures during the consecutive stretching cycle.
For the experiment with an airflow velocity of 0.05 $m\,s^{-1}$ there are negative values in

the first cycle for almost all experiment regardless the morphology (St=10.05; St=6.70) of the structure on the array. In these experiments the particle structure on the fiber move radial during stretching and remain within the fiber interspaces after relaxation (see Figure 7.11, Left and Right). The drag force of the air flow and the break up of the particle structure by stretching are not sufficient to achieve detachment at the fiber distance of 246 μm. Nevertheless in the most cases, except the experiment(St=10.05) and airflow velocity of 0.05 $m\,s^{-1}$, the RFPI value continues to increase as stretching cycles 2-5 progress. The bridges and agglomerates within the interspaces break during the following stretching cycle. In the case of the single exception, which is represented by the tests at St=10.05 and an airflow velocity of 0.05 $m\,s^{-1}$, negative values of down to -54 % are reached after a single stretching cycle (Figure 7.10, Left). Further the RFPI decreases with each subsequent stretching cycle, reaching as low as -80% after 5 stretching cycle. In these experiments the particle structure on the fiber move radial during stretching and remain within the fiber interspaces after relaxation. (see Figure 7.11, BOTTOM). The drag force of the air flow and the break up of the particle structure by stretching are not sufficient to achieve detachment at the fiber distance of 246 μm.

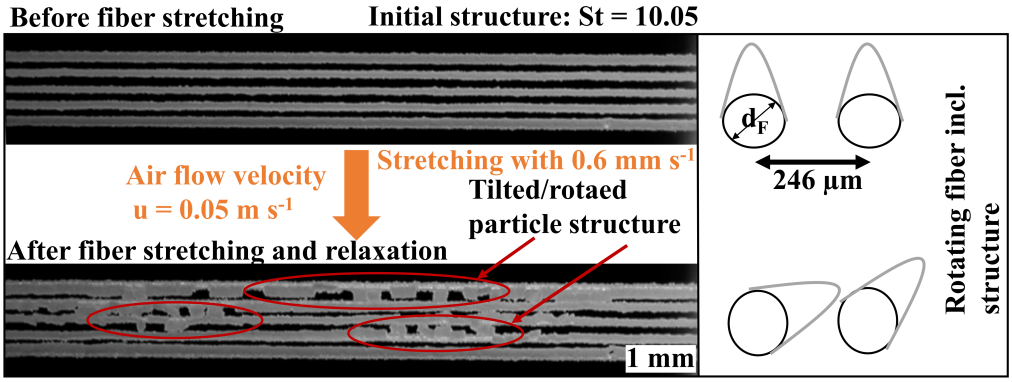


Figure 7.11: *Left: Image section of the fiber array before stretching and after the 2nd stretching cycle for compact structures with a Stokes number of 10.05. Right: Schematic representation of the tilting of the particle structures into the fiber interspaces during stretching. No reversal of the tilted particle structure after relaxation of the fiber.*

Since both compact and dendritic structures can occur in filtration processes using depth filters, it is important to investigate the detachment behavior of a dendritic initial structure from a fiber array during fiber stretching, in addition to the detachment behavior of compact structures. The initial structures formed under the corresponding flow conditions (St=3.62 and St=0.82) can be found in chapter 7.3.1. Figure 7.12 shows the corresponding values for the RFPI that have been reached during the five stretching cycles with simultaneous airflow.
The RFPI increases in all cases, regardless of the initial dendritic structure (St=3.62; St=0.82), flow velocity, and strain rate, with an increasing number of strain cycles. The qualitative behavior is similar, although the slope varies.
For both initial structures (St=3.62; St=0.82), a significantly lower increase and a final

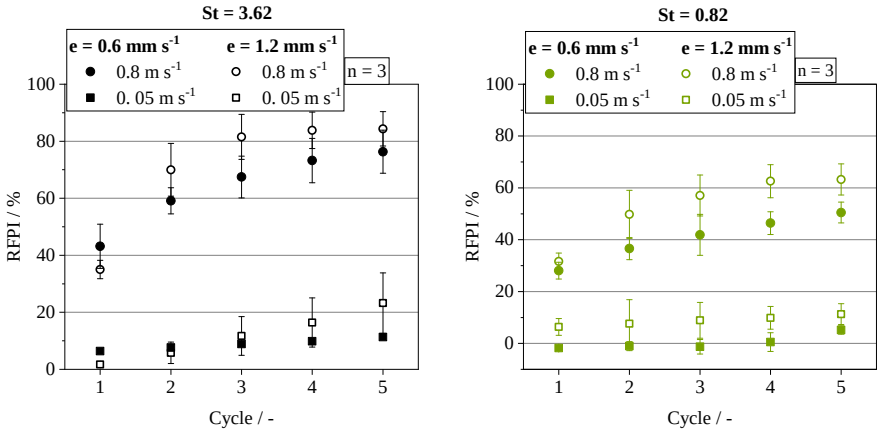


Figure 7.12: *RFPI plotted versus the number of stretching cycles for the investigated non-clogged dendritic particle structures (St=3.62 and St=0.82) on the fiber array for different air flow and stretching velocities*

value below 25% can be seen in the experiments with 0.05 $m\,s^{-1}$ flow velocity. It can also be seen that the highest final values for all experiments are obtained for the combination of a strain rate of 1.2 $mm\,s^{-1}$ and a flow velocity of 0.8 $m\,s^{-1}$, regardless of the initial structure. The values of RFPI for the experiments with a strain rate of 0.6 $mm\,s^{-1}$ are always lower than those with 1.2 $mm\,s^{-1}$, regardless of the initial structure and the incident flow velocity.
Further, there are no significant negative values of RFPI at the beginning of all experiments, which obtains that there is no rearrangement and rotation into the fiber interspaces of neighboring fibers during the stretching process as observed with the compact structure. Whether the particle structure remains on the fiber or the structure detaches during stretching.
In all experiments (St=3.62; St=0.82), regardless of the initial structure, it can be seen that increasing the flow velocity from 0.05 $m\,s^{-1}$ to 0.8 $m\,s^{-1}$ results in a significant increase of RFPI and also in the final values.

Overall lower final values of RFPI in the experiments with an initial structure deposited under deposition conditions of St=0.82 (see Figure 7.12, Right). For the experiments (St=0.82) with an incident flow of 0.05 $m\,s^{-1}$ there is very little increase and change in RFPI. The final value of RFPI is just under 5 %. It is assumed that the higher porosity of the initial structure results from the ability of the structure to respond to the induced stress states by strain through rearrangement.
Observations of the moment of detachment of the particle structures and their size in the region of the initial dendritic structures on the array show the size of the particle structures and the moment of detachment during the stretching cycle (see section 7.3.2.2)

7.3.4 Morphology and behavior of detachment of particulate structure on the fiber array after clogging

Figure 7.13 shows macroscopic images of the clogged fiber arrays. The particle structures are deposited on the fiber array before the stretching process. The loading process is stopped individually for each morphology type after closure of gaps at the corresponding TIF given in Table 7.1.

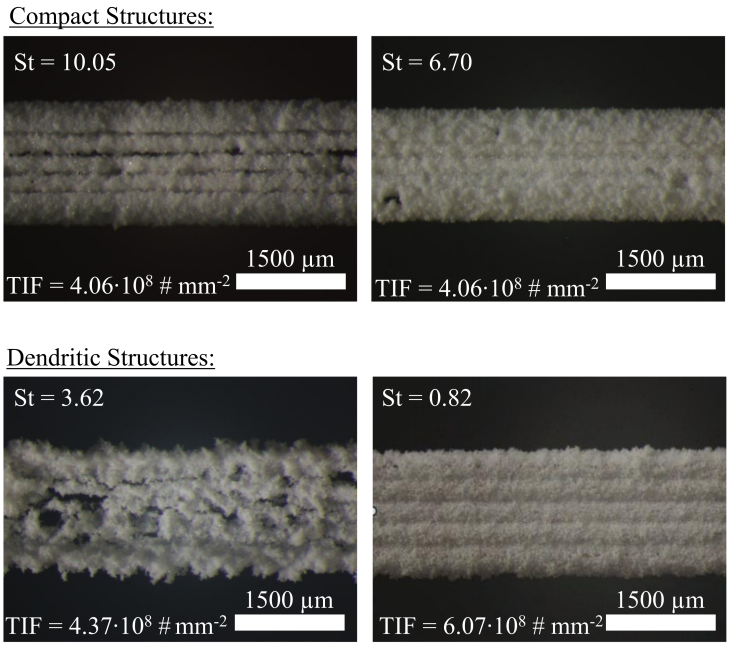


Figure 7.13: *Morphology of the clogged particle structures on the fiber array as a function of the Stokes number.*

The morphology of the clogged particle structures on the fiber array is a function of the Stokes number. Preliminary investigations on the development of the structures on the fiber array can be found in the studies of Poggemann et al [108]. Compact and clogged structures (Figure 7.13,TOP) are placed near to stagnation point of the fiber. The edges of the structure are mostly smooth and free of dendritic branches. If pores or gaps are still present, they tend to be elongated oriented parallel to the fiber interspaces.
All structures on the individual fibers grow into the fiber interspaces with increasing TIF. The structures on the outer fibers grow faster and therefore close the outer spaces more than the inner ones. In particular, the particle structure revealed at a Stokes number of 10.05, the structures on the two outer fibers are very large and wide. Some breakouts can be seen within the formed structures (at St= 3.62). These could be caused by particles or agglomerates within the aerosol hitting the fiber with high kinetic energy due to their mass and airflow velocity.

The two lower images in Figure 7.13 (BOTTOM) show the dendritic structures (St= 3.62; St=0.82) before the stretching experiment. Compared to the compact structures, the dendritic branches are clearly visible in both regimes of the Stokes number.
The branches are more pronounced in the structure with a Stokes number of 3.62. It can also be seen that in this structure, due to the higher kinetic energy of the particles caused by the aerosol velocity, significantly more breakouts occur in these structures (at St=3.62). Further the size of separated particles differs as they seem to be larger than for the structure at St=0.82 (see Figure 7.13, BOTTOM, RIGHT).
The structure formed at a Stokes number of 0.82, is completely clogged. Comparing the compact structure with the dendritic structure in the top view, it can also be seen that the dendritic structures grow much more into horizonal width starting from the fiber axis. zenith of the outer fibers than is the case with the compact structures.

7.3.5 Detachment of particle structures from a fiber array after clogging

7.3.5.1 General remarks on the behavior of clogged structures during stretching

In contrast to the non-clogged structures on the fiber at low TIF, clogged compact and dendritic structures exhibit significant differences in detachment behavior during stretching procedure. Nevertheless, three phases can again be distinguished here. Phase 1 of the behavior of the particle structure starts with the fiber stretching. During the first phase of stretching, the behavior of the particle structure is independent of the morphology of the structure and is similar to non-clogged structures. The structure on the fiber moves slightly with the stretching of the underlying fiber and undergoes elongation without visible cracking within the deposited structure (in phase 1). This observation may be attributed to the fact that the structure on the fiber rests higher on the substrate, causing a delay in cracking from the surface of the particle structure to the fiber. Rearrangement, as observed in the compact and non-clogged particle structures on the fiber array, plays a minor role at high airflow velocities. In some cases, small pores or weak spots in the structure may start to crack during stretching and phase 1.
In the second phase, visible crack formation is observed for the compact structures with increasing stretching. These cracks emerge perpendicular to the direction of stretching throughout the entire particle structure extending over multiple neighboring fibers. In contrast to non-clogged structures, several cracks appear within the clogged particle structure on the fiber array.
Due to their increased porosity, dendritic structures do not exhibit cracking across the whole structure on the array. Instead, the cracks emerge locally in the area of a fiber or only locally.
In the third phase, particle structures start to detach from the array on the fiber. Dendritic and compact structures detach from the fiber array, leaving a residual structure on the array.

In all experiments with a clogged structure on the fiber array (TIF=1.73 $\cdot 10^8$ # mm^{-2}) regardless of the morphology, no raidial rearramgement was detected in the first stretching cycle. Radial rearrangement of structures occurred only when particle structures were already detached from adjacent fibers. The rearragement process can then be based on the designs with an unclogged structure.

7.3.5.2 Moment of detachment of particle structures from an clogged fiber array

In addition to the experiments with a non-clogged structure on the fiber array, experiments were also carried out with a clogged particle structure on the fiber array.

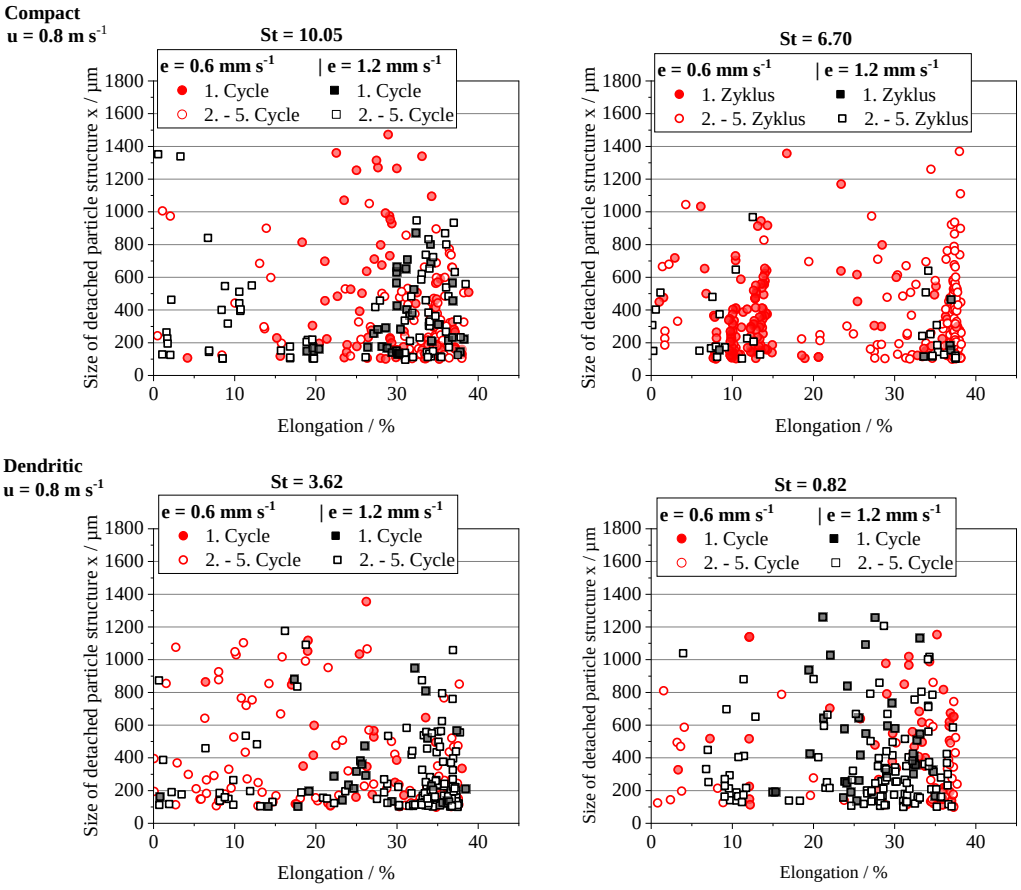


Figure 7.14: *Particle size as a function of structural morphology (BOTTOM: St = 3.62; TOP: St = 10.05), stretching velocity , and air flow velocity.*

The graph in Figure 7.14 plot the size of the released particle structure over the fiber elongation at the moment of detection for each detachment event. Detachment events during the first cycle are represented by solid symbols, while events in the 2.-5. cycle are consolidated marked by outlined symbols. Air flow velocity remained constant at 0.8 $m\,s^{-1}$ during all shown experiment in Figure 7.14.
As with non-clogged structures, most particle agglomerates detach at high elongations

between 25 to 38.50 % stretching regardless of the structure morphology on the fiber. The majority of detached structures in the first stretching cycle are seen here. The particle structures in the second to fifth stretching cycles detach much earlier in the range of 0-20 % fiber stretching, regardless of the morphology of the initial structure. The influence of the stretching velocity on the moment of detachment is negligible at the airflow velocity of 0.8 $m\,s^{-1}$ as the influence of the airflow is expected to be predominant. This can be concluded from the previous observations on the single fiber but also on the array. However, in all cases a lower stretching velocity of 0.6 $mm\,s^{-1}$ seems to favor the formation of larger detached structures.
Comparing the results to the experiments (u=0.8 $m\,s^{-1}$, e=0.6 $mm\,s^{-1}$) with a non-clogged structure, the detached structures in the experiment with a clogged structure have an average size of $350 \pm 28\,\mu m$, while the detached structures from a non-clogged structures had an average size of $265 \pm 59\,\mu m$. In addition, compared to the detachment in the experiment with the non-clogged structures (see chapter 7.3.2.2), there is a clear shift of the detachment area to lower fiber stretching (0-20 %), which is also noticeable regardless of the morphology of the structure on the fiber. The detached structures also show a significant increase in size compared to the non-clogged structures. As clogged structures are stretched, more large particle agglomerates detach due to the increased particulate loading with the clogged array.

In experiments with a dendritic clogged initial structure (see Figure 7.14, BOTTOM), fewer particle structures are detached in the first strain cycle than with a compact initial structure (see Figure 7.14, TOP). This is probably due to the internal strength and porosity of the structures. Dendritic structures can better absorb initial stretching and rearrangement, as well as the introduction of stress, without loss of particle material. In addition, the detached particle structures are slightly smaller than those of the tests with a compact clogged initial structure. With respect to the different strain rates, there is also no difference between the 0.6 $mm\,s^{-1}$ and 1.2 $mm\,s^{-1}$ experiments.

In the all experiments with an air flow of 0.05 $m\,s^{-1}$, little or no detachment of the particle structures was observed, regardless of stretching velocity, as can be seen in the results of the RFPI in the following section. It can be assumed that although the clogged particle structure on the fiber array can be loosened by stretching the fiber, the drag force is reduced and sufficient to overcome the particle-particle or fiber-particle adhesion forces. More information on the lack of detachment in the experiments with a clogged particle structure on the array and an airflow velocity of 0.05 $m\,s^{-1}$ can be found in chapter 7.3.5.3.

7.3.5.3 Development of RFPI for the clogged particle structure on the fiber array

Figure 7.15 shows the variation of RFPI versus the number of stretching cycles of the clogged particle structures (Stokes number of 10.05; 6.70; 3.62 and 0.82), for two air flow velocities (0.05 and 0.8 $m\,s^{-1}$) with variation of the stretching velocities.

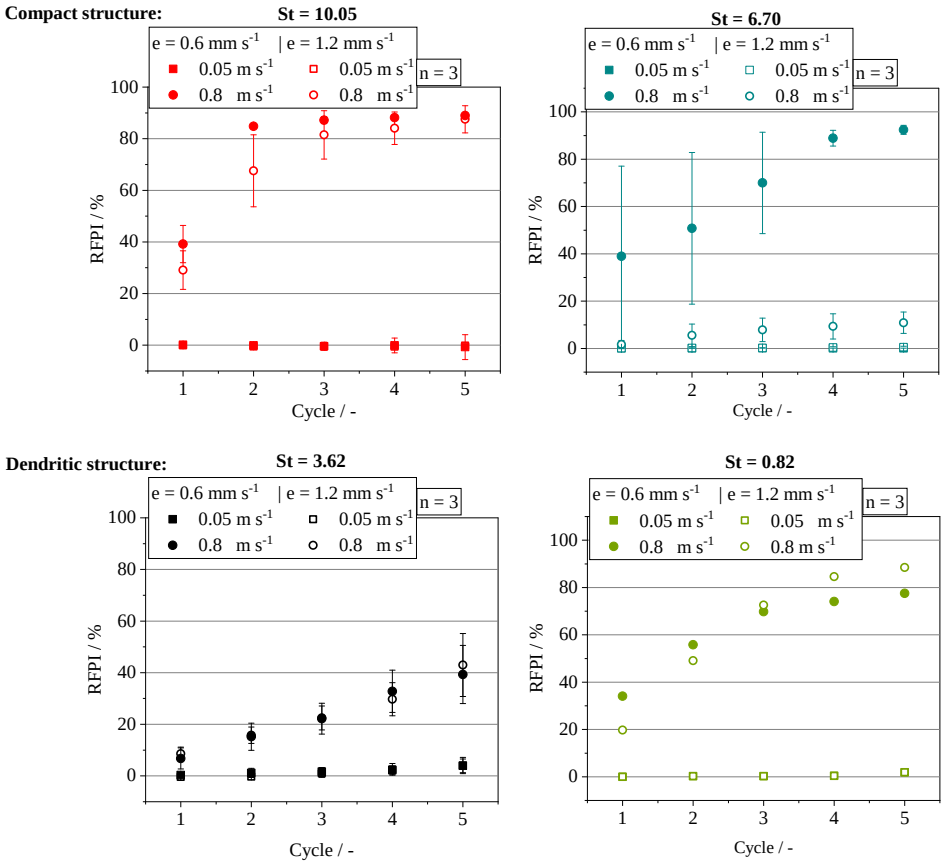


Figure 7.15: *RFPI after stretching procedure as a function of number of stretching cycles for the investigated clogged particle structures on the fiber array. Variation of air flow velocity, stretching velocities and morphology.*

For all experiments with a low air flow velocity of 0.05 $m\,s^{-1}$, values of RFPI close to 0 % are obtained for all morphology and stretching velocity. However, no detached particle structures were detected in these experiments (see section 7.3.5.2). Clogged structures show improved stability compared to non-clogged particle structures on the fiber array. Due to the clogged structure, the particle-free air bypasses the fiber array during stretching instead of passing through fiber interspaces. As a result, no local flow channels are created in the fiber interspaces of the array. In a potential stretchable filter however, the air flow must pass through the filter, so detachment would be conceivable even at low air flow velocities. Further, The reason the drag force is not large enough, which may be due to the fact that the resistance caused by the flow is not large enough, or that the face area of the particle structure is not increased by radial

rearrangement.
In the experiments with an increased airflow velocity of 0.8 $m\,s^{-1}$, large numbers of detached particle agglomerates were detected as shown in the results in section 7.3.5.2. As a consequence, the RFPI increases as a function of stretching cycle for all experiments (St=10.05; St=6.70; St=3.62; St=0.82) regardless of the stretching velocity or the morphology of the particle structure on the fiber array.
Apart from the influence of the airflow velocity during stretching, the stretching velocity of the fiber has a small influence on the final value of RFPI. There are only small differences between the detected values of RFPI of the experiments with 0.6 $mm\,s^{-1}$ or 1.2 $mm\,s^{-1}$. These are independent of the morphology of the structure.

7.3.6 Size of detached particle structures during stretching cycle

In the stretching experiment, the size of the particle structure's evolution over the five stretching cycles is crucial for the process, in addition to the process parameters and morphology. The size of particle structures determines whether the structures can be transferred into deeper layers of a filter or if they will remain suspended between or on the upstream fibers. This estimation is important for experiments involving both unclogged and clogged particle structures.
Fiber stretching initiates tensile and shear stress within the particle structure, leading to the introduction of cracks. Poggemann et al. demonstrated that large fragments detach from a single fiber due to dissolved cohesion during the first stretching cycle. In the subsequent elongation cycles, rather small residual structures are detached up to the empty fiber. In the tests involving compact structures on a single fiber, only the first stretching cycle and the second through fifth stretching cycles were analyzed [107].

Figure 7.16 shows the mean size of the detached structures for two morphology types (St = 10.05 and St = 0.82; non-clogged and clogged structure) as a function of each stretching cycle. The results listed here were all determined in tests with an air flow velocity of 0.8 $m\,s^{-1}$. The results for the tests with an air velocity of 0.05 $m\,s^{-1}$ can be found in SI, but do show a few time no significant values due to the lack of detachment of particle structures.
It can be seen that regardless of the particle structure present on the fiber array, the largest particle structures are detached from the fiber array in the first stretching cycle. As the number of stretching cycles increases, the size of the average detached particle structures in the stretching experiments with a stretching velocity of 0.6 $mm\,s^{-1}$ decreases continuously from initially 500 to 150 μm. As confirmed in all experiments and the shown result in section 7.3.2.2 and 7.3.5.2, large structures are detached from the fiber during the first cycle, similar to the description of the detachment process and observations. The bonds between particles, known as cohesion, dissolved first, so large structure detach. The isolated large structures between the cracks may be exposed to an increased flow force due to the airflow, as they offer a large face area. After the detachment of the large structures, a observed residual layer remains on the

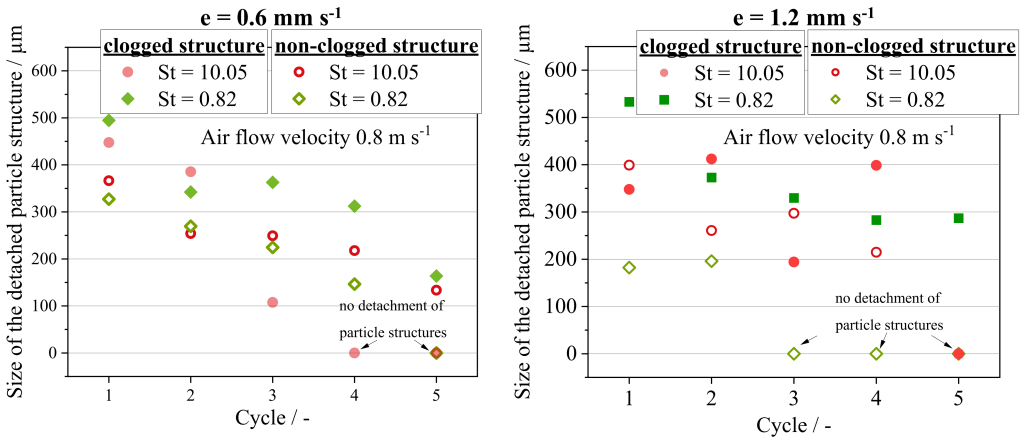


Figure 7.16: *Mean size of detached agglomerates from the fiber array as a function of each single stretching cycles for a compact and a dendritic initial structure. The stretching velocity is varied from 0.6 mm s^{-1} to 1.2 mm s^{-1}. Size values of 0 indicate "no detachment".*

fiber. In the following stretching cycles, this residual layer detached regardless of its size.

It is evident that the size of the detached structures in the clogged initial structure is generally larger than that of the non-clogged initial structure. This is due to the greater mass of particle material on the array, resulting in wider and taller particle structures.

However, the detached structures exhibit similar behavior to the compact structures, with a slight tendency towards larger structures in dendritic formations. This is likely due to the higher porosity of the agglomerates and the less compact structure of the fibers.

With increasing stretching velocity (see Figure 7.16, right), the tendency of size of detached structures to decrease with increasing number of stretching cycles remains, but is not nearly as pronounced. Overall, the average size of the detached agglomerates, if any are detached at all in a single stretching cycle, is at a higher level. Whether particle material is still present on the fibers or not varies from case to case. In tests with dendritic initial structures, a residual structure of particle material tends to be present. For comparison, corresponding images can be found in the SI.

In the SI, mean particle size data for the lower airflow velocity of 0.05 $m\,s^{-1}$ can be found. No significant trend toward decreasing or increasing size of the detached particles over the five stretching cycles was detected in this case.

7.3.7 Initiated multiaxial stress into particulate structure

The problem with uniaxial elongation and the tests performed on a clogged structure with an airflow velocity of 0.05 $m\,s^{-1}$ is that it causes cracking to occur across the entire width of the array, transverse to the fibers, resulting in minimal detachment. The original idea behind conducting further tests based on the previous ones on the array is to

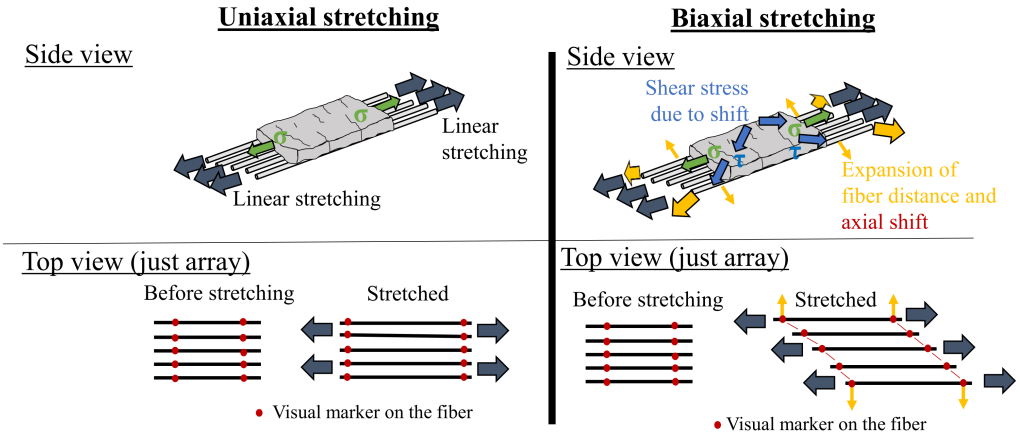


Figure 7.17: *Schematic on the differences between uniaxial and biaxial stretching in side and top view. The stretching and displacement of the fibers are indicated by visual markers in the case of biaxial elongation.*

induce cracking in diagonal arrangement (excluding a 90-degree angle to the fibers) in the area of the interfiber bridges. This aims to increase the shear stress in the deposited particle structure, leading to irregular breakage of the structure. The ultimate objective is to increase the likelihood of particle structure detachment. To increase the input of stress into the particle structure and especially to multiply the direction of the input as shown in Figure 7.17, the preliminary experiments were performed with a fiber clamping device where the fiber distance can be increased or decreased by 27 μm during the stretching process (see Figure 7.2 right hand). Figure 7.18 shows the images of the particle structures before and after five stretching cycles to compare the change within the particle structure with and without a change in the fiber distance during the stretching processes. The compact and dendritic structures are depicted after the stretching processes with simultaneously reducing and increasing the fiber distance. The left side of the figure shows the structure (compact and dendritic) without any change in fiber distance during stretching. Looking at the compact structure after five stretching cycles, the former cracks of a fractured structure can be seen in the circled enlargement. The images (refer to Figure 7.18, LEFT TOP & BOTTOM) from the tests with compact and dendritic structures on the fiber show minimal differences before and after the stretching cycles. Although cracks form during elongation, they subsequently push together again during relaxation, resulting in a structure with internal weak points and irregular edges. Additionally, a few areas exhibit obvious detachment. For a first qualitative comparison of the influence of multiaxial stretching, the images of the experiments under the same test conditions before and after the stretching cycles (0.6 $mm\,s^{-1}$ and 0.05 $m\,s^{-1}$; compact and dendritic structure), but with additional simultaneous change (reduction or extension) of the fiber distance, are shown in Figure 7.18.
Looking at the images of the experiments with fiber distance reduction (see Figure 7.18,

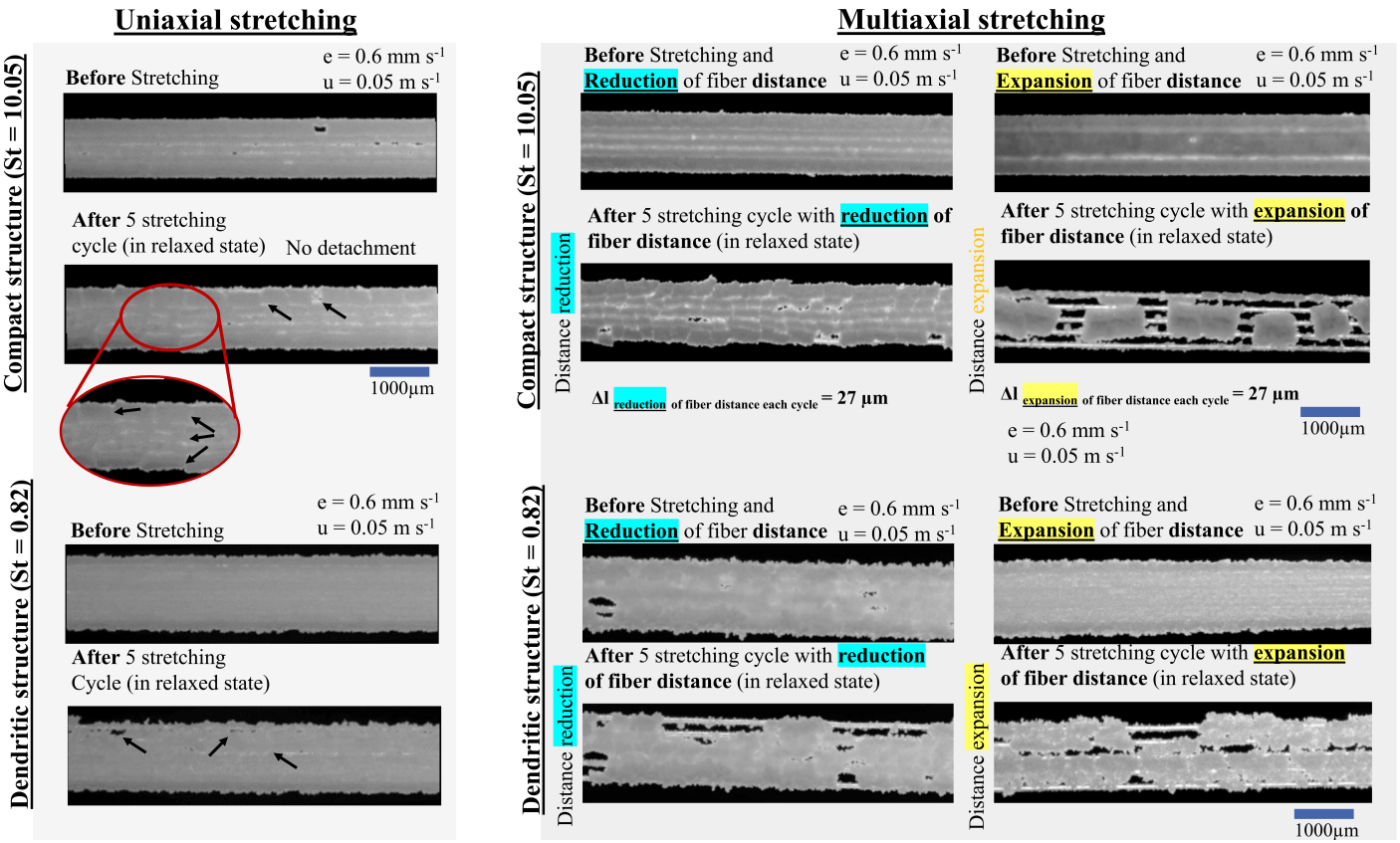


Figure 7.18: *Compact and dendritic particle structure before and after five elongation cycle without and with change of fiber distance during the elongation process.*

MIDDLE), it is noticeable that the compact structures are slightly broken diagonally compared to the experiments without fiber distance reduction. However, the individual structures on the array are shifted and displaced much more by the multiple application of multidimensional stress. In addition, clear gaps can be seen as a result of particle structure detachment. Pores have also formed in the area of the inner fibers.
When comparing the tests with compact structure and expanded fiber distance (as shown in Figure 7.18, RIGHT) to the tests with reduced fiber distance, the displacement and rearrangement are more pronounced. After 5 stretching cycles, the remaining large particle structures on the array are arranged diagonally on the fibers. It is evident that particle material has detached from the array. The increase in fiber distance, combined with stretching, leads to a more pronounced rearrangement of agglomerates, even if they are not directly detached from the array in the direction of flow. Some fibers also exhibit a residual structure. The breakup of the particle structures is similar to the breakup of a filter cake under shear stress and simultaneous dewatering/filtration.
The tests with a dendritic structure (see Figure 7.18, MIDDLE & RIGHT BOTTTOM) on the array show a similar picture, although with a different fracture and rearrangement pattern. The structures are much more porous and do not form serious agglomerates during the five stretching cycles. In both the stretching experiment with distance reduction or expansion, the structures are irregularly fractured. Applied stress has different effects on porous structures compared to compact structures due to clearly defined crack formation, as previously described by Thouless [153, 12].

7.4 Conclusion

In this study, the influence of stretching and simultaneous particle-free flow on the rearrangement and detachment of particle agglomerates from an deposited structure (dendritic or compact) on an array (5 fibers) was investigated. The particle structures consist of inert glass material and were deposited on the fiber via a filtration process. The evaluation of the rearrangement process during the stretching of the underlying fiber array was based on a quantitative analysis of the unblocked area in the fiber interspaces and the size of the detached particle structures. In addition, a qualitative analysis was performed to examine the fracture pattern and the different phases of the fracture and detachment process. The main results are:

- Identification of three phases during fiber stretching and detachment of particle structures independent of the morphology of the initial structure on the fiber array, but not on Time integrated flow (TIF).
- The radial rearrangement of the particle structures of a non-clogged initial structure led to unexpected clogging of the fiber interspaces at low inflow and elonga-

tion velocities.

- As already observed in the single fiber experiments, an increase of the inflow velocity leads to a premature detachment time of the particle structures.
- Significant increase in the final relative free projection area of fiber interspaces (RFPI) after 5 stretching cycles when the velocity of the particle-free inflow is increased from 0.05 $m\,s^{-1}$ to 0.8 $m\,s^{-1}$, regardless of the presence of TIF.
- The size of the detached particle structures decreases with increasing number of stretching cycles - independent of the morphology of the initial structure and partly also of the loading condition (non-clogged and clogged).
- The moment of detachment occurs prematurely with increasing stretching velocities.
- In preliminary tests it was found that in addition to the uniaxial elongation of the fiber array, the simultaneous change of the fiber distance (reduction or expansion of 27 μm) increases on the break-up and detachment of particle structures.

7.5 Outlook

As the results show, the expectation that the multiaxial stress introduction leads to an increased detachment of the particle structures from the collector is well justified in the preliminary experiments. However, the experiments on an array with a clogged particle structure have revealed new challenges of radial rearrangement and the blocking of fiber interspaces by rotating particle structures during fiber elongation and low air flow velocities.
Investigations of the rearrangement in the depth of the filter would be conceivable using a stacked multi-row arrangement of fibers as an array. This arrangement of fibers (in an array) would make it possible to study what happens to the first detached particulate material as it moves through the fiber arrangement in the direction of flow within a filter.
It might be also conceivable to perform a Discrete element method (DEM) simulation like Braschke et al. on an array with stretchable fiber to get an idea of the stress within the particle structure under multidimensional stretching situation [16]. First tests on a stretchable single fiber have already been performed in a DEM simulation environment.
In addition to these more fundamental aspects, the next step would be to look at the macro level of the experiment - on entire stretchable filter. The detachment of particle structures by stretching the filter matrix is a task for future investigations. In addition to the specific knowledge of detached or penetrated particulate material, it would then be possible to find the relationship between the rearrangement of particulate material and a potential change in pressure drop. Different cleaning strategies and the

influence of the multidimensional stress state could be initiated and experimentally tested with a three-dimensional filter matrix.

Funding: We gratefully acknowledge funding of this project by the Deutsche Forschungsgemeinschaft (DFG, German Research Foundation) – 427981860.

Acknowledgments: We kindly thank Freudenberg Filtration Technologies SE & Co. KG for donating fiber material. We gratefully acknowledge that this project was funded by the Deutsche Forschungsgemeinschaft (DFG, German Research Foundation) - 427981860. I would like to thank Marco Hummel and the mechanical workshop at MVM for their assistance in the design and manufacture of the parts produced.

Appendix A. Supplementary material: Supplementary data associated with this article can be found, in the online version, at https://doi.org/10.1016/j.seppur.2024.127887

8

Summarizing Conclusions

The separated particulate material within a fibrous filter affects the pressure drop which develops through three different stages (depth filter stage, transition stage and surface filter stage) [13, 54]. The implementation of a stretchable collector (fibers) is intended to cause *rearrangement and detachment of particle structures* from fibers within the upstream layers at low flow velocities. The deposited particle structures are transported further within the filter and clear up void space for an extension of filter service life that is defined by the overall mass capacity and a critical pressure drop. To gain a fundamental understanding of the changes in particle structure during stretching, this present work **investigated the rearrangement and detachment** of the particle structure on a **stretchable single fiber** and a **fiber array**. This approach follows the example of Löffler [81], who investigated the detachment of single particles and particle structures from **a non-stretchable single fiber**.
A stretching experiment, regardless of whether its with a single fiber or a fiber array, always consists of the separation of a particle structure on the collector and a subsequent stretching mostly with simultaneous particle-free air flow.

The sections 8.1, 8.2 and 8.3 presents the results and conclusions of experiments conducted using a **stretchable single fiber**. Additionally, a focuses was on the adhesion force and its relationship to changes in fiber surface roughness, as well as the ratio of adhesion force between fiber-particle and particle-particle. The **single fiber** represents the **micro level**, where the influence of process parameters during stretching like the number of stretching cycle, the stretching velocity and the air flow velocity are considered in an isolated form using a compact particle structure with different height on the fiber.
The next sections 8.4 and 8.5 presents the results of the particle structure separation as well as the **rearrangement and detachment** from the **fiber array**. The **fiber array** represents the **meso level**, which enables further investigations of the influence

of neighboring fibers during the stretching experiments. Similar to the experiments with a single fiber, these stretching experiments with a fiber array investigate the effects of varying process parameters with a compact and dendritic particle structures in non-clogged or clogged state. The development of particle structure on the fiber array was previously investigated in detail prior to the stretching experiments. Stretching experiments are also conducted while simultaneously changing the fiber spacing.

Although the results are categorized into micro and meso level, for an improved overview. There are correlations between the observations and measurements in the experiments with a single fiber and the fiber array.

8.1 Single stretching of a stretchable single fiber (micro level) with a compact particle structure

The first stretching cycle of an stretching experiment is a unique process because it introduces elongation and shear stresses into the separated particle structure for the first time. Therefore, it is discussed separately here in terms of its results and the feasibility of initiating the *rearrangement and detachment of particle structures* from a stretchable single fiber by a single-fiber stretching procedure.
For the stretching experiment with a single fiber a custom-designed fiber-mounting device for investigations on loaded stretchable filter fiber was constructed and applied for the first time 1.1.2. Before conducting any experiments with a single stretching cycle, a compact particle structure (St=6.52) was separated during the prior loading process with polydisperse particulate material on the stretchable single fiber. The particle loading time was 15 min. The initial structure height was maximum 350 μm based on image analysis. Stretching experiments with a stretching velocity between 0.4 $mm\,s^{-1}$ to 1.2 $mm\,s^{-1}$ have been performed with a single stretching cycle (incl. stretching & relaxation). The evaluation for this single stretching cycle was based on image analysis using a self-develop method named frame-fitting to adapt the analyzed frame to the fiber stretching and an image analysis for the relative particle projection area.

In all experiments cracking of particulate structure on the fiber could be initiated by stretching the fiber. The development of crack starts at the upstream side of the particle structure with a fiber elongation of 10 to 25 % elongation and develops further in a V-form as described by Thouless [153] and Beuth [12]. The cracks are evenly spaced, ranging from 300 μm to 1200 μm, due to the consistent loading height of the structures. During the experiments, it was observed that the particle structure rotates and radial rearrange up to 90° luv and lee to the air flow, regardless of the stretching velocity or air flow velocity. Due to this radial rearrangement and the rotation the Relative particle projection area (rPPA) is threefold. If the particle structure remains on the fiber, its rotation is only partially reversible.
The rotation is caused by internal stresses within the fiber and was also observed in experiments with an elongation velocity of 1.2 $mm\,s^{-1}$ where the fiber was elongated

without any air flow. No detachment of particles was detected in these experiments. Rotation of the fiber causes re-orientation and radial rearrangement of piles luv and lee of the fiber (Increase in rPPA by up to 170 %).
During fiber stretching with a stretching velocity rate of 1.2 $mm\,s^{-1}$ and an air flow velocity of 0.4 $m\,s^{-1}$, the first large rearrangement and detachment of a single fiber was detected. In the final third of the 39.7 % stretching, most of the particle structures become detached. Increasing the flow velocity from 0.4 $m\,s^{-1}$ to 0.8 $m\,s^{-1}$ causes the first detachment of particle structures to shift forward at a constant stretching velocity of 1.2 $mm\,s^{-1}$.

In all experiments, particle structures in the size range of 300 μm to 1200 μm were detected using image analysis. After the detachment of particle structures, a residual structure is found on the fiber in all experiments, which is higher and larger at low air flow velocities such as 0.4 $m\,s^{-1}$ than at 0.8 $m\,s^{-1}$.
During the relaxation process after stretching and the holding phase between stretching and relaxation, there was almost no detachment of particle structures from the fiber. There was no steep decrease of rPPA observed during the holding pause and relaxation process. Therefore, the detachment of particle structures during relaxation was not further considered in the subsequent stretching experiments. During the relaxation process, the fiber briefly crimped, but this was reversed by internal stretching.

8.2 Measurement of adhesion force between a single particle and polyurethane fiber

To understand the *rearrangement and detachment processes of particle structures* and changes in surface roughness the fiber during stretching, adhesion forces were measured between fibers and particles, particles and particles. The surface roughness of the polyurethane fiber in different states of stretching was characterized.
For the measurement of the adhesion force between the polyurethane fiber and a single particle made of Spheriglass5000 or Polystyrene (PS), a new customized setup for the Atomic Force Microscope (AFM)-measurement was developed. The unique feature of this customized setup incl. clamping device is the direct measurement of adhesion force at the zenith of the thin polyurethane fiber in the clamped state. To keep the fiber (d_F=82 μm) in the optimal position beneath the AFM-measurement head during the measuring procedure an additional bracket has been designed and integrated. Variation of elongation state (between 0 - 38.7 % stretching) was possible and enables the direct change of elongation state of the fiber before the measurement. The stretching velocity kept constant at 12 $mm\,s^{-1}$. In addition to the measurements of the adhesion force, measurements of the surface roughness of the fiber were carried out with the AFM and White Light Interferometry (WLI).

It was found that there is a difference of 80 nm in the Root Mean Square (RMS) of the fiber (maximum value 192 nm) between an unstretched and a stretched state

of 38.7% fiber elongation. The peak-to-peak distance decreases from 12000 nm to 10050 nm.
The measured adhesion force is in the range of 592 nN to 1332 nN regardless the particulate material and stretching state of the fiber. Further for the measured surface roughness of the polyurethane fiber is 192 nm at an elongation of 22 mm (38.4 %) fiber stretching, a reduction to the minimum of adhesion force is observed regardless the used particle size and material. The influence of moisture and electrostatic forces are neglected in the calculations (see chapter 4 which is based on the model by Rabinovich et al. [116].

Spheriglass particles with the size of 23.78 μm showed a maximum reduction of adhesion force by about 33% (440 nN) due to change of the surface roughness of the fiber. In the experiments with Spheriglass particles of sizes 10.38 μm and 17.13 μm, an uneven development in the adhesion force can be observed as a function of the uneven increase in surface roughness between the non-stretched and the fully stretched fiber of 38.4 % elongation. The maximum decrease in adhesion force between a Spheriglass particle ($d_p = 10.38\,\mu m$) and the polyurethane fiber was 210 nN. These result corresponds to the results of Kumar et al. [73] who observed a larger reduction of adhesion force for large particles ($d_p = 10.25\,\mu m$) than it was observed for particles of size 7.59 μm for same change in surface roughness. As Beach et al. [10] and Ditscherlein [30] showed adhesion force is affected by the change of roughness hence the number of contact points is changed. This increase in surface roughness results in a change in the number of contact points between the substrate and each particle as new elevations and distortions are formed. This phenomena has been described by Miwa et al. [89] for a different combination of materials and shapes.

For the experiments with the PS particle size of 12.30 μm a reduction of 373 nN results from a change of the surface roughness of the polyurethane fiber. In the experiments with the particles of the size 9.88 μm a reduction of 215 nN was determined. In general the modeled values of adhesion force for PS particle display a good agreement with the measured values by the AFM for high surface roughness (RMS=192 nm). In the range of low surface roughness (RMS=112 nm) the measured adhesion force is higher than the modeled. For the large PS-particle with diameter of 12.30 μm, there is an increased change in the adhesion force, since the reduction of the contact points is relatively larger compared to the total contact area. This trend was also found in the experiment with Spheriglass particles.

The model by Rabinovich et al. [116] was confirmed with this observed reduction of adhesion force due to change in surface roughness (ΔRMS=192 nm) for Spheriglass particle 270 nN (in average) and for PS-particle 260 nN (in average). The Rabinovich model usually underestimates the adhesion forces between the particles and the substrate compared to the experiment, despite the consideration of the surface roughness of the particles, other factors such as moisture on the surfaces, strength of the substrate or the particles, charge effects are part of the result in the experiment. Further the influence of the nanoscale roughness of the particles is not considered in the calcu-

lation. Thus, the PS particles are very smooth particles, since they are extracted from research material (monodisperse particles by microParticles GmbH, Berlin). The particles made of Spheriglass5000 are particle material used for the filtration experiments, which was taken from a bulk. The particles may exhibit bumps or potential deviations from spherical geometry as shown in chapter 4.

It can be concluded that increasing the surface roughness of the polyurethane fiber by approximately 80 nm results in an average reduction of the adhesion force by 265 nN, regardless of the particle size or material. This reduction contributes a small but significant amount to overcome the adhesion force between the particle and the fiber before the particle structures detach from the fiber. Nevertheless comparing the calculated adhesion forces between particles, the forces between particles and fibers are an order of magnitude greater. In a broader sense, this could be a possible reason for the appearance of residual structures on the fiber after the detachment of particle structures from the fiber or fiber array. The cohesion of the particle structure on the fiber fails significantly while a small particle layer or single particle still adheres to the fiber (see chapter 5 and chapter 7).

8.3 Multiple stretching of a single fiber (micro level) with a compact particle structure of different height

In previous experiments with a single fiber, a single stretching cycle, and low flow velocities, it was observed that the particle structure on the fiber does not completely detach. In order to achieve a full detachment of the particle structure, further experiments were conducted with 5 consecutive stretching cycle (each cycle includes stretching & relaxation). Based on the model by Tippayawong and Preechawuttipong [156], multiple external excitation (stretching) is expected to affect the threshold for particle detachment. To investigate the effects of repeated fiber stretching on *the rearrangement and detachment of particle structures*, a compact particle structure (St=6.52) was deposited on a stretchable single fiber. The particle structures were achieved with a loading time of either 5 or 15 min. Height of the particle structure measured starting from the fiber zenith was 103 μm for 5 min loading time and approximately 332 μm for 15 min loading time. A self developed measurement system, which measurement principle is based on light scattering, was constructed to record the size and moment of detachment of detached particle structures during the stretching process (see section 5.2.4). In addition an image-based in situ measurement technique was integrated to quantify the cumulative fraction of detached particle structure from total structure.

The application of multiple excitation/stretching cycles induces shear stress multiple times to the separated particle structure, enabling complete detachment of the large and compact particle structure (15 min loading time) from the stretchable filter fiber at low gas flow velocities of 0.05 $m\,s^{-1}$. As observed in the single stretching cycle experiments, residual structure can remain on the fiber even after multiple consecu-

tive stretching cycles. The observed failure of cohesion (breakage of particle-particle, normal structure) and adhesion (breakage of particle-fiber, residual structure) during rearrangement and detachment is consistent with the measured ratio of adhesion force from chapter 4.
Further, rotation of particle structures on the single fiber due to fiber rotation was observed in each stretching cycle, as in the experiments with a single stretching cycle. Cracks within the particle structure are formed in V-form in the first cycle (see chapter 3) and in the following cycle of the multiple stretching process. Compared to the experiments with only a single stretching cycle ($0.4\,ms^{-1}$ and $1.2\,ms^{-1}$), in the experiments with multiple stretching cycles (15 min particle loading time) with half the elongation velocity $0.6\,mms^{-1}$ and a lower air flow velocity of $0.05\,ms^{-1}$, complete detachment was achieved after a maximum of three out of five stretching cycles. In addition increase of the flow velocity (from $0.05\ ms^{-1}$ to $0.8\,ms^{-1}$) causes a shift of the main area for detachment from 25–35% fiber elongation to 10–25% fiber elongation for experiment with a large particle structure after 15 min loading time. The experiment with multiple stretching cycles showed the same observation for each cycle as the experiment with a single stretching cycle (see section 3).
In the experiments with multiple stretching cycle and a small particle structure (5 min particle loading time), the number of required stretching cycles for "complete detachment" of a small particle structure on the fiber (5 min) is also reduced by the increase of the elongation velocity ($0.6\,mms^{-1}$; $1.2\,mms^{-1}$ to $12\,mms^{-1}$) and a constant air flow velocity of $0.05\,ms^{-1}$. The higher stretching velocity suggests accelerated crack building due to higher shear stress as described by Nahta and Moran B. [93].

Since the exact size of the detached particle structures from the individual fiber is important, as it affects the possible transfer of particle structures through the fiber interspaces in a future filter, the following section will focus on the results of size dependencies of the detached particle structures in the experiment with multiple stretching cycle.
First focusing on the experiments with multiple stretching cycles and a high initial particle loading of 15 min on the fiber (similar to the experiments with one stretching cycle). The $d_{90,0}$ of particle structures detached from the fiber during whole stretching process was 977 μm for the experiments with air flow velocity of $0.05\,ms^{-1}$ decreased to 808 μm for the experiments with air flow velocity of $0.8\,ms^{-1}$ and a constant stretching velocity of $0.6\,mms^{-1}$. Regardless of the air flow velocity, the particle structures detached during the first stretching cycle are larger than those in the subsequent cycles (2nd-5th cycle). The mean size of detached particle structures in the first stretching cycle is reduced to the half in the 2nd to 5th cycle. In the first stretching cycle the mean size is $844\,\mu m$. After the first detachment of particle structures, residual structures are visible on the fiber, indicating a prior failure of cohesion within the particle structure. The smaller residual structures are then detached from the fiber in the following stretching cycle (2nd - 5th cycle), overcoming the adhesion of individual particles to the fiber.

Focusing on the experiments with multiple stretching cycle and a small particle structure (5 min) on the fiber, increasing the air flow velocity resulted in a decrease of $d_{90,0}$ with an average reduction of 133 μm when the flow was increased from 0.05 $m\,s^{-1}$ to 0.8 $m\,s^{-1}$. The maximum value was obtained in experiments with an stretching velocity of 12 $mm\,s^{-1}$ and an air flow velocity of 0.05$m\,s^{-1}$. When the stretching velocity of the single fiber was increased from 0.6 to 12 $mm\,s^{-1}$ in experiments with a small structure (5 min), the detached particle structures showed an average increase of 150 μm for the $d_{90,0}$. The average detached particle size showed a significant difference of 200 μm when the elongation velocity was increased from 0.6 to 12 $mm\,s^{-1}$, while maintaining a constant flow velocity of 0.8 $m\,s^{-1}$. For all experiments regardless the stretching velocity and the flow velocity the $d_{50,0}$ remains constant at about 190 to 210 μm for the experiment a low particle structure (5 min) and with multiple stretching cycle.

When comparing the size of detached particle structures in experiments with small (5 min) and large (15 min) particle structures at the beginning of the experiment, smaller values were observed with the smaller structure on the fiber at the start of the stretching. The smaller crack distances (l) observed in the experiments with a small particle structure (5 min particle loading time) are a result of the height of the particle structure (t) on the fiber, as crack distance is dependent on this factor [153].

8.4 Development of a compact or dendritic particle structure on a fiber array (meso level)

After evaluating process variables such as flow velocity and stretching velocity on *the rearrangement and detachment of particle structures from a single fiber (micro level)*, the next step is to investigate the processes at the fiber array (meso level). Further detailed studies are necessary to investigate the development of compact or dendritic particle structures on the fiber array using polydisperse particulate material. The influence of neighboring fibers is a main focus during the separation process on the fiber and in the rearrangement and detachment process afterwards.
Polydisperse Spheriglass was used to separate a compact or dendritic structure on a fiber array consisting of 5 stretchable polyurethane filter fibers (fiber distance 246 μm). An self developed camera technology was used to observe the growth of particle structure, enabling observation without disrupting the air flow from loading direction. The loading process was performed with a constant particle concentration of the aerosol until reaching a TIF of $2.8 \cdot 10^8\,\#\,mm^{-2}$.

At the start of the separation process, at a TIF of $1.1 \cdot 10^8\,\#\,mm^{-2}$ (before the clogging point), the relative accumulated particle material in the spacing evolves with the same slope for all experiments, whether compact or dendritic. It is noticeable that for the experiment with a compact structure (St=10.05) at a TIF of $1.73 \cdot 10^8\,\#\,mm^{-2}$ the value of relatively accumulated particle material in the spacing is 0.3, since very little particle material is deposited in the fiber interspaces. Compact structures are formed

at the stagnation point of the fiber, which is only noticeable when considering the deposited mass on array per fiber length and represents the highest value of 16 $\mu g\ mm^{-1}$. This is likely due to a significant compaction of the particle structure at the stagnation point of the fiber.
The highest value for relative accumulated particulate material in the fiber interspaces is observed in for the experiment with St=3.62. The structure is separated in a compact form at the stagnation point, but also with a dendritic branches on the sides of the fiber. The interspaces between the fibers are strongly closed according to the value of relative accumulated particulate material of 0.8 at a TIF of $1.73 \cdot 10^8\ \#\ mm^{-2}$. For the deposition of dendritic structures (St=1.30), a value of the relative accumulated particulate material in the spacing of 0.6 can be observed at a TIF of $1.73 \cdot 10^8\ \#\ mm^{-2}$. The dendritic structure grows into the interfiber spaces, maintaining a high porosity, as reflected in the corresponding mass on array per fiber length value of 4 $\mu g\ mm^{-1}$.
In the further process of the experiments starting from a TIF of $1.73 \cdot 10^8\ \#\ mm^{-2}$, the dendritic structure (St=1.30) obtain a steady growth up to a final value of the relatively accumulated particle material in the interspaces of the fiber of approximately 0.7 at a TIF of $2.8 \cdot 10^8\ \#\ mm^{-2}$. Steady growth up to a value of relatively accumulated particle material in the interspaces of the fiber of 0.4 can also be detected for the compact structures (St=10.05). In the experiment with the structure developed at St=3.62, the value for the relatively accumulated particle material in the spacing reaches 1 at a TIF of $2.5 \cdot 10^8\ \#\ mm^{-2}$, indicating complete closure of the fiber interspaces.

During the separation process, as the TIF increases, bridges emerge between the particle structures on the fibers as the individual structures grow together. This could affect the void space in the interfiber space and thus pressure loss in an entire future filter.
For dendritic structure (St=1.30, u=0.25 $m\,s^{-1}$) on the fiber array the size of bridges between the fibers remain in the range of 41 to 160 μm during the whole separation process. The number is around 10-times higher than for compact structures on the fiber, because the structure tend to grow in small fragile bridges in the horizontal level. Further the growth starts shortly before a TIF of $1.0 \cdot 10^8\ \#\ mm^{-2}$.
In the experiments with a compact structure (St=10.05, u=1.8 $m\,s^{-1}$) on the fiber array, long horizontal bridges are formed during the separation experiment. The size ranges from 41 to 401 μm. The growth starts at a TIF of $1.5 \cdot 10^8\ \#\ mm^{-2}$. The number of bridges ranges between 1-3 bridges for each size category whereas the most large bridges grow at the end of the separation experiment at a TIF of $2.6 \cdot 10^8\ \#\ mm^{-2}$. During the separation process, bridges form when the compact particle structure on neighboring fibers connect longitudinally along the fiber axis.

The spaces between fibers or remaining pores in a clogged structure are crucial for flow and the pressure drop of an entire future filter. Therefore, the change in hydraulic diameter d_h during the separation procedure is discussed in the following.
For the dendritic structures (St=1.30) on the fiber array the size (hydraulic diameter)

of pores ranges from 3 to 181 μm at the end of the stretching experiment. In the TIF range of $2 \cdot 10^8 \, \# \, mm^{-2}$ to $2.8 \cdot 10^8 \, \# \, mm^{-2}$ the hydraulic diameter of the majority of pores ranging from 3 to 70 μm. Larger pores are also detected at the end of the loading process and a TIF of $2.6 \cdot 10^8 \, \# \, mm^{-2}$ due to rebound and knock out of already deposited particulate material. At the end of the loading process (TIF = $2.8 \cdot 10^8 \, \# \, mm^{-2}$), there is a clear focus on the number of pores (more than 140 pores) in the range of 3-41 μm pore size.
For the compact structures (St=10.05) on the fiber array, the size of the pores (hydraulic diameter) ranges from 3 to 241 μm. The focus is clearly on pore sizes above 141 μm, where up to 8 pores are present at the end of the loading process (TIF = $2.8 \cdot 10^8 \, \# \, mm^{-2}$). As shown in chapter 6 there is a major presence of horizontal pores that form along the fiber axis. These pores grow evenly and the structure is widening the fibers. Furthermore, pores continue to form throughout the loading process, reaching a size range of 141-261 μm.

Overall, the phases of growth before (TIF = $1.7 \cdot 10^8 \, \# \, mm^{-2}$) and after (TIF = $2.8 \cdot 10^8 \, \# \, mm^{-2}$) the clogging point of some of the compact and dendritic particle structures on the array reveals valuable insights. These insights can help with root cause analysis for clogging of a fiber array and finding the optimal time for stretching.

8.5 Rearrangement and detachment of a particle structure on/from a stretchable fiber array

To evaluate the influence of the neighboring fibers of a fiber array (meso level) on *the rearrangement and detachment of particle structures*, stretching experiments with non-clogged particle structure (TIF = $1.73 \cdot 10^8 \, \# \, mm^{-2}$) and clogged particle structures (TIF $\geqq 4.06 \cdot 10^8 \, \# \, mm^{-2}$) were performed at stretching velocities of 0.6 $mm\,s^{-1}$ or 1.2 $mm\,s^{-1}$ and flow rates of 0.05 $m\,s^{-1}$ and 0.8 $m\,s^{-1}$. As with the single fiber, the experiments consisted of 5 stretching cycles (fiber distance 246 μm). In the separation process, dendritic (St=0.82; St=3.62) and compact (St=10.05; St=6.70) particle structures were separated on the fiber array using Spheriglass5000 particulate material.

8.5.1 Stretching experiments with a non-clogged particle structure on the fiber array

In all stretching experiments with a fiber array and a non-clogged particle structure regardless of the morphology (St=3.62; St=10.05), the most frequent area for detachment is the area is between 20 - 38.5 % of stretching. This focus area is independent from the stretching cycle, stretching velocity and air flow velocity. This observation is consistent with the experiments conducted with a single fiber. Increasing the air flow velocity from 0.05 $m\,s^{-1}$ to 0.8 $m\,s^{-1}$ shifts the first detachment of particle structures, in the first

and in the 2nd to 5th stretching cycle, to a lower stretching range of 0-20 %. When focusing on experiments with low air flow velocity (0.05 ms^{-1}), increasing stretching velocity from 0.6 to 1.2 mms^{-1} increases the amount of detached particles during the first cycle of the stretching experiment. This observation is independent of the particle structure's morphology on the fiber array. For a possible filtration application, this means that the stretching velocity needs to be doubled in order to achieve improved particle detachment at the end of the first cycle, while maintaining a constant flow velocity of 0.05 ms^{-1}. As shown in the experiments with single fiber stretching repeated stretching causes the separated particle structure to loosen due to induced cracking. Similar to the experiments with the single fiber, cracks emerge from the top side of the particle structure towards the surface of the fiber. In the non-clogged state of the particle structure on the fiber array. The cracks on the individual fibers occur with regular distances, completely independently.

As in the single fiber experiments, stretching of the fiber induces radial rearrangement and rotation of the particle structure on and with the fiber. However, in the case of a fiber array, this results in clogging of the fiber interspaces with radial rearranged and rotated particle structures at low air flow (0.05 ms^{-1}) and stretching velocities of 0.6 and 1.2 mms^{-1}, which was unexpected. The RFPI did not increase as steeply instead start in a negative area within the first 4 stretching cycles. In the experiment with a compact particle structure (non-clogged and St=10.05) and stretching velocity of 0.6 mms^{-1}, airflow velocity of 0.05 ms^{-1}, the RFPI decreased to -80 at the end of the 5th stretching cycle. This could be due to the low drag force of the air flow, which was not sufficient to detach the particle structure at the fiber distance of 246 μm. The rearrangement and detachment of particle structures would therefore not be sufficient in this combination of influencing factors. In the experiments with a non-clogged compact structure and an air flow velocity of 0.8 ms^{-1}, the release of fiber interspaces was excellent, regardless of the stretching velocity. RFPI values exceeding 70% were achieved. The detected RFPI for the stretching experiments with a dendritic structures on the fiber array (St=3.62, St=0.82) indicates that despite the detection of numerous small detached particle structures from the fiber, RFPI values of up to 20 % can be achieved. However, for experiments with an air flow velocity of 0.8 ms^{-1}, values of over 60 % are obtained regardless of the stretching velocity. No rotation of particle structure was observed as in the experiments with compact structure.

8.5.2 Stretching experiments with a clogged particle structure on the fiber array

In the experiment with an air flow velocity of 0.05 ms^{-1} little to no detachment of particle structures occurred during the stretching procedure, regardless of the stretching velocity or structure morphology (compact or dendritic). As a result, no significant increase in RFPI was observed in these experiments (values remained close to 0 %).
For the experiments with an air flow velocity of 0.8 ms^{-1} most particle structures de-

tach at fiber elongations between 25 to 38.50 % stretching during the first stretching cycle regardless of the structure morphology (dendritic or compact). This observation about the focus area for detachment is similar to the experiment with non-clogged structure. The cracks in the particle structures grow throughout the entire clogged particle structure on the fiber array. There is a slight displacement caused by the stretching or detachment of particle structures. However, it can be observed that the particle structure reassembles between stretching cycles despite the presence of cracks. For all experiment with an airflow velocity of $0.8\,ms^{-1}$ an increase of RFPI up to 80% is observed (regardless the stretching velocity) except the experiment with a structure of the experiment with St=3.62. So the interspaces of the fiber are freed of particulate material. If particle structures detach in the 2nd to 5th cycle, the particle structure detach more frequently in the range of 0 - 20 % fiber stretching. The influence of the stretching velocity on the moment of detachment is negligible at the airflow velocity of $0.8\,ms^{-1}$.

For all experiments with an air flow velocity of $0.8\,ms^{-1}$, regardless of the structure morphology, a lower stretching velocity of $0.6\,mms^{-1}$ compared to $1.2\,ms^{-1}$ appears to promote the formation of larger detached structures. On average, $d_{50,0}$ is $250\,\mu m$ larger. The detached particle structures from a clogged structure on the fiber have an average size of $350 \pm 28\,\mu m$, increase in size comparing to non-clogged structures where the $265 \pm 59\,\mu m$ for experiments with a air flow velocity of $0.8\,ms^{-1}$ and a stretching velocity of $0.6\,mms^{-1}$ have been detected. These results are regardless the structure morphology on the fiber array.
Furthermore, the size of detached particle structures decreases as the stretching cycle increases, resulting in an average difference of $260\,\mu m$ in size. The maximum difference in average structure size for the clogged dendritic structure (St=0.82) was obtained, when comparing the average size of the detached particle structure between the first and fifth stretching cycle. The difference in size was $331\,\mu m$ for experiments with stretching velocities of $0.6\,mms^{-1}$ and $1.2\,mms^{-1}$ and an air flow velocity of $0.8ms^{-1}$. Based on the results of these size measurement of the detached particle structures, it should be possible for the particle structures to pass through the other fiber interspaces in a future stretchable filter.

8.5.3 Multiaxial stretching of a fiber array with a clogged and compact particle structure

Further stretching experiments were conducted on a filter array with a multiaxial stretching induced by the simultaneous change in the fiber distance ($\Delta d_{fiber\,distance} = 27\,\mu m$) during the normal stretching procedure of the fiber array. In the experiments before, the stretching was uniaxial, meaning that the fiber was elongated in the direction of its axis.
In stretching experiments with a clogged structure (TIF $\geqq 4.06 \cdot 10^8\,\#\,mm^{-2}$) and an air flow velocities of $0.05\,ms^{-1}$ as well as a stretching velocity of $0.6\,mms^{-1}$, an improved crack building of the separated particle structure, as well as detachment

of particle structure could be demonstrated. For both cases, the increase in fiber distance of 27 μm and the a reduction in fiber distance of 27 μm, a enhanced cracking, rearrangement and detachment was observed. This has not been the case in the experiments with a uniaxial stretching. During elongation, the separated structures are simultaneously stressed with shear forces in multidimensional form due to the change in fiber spacing, but also due to the associated shift of the fiber along the fiber axis. For instance, increasing the fiber spacing during elongation at 0.6 $mm\,s^{-1}$ and an air flow velocity of 0.05 $m\,s^{-1}$ can cause detachment of approximately 40 % for a clogged and compact structure on the fiber array.
In contrast to previous experiments where stretching was performed without changing the fiber distance, this experiment resulted in solely cracks occurring within the structure along the fiber axis.

9 Outlook

This present work (dissertation) presents fundamental investigations of the rearrangement and detachment of particle structures from a single fiber and fiber array using stretchable filter fiber (see Figure 9.1 micro and meso level) as well as a detailed investigation on the ratio of adhesion force between stretchable fiber and particles. The single fiber and fiber array are simplified models of an entire filter. These models help to understand the basic interaction between the fiber and a separated particle structure during stretching of the collector. Investigation on the rearrangement and detachment of a particle structure at the single fiber (micro level) and the fiber array (meso level) enable isolated analysis of influencing variables such as stretching velocity or fiber distance during stretching. These variables cannot be clearly investigated in experiments with the entire filter medium due to the complex interactions of various process parameters.

In a future stretchable filter, the transfer of particle material into the downstream layers of the filter is intended to prevent the filter from becoming blocked and causing an increase in pressure drop during filtration. The rearrangement and detachment process will create more space for additional particle material and increase the capacity of the upstream layers. The aim is to increase the overall filter service life. In the consideration of the entire filter is interesting beside the aim of saving energy and resources, how exactly the pressure drop or the total mass capacity of the filter medium are influenced by the transfer or detachment of particulate structures.

The shown experiments in this work focus on the rearrangement and detachment of particle structure on/from a single fiber (micro level) and a fiber array (meso level) thus this provides a foundation for the development further investigation/studies of an entire stretchable filter medium (macro level) in gas-particle technology. It is recommended that future studies examine the entire stretchable filter medium (macro level) after analyzing the process on the single fiber (micro level) and on the fiber array

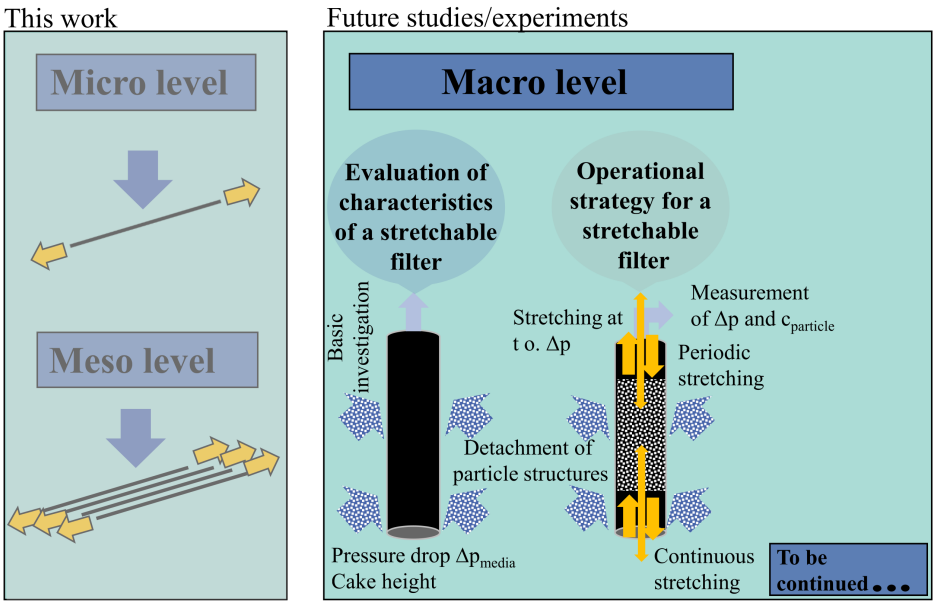


Figure 9.1: *Schematic overview of the focus of experiments in this work and future studies concentrating on the macro level which is represented by an entire stretchable filter.*

(meso level) in this work (see Figure 9.1). Further, the trend of the measured adhesion data might be used in a future DEM-simulation where a more detailed and reproductive analysis of rearrangement and detachment process on the fiber, fiber array or the entire filter is possible.

9.1 Evaluation of characteristics of a stretchable filter

Currently, there is no experience with experiments with an entire stretchable filter medium, and there are no measurement setups or techniques for stretching such a filter medium. Therefore, it is necessary to develop these techniques before conducting future studies. Additionally, it is important to **measure** the **fundamental material properties of the stretchable filter medium** to adjust the measurement setups accordingly.
As in the studies of chapter 3 with a single fiber, first the yield strength and stretching curve of the filter collector in this case entire filter medium (see Figure 9.1 macro level) should be determined. These properties are crucial for designing the corresponding clamping device and the measurement setup as for the first emerging of cracks in the particle structure a minimum stretching of 25 % is necessary (see chapter 3 and chapter 5). Further, the surface of the filter medium should be analyzed in various stretching states using the Laser Scanning Microscope (LSM), Scanning electron microscope (SEM), and porometer. Changes on the surface of the filter and the fiber matrix, as well as pore size distribution and fiber spacing of the filter, are clearly charac-

terized using this methods.
Further, **filtration properties of the new stretchable filter medium** (macro level) are **evaluated** by determining variables such as filter initial pressure drop Δp_{medium} and initial separation efficiency. Additionally, the stretching of the filter medium can be used to initiate rearrangement and detachment of particulate material. Similar to the experiments described in chapters 5 and 7 on single fiber and fiber arrays, first investigation should only concentrate on rearrangement and detachment behavior of particulate material from the filter.
Since a complete filter medium is being used, it is now possible to study particle separation on the surface, particle cake height on the filter medium, and the size and number of any detached structures. Quantifying the primary rearrangement behavior of particulate material and the residual structure on the collector surface after a single stretching cycle can be a useful method, as demonstrated in the single fiber and array experiments (see chapter 5 and 7). When dealing with an entire filter medium, it is now possible to quantify the pressure drop development during this first stretching cycle.
The operating areas utilized in this work's experiment can serve as a guide for selecting process variables in planned experiments with a total filter at a macro level. For instance, the likelihood of particle structures detaching from a single fiber or a fiber array is significantly greater at an incident flow velocity of 0.8 ms^{-1} compared to 0.05 ms^{-1}. With the same number of stretching cycles and a stretching speed of 1.2 mms^{-1}, a compact particle structures (5 min loading time) can be detached from a single fiber with similar success as with a stretching speed of 12 mms^{-1} (see chapter 5).
However, it is important to note that due to the complex structure of the filter matrix, similar influences from adjacent fibers may occur, as in the case of the fiber arrays (see chapter 7), where compact non-clogged particle structures rotate, radial rearrange and remain in the fiber interspaces.

9.2 Operational strategy for a stretchable filter

The experiments in this work are conducted with the single fiber (micro level) and a fiber array (meso level). The experiments mainly focuses on investigations on the rearrangement and detachment as on the isolated influencing parameters, such as air flow velocity (0.05 - 1.8 ms^{-1}) during stretching, stretching velocity of the fiber or fiber array (0.6 - 12 mms^{-1}), morphology of the particle structure before stretching (dendritic or compact structure), the height of separated particle structure, uniaxial or multiaxial stretching with a change in fiber distance of the array and the number of stretching cycle (1-5 stretching cycle).
The idea of an overall operating strategy or the timing of the particle transfer has only been superficially addressed. In the chapter 7, first steps were taken to gain some knowledge concerning this issue. Interest was paid to the detachment and rearrangement of particle structure from the fiber array whether the particle structure was non-clogged or clogged. The non-clogged and clogged particle structure mark different sta-

tus during a filtration process. For detachment of the clogged particle structure at low air flow velocities ($0.05\,m\,s^{-1}$) a multiaxial stretching in 5 consecutive cycle with an increase in fiber distance of $27\,\mu m$ is necessary.

For future studies with an **entire stretchable filter (macro level)**, it is interesting to move away from the investigation of the basic mechanism and observation of isolated processes and **to test full operating strategies**. Based on the multiple cycle experiments with 5 stretching cycle presented in this work (see chapter 5 and 7), **periodic stretching** and **relaxation** of the **filtration medium** is interesting for further investigation. After five cycles of repeated stretching, there was up to a 73% (average) increase in detachment of particulate material, as measured on the relative projection surface, in both the single fiber and fiber array experiments (see chapter 5 and chapter 7). These investigation will be carried out with regard to the influence on **pressure drop**, **separation efficiency** and the occupancy with particulate material of the filter medium (**degree of regeneration**). The start of stretching (of a period) of the filter medium could be triggered by **reaching a certain filtration time** or a **critical pressure drop**.

To avoid separate phases of particle separation and filter stretching during the filtration process, it may be worth considering **continuous stretching** and **relaxation** in a further step. Unlike the experiments with a single fiber and fiber array in this work, the **particle loading** of the filter medium **is permanent and continuous (during stretching)** in all cases of the operating strategy tests.

Researching operational strategies and introducing them to stretchable filter medium can introduce an overall improve the usage of depth filter capacity and the development of pressure drop, which could be a first step towards sustainable filter medium use.

Abbreviations

AFM Atomic Force Microscope

CAG Contact angle goniometry

CP Clopgging Point

SEM Scanning Electron Microscope

DEM Discrete element method

LSDS Laser Structure Detection System

LSM Laser Scanning Microscope

MFC Mass Flow Controller

OPC Optical particle counter

PD Particle distribution

PM Photomultiplier

PS Polystyrene

ROI Region of Interest

RFPI relative free projection area of fiber interspaces

RMS Root Mean Square

rPPA Relative particle projection area

SDAM Scanning droplet adhesion microscopy

SEM Scanning electron microscope

SI Supporting Information

TIF Time integrated flow

WLI White Light Interferometry

Symbols

Symbols	Unit	Description
A	m^2	Cross-sectional area
A_{area}	m^2	Contact area
$A_{i,j}$	J	Hamaker constant
$A_{pore,i}$	m^2	Area of pore
a	m	Characteristic distance
β	-	Bounce parameter
c_p	$\#\, m^{-3}$	Particle concentration
C_D	-	Drag coefficient
d	m	Size of particle structure
d_p	m	Particle diameter
d_F	m	Fiber diameter
$D_{Diffusion}$	$m^2\, s^{-1}$	Diffusion coefficient
$d_{1,2}$	m	Sauter mean diameter
d_{equi}	m	Equivalent circle
$d_{particle}$	m	Diameter particle
d_{fibre}	m	Diameter fiber
$d_{50,3}$	m	Volume based median
$d_{50,0}$	m	Number based median
d_h	m	Hydraulic diameter
e	$mm\, s^{-1}$	Stretching velocity
ϵ_0	$(As)/(V\, m)$	Electric constant
E	Pa	Young modulus
η_{fluid}	$Pa\, s$	dynamic viscosity of fluid

Symbols	Unit	Description
ϵ	-	Porosity
$e_{stretch}$	%	Elongation
$f_{correct}$	-	Correction factor
F_{adh}	N	Adhesion force
F_{Drag}	N	Drag force
$f_{correct}$	-	Correction factor
F_{vdW}	N	Van-der-Waals force
$F_{adh,liquid}$	N	Liquid bridge adhesion
$F_{adh,electric}$	N	Electrostatic adhesion
F_{Rumpf}	N	Adhesion force according to Rumpf
F_{ad}	N	Adhesion force according to Rabinovich
F_{DMT}	N	Adhesion force according to DMT-Model
F_{JKR}	N	Adhesion force to JKR-Model
$F_{Pull off force}$	N	Pull-off force
Γ	-	Geometry factor
H_0	m	distance of closest approach between surfaces
$L_{sampling}$	m	Sampling length
$\gamma_{1,2}$	$N\,m^{-1}$	Surface tension/adhesion energy
J(t)	$\#\,m^{-1}$	Time integrated flow
j_i	$\#\,s^{-1}\,m^{-2}$	Particle flux density
k_1	-	Proportional factor
γ_{stress}	°	Angle stress
$n_{refractive index}$	-	Refractive index
n	-	Number
L	m	Length
l	m	Length of the particle fragments
λ	m	Peak-to-peak distance
λ_{laser}	m	Wave length laser
L_0	m	Initial length
m_{array}	$kg\,m^{-1}$	Mass on array per fiber length
P	m	Perimeter
p	Pa	Pressure
Pe	-	Péclet number

Symbols	Unit	Description
p_k	Pa	Capillary pressure
Δp_{medium}	Pa	Pressure drop filter medium
q_i	As^{-1}	Point charges
ρ_{bulk}	$kg\,m^{-3}$	Density bulk
$\rho_{material}$	$kg\,m^{-3}$	Density Fluid
ρ_{fluid}	$kg\,m^{-3}$	Density Fluid
r	m	Radius
R	-	Interception parameter
r_{min}	m	Minimal radius
RMS	m	Root Mean Square roughness
rms	m	Roughness for close-packed hemispherical asperity
$\rho_{particle}$	$kg\,m^{-3}$	Density particle
Re_x	none	Reynolds number
St	-	Stokes number
σ	$N\,m^{-2}$	Stress
σ_{break}	$N\,m^{-2}$	Stress for breakage
t	m	Height of particle structure/thin film
t	s	Time
T	$°C$	Temperature
τ	$N\,m^{-2}$	Shear stress
u	$m\,s^{-1}$	Air flow velocity
u_s	$m\,s^{-1}$	Superficial flow velocity
$\dot{V}_{loading}$	$L\,min^{-1}$	Loading flow
$\dot{V}_{excess}$	$L\,min^{-1}$	Excess flow
ν		Poisson's ratio
z	nm	Depth of cracks
z_{travel}	mm	Travel distance cantilever
$z_{charges}$	m	Distance between charges

Acknowledgment

This work was funded by the Deutsche Forschungsgemeinschaft (DFG, German Research Foundation) – 427981860.

Declaration of Generative AI and AI-assisted technologies in the writing process

During the preparation of this work the authors used DeepL in order to integrate figures and to examine sections of the manuscript for spelling and grammar. After using this tool, the authors reviewed and edited the content as needed and take full responsibility for the content of the publication.

List of Publications

Peer-Reviewed Journal Papers

Poggemann, L., Meyer, J., Dittler, A. (2021). *A novel method to investigate detachment of particulate structures from an elastic single fiber at low gas flow velocities* In: Journal of Aerosol Science, 156, 105785, https://doi.org/10.1016/j.jaerosci.2021.105785

Poggemann, L., Meyer, J., Dittler, A. (2022). *Experimental detection of particle structures detachment from a stretchable single fiber during multiple consecutive stretching cycles* In: Separations, 9, 168, https://doi.org/10.3390/separations9070168

Poggemann, L., Thelen, R., Meyer, J., Dittler, A. (2023). *Experimental investigation on the change of pull-off force between bulk particulate material and an elastic polymeric filter fiber* In: Journal of colloid and interface science, 641, 105785, https://doi.org/10.1016/j.jcis.2023.03.051

Poggemann, L., King, B., Meyer, J., Dittler, A. (2023). *Morphology of Particulate Structures on a Fiber Array before and at Clogging Point of an Aerosol Filtration Process* In: Separations, 10(9), 462, https://doi.org/10.3390/separations10090462

Poggemann, L., Längle, P., Meyer, J., Dittler, A. (2024). *Detachment of particulate structures from a fiber array due to stretching and simultaneous gas flow* In: Journal of Separation and Purification Technology, 127887, 1383-5866, https://doi.org/10.1016/j.seppur.2024.127887

Asylbekov, E., Poggemann, L., Dittler, A., Nirschl, H. (2024) *Discrete element method simulation of particulate material fracture behavior on a stretchable single filter fiber with an additional gas flow* In: Powders, 3(3), 367-391; https://doi.org/10.3390/powders3030021

Ullmann, K., Poggemann, L., Nirschl, H., Leneweit, G. (2020). *Adsorption process for phospholipids of different chain lengths at a fluorocarbon/water interface studied by Du Noüy ring and spinning drop* In: Colloid & polymer science, 298 (4-5), 407–417. doi:10.1007/s00396-020-04618-3

Conference Talks

Messung von abgelösten Partikelstrukturen von einer dehnbaren Filterfaser mit Laserschnitt-Messtechnik bei Vorgabe von Kalibriermaterial unterschiedlicher Form - Jahrestreffen der DECHEMA-Fachgruppen Aerosoltechnik (AT), Gasreinigung (GAS), Mehrphasenströmung (MPH) und Partikelmesstechnik (PMT) 2023, Poggemann, L., Meyer, J., Dittler, A.

Influence of structure morphology on detachment behavior of deposited agglomerates from a stretchable single fiber during multiple fiber elongations - FILTECH 2022, The Filtration Event - Poggemann, L., Meyer, J., Dittler, A.

Adaptronik in der Filtertechnik - Charakterisierung der Partikelstrukturablösung bei Dehnung einer Filterfaser - Industrieworkshop "Digitalisierung in der Trenntechnik", 2020 - Poggemann, L., Meyer, J., Dittler, A.

Conference Posters

Untersuchung der residualen Partikelstrukturen bei vorheriger Ablösung von Partikelagglomeraten von einer angeströmten dehnbaren Einzelfaser - Jahrestreffen der ProcessNet-Fachgruppen Gasreinigung und Partikelmesstechnik 2021 - Poggemann, L., Meyer, J., Dittler, A.

Erste Versuche zum Abscheiden und Ablösen von Partikeln auf/von einer dehnbaren Einzelfaser - Jahrestreffen der ProcessNet-Fachgruppen Computational Fluid Dynamics und Gasreinigung 2020 - Poggemann, L., Meyer, J., Dittler, A.

A new set-up for characterisation of particle and agglomerate detachment from an elastic single fibre exposed to airflow at low velocity - FILTECH 2019, The Filtration Event - Poggemann, L., Meyer, J., Dittler, A.

Bibliography

[1] Abts, G. *Kunststoff-Wissen für Einsteiger*. Hanser, 2010.

[2] Alim, K., Parsa, S., Weitz, D. A., and Brenner, M. P. "Local Pore Size Correlations Determine Flow Distributions in Porous Media." In: *Phys. Rev. Lett.* 119 (14 2017), p. 144501. DOI: 10.1103/PhysRevLett.119.144501.

[3] Amitay-Sadovsky, E., Ward, B., Somorjai, G. A., and Komvopoulos, K. "Nanomechanical properties and morphology of thick polyurethane films under contact pressure and stretching." In: *Journal of Applied Physics* 91.1 (2002), p. 375. DOI: 10.1063/1.1417990.

[4] ANSI. *Surface Texture: Surface Roughness, Waviness, and Lay*. 2019. URL: https://www.beuth.de/de/norm/asme-b46-1/325928583.

[5] ASHRAE. *Standard 52-76, Method of testing air-cleaning devices used in general ventilation for removing particulate matter*. Tech. rep. 1976.

[6] Ata, A., Rabinovich, Y. I., and Singh, R. K. "Role of surface roughness in capillary adhesion." In: *Journal of Adhesion Science and Technology* 16.4 (2002), pp. 337–346. DOI: 10.1163/156856102760067145.

[7] Bahners, T. and Schollmeyer, E. *Computer simulation of the filtration process in a fibrous filter collecting polydisperse dust*. Vol. 17. 1986. DOI: 10.1016/0021-8502(86)90066-2.

[8] Bamberg, E., Grippo, C. P., Wanakamol, P., Slocum, A. H., Boyce, M. C., and Thomas, E. L. "A tensile test device for in situ atomic force microscope mechanical testing." In: *Precision Engineering* 30.1 (2006), pp. 71–84. DOI: 10.1016/j.precisioneng.2005.05.001.

[9] Bargel, H.-J. and Schulze, G. *Werkstoffkunde*. Springer Berlin Heidelberg, 2008. DOI: 10.1007/978-3-540-79297-0.

[10] Beach, E. R., Tormoen, G. W., Drelich, J., and Han, R. "Pull-off force measurements between rough surfaces by atomic force microscopy." In: *Journal of colloid and interface science* 247.1 (2002), pp. 84–99. DOI: 10.1006/jcis.2001.8126.

[11] Berry, G., Beckman, I., and Cho, H. "A comprehensive review of particle loading models of fibrous air filters." In: *Journal of Aerosol Science* 167 (2023), p. 106078. DOI: 10.1016/j.jaerosci.2022.106078.

[12] Beuth, J. L. "Cracking of thin bonded films in residual tension." In: *International Journal of Solids and Structures* 29.13 (1992), pp. 1657–1675. DOI: 10.1016/0020-7683(92)90015-L.

[13] Bourrous, S., Bouilloux, L., Ouf, F. X., Appert-Collin, J. C., Thomas, D., Tampère, L., and Morele, Y. "Measurement of the Nanoparticles Distribution in Flat and Pleated Filters During Clogging." In: *Aerosol Science and Technology* 48.4 (2014), pp. 392–400. DOI: 10.1080/02786826.2013.878453.

[14] Bourrous, S., Bouilloux, L., Ouf, F.-X., Lemaitre, P., Nerisson, P., Thomas, D., and Appert-Collin, J. C. "Measurement and modeling of pressure drop of HEPA filters clogged with ultrafine particles." In: *Powder Technology* 289 (2016), pp. 109–117. DOI: 10.1016/j.powtec.2015.11.020.

[15] Brach, R. M. and Dunn, P. F. "Models of rebound and capture for oblique microparticle impacts." In: *Aerosol Science and Technology* 29.5 (1998), pp. 379–388. DOI: https://doi.org/10.1080/02786829808965577.

[16] Braschke, K., Zoller, J., Zargaran, A., Dittler, A., and Janoske, U. "Analytical and numerical calculation of the detachment of particle structures from fibers." In: *Aerosol Science and Technology* 56.1 (2022), pp. 1–11. DOI: 10.1080/02786826.2021.1972085.

[17] Broßmann, R. *Die Lichtstreuung an kleinen Teilchen als Grundlage einer Teilchengrößenbestimmung*. 1966.

[18] Brown, R. C. "A many-fibre model of airflow through a fibrous filter." In: *Journal of Aerosol Science* 15.5 (1984), pp. 583–593. DOI: 10.1016/0021-8502(84)90021-1.

[19] Brown, R. C. *Air Filtration: An Integrated Approach to the Theory and Applications of Fibrous Filters*. Pergamon Press Ltd., 1993.

[20] Cai, R.-R. and Zhang, L.-Z. "Modeling of dynamic deposition and filtration processes of airborne particles by a single fiber with a coupled lattice Boltzmann and discrete element method." In: *Building and Environment* 106 (2016), pp. 274–285. DOI: https://doi.org/10.1016/j.buildenv.2016.07.001.

[21] Cassie, A. B. D. and Baxter, S. "Wettability of porous surfaces." In: *Transactions of the Faraday Society* 40.0 (1944), p. 546. DOI: 10.1039/TF9444000546.

[22] Charvet, A., Wingert, L., Bardin-Monnier, N., Pacault, S., Godoy, C., Ribeyre, Q., and Thomas, D. "Visualization of airborne nanoparticle deposits onto spherical collectors." In: *Separation and Purification Technology* 172 (2017), pp. 119–129. DOI: 10.1016/j.seppur.2016.07.045.

[23] Coetzee, C. "Calibration of the discrete element method: Strategies for spherical and non-spherical particles." In: *Powder Technology* 364 (2020), pp. 851–878. DOI: 10.1016/j.powtec.2020.01.076.

[24] Daniel, D., Lay, C. L., Sng, A., Jun Lee, C. J., Jin Neo, D. C., Ling, X. Y., and Tomczak, N. "Mapping micrometer-scale wetting properties of superhydrophobic surfaces." In: *Proceedings of the National Academy of Sciences of the United States of America* 116.50 (2019), pp. 25008–25012. DOI: 10.1073/pnas.1916772116.

[25] Davies, C. "The clogging of fibrous aerosol filters." In: *Journal of aerosol science* 1.1 (1970), pp. 35–39.

[26] Derjaguin, B., Muller, V., and Toporov, Y. "Effect of contact deformations on the adhesion of particles." In: *Journal of colloid and interface science* 53.2 (1975), pp. 314–326. DOI: 10.1016/0021-9797(75)90018-1.

[27] DIN 3677, VDI. *VDI 3677; Filternde Abscheider: Verein Deutscher Ingenieure*. 2004.

[28] DIN 779, E. "779: 2012-10 Partikel-Luftfilter für die allgemeine Raumlufttechnik Bestimmung der Filterleistung." In: *Deutsche Fassung EN* 779 (2012).

[29] DIN Deutsches Institut für Normung e. V., DIN German Institute for Standardization. *Geometrische Produktspezifikation (GPS) - Oberflächenbeschaffenheit: Flächenhaft - Teil 2: Begriffe, Definitionen und Oberflächen-Kenngrößen (ISO/DIS 25178-2:2019): DIN EN ISO 25178-2 (2020-02-00)*.

[30] Ditscherlein, L. "Beitrag zur Berechnung von Haftkräften auf rauen Oberflächen am Beispiel keramischer Filtersysteme bei der Metallschmelzefiltration." PhD thesis. 2021.

[31] Dong, M., Li, J., Shang, Y., and Li, S. "Numerical investigation on deposition process of submicron particles in collision with a single cylindrical fiber." In: *Journal of Aerosol Science* 129 (2019), pp. 1–15. DOI: https://doi.org/10.1016/j.jaerosci.2018.12.001.

[32] Duparré, A., Ferre-Borrull, J., Gliech, S., Notni, G., Steinert, J., and Bennett, J. M. "Surface characterization techniques for determining the root-mean-square roughness and power spectral densities of optical components." In: *Applied Optics* 41.1 (2002), pp. 154–171. DOI: 10.1364/AO.41.000154.

[33] Eichenlaub, S., Chan, C., and Beaudoin, S. P. "Hamaker constants in integrated circuit metalization." In: *Journal of colloid and interface science* 248.2 (2002), pp. 389–397. DOI: 10.1006/jcis.2002.8241.

[34] Götzinger, M. and Peukert, W. "Particle adhesion force distributions on rough surfaces." In: *Langmuir* 20.13 (2004), pp. 5298–5303. DOI: 10.1021/la049914f.

[35] Gradoń, L. *Resuspension of particles from surfaces: Technological, environmental and pharmaceutical aspects*. Vol. 20. 2009. DOI: 10.1016/j.apt.2008.10.009.

[36] Griffiths, I., Mitevski, I., Vujkovac, I., Illingworth, M., and Stewart, P. "The role of tortuosity in filtration efficiency: A general network model for filtration." In: *Journal of Membrane Science* 598 (2020), p. 117664. DOI: 10.1016/j.memsci.2019.117664.

[37] Haarmann, A. and Schmidt, E. "Measurement of the Adhesion Moment of a Particle on a Wall in a Gaseous Environment and Comparison to Simulated Data." In: *Particles in Contact*. 2019, pp. 417–436. DOI: 10.1007/978-3-030-15899-6{\textunderscore}14.

[38] Hamamatsu Photonics K.K. Electron Tube Division. *Photomultiplier Tubes: Basics and Application*. Third Edition. 2007.

[39] Hauf-Hartung, K. "Capillary Suspensions with Polymeric Bridges." PhD thesis. Karlsruhe Institut für Technologie (KIT), 2019. DOI: 10.5445/IR/1000098700.

[40] HC Hamaker. "The London—van der Waals attraction between spherical particles." In: *Physica 4* (1937), pp. 1058–1072. DOI: https://doi.org/10.1016/S0031-8914(37)80203-7.

[41] Heim, L.-O., Blum, J., Preuss, M., and Butt, H.-J. "Adhesion and Friction Forces between Spherical Micrometer-Sized Particles." In: *Physical Review Letters* 83.16 (1999), pp. 3328–3331. DOI: 10.1103/PhysRevLett.83.3328.

[42] Hiller, R. and Löffler, F. "Einflussgrad von Auftreffgrad und Haftanteil auf die Partikelabscheidung in Faserfiltern." In: *Staub Reinhaltung der Luft, Air Quality Control* 40 (1980).

[43] Hinds, W. C. *Aerosol Technology: Properties, Behavior and measurement of Aiborne Particles*. 1999.

[44] Hokkanen, M. J., Backholm, M., Vuckovac, M., Zhou, Q., and Ras, R. H. A. "Force-Based Wetting Characterization of Stochastic Superhydrophobic Coatings at Nanonewton Sensitivity." In: *Advanced Materials* 33.42 (2021), e2105130. DOI: 10.1002/adma.202105130.

[45] Hoppe, K., Schaldach, G., Zielke, R., Tillmann, W., Thommes, M., and Pieloth, D. "Experimental analysis of particle deposition in fibrous depth filters during gas cleaning using X-ray microscopy." In: *Aerosol Science and Technology* 56.12 (2022), pp. 1114–1131. DOI: https://doi.org/10.1080/02786826.2022.2132133.

[46] Hoppe, K., Maricanov, M., Schaldach, G., Zielke, R., Renschen, D., Tillmann, W., Thommes, M., and Pieloth, D. "Modeling the separation performance of depth filter considering tomographic data." In: *Environmental Progress & Sustainable Energy* (2020). DOI: 10.1002/ep.13423.

[47] Hoppe, K., Wischemann, L., Schaldach, G., Zielke, R., Tillmann, W., Thommes, M., and Pieloth, D. "Filtration Kinetics of Depth Filters—Modeling and Comparison with Tomographic Data of Particle Depositions." In: *Atmosphere* 14.4 (2023), p. 640. DOI: https://doi.org/10.3390/atmos14040640.

[48] Hosseini, S. and Tafreshi, H. V. "Modeling particle-loaded single fiber efficiency and fiber drag using ANSYS–Fluent CFD code." In: *Computers & Fluids* 66 (2012), pp. 157–166. DOI: https://doi.org/10.1016/j.compfluid.2012.06.017.

[49] Ibrahim, A. H., Dunn, P. F., and Brach, R. M. "Microparticle detachment from surfaces exposed to turbulent air flow: Effects of flow and particle deposition characteristics." In: *Journal of Aerosol Science* 35.7 (2004), pp. 805–821. DOI: 10.1016/j.jaerosci.2004.01.002.

[50] Israelachvili, J. N. *Intermolecular and surface forces*. Third edition. Elsevier, 2011.

[51] Jackiewicz, A., Jakubiak, S., and Gradoń, L. "Analysis of the behavior of deposits in fibrous filters during non-steady state filtration using X-ray computed tomography." In: *Separation and Purification Technology* 156 (2015), pp. 12–21. DOI: https://doi.org/10.1016/j.seppur.2015.10.004.

[52] Jackiewicz, A., Jakubiak, S., and Gradoń, L. "Analysis of the behavior of deposits in fibrous filters during non-steady state filtration using X-ray computed tomography." In: *Separation and Purification Technology* 156 (2015), pp. 12–21. DOI: 10.1016/j.seppur.2015.10.004.

[53] Jankowska, E., Reponen, T., Willeke, K., Grinshpun, Sergey, A., and Choi, K.-J. "Collection of fungal spores on air filters and spore reentrainment from filters into air." In: *Journal of Aerosol Science* 31 (2000), pp. 969–978. DOI: https://doi.org/10.1016/S0021-8502(00)00017-3.

[54] Japuntich, D. A. "Clogging of fibrous filter with monodispers aerosols." PhD thesis. Loughborough University of Technology, March, 1991.

[55] Japuntich, D. A., Stenhouse, J. I., and Liu, B. Y. H. "Effective Pore Diameter and Monodisperse Particle Clogging of Fibrous Filters." In: *Journal of Aerosol Science* 28 (1997), pp. 147–158. DOI: https://doi.org/10.1016/S0021-8502(96)00064-X.

[56] Japuntich, D. A., Stenhouse J. Ian T., and Liu, B. Y. H. "Experimental Results of solid monodisperse particle clogging of fibrous filters." In: *Journal of Aerosol Science* 25 (1994), pp. 385–393. DOI: https://doi.org/10.1016/0021-8502(94)90089-2.

[57] Jia, C., Wang, Z., Zhang, D., Zhang, T., and Meng, X. "Fracture of films caused by uniaxial tensions: a numerical model." In: *Applied Mathematics and Mechanics* 44.12 (2023), pp. 2093–2108. DOI: 10.1007/s10483-023-3061-7.

[58] Jiang, R., Liu, M., Zheng, X., and Zhou, X. "Metal-Free, Low-Surface Energy, and Self-Healing Polyurethane Coating with an Excellent Antifouling Property." In: *ACS Applied Polymer Materials* 4.11 (2022), pp. 8594–8603. DOI: 10.1021/acsapm.2c01503.

[59] Jodeit, H. "Untersuchungen zur Partikelabscheidung in technischen Tiefenfiltern." PhD thesis. Universität Karlsruhe, 1985.

[60] Johnson, K. L. and Kendall,K. Roberts, A.D. “Surface energy and the contact of elastic solids.” In: *Procedings Royal Society London* 324 (1971), pp. 301–313. DOI: https://doi.org/10.1098/rspa.1971.0141.

[61] Jones, R., Pollock, H. M., Cleaver, J. A. S., and Hodges, C. S. “Adhesion Forces between Glass and Silicon Surfaces in Air Studied by AFM: Effects of Relative Humidity, Particle Size, Roughness, and Surface Treatment.” In: *Langmuir* 18.21 (2002), pp. 8045–8055. DOI: 10.1021/la0259196.

[62] Jung, C. H., Park, H. S., and Kim, Y. P. “Moment approach to the polydispersed particle size distribution of dust–loaded fibers due to convective diffusion.” In: *Environmental Progress & Sustainable Energy* 31.3 (2012), pp. 397–406. DOI: 10.1002/ep.10562.

[63] Kajiyama, T. and MacKnight, W. J. “Relaxation in Polyurethanes in the Glass Transition Region.” In: *Transactions of The Society of Rheology* 13.4 (1969), pp. 527–546. DOI: 10.1122/1.549149.

[64] Kampa, D., Wurster, S., Buzengeiger, J., Meyer, J., and Kasper, G. “Pressure drop and liquid transport through coalescence filter media used for oil mist filtration.” In: *International Journal of Multiphase Flow* 58 (2014), pp. 313–324. DOI: 10.1016/j.ijmultiphaseflow.2013.10.007.

[65] Kanaoka, C., Emi, H., Hiragi, S., and Myojo, T. “Morphology of particulate agglomerates on a cylindrical fiber and a collection efficiency of a dust loaded fiber.” In: *Aerosols: Formation and Reactivity 2nd Aerosol Conf. Berlin* (1986), pp. 674–677.

[66] Kanaoka, C. and Hiragi, S. “Pressure Drop Of Air Filter With Dust Load.” In: *Journal of Aerosol Science* 21 (1990), pp. 127–137. DOI: https://doi.org/10.1016/0021-8502(90)90027-U.

[67] Kanaoka, C. “Fine Particle Filtration Technology Using Fiber as Dust Collection Medium.” In: *KONA Powder and Particle Journal* 36.0 (2019), pp. 88–113. DOI: 10.14356/kona.2019006.

[68] Kanaoka, C., Emi, H., and Myojo, T. “Simulation of the growing process a particle dendrite and evaluation of a single fiber collection efficiency with dust load.” In: *Journal of Aerosol Science* 1980.11 (1979), pp. 377–389. DOI: https://doi.org/10.1016/0021-8502(80)90046-4.

[69] Kappl, M. and Butt, H.-J. “The Colloidal Probe Technique and its Application to Adhesion Force Measurements.” In: *Particle & Particle Systems Characterization* 19.3 (2002), p. 129. DOI: 10.1002/1521-4117(200207)19:3{\textless}129::AID-PPSC129{\textgreater}3.0.CO;2-G.

[70] Kasper, G., Schollmeier, S., and Meyer, J. “Structure and density of deposits formed on filter fibers by inertial particle deposition and bounce.” In: *Journal of Aerosol Science* 41.12 (2010), pp. 1167–1182. DOI: 10.1016/j.jaerosci.2010.08.006.

[71] Katainen, J., Paajanen, M., Ahtola, E., Pore, V., and Lahtinen, J. "Adhesion as an interplay between particle size and surface roughness." In: *Journal of colloid and interface science* 304.2 (2006), pp. 524–529. DOI: 10.1016/j.jcis.2006.09.015.

[72] Kostoglou, M. and Konstandopoulos, A. G. "Particulate deposit shape evolution on cylinders in cross flow at high stokes numbers." In: *Journal of Aerosol Science* 31 (2000), pp. 427–436. DOI: https://doi.org/10.1016/S0021-8502(99)00066-X.

[73] Kumar, A., Staedler, T., and Jiang, X. "Role of relative size of asperities and adhering particles on the adhesion force." In: *Journal of colloid and interface science* 409 (2013), pp. 211–218. DOI: 10.1016/j.jcis.2013.07.039.

[74] Kuwabara, S. "The Forces experienced by Randomly Distributed Parallel Circular Cylinders or Spheres in a Viscous Flow at Small Reynolds Numbers." In: *Journal of the Physical Society of Japan* 14.4 (1959), pp. 527–532. DOI: 10.1143/JPSJ.14.527.

[75] Larsen, R. I. "The Adhesion and Removal of Particles Attached to Air Filter Surfaces." In: *American Industrial Hygiene Association journal* 19 (1958). DOI: 10.1080/00028895809343591.

[76] Lehmann, M. J. "Untersuchung zur Struktur und zur Beladungskinetik von Tiefenfiltern." PhD thesis. 2005.

[77] Lehmann, M. J. and Kasper, G. "Simulation zur Beladungskinetik an Einzelfasern - Literaturübersicht und neue Ergebnisse." In: *Filtertechnik Workshop* (2005).

[78] Leschonski, K. "Partikelmeßtechnik." In: *Berichte der Bunsengesellschaft für physikalische Chemie* 88.11 (1984), pp. 1112–1123. DOI: 10.1002/bbpc.198400017.

[79] Leung, W. W.-F. and Choy, H.-F. "Transition from depth-to-surface filtration for a high-efficiency, high-skin effect, nanofiber filter under continuous nanoaerosol loading." In: *Chemical Engineering Science* 182 (2018), pp. 67–76. DOI: 10.1016/j.ces.2018.02.024.

[80] Liimatainen, V., Vuckovac, M., Jokinen, V., Sariola, V., Hokkanen, M. J., Zhou, Q., and Ras, R. H. A. "Mapping microscale wetting variations on biological and synthetic water-repellent surfaces." In: *Nature Communications* 8.1 (2017), p. 1798. DOI: 10.1038/s41467-017-01510-7.

[81] Löffler, F. "Abblasen von an Filterfasern abgeschiedenen Feststoffteilchen." In: *Verfahrenstechnik* 6 (1972), pp. 3–7.

[82] Löffler, F. *Staubabscheiden: Friedrich Löffler*. Thieme, 1988.

[83] Löffler, F. and Muhr, W. "Die Abscheidung von Feststoffteilchen und Tropfen an Kreiszylindern infolge von Trägheitskräften." In: (1972). DOI: https://doi.org/10.1002/cite.330440804.

[84] Löffler, F. and Umhauer, H. "Eine optische Methode zur Teilchenabscheidung an Filterfasern." In: *Staub* 31.51/55 (1971).

[85] Lowden, R. A. and Stinton, D. P. “Interface Modification in Nicalon®/SiC Composites.” In: *Ceramic Engineering and Science Proceedings* 9 (1988), pp. 705–122.

[86] M. Schilling, S. Schütz, and M. Piesche. “Numerical simulation of the transport and deposition behaviour of particles on filter fibres using Euler–Lagrange Method and coupling of CFD and DEM.” In: *AIP Conference Proceedings* 1207.1 (2010), p. 789. DOI: 10.1063/1.3366464.

[87] Mader-Arndt, K., Kutelova, Z., Fuchs, R., Meyer, J., Staedler, T., Hintz, W., and Tomas, J. “Single particle contact versus particle packing behavior: model based analysis of chemically modified glass particles.” In: *Granular Matter* 16.3 (2014), pp. 359–375. DOI: 10.1007/s10035-013-0478-9.

[88] Mak, L. H., Knoll, M., Weiner, D., Gorschlüter, A., Schirmeisen, A., and Fuchs, H. “Reproducible attachment of micrometer sized particles to atomic force microscopy cantilevers.” In: *Review of Scientific Instruments* 77.4 (2006), p. 046104. DOI: 10.1063/1.2190068.

[89] Miwa, T., Miya, G., and Kanno, S. “Effect of surface roughness on small particle adhesion forces evaluated by atomic force microscopy.” In: *Japanese Journal of Applied Physics* 59.7 (2020), p. 076504. DOI: 10.35848/1347-4065/ab9e48.

[90] Müller, T. K., Meyer, J., Thébault, E., and Kasper, G. “Impact of an oil coating on particle deposition and dust holding capacity of fibrous filters.” In: *Powder Technology* 253 (2014), pp. 247–255. DOI: 10.1016/j.powtec.2013.11.036.

[91] Müller, T. “Trägheitsabscheidung von Partikeln an parallelen Faserarrays.” PhD thesis. Karlsruher Institut für Technologie (KIT), 2017.

[92] Müller, T., Meyer, J., and Kasper, G. “Low Reynolds number drag and particle collision efficiency of a cylindrical fiber within a parallel array.” In: *Journal of Aerosol Science* 77 (2014), pp. 50–66. DOI: 10.1016/j.jaerosci.2014.07.007.

[93] Nahta, R. and Moran B. “Crack Spacing in Brittle Films on Dissimilar Planar and Axisymmetric Elastic Substrates.” In: *Engineering Fracture Mechanics* 52 (1995), pp. 513–524. DOI: https://doi.org/10.1016/0013-7944(94)00283-N.

[94] Nahta, R. and Moran B. “Film cracking and debonding in a coated fiber.” In: *Inernational Journal of Fracture* 79 (1996), pp. 351–372. DOI: https://doi.org/10.1007/BF00018596.

[95] Ochiai, S. and Murakami, Y. “Theoretical prediction of tensile strength of fibers as a function of thickness of brittle zones on fiber surfaces.” In: *Metallurgical Transactions A* 12A (1981), pp. 1155–1161. DOI: https://doi.org/10.1007/BF02642329.

[96] Opdahl, A. and Somorjai, G. A. “Stretched polymer surfaces: Atomic force microscopy measurement of the surface deformation and surface elastic properties of stretched polyethylene.” In: *Journal of Polymer Science Part B: Polymer Physics* 39.19 (2001), pp. 2263–2274. DOI: 10.1002/polb.1200.

[97] Otsu, N. "A Threshold Selection Method from Gray-Level Histograms." In: *IEEE Transactions on Systems, Man, and Cybernetics* 9.1 (1979), pp. 62–66. DOI: 10.1109/TSMC.1979.4310076.

[98] Papapostolou, V., Zhang, H., Feenstra, B. J., and Polidori, A. "Development of an environmental chamber for evaluating the performance of low-cost air quality sensors under controlled conditions." In: *Atmospheric Environment* 171 (2017), pp. 82–90. DOI: 10.1016/j.atmosenv.2017.10.003.

[99] Payatakes, A. C. and Gradoń, L. "Dendritic deposition of aerosols by convective Brownian diffusion for small, intermediate and high particle Knudsen numbers." In: *AIChE Journal* 26 (1980), pp. 443–454. DOI: https://doi.org/10.1016/0021-8502(76)90067-7.

[100] Payatakes, A. C. and Tien, C. "Particle deposition in fibrous media with dendrite-like pattern: A preliminary model." In: *Journal of Aerosol Science* 7.2 (1976), pp. 85–100. DOI: https://doi.org/10.1016/0021-8502(76)90067-7.

[101] Payet, S., Boulaud, D., Madelaine, G., and Renoux, A. "Penetration and pressure drop of HEPA Filter during loading with submicron liquid particle." In: *Journal of Aerosol Science* 23 (1992), pp. 723–735. DOI: https://doi.org/10.1016/0021-8502(92)90039-X.

[102] Peart, J. "Powder electrostatics: theory, techniques and applications." In: *KONA Powder and Particle Journal* 19 (2001), pp. 34–45. DOI: 10.14356/kona.2001009.

[103] Penicot, P., Thomas, D., Contal, P., Leclerc, D., and Vendel, J. "Clogging of HEPA Fibrous Filters by Solid and Liquid Aerosol Particles: An Experimental Study." In: *Filtration and Separation* (1999). DOI: https://doi.org/10.1016/S0015-1882(99)80036-6.

[104] Petean, P. and Aguiar, M. L. "Determining the adhesion force between particles and rough surfaces." In: *Powder Technology* 274 (2015), pp. 67–76. DOI: 10.1016/j.powtec.2014.12.047.

[105] Poggemann, L., King, B., Meyer, J., and Dittler, A. "Morphology of Particulate Structures on a Fiber Array before and at Clogging Point of an Aerosol Filtration Process." In: *Separations* 10.9 (2023), p. 462. DOI: 10.3390/separations10090462.

[106] Poggemann, L., Meyer, J., and Dittler, A. "A novel method to investigate detachment of particulate structures from an elastic single fiber at low gas flow velocities." In: *Journal of Aerosol Science* 156 (2021), p. 105785. DOI: 10.1016/j.jaerosci.2021.105785.

[107] Poggemann, L., Meyer, J., and Dittler, A. "Experimental Detection of Particle Structures Detachment from a Stretchable Single Fiber during Multiple Consecutive Stretching Cycles." In: *Separations* 9.7 (2022), p. 168. DOI: 10.3390/separations9070168.

[108] Poggemann, L., Thelen, R., Meyer, J., and Dittler, A. "Experimental investigation on the change of pull-off force between bulk particulate material and an elastic polymeric filter fiber." In: *Journal of Colloid and Interface Science* 641 (2023), pp. 903–915. DOI: https://doi.org/10.1016/j.jcis.2023.03.051.

[109] Prokopovich, P. and Starov, V. "Adhesion models: from single to multiple asperity contacts." In: *Advances in Colloid and Interface Science* 168.1-2 (2011), pp. 210–222. DOI: 10.1016/j.cis.2011.03.004.

[110] Przekop, R., Grzybowski, K., and Gradoń, L. "Energy-Balanced Oscillatory Model for Description of Particles Deposition and Re-Entrainment on Fiber Collector." In: *Aerosol Science and Technology* 38.4 (2004), pp. 330–337. DOI: 10.1080/02786820490427669.

[111] Przekop, R., Moskal, A., and Gradoń, L. "Lattice-Boltzmann approach for description of the structure of deposited particulate matter in fibrous filters." In: *Journal of Aerosol Science* 34.2 (2003), pp. 133–147. DOI: https://doi.org/10.1016/S0021-8502(02)00153-2.

[112] Qian, Y., Willeke, K., Grinshpun, S. A., and Donnelly, J. "Performance of N95 respirators: reaerosolization of bacteria and solid particles." In: *American Industrial Hygiene Association Journal* 58.12 (1997), pp. 876–880.

[113] Qian, Y., Willeke, K., Ulevicius, V., and Grinshpun, S. A. "Particle Reentrainment from Fibrous Filters." In: *Aerosol Science and Technology* 27.3 (1997), pp. 394–404. DOI: 10.1080/15428119791012216.

[114] R. Maus and H. Umhauer. "Collection and adhesion efficiency of biological particles on single fibers." In: *Journal of Aerosol Science* 27 (1996). DOI: 10.1016/0021-8502(96)00200-5.

[115] Raasch, J. and Umhauer, H. "Grundsätzliche Überlegungen zur Messung der Verteilungen von Partikelgröße und Partikelgeschwindigkeit disperser Phasen in Strömungen." In: *Chemie Ingenieur Technik* 49.12 (1977), pp. 931–941. DOI: 10.1002/cite.330491203.

[116] Rabinovich, Y. I., Adler, J. J., Ata, A., Singh, R. K., and Moudgil, B. M. "Adhesion between Nanoscale Rough Surfaces: I. Role of Asperity Geometry." In: *Journal of Colloid and Interface Science* 232.1 (2000), pp. 10–16. DOI: https://doi.org/10.1006/jcis.2000.7167.

[117] Rabinovich, Y. I., Adler, J. J., Ata, A., Singh, R. K., and Moudgil, B. M. "Adhesion between Nanoscale Rough Surfaces: II. Measurement and Comparison with Theory." In: *Journal of Colloid and Interface Science* 232.1 (2000), pp. 17–24. DOI: https://doi.org/10.1006/jcis.2000.7168.

[118] Rembor, H.-J. "Das Verhalten von Tiefenfiltern bei zunehmender Staubbeladung." PhD thesis. Universität Karlsruhe, 2002.

[119] Rembor, H.-J. and Kasper, G., eds. *Morphology of Particulate Structures on Dust Loaded Single Fibres*. Delft University Press, 1999.

[120] Rembor, H.-J., Maus, R., and Umhauer, H. "Measurements of Single Fibre Efficiencies at Critical Values of the Stokes Number." In: *Particle & Particle Systems Characterization* 16 (1999), pp. 54–59. DOI: https://doi.org/10.1002/(SICI)1521-4117(199906)16:2<54::AID-PPSC54>3.0.CO;2-P.

[121] Rhee, S. K. "Surface energies of silicate glasses calculated from their wettability data." In: *Journal of Materials Science* 12.4 (1977), pp. 823–824. DOI: 10.1007/BF00548176.

[122] Rimai, D. S., Demejo, L. P., Vreeland, W., Bowen, R., Gaboury, S. R., and Urban, M. W. "The effect of Young's modulus on the surface–force–induced contact radius of spherical glass particles on polyurethane substrates." In: *Journal of Applied Physics* 71.5 (1992), pp. 2253–2258. DOI: 10.1063/1.351123.

[123] Rumpf. "Zur Theorie der Zugfestigkeit von Agglomeraten bei Kraftübertragung an Kontaktpunkten." In: *Chem. Ing. Technik* 42 (1970), pp. 538–540. DOI: https://doi.org/10.1002/cite.330420806.

[124] Rumpf, H. "Grundlagen und Methoden des Granulierens." In: *Chemie Ingenieur Technik - CIT* 30.3 (1958), pp. 144–158. DOI: 10.1002/cite.330300307.

[125] Rumpf, H. C. H. "Zur Theorie der Zugfestigkeit von Agglomeraten bei Kraftübertragung an Kontaktpunkten." In: *Chemie Ingenieur Technik* 42.8 (1970), pp. 538–540. DOI: 10.1002/cite.330420806.

[126] Rumpf, H. "Die Wissenschaft des Agglomerierens." In: *Chemie Ingenieur Technik - CIT* 46.1 (1974), pp. 1–11. DOI: 10.1002/cite.330460102.

[127] Rumpf, H. *Particle technology*. Vol. 1. Springer Science & Business Media, 2012.

[128] Santos, H. R. and Leal, V. M. "Energy vs. ventilation rate in buildings: A comprehensive scenario-based assessment in the European context." In: *Energy and Buildings* 54 (2012), pp. 111–121. DOI: https://doi.org/10.1016/j.enbuild.2012.07.040.

[129] Schaefer, D. M., Carpenter, M., Gady, B., Reifenberger, R., Demejo, L. P., and Rimai, D. S. "Surface roughness and its influence on particle adhesion using atomic force techniques." In: *Journal of Adhesion Science and Technology* 9.8 (1995), pp. 1049–1062. DOI: 10.1163/156856195X00897.

[130] Schmidt, E. "Simulation of three-dimensional dust structures via particle trajectory calculation for cake-foming filtration." In: *Powder Technology* 86 (1995), pp. 113–117. DOI: https://doi.org/10.1016/0032-5910(95)03044-1.

[131] Schollmeier, S. "Beladungskinetik von Faserfiltern." PhD thesis. 2008.

[132] Schubert, H. "Grundlagen des Agglomerierens." In: *Chem. Ing. Technik* 51 (1979), pp. 266–270. DOI: https://doi.org/10.1002/cite.330510404.

[133] Schubert, H. "Tensile strength of agglomerates." In: *Powder Technology* 11.2 (1975), pp. 107–119. DOI: 10.1016/0032-5910(75)80036-2.

[134] Schubert, H. *Kapillarität in porösen Feststoffsystemen*. Springer Berlin Heidelberg, 1982.

[135] Schütz, W. and Schubert, H. "Der Einfluß von Anpreßkräften auf die Partikelhaftung." In: *Chem. Ing. Technik* 48 (1976), p. 567. DOI: https://doi.org/10.1002/cite.330480622.

[136] Schweers, E. "Realistic modelling of the behaviour of fibrous filters through consideration of filter structure." In: (1994). DOI: https://doi.org/10.1016/0032-5910(94)02850-8.

[137] Schweers, E. and Löffler, F. "Analyse der Struktur technischer Fiefenfilter: Verteilung der lokalen packungsdichte und Orientierung der Fasern." In: *Staub, Reinhaltung der Luft* 53 (1993).

[138] Schweers, E. and Löffler, F. "Realistic modelling of the behaviour of fibrous filters through consideration of filter structure." In: (1994). DOI: https://doi.org/10.1016/0032-5910(94)02850-8.

[139] Schweers, E., Umhauer, H., and Löffler, F. "Experimental Investigation of Particle Collection on Single Fibres of Different Configurations." In: *Particle & Particle Systems Characterization* (1994), pp. 275–283. DOI: https://doi.org/10.1002/ppsc.19940110402.

[140] Shi, K., Jin, G., Yan, W., and Xing, H. "Permeability estimation for deformable porous media with convolutional neural network." In: *International Journal of Numerical Methods for Heat & Fluid Flow* (2024). DOI: https://doi.org/10.1108/hff-10-2023-0644.

[141] Shyam, S., Misra, S., and Mitra, S. K. "A universal capillary-deflection based adhesion measurement technique." In: *Journal of colloid and interface science* 630.Pt A (2023), pp. 322–333. DOI: 10.1016/j.jcis.2022.09.140.

[142] Siena, M., Riva, M., Hyman, J., Winter, C., and Guadagnini, A. "Relationship between pore size and velocity probability distributions in stochastically generated porous media." In: *Physical review. E, Statistical, Nonlinear, and Soft Matter Physics* 89.1 (2014), pp. 013018–013018. DOI: https://journals.aps.org/pre/abstract/10.1103/PhysRevE.89.013018.

[143] Soltani, M. and Ahmadi, G. "Particle Removal Mechanisms Under Substrate Acceleration." In: *The Journal of Adhesion* 44.3 (1994), pp. 161–175. DOI: 10.1080/00218469408027075.

[144] Song, C. B., Park, H. S., and Lee, K. W. "Experimental study of filter clogging with monodisperse PSL particles." In: *Powder Technology* 163.3 (2006), pp. 152–159. DOI: 10.1016/j.powtec.2006.01.016.

[145] Song, Y. and Shim, E. “Structure characterization of the clogging process of coarse fibrous filter media during solid particle loading with X-ray micro-computed tomography.” In: *Separation and Purification Technology* 273 (2021), p. 118980. DOI: https://doi.org/10.1016/j.seppur.2021.118980.

[146] Song, Y. and Shim, E. “3D X-ray tomographic microstructure analysis of dust-clogging inside nonwoven fibrous filter media.” In: *Journal of Membrane Science* 664 (2022), p. 121067. DOI: https://doi.org/10.1016/j.memsci.2022.121067.

[147] Song, Y. and Shim, E. “High-fidelity 3D simulation of dust-loading behavior and clogging process of coarse nonwoven filter media considering collision effect.” In: *Separation and Purification Technology* 344 (2024), p. 127046. DOI: https://doi.org/10.1016/j.seppur.2024.127046.

[148] Szabadi, J., Meyer, J., and Dittler, A. “In situ characterization of particle structures generated at different flow velocities on a single fiber in the gas phase.” In: *Journal of Aerosol Science* 173 (2023), p. 106197. DOI: https://doi.org/10.1016/j.jaerosci.2023.106197.

[149] Szabadi, J., Meyer, J., and Dittler, A. “Particulate Matter Detachment from a Magnetizable Single Fiber Applying Magnetic Forces in Ambient Air.” In: *Separations* 10.5 (2023), p. 297. DOI: 10.3390/separations10050297.

[150] Szabadi, J., Meyer, J., and Dittler, A. “Particulate Matter Detachment from a Magnetizable Single Fiber Applying Magnetic Forces in Ambient Air.” In: *Separations* 10.5 (2023). DOI: 10.3390/separations10050297.

[151] Tao, R., Yang, M., and Li, S. “Effect of adhesion on clogging of microparticles in fiber filtration by DEM-CFD simulation.” In: *Powder Technology* 360 (2020), pp. 289–300. DOI: 10.1016/j.powtec.2019.09.083.

[152] Thomas, D., Penicot, P., Contal, P., and Leclerc, D. Vendel, J. “Clogging of fibrous filters by solid aerosol particles Experimental and modelling study.” In: *Chemical Engineering Science* 56 (2001), pp. 3549–3561. DOI: https://doi.org/10.1016/S0009-2509(01)00041-0.

[153] Thouless, M. D. “Crack Spacing in Brittle Films on Elastic Substrates.” In: *Journal of the American Ceramic Society* 73 (1990), pp. 2144–2146. DOI: https://doi.org/10.1111/j.1151-2916.1990.tb05290.x.

[154] Thundat, T., Zheng, X.-Y., Chen, G., and Warmack, R. “Role of relative humidity in atomic force microscopy imaging.” In: *Surface Science Letters* 294.1 (1993), pp. L939–L943. DOI: https://doi.org/10.1016/0167-2584(93)91119-9.

[155] Tippayawong, N. and I., P. “Analytical prediction of particle detachment from a flat surface by turbulent air flows.” In: (2011). DOI: https://www.thaiscience.info/journals/article/cmjs/10905401.pdf.

[156] Tippayawong, N. and Preechawuttipong, I. “Modified kinetic model of particle detachment by aerodynamic drag and vibration.” In: *Proceedings of the World Congress on Engineering and Computer Science 2010 Vol II* (2010). DOI: https://www.iaeng.org/publication/WCECS2010/WCECS2010_pp783-787.pdf.

[157] Tsai, C.-J., Pui, D. Y. H., and Liu, B. Y. H. “Elastic Flattening and Particle Adhesion.” In: *Aerosol Science and Technology* 15.4 (1991), pp. 239–255. DOI: 10.1080/02786829108959531.

[158] Tsukada, M., Irie, R., Yonemochi, Y., Noda, R., Kamiya, H., Watanabe, W., and Kauppinen, E. “Adhesion force measurement of a DPI size pharmaceutical particle by colloid probe atomic force microscopy.” In: *Powder Technology* 141.3 (2004), pp. 262–269. DOI: 10.1016/j.powtec.2004.03.008.

[159] Umhauer, H., Berbner, S., and Hemmer, G. “Optical In Situ Size and Concentration Measurement of Particles Dispersed in Gases at Temperatures up to 1000°C.” In: *Particle & Particle Systems Characterization* (1999). DOI: https://doi.org/10.1002/(SICI)1521-4117(200003)17:1<03::AID-PPSC3>3.0.CO;2-N.

[160] Valdes, J. R. and Santamarina, J. C. “Clogging: bridge formation and vibration-based destabilization.” In: *Canadian Geotechnical Journal* 45.2 (2008), pp. 177–184. DOI: 10.1139/T07-088.

[161] Wang, H., Zhao, H., Wang, K., He, Y., and Zheng, C. *Simulation of filtration process for multi-fiber filter using the Lattice-Boltzmann two-phase flow model*. Vol. 66. 2013. DOI: 10.1016/j.jaerosci.2013.08.016.

[162] Wang, Q., Lin, X., and Chen, D.-R. “Effect of dust loading rate on the loading characteristics of high efficiency filter media.” In: *Powder Technology* 287 (2016), pp. 20–28. DOI: https://doi.org/10.1016/j.powtec.2015.09.032.

[163] Wang, Q., Lin, X., and Chen, D.-R. “Effect of dust loading rate on the loading characteristics of high efficiency filter media.” In: *Powder Technology* 287 (2016), pp. 20–28. DOI: 10.1016/j.powtec.2015.09.032.

[164] Wanka, S., Kappl, M., Wolkenhauer, M., and Butt, H.-J. “Measuring adhesion forces in powder collectives by inertial detachment.” In: *Langmuir : the ACS journal of surfaces and colloids* 29.52 (2013), pp. 16075–16083. DOI: 10.1021/la404014d.

[165] Wongsri, M., Tanthapanichakoon, W., Kanaoka, C., and EMI, H. “Convective diffusional collection of polydisperse aerosols on a dust loaded fiber.” In: *Advanced Powder Technology* 2.1 (1991), pp. 11–23. DOI: 10.1016/S0921-8831(08)60717-7.

[166] Wu. *Polymer Interface and Adhesion*. 1st ed. CRC Press, 1982.

[167] Wu, S. “Interfacial and Surface Tensions of Polymers.” In: *Journal of Macromolecular Science, Part C* 10.1 (1974), pp. 1–73. DOI: 10.1080/15321797408080004.

[168] Wurster, S., Meyer, J., and Kasper, G. “On the relationship of drop entrainment with bubble formation rates in oil mist filters.” In: *Separation and Purification Technology* 179 (2017), pp. 542–549. DOI: 10.1016/j.seppur.2017.02.036.

[169] Wurster, S., Meyer, J., Kolb, H. E., and Kasper, G. "Bubbling vs. blow-off – On the relevant mechanism(s) of drop entrainment from oil mist filter media." In: *Separation and Purification Technology* 152 (2015), pp. 70–79. DOI: 10.1016/j.seppur.2015.08.012.

[170] Wurster, S. "Entrainment von Öltropfen an der Rückwand eines Faserfilters." PhD thesis. Karlsruher Institut für Technologie (KIT), 2017.

[171] YANG, C. "Aerosol Filtration Application Using Fibrous Media-An Industrial Perspective." In: *Chinese Journal of Chemical Engineering* 20.1 (2012), pp. 1–9. DOI: 10.1016/S1004-9541(12)60356-5.

[172] Yang, M., Li, S., and Yao, Q. "Mechanistic studies of initial deposition of fine adhesive particles on a fiber using discrete-element methods." In: *Powder Technology* 248 (2013), pp. 44–53. DOI: 10.1016/j.powtec.2012.12.016.

[173] Zhang, Q. "Online–Partikelmessung im Reingas zu Beginn der kuchenbildenden Staubabscheidung mit Nadelfilzen in der Gasreinigung." In: *Chemie Ingenieur Technik* 94.4 (2022), pp. 572–584. DOI: 10.1002/cite.202100053.

[174] Zhu, H., Qi, C., Fu, H., and Kang, Y. "Morphologies of particles deposit on a single fiber due to the inertia interception." In: *2015 4th International Conference on Sustainable Energy and Environmental Engineering* (2016), pp. 1193–1199. DOI: 10.2991/icseee-15.2016.212.

[175] Zimon, A. *Adhesion of Dust and Powder*. Springer, 2014.

[176] Ziskind, G. "PARTICLE RESUSPENSION FROM SURFACES: REVISITED AND REEVALUATED." In: *Reviews in Chemical Engineering* 22.1-2 (2006), pp. 1–123. DOI: 10.1515/REVCE.2006.22.1-2.1.

[177] Ziskind, G., Fichman, M., and Gutfinger, C. "Adhesion moment model for estimating particle detachment from a surface." In: *Journal of Aerosol Science* 28.4 (1997), pp. 623–634. DOI: 10.1016/S0021-8502(96)00460-0.

[178] Zoller, J. "Abscheidung reaktiver und inerter Partikeln aus Aerosolen auf einzelnen Fasern und Ablösung der entstandenen Strukturen durch Umströmung bei gleichzeitiger Reaktion." German. PhD thesis. Karlsruher Institut für Technologie (KIT), 2023. 141 pp. DOI: 10.5445/IR/1000165523.

[179] Zoller, J., Zargaran, A., Braschke, K., Meyer, J., Janoske, U., and Dittler, A. "Experimental Investigation of Reactive-Inert Particulate Matter Detachment from Metal Fibres at Low Flow Velocities and Different Gas Temperatures." In: *Aerosol Science and Engineering* (2020). DOI: 10.1007/s41810-020-00081-3.

[180] Zoller, J., Zargaran, A., Braschke, K., Meyer, J., Janoske, U., and Dittler, A. "Morphology of particulate deposits formed on a single filter fibre by exposure to mixed aerosol flow." In: *Journal of Aerosol Science* (2020), p. 105718. DOI: 10.1016/j.jaerosci.2020.105718.

[181] Zoller, J., Zargaran, A., Braschke, K., Meyer, J., Janoske, U., and Dittler, A. “A Novel Apparatus for Simultaneous Laser-Light-Sheet Optical Particle Counting and Video Recording in the Same Measurement Chamber at High Temperature.” In: *Sensors* 22.4 (2022), p. 1363. DOI: 10.3390/s22041363.

[182] Zoller, J., Zargaran, A., Braschke, K., Meyer, J., Janoske, U., and Dittler, A. “A Novel Apparatus for Simultaneous Laser-Light-Sheet Optical Particle Counting and Video Recording in the Same Measurement Chamber at High Temperature.” In: *Sensors* 22.4 (2022), p. 1363. DOI: 10.3390/s22041363.

Appendix

A List of Figures

1.1 Qualitative progress of pressure drop over filtration time. Modified from Penicot et al. [103] and Thomas et al. [152]. 1

1.2 Schematic of separation of particles at a single fiber with different separation mechanism a) diffusion, b) interception, c) inertia adapted from Löffler [81], Kanaoka et al. [65], and Zoller [178]. Below the resulting particle structure on the fiber with the assumed form/morphology as Kanaoka et al. [65] showed in his studies. It is assumed that fiber and particles are electrically neutral and that the air flow is constant and perpendicular. 4

1.3 Simple process flow diagram of the loading procedure for the separation of a particle structure in the stretchable single fiber and fiber array. . . 8

1.4 Fiber clamping device for the separation of a particle structure on a single fiber and subsequent stretching procedure. The design of the fiber clamping device for the fiber array is equal, except for the fiber combs, which ensures a constant distance of 246 μm. 9

1.5 Schematic of the two possible cases for a breakage of an agglomerate on the fiber: a) breakage of a particle structure due to applied drag force, and b) breakage of the particle structure due to fiber stretching. 13

1.6 a) Schematic of an elastomer molecule chain in the unstretched (I.) and the stretched state (II.) due to an applied vertical force as shown by Amitay-Sadovsky et al. [3]. b) Schematic of tension of the fiber c) fiber in the oringinal state tangled d) fiber surface entangled in a SEM image. 17

1.7 Simple schematic of the AFM measurement setup for the measurement of adhesion force between a particle and the polyurethane fiber in different state of elongation. The illustration is not to scale. 18

1.8 Simple schematic of the measurement setup laser light sheet 19

2.1 Schematic structure of this work. The publications in this dissertation are categorized into investigation on detachment within the micro- and meso level. 24

3.1 : Collection efficiency and pressure drop over collected particle mass of a stiff filtration matrix and of a potential time adjustable fiber structure. Modified from [152] 31

3.2 Schematic relationship between the deposit structure and filtration conditions in detail of the dimensionless numbers Peclét, Stokes-number and interception parameter R. Highlighted the compact deposition morphology with higher Stokes-number. Modified from Kanaoka [65] 34

3.3 a) Fiber in their original state, entangled, white polymeric structure. b) Fiber disentangled and clamped under the SEM – straightened, unstrechted with initial diameter of around 82 µm 36

3.4 a) Particle size distribution of used Spheriglass 5000 CP00 in the storage tank of the dust generator. Measured offline by HELOS & RODOS, Sympatec b) An according SEM image of the glass particles. 36

3.5 Process flow diagram of the loading procedure including the fiber-mounting device. 37

3.6 Image of the designed fiber-mounting device for stretching the elastic fiber 39

3.7 Schematic set-up used for fiber stretching including the fiber-mounting device with loaded fiber and the microscope camera. 39

3.8 Schematic illustrating the size of projection area of two consecutive frames when stretching the elastic fiber. 40

3.9 Schematic of the changing size of the Region of Interest (ROI). ROI is adapted for each frame separately before the image analysis. 42

3.10 Procedure for image analysis of the recorded data. Determine of PPA as an indicator for detachment and change in structure of the particle loading on the fiber. 43

3.11 Photographs (inverted) of the deposited particulates structure during one stretching and relaxation cycle of a particle loaded fiber. Without a superficial airflow. Elongation/contraction rate of 0.4 $mm\,s^{-1}$. Compact structure at the beginning. Above the images denoted: the elongation length of the fiber, the time of stretching experiment. Pictograms of the loaded fiber indicate the rotation of the fiber and the change in particle loading. No frame-fitting within this images. 44

3.12 Photographs (inverted) of the deposited particulates structure during one stretching and relaxation cycle of a particle loaded fiber. Without a superficial airflow. Elongation/contractions rate of 1.2 $mm\,s^{-1}$. Compact structure at the beginning. Above the images denoted: the elongation length of the fiber, the time of stretching experiment. Pictograms of the loaded fiber indicate the rotation of the fiber and the change in particle loading. No frame-fitting within this images. 46

3.13 Photographs (inverted) of the deposited particulate structure during one stretching and relaxation cycle of a particle loaded fiber. With a superficial airflow of 0.8 $m\,s^{-1}$. Compact particle structure on the fiber at the beginning. Above the images denoted: the elongation length of the fiber, the time of stretching experiment. Pictograms of the loaded fiber indicate the rotation of the fiber and the change in particle loading. No frame-fitting within this images. 47

3.14 rPPA plotted versus elongation and time during the stretching and relaxing procedure without and with an airflow. Constant elongation/-contraction rate of 0.4 $mm\,s^{-1}$. The pictograms indicate the rotation of the fiber and detachment phenomena occurring on the fiber like in Figure 3.11 & Figure 3.13. 49

3.15 Photographs (inverted) of the loaded fiber during detachment experiments with a constant elongation/contraction rate of 1.2 $mm\,s^{-1}$ and various superficial velocities of the airflow. a) 0.4 $m\,s^{-1}$, b) 0.6 $m\,s^{-1}$, c) 0.8 $m\,s^{-1}$ 51

3.16 rPPA of stretching experiments with different superficial airflow velocities and one elongation/contraction rate of 1.2 mms^{-1}. 54

3.17 Schematic of the stress model on a plane substrate covered with a matrix layer. Applied stress to the substrate. Modified from [93]. 56

4.1 Schematic of a contact between a) An ideal smooth surface and ideal spherical particle. b) A Rough surface of a non-stretched fiber and spherical particle. c) The surface of a stretched fiber with increased surface roughness. The interaction area (blue) is reduced to contact points by the increase of surface roughness. 64

4.2 a) Schematic of the experimental measurement setup placed beneath the AFM-measurement head. Showing the key components and the adjustment axis. The front camera is mounted on a long lever connected to the AFM base. b) Front view image of the clamped fiber beneath the cantilever and the bracket. Magnification of the cantilever carrier with the bracket in the notch. 68

4.3 Procedure for adhesion measurement on the non-stretched and stretched fiber 69

4.4 Images (Cutout) of the fiber surface in the non-stretched state (TOP) (0 %, 0 *mm*) and after stretching (BOTTOM) (22 *mm*, 38.7 %). Images generated with AFM (LEFT) and WLI (RIGHT) including the respective Height-Scale. 74
4.5 Images (Cutout) of the fiber surface at different stretching states 3.976 *mm* (7 %), 9.656 *mm* (17 %) and 15.3 *mm* (27 %). Three different fiber are shown. For each investigation of a stretching state, a new fiber was used. The images were generated using AFM (LEFT) and WLI (RIGHT). 75
4.6 Calculated roughness index RMS from WLI (red squares) and R_a (blue triangle) from AFM as a function of fiber stretching. Measured peak-to-peak distance (black circles) using WLI. 77
4.7 Pull-off force as a function of RMS of the elongated fiber - measured with AFM (blank symbols). Calculated adhesion force based on the model of Rabinovich et al. using the measured RMS and Peak-to-Peak distance at each elongation state (filled symbols) [116]. Polynomial fit for measured and calculated values (including measured roughness values). 78
4.8 Pull-off force as a function of RMS of the elongated fiber - measured with AFM. Calculated adhesion force (including measured roughness values and peak-to-peak values) according to Rabinovich model. [116] 80

5.1 Schematic of the filter matrix, in a cross section. LEFT: Normal mass accumulation matrix during the first (depth filter step) and the second filter step (transition step). [14] RIGHT: Potential distribution of particulate material after detachment and rearrangement of particles within the filter matrix. Fiber stretching was used to initiate detachment to clear up some void space. Modified from VDI 3677 [27]. 91
5.2 Schematic setup to produce an aerosol containing glass spheres and the deposition on a single fibre that is clamped at the fiber mounting device [106]. 94
5.3 (**LEFT**): Images (in the side view) of the loaded fiber after 5 min loading time (TOP) and after 15 min loading time (BOTTOM).Direction of airflow from the top to the bottom. Illumination from the front. (**RIGHT**): Schematic of the loaded fiber in the non-stretched state. Marked is the state of the interfacial layer and the condition of stress. 94
5.4 Procedure of a stretching experiment including the multiple stretching cycles (5 times). 96
5.5 Image (**A**) and schematic diagram (**B**) of the laser-light sheet measurement system. An expanded laser beam (thin sheet) runs below the fiber (shown in Figure 5.6B). The scattered light within the measurement area is captured focused onto a Photomultiplier (PM) and transferred into electrical impulses. 98

5.6 (**A**): Relative signal of beam intensity profile, measured in horizontal direction of laser sheet (below the fiber), total horizontal length of laser sheet 16 mm. (**B**): Image of laser sheet in the measurement chamber. Here the laser light sheet is projected onto a piece of paper below the stretchable fiber. Distorted view due to viewing angle. 99

5.7 (**TOP**) Size and cumulative number of detached particle structures measured with the Laser Structure Detection System (LSDS) during the five cycles of fiber stretching, comparing low (5 min loading time, green) and high (15 min loading time, red) particle loading of the fiber for two superficial velocities ($u_s = 0.05\, m\, s^{-1}$, left and $u_s = 0.8\, m\, s^{-1}$, right, respectively). (**BOTTOM**) Cumulative fraction of the detached particle structures from total particle structure determined with image analysis during the 5 cycles of fiber stretching. 101

5.8 (**LEFT**): Images (side view) of the loaded fiber after 5 min loading time (TOP) and after 15 min loading time (BOTTOM) at 8 % fiber elongation during the first stretching cycle. Same elongation velocity of 0.6 $mm\, s^{-1}$. Illumination of the structure from the front. (**RIGHT**): Schematic of the loaded fiber in the stretched state. Marked the physical state of the interfacial layer. 103

5.9 (**LEFT**): Images (side view) of the loaded fiber after 5 min loading time (TOP) and after 15 min loading time (BOTTOM) at 20 % fiber elongation during the second stretching cycle. Same elongation velocity of 0.6 mm s^{-1}. Illumination of structure from the front. (**RIGHT**): Schematic of the loaded fiber in the stretched state. Marked the physical state at the interfacial layer. 104

5.10 (**TOP**) Size and cumulative number of detached particle structures measured with the LSDS during the 5 cycles of fiber stretching. Comparing two different elongation velocities (1.2 $mm\, s^{-1}$, left; 12 mm s^{-1}, right) for two different superficial velocities during the stretching procedure (0.8 m s^{-1} and 0.05 $m\, s^{-1}$, respectively). (**BOTTOM**) Cumulative fraction of the detached particle structures from total particle structure. 105

5.11 $d_{50,0}$ and $d_{90,0}$ values of detached particle structures as function of elongation velocity (LEFT) and superficial velocity (RIGHT). All structures detached within 5 cycles of fiber stretching with the given parameters. Linear fits of the development of $d_{90,0}$ values. 108

6.1 LEFT: Pressure drop as a function of particle mass during the filtration time. RIGHT: Schematic of the filtration phases during a depth filtration process. a) Depth filter phase, b) Transition phase, c) Surface filter phase. 115

6.2 Fiber clamping device with five fibers. Enlarged view on the right: The fibers fixed to the comb have a spacing of 246 μm [90]. 118

6.3 Process flow diagram of the array loading procedure, including the optical equipment at the top of the inlet pipe for the observation of the clogging process on the fiber array. 119
6.4 Images of the non-loaded and loaded fiber before (**top**) and after processing (**bottom**) with MATLAB. (**right**) The free space is marked red. (**left**) The accumulated particle material in the spacing is marked turquoise. 122
6.5 Borderline of a loaded fiber after processing with MATLAB. The orange line symbolizes a single borderline of an unloaded fiber. bottom: Equation for the calculation of the ratio between the borderline of the particle structure to the borderline of the initial structure. Only the two inner fiber spacings are considered. 122
6.6 (**left**) Cut-out of a frame—original image. (**right**) Cut-out of a frame/schematic with bridges (red) in the interspaces between the fibers. Particulate material is colored white. The fiber is purple. 123
6.7 Schematic detection procedure of a bridge within the emerging particle structure on the array. The bridges are formed in the interspace between two fibers. A bridge divides one pore into two pores. 124
6.8 Development of mass on the array over fiber length (5 equally spaced fibers) as a function of TIF. 125
6.9 Relative accumulated particulate material in the spacing at the initial three evaluation points of the experiment, representing the depth filter phase and transition phase. A growth rate analysis was conducted for each curve to determine particle accumulation in the interspaces of the fiber array. 127
6.10 Particulate material on the fiber for two different flow velocities. All experiments were performed three times. 128
6.11 Rate of particle accumulation as a function of Stokes before Clopgging Point (CP). 129
6.12 Particle structures in experiments with three different superficial velocities at 4 evaluation points. 130
6.13 Particulate material on the array and the corresponding total number of bridges. All experiments were performed three times. 132
6.14 Images of the development of particle structure of the array in experiments with three different superficial velocities. 133
6.15 Development of boundary line for the three representative flow velocities over the complete duration of the experiments. The particle concentration in the feed flow was 1.6×10^5 #/cm^3. All experiments were performed three times. 134
6.16 Size and number of bridges between the fibers in the experiments up to CP. At 1.8 $m\,s^{-1}$, 0.65 $m\,s^{-1}$, and 0.25 $m\,s^{-1}$. Scaling of colors (number) is logarithmic. Size of bridges parallel to the axis of the fiber. 135

6.17 Images of the characteristic pores and bridges at three different airflow velocities during the loading procedure at the corresponding TIF. . . . 136

6.18 Hydraulic diameter of the pores between the fibers in the experiments before reaching CP. At 1.8 $m\,s^{-1}$, 0.65 $m\,s^{-1}$, and 0.25 $m\,s^{-1}$. Grayscale (total number) is logarithmic. The pores at TIF = 0 are the interspaces between the fibers. Plot for 0.65 $m\,s^{-1}$: Hole in the clogged particle structure. 137

7.1 Cummulative number based (Q_0) and volume based (Q_3) size distribution of the used polydisperse particulate material Spheriglass5000CP. . 147

7.2 a) Clamping device for just stretching the fiber array b) Clamping device for simultaneous stretching and changing the fiber distance by rotating the clamping combs. 147

7.3 Schematic representation of two clamped fibers. It is possible to enlarge and reduce the fiber distance by rotation of the fiber clamp. Here the increase in the fiber spacing. 148

7.4 Schematic setup to produce an aerosol containing glass spheres and the deposition on an fiber array that is clamped at the fiber mounting device [107]. 149

7.5 Schematic diagram of the laser thin film measurement system. An expanded laser beam (thin sheet) passes beneath the fiber array. The scattered light within the measurement area is focused onto a photomultiplier and converted into electrical pulses. 151

7.6 Schematic procedure for determining the proportion of unblocked area in the fiber interspaces of the array. 153

7.7 Morphology of the non-clogged particle structures on the fiber array as a function of the Stokes number. 154

7.8 Schematic of the three phases of detachment. Left: compact structures, Right: dendritic structures. Crack building, radial rearrangement of particle structures and detachment are visible. 155

7.9 Size of the detached particle structures as a function of the structural morphology (TOP: St = 10.05; BOTTOM: St = 3.62; Left: 0.6 mms^{-1}; Right: 1.2 mms^{-1}), as well as the elongation and flow velocity. 158

7.10 RFPI of the stretching experiments with a compact particle structure on the fiber array. 159

7.11 Left: Image section of the fiber array before stretching and after the 2nd stretching cycle for compact structures with a Stokes number of 10.05. Right: Schematic representation of the tilting of the particle structures into the fiber interspaces during stretching. No reversal of the tilted particle structure after relaxation of the fiber. 160

7.12 RFPI plotted versus the number of stretching cycles for the investigated non-clogged dendritic particle structures (St=3.62 and St=0.82) on the fiber array for different air flow and stretching velocities 161
7.13 Morphology of the clogged particle structures on the fiber array as a function of the Stokes number. 162
7.14 Particle size as a function of structural morphology (BOTTOM: St = 3.62; TOP: St = 10.05), stretching velocity , and air flow velocity. 164
7.15 RFPI after stretching procedure as a function of number of stretching cycles for the investigated clogged particle structures on the fiber array. Variation of air flow velocity, stretching velocities and morphology. . . . 166
7.16 Mean size of detached agglomerates from the fiber array as a function of each single stretching cycles for a compact and a dendritic initial structure. The stretching velocity is varied from 0.6 $mm\,s^{-1}$ to 1.2 $mm\,s^{-1}$. Size values of 0 indicate "no detachment". 168
7.17 Schematic on the differences between uniaxial and biaxial stretching in side and top view. The stretching and displacement of the fibers are indicated by visual markers in the case of biaxial elongation. 169
7.18 Compact and dendritic particle structure before and after five elongation cycle without and with change of fiber distance during the elongation process. 170

9.1 Schematic overview of the focus of experiments in this work and future studies concentrating on the macro level which is represented by an entire stretchable filter. 188

B List of Tables

3.1 Data of stretching procedure 40
3.2 Schematic of hypothesis on behavior of agglomerates and particles during fiber stretching. 55

4.1 Pull-off force measurements in combination with roughness. The applied method was either theoretical (theo.) or theoretical&experimental (theo.&exp.). 65
4.2 Median of pull-off force between Spheriglass particle with diameter 10.37 μm and polymeric fiber clamped in different specimen device. . . 70
4.3 Data used for the calculation of the Rabinovich Model [116] 73
4.4 Parameter of polynominal fit for the measured data for a given function of $y = Intercept + B1 * x^1 + B2 * x^2$ 81

5.1 Variation of loading time, average flow velocity, superficial velocity and elongation velocity 96

6.1 Characteristic numbers for the tested flow velocities. 120
6.2 TIF at the evaluation points for video-based analysis of the fiber array. 126

7.1 Dimensionless numbers of the loading procedure 150
7.2 Parameters for the stretching process. All parameters were combined and applied in each range of particle structure morphology. Experiments are performed, both with and without changing the fiber distance. 151